Departamento de Ingeniería Industrial II
Escuela Politécnica Superior
University of La Coruña

Experimental Validation of a Multibody Model for a Vehicle Prototype and its Application to Automotive State Observers

Roland Pastorino

A thesis submitted for the degree of

Doctor Ingeniero Industrial

Advisor: Miguel Ángel Naya Villaverde
Co-advisor: Javier Cuadrado Aranda

Ferrol, June 2012

A ma famille pour son soutien inconditionnel depuis toujours.

Resumen

Introducción

La dinámica de vehículos ha sido un campo de aplicación de la mecánica desde hace varias décadas. Antes de la llegada de los ordenadores personales en los años setenta, la dinámica de vehículos se estudiaba de forma analítica debido a las limitaciones de las matemáticas para resolver grandes sistemas. Hasta el momento, los modelos de vehículo eran relativamente simples ya que tenían que ser formulados de manera analítica. Con la aparición de los ordenadores comenzó a desarrollarse la disciplina relacionada con la simulación de sistemas multicuerpo. Esta disciplina está basada en métodos computacionales como la integración numérica para el cálculo de la dinámica de sistemas mecánicos complejos. Desde entonces las características de los ordenadores y las simulaciones multicuerpo han mejorado sustancialmente. Los modelos multicuerpo de vehículo y los programas de simulación destinados al análisis de la dinámica de vehículos pronto han aparecido en los años ochenta para compensar la falta de modelos completos de vehículos (Körtum, 1985). Estos modelos han ganado en complejidad y precisión para incluir algunos comportamientos y características de los componentes del vehículo y de sus subsistemas que no se consideraban anteriormente. Como consecuencia de esta evolución, el campo de la dinámica de vehículos se ha dividido en subcampos de aplicaciones como por ejemplo las simulaciones de vehículos para su ejecución en tiempo real, el análisis del comportamiento o del confort.

El Laboratorio de Ingeniería Mecánica de la Universidad de La Coruña se ha especializado en la simulación de modelos multicuerpo en tiempo real (Cuadrado et al., 2000, 2004a,b). La dinámica de vehículos en tiempo real es uno de sus campos de aplicación. Las coordenadas naturales y una formulación multicuerpo desarrollada en el Laboratorio, que permite simular mecanismos complejos en tiempo real con precisión y robustez, son las elecciones preferidas para modelizar vehículos en el Laboratorio (Naya et al., 2007). Esta tesis pretende aportar nuevos elementos para un mejor entendimiento de esta línea de investigación. En la práctica, la fiabilidad y la validez, que representan características de gran importancia a la hora de desarrollar modelos de vehículo, deben ser investigadas para los métodos de modelización de vehículos desarrollados en el Laboratorio. En efecto, es primordial verificar que la implementación sea correcta y también ajustar el grado de precisión del modelo a los requerimientos de la aplicación. A. H. Hoskins ha expresado claramente la necesidad de la validación afirmando que "Sin validación de la dinámica del vehículo solamente existe especulación que un modelo determinado prediga con precisión la respuesta del vehículo" (Hoskins and El-Gindy, 2006). Cualquier validación implica realizar ensayos experimentales para recabar datos de referencia que se comparan con los resultados de las simulaciones. La metodología de realización de los ensayos debe permitir generar los mejores datos de referencia posibles. Una de las únicas y la más completa metodología de validación de modelos de vehículos es la que se ha desarrollado para validar el *National Advanced Driving Simulator* (Garrott et al., 1997). Por consiguiente, se ha empleado en esta investigación.

Hoy en día, varios modelos simplificados de vehículo se emplean comúnmente en contro-

ladores de estabilidad embarcados (Tseng et al., 1999). El siguiente paso en la evolución de estos controladores sería el uso de modelos multicuerpo que se ejecutan en tiempo real. Esta evolución es comparable a la pasada evolución de las simulaciones de la dinámica de vehículos de modelos clásicos de vehículo a modelos multicuerpo. El uso de modelos multicuerpo de vehículo que se ejecutan en tiempo real en observadores de estados es un tema de investigación recientemente iniciado en el Laboratorio de Ingeniería Mecánica (Cuadrado et al., 2010, 2011). El empleo de técnicas de estimación de estados y modelos de vehículos altamente detallados debería proporcionar información no disponible si se usan modelos clásicos de vehículos. La substitución de los modelos clásicos por modelos multicuerpo no es trivial. Se deben investigar las diferentes maneras de escribir las ecuaciones del movimiento que aparecen en las varias formulaciones multicuerpo para que puedan ser empleadas con la máxima eficiencia posible en los observadores más comunes para sistemas nolineales (Grewal and Andrews, 2008). También cabe investigar los observadores para sistemas nolineales más recientes y ver si se adaptan mejor cuando se emplean con modelos multicuerpo (Julier and Uhlmann, 2004).

Metodología

Una precisa metodología ha sido empleada a lo largo de todo este trabajo. Para cada parte de éste, un estudio exhaustivo de los mejores artículos científicos, libros sobre la materia, grupos nacionales e internacionales de investigación ha sido llevado a cabo con el objetivo de conocer las prácticas actuales así como las líneas de investigación de otros grupos. La información recabada ha servido para valorar y guiar la investigación durante el transcurso de esta tesis. Periódicamente y desde el principio de esta investigación, los avances más significativos de ésta se han recopilado y presentados en los principales congresos nacionales e internacionales del campo correspondiente, con el fin de comprobar la calidad y la pertinencia del trabajo así como de constatar el interés suscitado. Fruto de estos valiosos comentarios críticos, algunos de estos trabajos se han mejorado y ampliado para ser publicados en las revistas científicas más prestigiosas de cada campo abarcado por este trabajo. Una lista de todos los artículos que se han publicado o que han sido aceptados y están a punto de ser presentados o publicados se encuentra a continuación. Según esta metodología, los últimos artículos en haber sido presentados en congresos se mejorarán y ampliarán para ser enviados a revistas científicas después o durante los últimos meses de esta tesis.

Por otra parte, como lo indica el título de esta tesis, uno de sus objetivos de esta investigación es la validación de un modelo multicuerpo de un prototipo de vehículo. Con el fin de obtener los mejores datos experimentales para validar este modelo, la completa y reconocida metodología de validación del *National Advanced Driving Simulator* ha sido aplicada. Comparaciones entre estos datos experimentales y los resultados de las simulaciones son la clave para demostrar la validez y la precisión del modelo multicuerpo desarrollado.

Conclusiones

Este trabajo se ha centrado en la investigación sobre modelos multicuerpo de vehículos para su ejecución en tiempo real y su aplicación a observadores de estados. Su aportación principal ha sido la elaboración de directrices para el desarrollo de dichos modelos y para la investigación teórica y práctica sobre su uso en observadores de estados

Primero, para evaluar la validez de las predicciones de las simulaciones, parte de la completa

metodología desarrollada para validar el modelo multicuerpo de vehículo del *National Advanced Driving Simulator* ha sido aplicada. Un prototipo de vehículo automatizado ha sido construido con el objetivo de repetir maniobras de referencia y generar datos de referencia para la validación. Durante el desarrollo de este prototipo, se ha hecho especial hincapié en el sistema de retorno de fuerzas al conductor que forma parte del sistema de dirección por cables (steer–by–wire). Un enfoque general para modelizar con precisión el conjunto amplificador–motor–reductora ha sido desarrollado y validado empleando el sistema de retorno de par al conductor de bajo coste compuesto por una reductora con planetarios de dos etapas, un motor de corriente continua con imanes permanentes y sin núcleo, y finalmente un amplificador lineal de cuatro cuadrantes. Este enfoque, que tiene en cuenta los juegos, la flexibilidad, el rozamiento estático y dinámico, así como los procedimientos de identificación, es aplicable a una gama amplia de conjuntos amplificador–motor–reductora. Una vez que el prototipo de vehículo se ha automatizado completamente, dos maniobras a bajas velocidades implicando la dinámica longitudinal del vehículo y también la lateral han sido repetidas 7 veces en una zona del campus de la escuela de Ingeniería. Los datos experimentales de referencia han sido obtenidos de las dos maniobras con el objetivo de validar el modelo de vehículo.

Después, la segunda parte de esta tesis ha sido dedicada al desarrollo de un modelo matemático del prototipo de vehículo automatizado mencionado anteriormente. Se trata de un modelo multicuerpo, con 14 grados de libertad, que se ejecuta en tiempo real y que ha sido preparado utilizando una librería para modelos multicuerpo en lenguaje `FORTRAN` así como un entorno de simulación programado en `C++` que incluye un entorno gráfico fiel a la realidad, un perfil preciso de la pista de prueba y detección de colisiones. El perfil preciso de la pista de pruebas ha sido obtenido mediante un levantamiento topográfico. Los subsistemas como los neumáticos o los frenos también han sido modelizados. Con el fin de comprobar la validez del modelo, los datos experimentales de referencia obtenidos de los sensores del vehículo han sido usados como entradas para el modelo para repetir las dos maniobras de referencia en el entorno de simulación. Entonces, determinadas variables de simulación han sido comparadas a sus homólogas experimentales provistas de un intervalo de confianza que caracteriza los errores del proceso de prueba en pista. Se han interpretado los resultados de las comparaciones para extraer directrices prácticas a la hora de preparar modelos de vehículo que se ejecutan en tiempo real.

Finalmente, el uso de modelos multicuerpo para simulaciones en tiempo real con observadores de estados ha sido investigado. El primer observador considerado ha sido el filtro de Kalman extendido en forma continua. Se ha investigado el empleo de dos formulaciones multicuerpo (la formulación matriz–R y la formulación por penalizadores) usando un mecanismo de 4 barras. El método de matriz–R, que ha demostrado tener mejor comportamiento y eficiencia que la formulación por penalizadores, se ha aplicado a un modelo multicuerpo complejo: el modelo de un Volkswagen Passat. A pesar de la precisión del filtro, no fue posible simular el modelo en tiempo real. Por consiguiente, nuevos desarrollos teóricos e implementaciones prácticas utilizando otro tipo de observadores nolineales, los filtros de Kalman de tipo sigma–point, han sido llevados a cabo con un mecanismo de 5 barras. Como resultado de la aplicación de estos observadores, se ha demostrado que el uso de integradores implícitos apenas aporta mejora comparado con el uso de sus homólogos explícitos, llevando de esta manera a una menor carga computacional para todos los filtros mencionados. Los filtros de Kalman de tipo sigma–point han demostrado tener mejor precisión pero una carga computacional más elevada que el filtro

de Kalman extendido en su forma continua. Sin embargo, presentan varias ventajas sobre este último: una implementación más sencilla, una estructura fácilmente paralelizable que ayuda a alcanzar el tiempo real y el posible uso de cualquier formulación multicuerpo que también ayude a reducir el coste computacional. A la vista de estos resultados, la elección del conjunto *observador, formulación multicuerpo e integrator* depende de los requisitos de la aplicación y es un compromiso entre la precisión de la estimación y la eficiencia computacional.

Lista de publicaciones científicas

Un total de once artículos han sido publicados en diversas revistas científicas de prestigio y congresos internacionales y nacionales. Un último artículo será presentado en el mes de noviembre en el Congreso Nacional de Ingeniería Mecánica.

Artículos de revistas científicas

Cuadrado J. , Dopico D. , Pérez J. A. , and Pastorino R. . Automotive observers based on multibody models and the Extended Kalman Filter. *Multibody System Dynamics*, 27(1): 3–19, 2011. doi: 10.1007/s11044-011-9251-1. iv, 4, 105, 112

Pastorino R. , Naya M. A. , Pérez J. A . , and Cuadrado J. . Geared PM coreless motor modelling for driver's force feedback in steer–by–wire systems. *Mechatronics*, 21(6):1043–1054, 2011. doi: 10.1016/j.mechatronics.2011.05.006. 20

Artículos de congresos internacionales y nacionales

Cuadrado J. , Dopico D. , Pérez J. A. , and Pastorino R. . Influence of the sensored magnitude in the performance of observers based on multibody models and the extended Kalman filter. In *Proceedings of the Multibody Dynamics ECCOMAS Thematic Conference*, Warsaw, Poland, June 2009. 4, 100, 111

Cuadrado J. , Dopico D. , Naya M. A. , and Pastorino R. . Automotive observers based on multibody models and the extended Kalman filter. In *The 1st Joint International Conference on Multibody System Dynamics*, Lappeenranta, Finland, May 2010. iv, 4, 105, 112

Pastorino R. . La simulation des systèmes multicorps dans l'automobile. *Interface, revue des ingénieurs des INSA de Lyon, Rennes, Rouen, Toulouse*, (111):22, 3ème et 4ème trimestre 2011.

Pastorino R. , Naya M. A. , Pérez J. A. , and Cuadrado J. . X–by–wire vehicle prototype: a steer–by–wire system with geared PM coreless motors. In *Proceedings of the 7th EUROMECH Solid Mechanics Conference*, Lisbon, Portugal, September 2009. 10

Pastorino R. , Naya M. A. , Luaces A. , and Cuadrado J. . X–by–wire vehicle prototype: automatic driving maneuver implementation for real–time MBS model validation. In *Proceedings of the 515th EUROMECH Colloquium*, Blagoevgrad, Bulgaria, 2010. 10, 14

Pastorino R. , Dopico D. , Sanjurjo E. , and Naya M. A. . Validation of a multibody model for an x–by–wire vehicle prototype through field testing. In *Proceedings of the ECCOMAS Thematic Conference Multibody Dynamics 2011*, Brussels, Belgium, 2011a.

Pastorino R. , Naya M. A. , Luaces A. , and Cuadrado J. . X–by–wire vehicle prototype : a tool for research on real–time vehicle multibody models. In *Proceedings of the 13th EAEC European Automotive Congress*, Valencia, Spain, June 2011b.

Pastorino R. , Richiedei D. , Cuadrado J. , and Trevisani A. . State estimation using multibody models and unscented Kalman filters. In *Proceedings of the 524th EUROMECH Colloquium*, Enschede, Netherlands, 2012a.

Pastorino R. , Richiedei D. , Cuadrado J. , and Trevisani A. . State estimation using multibody models and nonlinear Kalman filters. In *The 2nd Joint International Conference on Multibody Systems Dynamics*, Stuttgart, Germany, May 2012b.

Sanjurjo E. , Pastorino R. , Dopico D. , and Naya M. A. . Validación experimental de un modelo multicuerpo de un prototipo de vehículo automatizado. In *XIX Congreso Nacional de Ingeniería Mecánica (to be presented)*, Castellón, Spain, Nov. 2012.

Abstract

The simulation of multibody system dynamics is a key element of *Computer–Aided Design* and also a well–established tool in the development of new vehicles. A vehicle model is a typical multibody system made of rigid and/or flexible bodies that are interconnected by joints and usually undergo large translational and rotational displacements. In the last decade, real–time simulations of vehicle multibody models have gained interest thanks to the development hardware– or human–in–the–loop applications. Efficient multibody formulations must be employed to simulate complex systems in real–time and reliability of the models and validity are of the highest importance.

This thesis focuses first on the study of the validity of real–time vehicle multibody models developed at the *Laboratorio de Ingeniería Mecánica* of the University of La Coruña. For this purpose, a vehicle prototype has been built and automated in order to repeat reference maneuvers. The numerous sensors on the prototype gather the most relevant magnitudes of the vehicle motion (roll–pitch–yaw rates, wheel speeds, etc). Two low speed maneuvers involving the longitudinal and lateral vehicle dynamics have been repeated several times in a test area at the campus of the engineering school. A real–time multibody model of the vehicle prototype has been prepared as well as a simulation environment that includes a close graphical environment, a true road profile and collision detection. Subsystems like brakes or tires have also been modeled. Both test maneuvers have been repeated with the developed multibody model in the simulation environment using inputs that have been measured experimentally. Selected simulation variables have then been compared to their experimental counterparts provided with a confidence interval that characterizes the field testing process errors. The results of the comparisons have then been interpreted to extract useful guidelines to build real–time vehicle multibody models.

Once a real–time vehicle model is validated, it not only raises the possibility to be used in hardware– or human–in–the–loop applications but also in on–board stability controllers. Nowadays simplified vehicle models coming from the classical vehicle dynamics theory are commonly employed in on–board stability controllers. The use of real–time vehicle multibody models in state observers (a widely–used control technique in stability controllers) is a research subject initiated a few years before the beginning of this thesis at the *Laboratorio de Ingeniería Mecánica*. The last part of this thesis goes first over the developed implementation of the Extended Kalman filter, a common state observer for nonlinear systems, with multibody models and, after that presents several new implementations using this filter and other filters coming from the family of the sigma–point Kalman filters.

Résumé

La simulation de la dynamique des systèmes multicorps est un élément clef de la *conception assistée par ordinateur (CAO)* et aussi un outil bien établi dans le développement de nouveaux véhicules. Un modèle de véhicule est un système multicorps typique composé de corps rigides et/ou flexibles qui sont interconnectés par des liaisons mécaniques et qui généralement subissent de grands déplacements autant en translation qu'en rotation. Au cours de la dernière décennie, les simulations de modèles multicorps de véhicules en temps réel ont suscité un grand intérêt grâce au développement de simulations hybrides interactives. Des formulations multicorps efficaces doivent être employées pour simuler des systèmes complexes en temps réel et la fiabilité et la validité de ces modèles sont d'importance vitale.

Cette thèse se concentre d'abord sur l'étude de la validité des modèles multicorps de véhicule qui se développent pour des applications en temps réel au *Laboratorio de Ingeniería Mecánica* de l'Université de La Corogne. Pour ce faire, un prototype de véhicule a été fabriqué et automatisé dans le but de répéter des manœuvres de référence. De nombreux capteurs montés dans le prototype recueillent les magnitudes les plus pertinentes du mouvement du véhicule (roulis–tangage–lacet, vitesses des roues, etc). Deux manœuvres à basse vitesse qui impliquent la dynamique longitudinale et latérale du véhicule ont été répétées plusieurs fois dans une zone du campus de l'école d'ingénieurs. Un modèle multicorps temps réel du prototype de véhicule a été préparé ainsi qu'un environnement de simulation qui inclut un environnement graphique réel, un profil réaliste de la piste d'essai et détection de collisions. Les sous–systèmes comme les freins ou les pneumatiques ont aussi été modélisés. Les deux manœuvres d'essai ont été répétées avec le modèle multicorps dans l'environnement de simulation en utilisant des entrées mesurées expérimentalement. Certaines variables de simulation ont été ensuite comparées avec leurs homologues expérimentales pourvues d'un intervalle de confiance qui caractérise les erreurs du procédé d'essai sur piste. Les résultats de la comparaison sont alors interprétés pour soustraire des règles utiles dans le développement de modèles multicorps temps réel de véhicules.

Une fois qu'un modèle multicorps a été validé, il n'est pas seulement envisageable de l'utiliser pour des simulations hybrides ou interactives mais aussi pour des contrôleurs de stabilité embarqués. Dans l'actualité, des modèles de véhicule simplifiés provenant de la théorie classique de la dynamique du véhicule s'utilisent communément dans des contrôleurs de stabilité embarqués. L'utilisation de modèles multicorps temps réel de véhicule dans des observateurs d'état (une technique de contrôle très connue pour les contrôleurs de stabilité) est un sujet de recherche initié quelques années avant le début de cette thèse au *Laboratorio de Ingeniería Mecánica*. La dernière partie de cette thèse examine d'abord en détail l'implémentation développée jusqu'à présent utilisant filtre de Kalman étendu, un observateur d'état habituel pour les systèmes nonlinéaires et modèles multicorps. Ensuite de nouvelles implémentations utilisant ce même filtre ainsi que d'autres filtres provenant de la famille des filtres de Kalman de type *sigma–point* sont présentées .

Resumo

A simulación da dinámica de sistemas multicorpo é un elemento clave do deseño asistido por ordenador. É tamén unha ferramenta ben establecida no desenvolvemento dos novos vehículos. Un modelo de vehículo é un sistema multicorpo típico composto por corpos ríxidos e/o flexibles interconectados por unións. Xeralmente, estos corpos experimentan grandes desplazamentos tanto na traslación como na rotación. Nesta derradeira década, simulacións de modelos multicorpo de vehículo en tempo real suscitou especial interese. Este tipo de simulacións vai destinado a aplicacións hardware– o human–in–the–loop. Deben ser empregadas formulacións multicorpo eficientes para simular sistemas complexos en tempo real. A fiabilidade e a validez destes modelos son de vital importancia.

Esta tese céntrase no estudio da validez dos modelos multicorpo que desenvólvense para aplicacións en tempo real no *Laboratorio de Enxeñería Mecánica* da Universidade da Coruña. Con este fin, un prototipo de vehículo fabricouse e automatizouse co obxectivo de repetir manobras de referencias. Numerosos sensores recollen as magnitudes máis relevantes do movemento do vehículo (balanceo–cabeceo–guiñada, velocidades das rodas, etc). Dos manobras a baixas velocidades que involucrán a dinámica lonxitudinal e lateral do vehículo foron repetidas varias veces nunha zoa do campus da escola de enxe?ería. Preparouse un modelo multicorpo do prototipo do vehículo para unha execución en tempo real e un entorno de simulación que integra un entorno gráfico real, o verdadeiro perfil da pista e unha detección de colisións. Tamén foron modelados subsistemas como os freos e os neumáticos. Ambas manobras de proba foron medidas experimentalmente. A continuación, determinadas variables de simulación foron comparadas coas súas homólogas experimentais provistas dun intervalo de confianza que caracteriza os errores do proceso de ensaio na pista. Entón, o resultados da comparación foron interpretados para extraer pautas útiles para desenvolver modelos multicorpo de véhiculos que execútanse en tempo real.

Unha vez que o modelo multicorpo do vehículo é validado, no soamente surxe a posibilidade de usarlo en aplicacións hardware– y/o human–in–the–loop mais tamén en controladores de estabilidade embarcados. Na actualidade, modelos de vehículos simplificados provintes da teoría clásica da dinámica de vehículos empréganse comúnmente en controladores de estabilidade embarcados. O uso de modelos multicorpo de vehículos capaces de executarse en tempo real en observadores de estados (unha técnica de control ampliamente coñecida en controladores de estabilidade) é un tema de investigación iniciado poucos anos antes do inicio desta tese no *Laboratorio de Enxeñería Mecánica*. A derradeira parte desta tese trata primeiro a implementación desenvolta ata agora co filtro de Kalman estendido en modelos multicorpo. Despois preséntanse novas implementacións empregando este mismo filtro así como outros pertencentes a familia dos filtros de Kalman tipo *sigma–point*.

Acknowledgements

It is an undeniable fact that a thesis is first and foremost a personal achievement. However the integration into a research group is one of the keys of any thesis. Among all the researchers that surrounded me since my arrival to the *Laboratorio de Ingeniería Mecánica (LIM)* at the end of 2007, I wish first to warmly thank my advisors, Miguel and Javier, whose invaluable support has been a factor of success. I would also like to express my gratitude to the *LIM* research team: Alberto, Daniel, Urbano, Fran, Manuel, Amelia, Emilio and Jairo, who with their advice showed me the way in the darkest parts of my thesis. Special thanks go to Dario Richiedei and Alberto Trevisani, as well as the whole research team of the Mechatronics laboratory of Vicenza, for the fruitful collaboration. Usually, research laboratories mainly rely on public funds, so I would like to thank the Spanish Ministry of Science and Innovation and ERDF funds through the grant TRA2009-09314 too for its support in this research.
During a thesis, the working-day does not end when you close the door of the laboratory late in the evening. For this reason, I wholeheartedly want to thank my parents (Denise and Jean-Yves) and my brothers (Nicolas and David) for their unconditional support, as well as to apologize for my too short and sporadic stays at home. Last but not least, I want to thank Carolina for encouraging me despite having bravely endured countless and incomprehensible scientific lucubrations.

Agradecimientos

Es un hecho indiscutible que una tesis es ante todo un logro personal. Sin embargo la integración en un grupo de investigación constituye una de las claves de cualquier tesis. Entre todos los investigadores que me rodearon desde mi llegada al *Laboratorio de Ingeniería Mecánica (LIM)* a finales de 2007, quisiera primero dar las gracias a mis directores, Miguel y Javier, cuyo apoyo inestimable ha sido un factor de éxito. Me gustaría también expresar mi gratitud al grupo de investigación del *LIM*: Alberto, Daniel, Urbano, Fran, Manuel, Amelia, Emilio y Jairo, quienes con sus consejos me orientaron en las partes más oscuras de mi tesis. Dirijo unos agradecimientos especiales a Dario Richiedei y Alberto Trevisani, así como a todo el grupo de investigación del Laboratorio de Mecatrónica de Vicenza, por la fructífera colaboración. Generalmente, los laboratorios de investigación dependen principalmente de fondos públicos, por lo que quisiera agradecer el apoyo del Ministerio de Ciencia e Innovación así como de los fondos ERDF a través de la subvención TRA2009-09314.

Durante una tesis, la jornada laboral no se termina al cerrar la puerta del laboratorio tarde por la noche. Por esta razón, quiero de todo corazón dar las gracias a mis padres (Denise y Jean-Yves) y a mis hermanos (Nicolas y David) por su apoyo incondicional, así como disculparme por mis estancias en casa demasiado cortas y esporádicas. Por último, si bien no menos importante, quisiera dar las gracias a Carolina por haberme animado a pesar de haber soportado innumerables e incomprensibles elucubraciones científicas.

Remerciements

Il est irréfutable qu'une thèse est avant tout une réussite personnelle. Cependant l'intégration dans un groupe de recherche est une des clefs de n'importe quelle thèse. Parmi tous les chercheurs que j'ai côtoyés depuis mon arrivée au *Laboratorio de Ingeniería Mecánica (LIM)* à la fin de l'année 2007, je voudrais d'abord chaleureusement remercier mes directeurs, Miguel et Javier, dont le soutien inestimable a été un facteur de réussite. Je souhaiterais exprimer également ma reconnaissance à toute l'équipe de recherche du LIM : Alberto, Daniel, Urbano, Fran, Manuel, Amelia, Emilio et Jairo, qui avec leurs conseils m'ont montré le chemin dans les parties les plus obscures de ma thèse. Des remerciements spéciaux vont à Dario Richiedei et Alberto Trevisani, ainsi qu'à tout le groupe de recherche du Laboratoire de Mécatronique de Vicence, pour la collaboration fructueuse. Généralement, les laboratoires de recherche dépendent principalement de fonds publiques pour ce que je voudrais remercier le soutien du Ministère des Sciences et de l'Innovation espagnol ainsi que les fonds ERDF à travers de la subvention TRA2009-09314.

Au cours d'une thèse, la journée de travail ne se termine pas lorsque l'on ferme la porte du laboratoire tard le soir. Pour cette raison, je veux de tout cœur remercier mes parents (Denise et Jean-Yves) et mes frères (Nicolas et David) pour leur soutien inconditionnel, et aussi leurs présenter mes excuses pour mes séjours à la maison trop courts et sporadiques. Mon dernier remerciement, et non des moindres, va à Carolina pour m'avoir encouragé en dépit d'avoir enduré d'innombrables et incompréhensibles élucubrations scientifiques.

Contents

List of Figures

List of Tables

List of Datasheets

Acronyms

AC	alternating current. 20
AL	augmented Lagrangian. 48, 49
BBW	brake-by-wire. Brake-by-wire systems are electronically controlled braking systems. 11, 14, 15, 40, 42, *see* XBW
CAD	computer-aided design. 10, 11, 15, 17, 53, 82–84
CDKF	central difference Kalman filter. A SPKF variant. 100, *see* SPKF
CEMF	counter electromotive force. 36, 38
CI	confidence interval. 89, 90, 92, 96
COG	center of gravity. 53–71
CPR	number of full quadrature cycles per full shaft revolution (360 mechanical degrees). 16
CPU	central processing unit. 111, 114, 123, 125
DAE	differential algebraic equation. 3, 48, 49, 100, 102, 103
DAS	data acquisition system. 12, 14–18, 21, 34, 40, 53, 81, 113, 129
DC	direct current. 15, 19–21, 23, 26, 30, 33, 38, 128
DOF	degrees of freedom. 52–64, 66, 68, 70–72, 103, 112–114, 128
EKF	extended Kalman filter. Kalman filter for nonlinear systems that linearizes about the current mean and covariance. 5, 100, 104, 105, 108, 109, 111, 112, 114, 117–119, 122–125, 128, 129
FE	finite element. 74
FM	frequency modulation. 17
FT	field testing. xxxv, xxxvii–xxxix, 8–10, 17
GRV	Gaussian random variable. 105
HIL	hardware-in-the-loop. 3
HITL	human-in-the-loop. 3
I3AL	index 3 augmented Lagrangian. 48
IMU	inertial Measurement Unit. Electronic device fitted with acceleration, velocity and orientation sensors. 19
KF	Kalman filter. A mathematical method (recursive estimator) named after Rudolf E. Kálmán.. xxxv–xxxix, 100, 103–105, 114
LIM	Laboratorio de Ingeniería Mecánica. 2, 4, 5, 81
LKF	linearized Kalman Filter. 100

LRKF linear regression Kalman filter. This name is sometimes used for the SPKF. 100

MB multibody. xxxv–xxxix, 2–5, 9, 10, 17, 18, 48, 54, 57, 71, 73–75, 80–84, 89, 90, 92, 96, 97, 100, 102–105, 109, 111, 112, 114, 117, 120, 122, 125, 128, 129

NADS National Advanced Driving Simulator. A high-fidelity driving simulator situated at the University of Iowa. 4, 8, 9, 128
NVH Noise Vibration and Harshness. 74

ODE ordinary differential equation. 49, 101, 103–105, 108

PC personal computer. 12, 129
PI proportional-integral. A PI controller is a control loop-feedback controller. 22, 36
PID proportional-integral-derivative. A PID controller is a control loop-feedback controller. 16, 17
PM permanent magnet. 15, 20, 23, 38, 128
PSU power supply unit. It supplies current to computer's components. 12

RHS right–hand side. 107
RK2 Runge–Kutta 2 method. A second order explicit integrator. 104, 119, 122, 125
RMSE root mean squared error. 123, 125
RWM road wheel motor. Actuator that steers the wheels of a vehicle equipped with a SBW system. 15–17, *see* SBW

SBW steer-by-wire. Steer-by-wire systems are electronically controlled steering systems. 5, 11, 15–17, 19, 20, 38, 42, 128, 129, *see* XBW
SPKF sigma-point Kalman filter. 5, 100, 104, 111, 114, 123, 124, 128
SSUKF spherical simplex unscented Kalman filter. A SPKF variant based on the unscented transform. 100, 114, 119, 120, 122, 125, *see* SPKF & UKF
SWM steering wheel motor. Actuator that generates a driver's force feedback for a SWS system. 15–17, 19, 20, *see* SWS
SWS steering wheel system. Driver's force feedback system for SBW systems. xxxv–xxxix, *see* SBW

TBW throttle-by-wire. Throttle-by-wire systems are systems that control electronically the throttle pedal or valve. 11, 14, 40, 42, *see* XBW
TR trapezoidal rule. A second order implicit integrator. 104, 106, 108, 119, 120, 122, 125

UKF unscented Kalman filter. A SPKF variant based on the unscented transform. 100, 114, 117, 119, 120, 122, 125, *see* SPKF

VDANL Vehicle Dynamics Analysis, Non-Linear. Vehicle dynamics simulation code developed by *Systems Technology, Inc.*. 8
VDM Road Vehicle Dynamics Models for Roadway Analysis and Design. Vehicle dynamics simulation code developed by the *University of Michigan – Transportation Research Institute*. 8
VRTC Vehicle Research and Test Center. This is an American federal research facility. 9

XBW X-by-wire. X-by-wire systems refer to systems controlled electronically (brake-by-wire, throttle-by-wire...) in contrast to the traditional systems controlled mechanically. 9, 10, 15, 17, 20, 40, 48, 71, 75, 89, 128, 129

ZOH zero–order hold. 123

Glossary

In the whole document, the following typesetting rules for the mathematical notation have been adopted:

- vectors and matrices are in upright and bold types
- scalars are in italics and normal font types
- each glossary entry is followed by one of these three abbreviation: FT for field testing notation, SWS for the notation related to the steering wheel system, MB for the multibody notation or KF for the Kalman filtering notation.

Notation	Description	Page List
a	radial stiffness tire coefficient (MB)	76
a_1	coefficient of the differential equation of the longitudinal deflection of the tire (MB)	79, 80
a_2	coefficient of the differential equation of the longitudinal deflection of the tire (MB)	79
a_3	coefficient of the differential equation of the longitudinal deflection of the tire (MB)	79, 80
α	primary scaling factor defining the extension of the spread of the sigma–points around the mean of the estimates (KF)	117, 118
$\boldsymbol{\alpha}$	penalty factors (MB)	48–50, 103, 104, 108–111
α_1	load dependent coefficient for the gearbox. Unit: N m^{-1} (SWS)	26, 28, 32, 33
α_2	load dependent coefficient for the gearbox. Unit: N m^{-1} (SWS)	26, 28, 32, 33
α_3	load dependent coefficient for the gearbox. Unit: s/N m (SWS)	26, 32, 33
α_1'	load dependent coefficient for the motor. Unit: – (SWS)	26, 28, 32, 33
α_2'	load dependent coefficient for the motor. Unit: – (SWS)	26, 28, 32, 33
α_3'	load dependent coefficient for the motor. Unit: – (SWS)	26, 32, 33
b_1	coefficient of the differential equation of the lateral deflection of the tire (MB)	79, 80
b_2	coefficient of the differential equation of the lateral deflection of the tire (MB)	79, 80
b_3	coefficient of the differential equation of the lateral deflection of the tire (MB)	79, 80
β	scaling factor used to control the weighting of the zeroth sigma–point (KF)	118
b_g	constant parameter for the viscous term of the gearbox torque τ_g. Unit: A (SWS)	24, 25, 33
$\mathbf{C}$	damping matrix (MB)	49, 106–109
$\boldsymbol{\chi}$	sigma–point (KF)	117–119
c_x	longitudinal stiffness coefficient of the tire (MB)	78–80
c_y	lateral stiffness coefficient of the tire (MB)	78–80
d	radial tire damping coefficient (MB)	76
Δt_i	integration time step (MB)	79, 80, 122, 125

Notation	Description	Page List
Δt_s	update time step of the sensors (KF)	122, 123, 125
d_x	longitudinal damping coefficient of the tire (MB)	78–80
d_y	lateral damping coefficient of the tire (MB)	78–80
$\mathbf{e_n}$	contact normal (MB)	74, 75
$\mathbf{e_x}$	unit vector giving the direction of the longitudinal tire force (MB)	74, 75
$\mathbf{e_y}$	unit vector giving the direction of the lateral tire force (MB)	74, 75
$\mathbf{e_{yR}}$	unit vector defining the wheel plane (MB)	74, 75
$\mathbf{e_{zR}}$	unit vector defining the wheel orientation (MB)	74
$\mathbf{f}$	dynamics system function (KF)	101, 104, 105, 107–109
$\mathbf{F}$	linearization of the dynamics system function (KF)	101, 105, 107, 109
$\boldsymbol{\mathcal{F}}$	Function that expresses the dependent acceleration as function of the dependent coordinates and velocities (MB)	103, 104
F	tire force. Unit: N m (SWS)	76–80
F	friction force. Unit: N m (SWS)	26, 27
F_c	Coulomb friction level. Unit: N m (SWS)	25–27
F_s	level of the stiction force. Unit: N m (SWS)	25–27
F_z	vertical force of the tire. Unit: N (MB)	76
$\mathbf{g}$	nonlinear function to be solved using Newton–Raphson scheme (MB)	49, 50, 106–109
$\mathbf{G}$	coupling matrix between process noise and the state of a linear dynamic system (KF)	101, 102, 105
γ^*	tire camber angle. Unit: rad (MB)	75
γ	scaling factor defining the extension of the spread of the sigma–points around the mean of the estimates (KF)	117
$\mathbf{H}$	linearization of the measurement sensitivity matrix (KF)	101, 102, 105, 106, 108, 109
$\mathbf{h}$	measurement sensitivity matrix (KF)	101, 102, 105–107, 118
i	index used for iterative processes (MB and KF)	48–50, 106
i_a	motor's armature current. Unit: A (SWS)	22, 23, 34, 36, 37
i_{avg}	average current drawn by the motor. Unit: A. (SWS)	27
i_{dap}	current reference given by the digital acquisition processor. Unit: A. (SWS)	22, 34
i_{ref}	reference current for the amplifier. Unit: A (SWS)	22, 23, 34
i_{sat}^-	lower bound of i_{dap}. Unit: A (SWS)	22, 23
i_{sat}^+	upper bound of i_{dap}. Unit: A (SWS)	22, 23
J_1	inertia of the gearbox. Unit: kgm^2 (SWS)	29
J_2	inertia of the coupling. Unit: kgm^2 (SWS)	29
J_g	sum of the inertia of the gearbox and the coupling inertia. Unit: kgm^2 (SWS)	25, 29
J_m	inertia of the DC motor. Unit: kgm^2 (SWS)	23, 25, 29
J_{sw}	inertia of the steering wheel. Unit: kgm^2 (SWS)	25, 29
J_{tot}	inertia at the output shaft of the gearbox: $J_g + J_{sw}$. Unit: kgm^2 (SWS)	25
k	index used to indicate the time step (MB and KF)	49, 50, 101, 102, 104, 106–109, 117–120
$\mathbf{K}$	stiffness matrix (MB)	49, 106–109

Notation	Description	Page List
k_1	coeff. when $\lvert i_{ref}\rvert < \lvert i_a\rvert$. Unit: Ω (SWS)	22, 23
k_2	Coeff. when $\text{sign}(i_{ref}) \neq \text{sign}(i_a)$. Unit: Ω (SWS)	22, 23
κ	user–defined tuning parameter for the UKF (KF)	117
$\bar{\mathbf{K}}$	Kalman gain matrix (KF)	101, 102, 105–109, 111, 118–120
k_{g1}	constant parameter for the gearbox. Unit: N m/rad (SWS)	24, 29
k_{g3}	constant parameter for the gearbox. Unit: N m/rad^3 (SWS)	24, 29
k_{g5}	constant parameter for the gearbox. Unit: N m/rad^5 (SWS)	24, 29
K_i	integral coefficient for PI or PID controllers. Unit: N (SWS)	36
$k_{m,avg}$	DC motor torque constant. Unit: N m/A (SWS)	23, 27
K_p	proportional coefficient for PI or PID controllers. Unit: N (SWS)	36
k_s	stiffness of the torque sensor. Unit: N m/rad (SWS)	30
k_v	DC motor voltage constant. Unit: V/rad/s (SWS)	23
L	distance between two points. Unit: m (MB)	50, 51, 54–63, 65, 70
L	dimension of the state vector (KF)	117–119
L_a	leakage inductance in the armature winding of the DC motor. Unit: H (SWS)	23
λ	parameter of the UKF (KF)	117, 118
$\boldsymbol{\lambda}$	vector of Lagrange multipliers (MB)	48, 49, 102, 103
$\mathbf{M}$	wheel center coordinates (MB)	75
m	number of Lagrange multipliers (MB)	48
$\mathbf{M}$	positive definite mass matrix (MB)	48, 49, 102–111
n	sample number (FT)	89
n	gearbox ratio (ω_{in}/ω_{out}) (SWS)	24, 25, 33
n_d	number of dependent coordinates (MB)	48, 103, 104
n_i	number of independent coordinates (MB)	103–105, 107, 108, 112, 114
n_{sp}	number of sigma–points (KF)	117–119
ν	velocity of displacement (SWS)	26, 27
ν_n	small velocity used to avoid numerical problems (SWS)	76, 78, 80
ν_s	Stribeck velocity (SWS)	26–28, 33
ν_x	longitudinal velocity of the contact point (MB)	75–80
ν_x^*	modified tangential velocity of the tire tread (MB)	78, 79
ν_y	lateral velocity of the contact point (MB)	75–80
ν_y^*	modified tangential velocity of the tire tread (MB)	78–80
Ω	wheel angular velocity (MB)	76, 78–80
$\boldsymbol{\omega}$	natural frequencies of the constraints for the penalty formulation (MB)	48, 103, 104, 108, 109, 111
ω_m	DC motor angular velocity. Unit: rad/s (SWS)	23, 32, 34, 37
$\mathbf{P}$	geometric contact point coordinates (MB)	74, 75
$\mathbf{P}$	covariance matrix of state estimation uncertainty (KF)	101, 102, 105, 106, 117, 118
$\boldsymbol{\Phi}$	linearization of the state transition matrix (KF)	102
$\boldsymbol{\phi}$	state transition matrix (KF)	101, 102, 117, 118, 120
$\boldsymbol{\Phi}$	vector of constraints (MB)	48–50, 102–104, 108–111
ϕ	angle between two vectors or segments. Unit: rad (MB)	50, 51, 54–59, 61–63, 65–70, 72, 73, 120

Notation	Description	Page List
$\mathbf{Q}$	vector containing the external forces, the velocity–dependent inertia forces and those obtained from a potential (MB)	48, 49, 102–109, 111
$\boldsymbol{\mathcal{Q}}$	covariance matrix of the process noise (KF)	101, 102, 105
$\mathbf{q}$	vector of dependent coordinates (MB)	48–50, 102–104, 107–111, 120
$\mathbf{R}$	matrix defining a basis of the nullspace of the Jacobian matrix of the constraints (MB)	103, 105–108, 120
$\boldsymbol{\mathcal{R}}$	covariance matrix of measurement uncertainty (KF)	101, 102, 105
$\mathbf{r}$	reference point coordinates. Unit: m (MB)	50–52, 54–63, 65, 70
$\mathrm{R_a}$	resistance of the armature winding of the DC motor. Unit: Ω (SWS)	23
$\mathrm{r_D}$	dynamic rolling radius. Unit: m (MB)	76, 78, 79
s	varying distance. Unit: m (MB)	51, 70–72, 109–111
$\mathrm{s_c}$	critical generalized slip. Unit: - (MB)	76, 79, 80
S	sample standard deviation (FT)	89
$\mathrm{s_g}$	generalized slip. Unit: - (MB)	76, 78–80
σ_0	stiffness of the bristles. Unit: N m (SWS)	26–28, 32, 33
σ_1	damping coefficient of the bristles. Unit: N m/rad/s (SWS)	26, 27
σ_2	damping coefficient. Unit: N m/rad/s (SWS)	26–28
$\hat{\mathrm{s}}_\mathrm{x}$	normalizing factor for the longitudinal slip (MB)	76, 78
$\mathrm{s_x}$	longitudinal slip. Unit: - (MB)	76, 78–80
$\hat{\mathrm{s}}_\mathrm{y}$	normalizing factor for the lateral slip (MB)	76, 78
$\mathrm{s_y}$	lateral slip. Unit: - (MB)	76, 78–80
t	student's t distribution (FT)	89
t	time (MB and KF)	48–50, 101, 103–109, 123
τ_d	driver's torque acting on the steering wheel. Unit: Nm (SWS)	25, 36
τ_fg	friction torque that models the friction between the inner gears of the second stage and the ring gear of the two stage planetary gearbox. Unit: Nm (SWS)	25, 27
τ_fm	friction between the shaft and the armature as well as the friction between the inner gears of the first stage and the ring gear of the two stage planetary gearbox. Unit: Nm (SWS)	23, 25, 27
$\tau_\mathrm{f,no-load}$	friction force without load. Unit: Nm (SWS)	27
τ_g	gearbox's torque. Unit: Nm (SWS)	25, 26
$\tau_\mathrm{g\_elastic}$	elastic term of the gearbox torque. Unit: Nm (SWS)	24, 25
$\tau_\mathrm{g\_visc}$	viscous term of the gearbox torque. Unit: Nm (SWS)	24, 25
τ_m	motor's torque. Unit: Nm (SWS)	23, 25
θ_a	twist of the gearbox. Unit: rad (SWS)	24
$\dot{\theta}_\mathrm{a}$	first derivative of the twist of the gearbox. Unit: rad/s (SWS)	24
θ_g	gearbox angle. Unit: rad (SWS)	24, 36
$\ddot{\theta}_\mathrm{g}$	second derivative of the gearbox angle. Unit: rad/s^2 (SWS)	25
θ_m	motor angle. Unit: rad (SWS)	24, 32, 36
$\ddot{\theta}_\mathrm{m}$	second derivative of the motor angle. Unit: rad/s^2 (SWS)	25
$\mathbf{u}$	unit vector (MB)	50–59, 61–63, 65–72
$\mathbf{v}$	vector containing the coordinate vector and its first time–derivative (MB)	104
$\boldsymbol{v}$	measurement noise vector (KF)	101, 102, 105, 118
$\mathrm{V_a}$	voltage of the motor. Unit: V (SWS)	22, 23, 34–37
$\mathrm{V_{sat}^-}$	motor's voltage lower bound. Unit: V (SWS)	23

Notation	Description	Page List
V_{sat}^{+}	motor's voltage upper bound. Unit: V (SWS)	22, 23, 34
$\boldsymbol{w}$	process noise vector (KF)	101, 102, 105, 118, 120
w	weight for the SPKFs (KF)	118, 119
W	weight of the objective function for the projections (MB)	49, 50
$\mathbf{w}$	vector of dependent velocities (MB)	104–109, 111
x	sample (FT)	89
x	Cartesian coordinate (MB)	109, 120
$\mathbf{x}$	state vector (KF)	89, 101, 102, 105–110, 117–119
$\dot{x}_e$	longitudinal tire deflection velocity (MB)	77–80
x_e	longitudinal tire deflection (MB)	78–80
x_{e0}	initial longitudinal tire deflection for each integration time step (MB)	79, 80
$\boldsymbol{\mathcal{Y}}$	sigma–point propagated through the measurement sensitivity matrix (KF)	118
y	Cartesian coordinate (MB)	109, 120
$\mathbf{y}$	measurement vector (KF)	101, 102, 105–108, 111, 118–120, 123
$\dot{y}_e$	lateral tire deflection velocity (MB)	77–80
y_e	lateral tire deflection (MB)	78–80
y_{e0}	initial lateral tire deflection for each integration time step (MB)	79, 80
$\boldsymbol{\zeta}$	damping ratios of the penalty formulation (MB)	48, 103, 104, 108, 109, 111
z	average deflection of the bristles (SWS)	26, 27
z	vertical deflection of the tire. Unit: m (MB)	76
$\mathbf{z}$	independent coordinate vector (MB)	103–108, 119, 120

Chapter 1

Introduction

1.1 Motivations

Vehicle dynamics has been a privileged field of application of mechanics for decades. Before the advent of personal computers in the 1970s, vehicle dynamics were only studied in analytical form due to the mathematical limitations in solving large problems. Until that date, vehicle models remained relatively simple as they had to be expressed in closed-form. Since then, computer performances and multibody (MB) simulations have substantially improved. Vehicle MB models and simulation software to analyze vehicle dynamics rapidly appeared in the 1980s to make up for the lack of comprehensive vehicle models (Körtum, 1985). These models have gained in complexity and accuracy to include some behaviors, characteristics of vehicle components and subsystems that were not considered previously. As a consequence of this evolution, the vehicle dynamics field has divided into application sub-fields such as for instance vehicle real-time simulations, handling analysis or ride comfort analysis.

The Laboratorio de Ingeniería Mecánica (LIM) of the *University of La Coruña* has specialized in real-time MB simulations. Real-time vehicle dynamics is one of its application fields. Natural coordinates and a self-developed MB formulation that enables the simulation of complex systems to run in real-time with efficiency and robustness (Naya et al., 2007) are the preferred choices to model vehicles in the LIM. This thesis pretends to gain new insights into this research line. In practice, reliability and validity which are major concerns when developing vehicle models, must be investigated for the vehicle modeling methods developed in the LIM. Indeed, it is essential to check the correctness of the implementation and to adjust the level of accuracy of the model to the application requirements. In the automotive domain, this implies vehicle field testing to gather experimental data that is then compared to the predictions of the simulation. A. H. Hoskins clearly formulated the need for validation claiming that "Without validation of the vehicle dynamics there is only speculation that a given model accurately predicts a vehicle response" (Hoskins and El-Gindy, 2006).

Nowadays simplified vehicle models are commonly employed in on-board stability controllers (Tseng et al., 1999). The next step in the evolution of these controllers should be the use of validated real-time MB models. This can be compared to the past evolution of vehicle dynamics simulations from classical vehicle models to MB models. The use of real-time vehicle MB models in state observers is a research subject recently initiated at the LIM. Using state estimation techniques and highly-detailed vehicle models should provide information to the controllers that is not available when using classical vehicle models. The substitution of classical vehicle models by MB models is not trivial. Both theory and implementation aspects need to be deeply investigated.

1.2 State of the art of multibody analysis in the automotive field

In the last decade, MB analysis has become a standard to speed up the development process of vehicles (Fischer, 2007; Lugner and Plöch, 2004; Rauh, 2003). The reduction in cost, risk and time during the development is one of the most relevant contributions of MB techniques. MB models are not intended to replace vehicle models from the classical vehicle dynamics theory (Gillespie, 1992; Jazar, 2008; Wong, 2001) but to augment the range of the vehicle models. Vehicle models are at present divided into several groups that are employed at different stages of the vehicle development process. Rauh (2003) identified four groups. The

first, called *partial aspect models*, roughly describes certain aspects of the motion of the vehicle or the behavior of certain parts of the vehicle. The second group, named *behavior models*, outlines the main characteristics of the vehicle dynamics. The third group is made of *3D functional models* which allow to simulate the overall vehicle behavior and normally take into account inputs of the driver, 3D motion, four wheels, suspension elements, etc. The last group, composed of *3D component oriented models*, is the specific field of MB models. These highly detailed models represent each individual component based on its physical properties. The more detailed the model is, the more accurate the simulation predictions of the future vehicle dynamics are. In light of this classification, MB models do not appear to replace classical vehicle models but to widen the range of vehicle models. Literature that links MB books and classical vehicle dynamics books is slowly appearing (Blundell and Harty, 2004; Popp and Schielhen, 2010).

MB models are built either using self-developed specific tools and methods that guarantee efficiency and customizability, or using commercial MB softwares allowing greater ease of use at the expense in most cases of adaptability to new requirements and end-product integration. Typical MB softwares are *SIMPACK* from *SIMPACK AG*, *ADAMS* from *MSC* or even *Virtual.Lab Motion* from *LMS*. It is worth mentioning that MB models in the automotive industry have five different objectives that imply different modeling strategies: handling analysis, ride analysis, durability analysis, real-time applications and crash analysis. It should also be mentioned that due to the continuous improvement of computer performances and MB formulations, MB vehicle models are being used in more and more automotive subfields previously reserved to classical vehicle models. The five objectives are discussed hereafter.

The first three objectives (handling, ride and durability analysis) have similar model requirements. Vehicle handling analysis, the most common objective, aims at characterizing the vehicle dynamics. Ride analysis focuses on ride comfort while the objective of durability analysis is to improve the service life of vehicle components. For these analysis, real-time execution is not required but accuracy and ease of use are essential. Numerous MB models (self-developed or developed using commercial MB software) have been developed following these objectives. They are highly detailed models that normally include all the vehicle components with their nonlinear characteristics in order to quantitatively characterize the vehicle nonlinear behavior. The equations of motion of the vehicle are generally a set of differential algebraic equation (DAE). Since variable step size integration schemes adapt themselves to the system natural frequencies, they are commonly used to guarantee accurate solutions. As listing exhaustively all the MB models that were developed up to now for handling, ride and durability analysis would be a highly intensive task, a selection of relevant scientific papers is presented below instead. Hegazy et al. (2000) presented a 94 degrees of freedom nonlinear MB model. This model takes into consideration all the compliance sources. MB models with flexible chassis were developed using flexible MB formulations (Ambrósio and Goncalves, 2001; Cuadrado et al., 2004b). Rill (2006b) presented vehicle modeling by subsystems. Aerodynamic interactions were taken into account by Hussain et al. (2007) for a 102 degrees of freedom nonlinear MB model.

The fourth objective of MB models is related to real-time simulations. These simulations are used in human-in-the-loop (HITL) applications like high fidelity driving simulators or in hardware-in-the-loop (HIL) applications like component behavior evaluation systems. Real-time full-vehicle MB models can be built following two different approaches: complete

development of the model or reduction of a higher-detailed MB model. The first approach consists in creating vehicle models using, in most cases, rigid bodies and kinematic joints. On the one hand, the equations of motion can be symbolically derived like in *VehicleSim* (the symbolic multibody code generator of *CarSim*) or in *MapleSim* from *MapleSoft*. Real-time simulations using symbolic derivation were successfully implemented for example by Sayers (1996, 1999). Specific books on this MB modeling technique are available (Samin and Fisette, 2004). On the other hand, the equations of motion can be solved numerically leading also to real-time simulations (García de Jalón and Bayo, 1994). For example a recursive formulation with rigid bodies connected in an open loop structure or in a spanning tree was employed for the vehicle dynamics modeling of the National Advanced Driving Simulator (NADS) (Heydinger et al., 2002). A method that analyzes independently vehicle subsystems with a virtual reference body was proposed for real-time purpose (Kim, 2002b). The same author also employed quasi-static analysis to take into account bush compliance in real-time MB models (Kim and Jeong, 2009). Bae et al. (2000) presented an explicit integration method for real-time simulations of MB vehicle models. Efficient simulations of large vehicle systems were also studied (Rill and Cornelius, 2007). The aforementioned second approach to real-time full-vehicle MB models aims at increasing the reusability of these ones. Several authors have studied the transition from off-line highly-detailed MB models to real-time reduced MB models using model reduction techniques and modular vehicle modeling (Kim, 2002a; Pankiewicz and Rulka, 2003; Rulka and Pankiewicz, 2005). Independently of the modeling approach, an increasing number of real-time simulations were implemented in driving simulators (Salaani et al., 2007; Shiiba, 2002; Shiiba and Suda, 2007) as well as for automotive component evaluation (Kim et al., 2006; Naya et al., 2007). Recently, researchers from the LIM of the *University of La Coruña* have extended the use of real-time MB models to state estimation (Barreiro et al., 2008; Cuadrado et al., 2008, 2009a,b) and in particular to automotive state observers (Cuadrado et al., 2010, 2011). Even if the developed automotive observer does not run in real-time, the research has shown that real-time automotive observers using MB models will soon be available.

The last objective of MB models is associated to crash analysis. Recent works have looked into MB vehicle models with plastic deformation capability (Ambrósio, 2005; Carvalho, 2010; Sousa et al., 2008). This enables the analysis of vehicle handling taking into account crashworthiness.

The development of MB vehicle models following the five aforementioned objectives is spreading quickly and clearly expresses the need to extend the classical handling analysis to other types of analysis.

1.3 Objectives

The objectives of this thesis are the followings:

- To set up a vehicle prototype able to automatically repeat reference maneuvers. This prototype must be outfitted with numerous sensors to capture the vehicle motion magnitudes of interest. The driver's force feedback system has to be carefully modeled to enable the design of steering wheel torque controllers. One low speed maneuver involving the longitudinal dynamics of the vehicle prototype and another involving the lateral dynamics have to be performed and data of the sensors post-processed.

- To build a real-time MB model of the vehicle prototype using rigid bodies and kinematic joints. The equations of motion have to be solved numerically using among others the efficient MB formulation developed at the LIM. Subsystems (tires, brakes, etc) models have to be included. The simulation environment must include a close graphical environment, a true road profile and collision detection.

- To compare the field testing data with the simulation predictions to obtain the first validation results. In the light of these results, validity of the developed MB model has to be discussed.

- To develop the theory necessary to employ MB models with nonlinear Kalman filters. Observer variants and different MB formulations have to be taken into account. It is also necessary to investigate the implication for each observer in the selection of one or another MB formulation. Filter performance comparisons have to be carried out using simple mechanisms. Some observers have to be tested using real-time MB vehicle models.

1.4 Thesis structure

This thesis has been divided into six chapters:

Chapter 1 introduces the motivations that gave rise to this thesis. After that, this work is situated in the automotive field by a state of the art of MB analysis in this field. Finally, the objectives of this thesis are quickly described and the structure is presented.

Chapter 2 deals with vehicle field testing with a view to MB model validation. After the presentation of the validation methodology, the vehicle prototype prepared for field testing is extensively described. Special attention is payed to the driver's force feedback of the steer-by-wire (SBW) system. Lastly, the test maneuvers performed are presented as well as the most relevant vehicle dynamics magnitudes.

Chapter 3 treats first the vehicle modeling, including the MB formulation, details of the model and the modeling of the subsystems. The three main parts of the simulation environment (graphical environment, road profile, collision detection) are then presented.

Chapter 4 defines a confidence interval for the field testing data (gathered during the test maneuvers) that is employed in comparisons with simulation predictions. The results of these comparisons are discussed.

Chapter 5 is dedicated to state estimation using Kalman filters and MB models in the automotive field. First, the theory related to the extended Kalman filter (EKF) with MB models is presented. Then, the performances of this observer are studied using both a 4–bar linkage and a MB vehicle model. Lastly, the theory of sigma-point Kalman filter (SPKF) using MB models is introduced and test performances with a 5–bar linkage are performed.

Chapter 6 draws the conclusions and proposes possible future research lines.

Chapter 2

Field testing using an X–by–wire vehicle prototype

2.1 The validation methodology

2.1.1 Background and state of the art of vehicle model validation

When designing a vehicle model, reliability is a major concern. Indeed it is essential to adjust the level of accuracy of the model to the application requirements. In the automotive domain, this implies vehicle field testing (FT) to gather experimental data in order to evaluate the accuracy of the model through comparison. A. H. Hoskins clearly expressed the necessity to validate vehicle models:

> "Without validation of the vehicle dynamics there is only speculation that a given model accurately predicts a vehicle response" (Hoskins and El-Gindy, 2006).

Despite the omnipresence of vehicle models in the automotive industry, validation studies are scarce. Several reasons explain the lack of such studies in the literature. First, extensive FT using commercial vehicles for validation purposes is very expensive. Such validation studies are reserved for vehicle research centers or vehicle manufacturers as universities can normally not afford the cost. Next, the major part of these studies can not be published for confidentiality reasons. As a result of this situation, up to now, the validation study developed for the NADS is one of the few and by far the most important published validation research in the automotive field (Garrott et al., 1997). Also, the fact that the experimental data of the NADS's FT have been made available to anyone for free, can explain the small number of validation studies. Companies and research centers took advantage of this source of information to test the accuracy of their simulations. This has been the case for some famous vehicle models like Vehicle Dynamics Analysis, Non-Linear (VDANL) from *Systems Technology, Inc.* or even Vehicle Dynamics Models for Roadway Analysis and Design (VDM Road) from the *University of Michigan – Transportation Research Institute* (Chrstos and Heydinger, 1997). Vehicle simulation softwares like *CarSim* (Kinjawadekar et al., 2009; Sayers, 1999), *ADAMS* (Rao et al., 2009) or *SimCreator* (Romano, 2003) have also tested their simulation codes against the FT data of the NADS. The rest of vehicle dynamics validations using FT that have been published are related to specific vehicles or conditions like trailers (Evers et al., 2009), light-duty vehicles (Cheli and Sabbioni, 2007; Wei-qun et al., 2003), military vehicles (Romano and Schultz, 2004), vehicles in winter conditions (Parker et al., 2009), forklifts (Rebelle et al., 2009), agricultural tractors (Lehtonen, 2005). Some vehicle models are also validated against famous vehicle simulation softwares (Kim et al., 2005).

When model validation is concerned, it is necessary to define the meaning of *simulation validity*. Nevertheless, it is a difficult task as this is a subjective concept that greatly depends on the objectives of the research. A general definition that encompasses a wide variety of validation types has been proposed by W. R. Garrott:

> "A simulation will be considered to be valid if, within some specified operating range of the physical system, a simulation's predictions of the system's responses of interest to specified input(s) agree with the actual physical system's responses to the same input(s) to within some specified level of accuracy" (Garrott et al., 1997)

In every validation process, apart from defining the meaning of *simulation validity*, the validation methodology has also to be defined precisely. As previously mentioned, vehicle

Figure 2.1: The National Advanced Driving Simulator

model validation is achieved through FT. This can be done in many different ways that involve distinct vehicle types. To cite the most common, the FT vehicle can be a scalable vehicle, a commercial vehicle or even a vehicle prototype. Albeit the dynamics of a scalable vehicle differs substantially from the dynamics of a full scale vehicle, its reduced cost makes it an attractive solution for some tasks like evaluating MB formulation efficiency or MB model accuracy. Next, the use of commercial vehicles appears to be the best solution for FT. However, it has some important drawbacks such as the difficulty to automate the vehicle for autonomous maneuvers or even the lack of information concerning the vehicle parts. Therefore, to overcome these difficulties, deep modifications have to be done on the vehicle to instrument it, and then, a great amount of identification tests have to be performed on each part. All this leads to an expensive validation process. Another option is to employ a self-developed vehicle prototype. Being self-developed, all the parameters of the vehicle are known. Only a few identification tests for some commercial parts (i.e. engine, etc) must be performed. Besides, the automation of the vehicle as well as special spaces and locations for sensors and for the data acquisition system can be included in the design of the prototype at an early stage thus avoiding excessive costs. In this research, this last solution has been selected. The designed vehicle prototype is a full scale vehicle outfitted with several by-wire systems. This X-by-wire (XBW) vehicle prototype is presented in detail in section 2.2.

2.1.2 The validation methodology developed for the NADS

The methodology employed in this research is deeply inspired by the one developed to validate the vehicle dynamics simulation of the NADS: *NADSdyna* (Garrott et al., 1997). The NADS, situated at the University of Iowa, is one of the most famous high-fidelity driving simulator in the world. *NADSdyna* is a real-time multibody dynamics software supplemented with vehicle dynamics specific modules. In the last decade, the NADS has been improved and validated by the Vehicle Research and Test Center (VRTC). Figure 2.1 shows the NADS's bay.

Below follows a quick summary of the three main phases of the NADS validation methodology. The first phase concerns the experimental data collection through vehicle FT (Chrstos and Grygier, 1997; Heydinger et al., 2007; Salaani and Heydinger, 2000; Salaani et al., 2001). The driving maneuvers have to be carefully chosen to cover a broad range of vehicle operating conditions: longitudinal and lateral dynamics, low and high speeds, transient

and steady state, etc. Next, to discard any error due to sensor noise and errors, external disturbances, filtering, post-processing, etc, during vehicle dynamic responses measuring, each maneuver is repeated several times. In that way, the experimental benchmark data, that are employed to validate the MB vehicle model, is obtained from the average over the repetitions of each sensor data. This increases the quality of the benchmark data. Consequently, to manage to repeat the test maneuvers, the test vehicle must be automated. Aside from the improvement of the experimental benchmark data, another interesting advantage of data averaging over several identical maneuvers is the determination of the uncertainty of the experimental testing and measurement process. During the first phase of this validation methodology, special attention has to be paid to maneuver repeatability when automating the vehicle. A poor repeatability would be worst than a single maneuver while a good repeatability can greatly improve the experimental benchmark data and also define the error zone. Finally, the last point of this first phase is an extensive post-processing that includes extraction of the time zone of interest, offset removing, digital filtering, etc.

The second phase of the validation methodology focuses on the determination of the vehicle parameters (Salaani et al., 2007, 1997a). These simulation parameters (mass moments of inertia of the different parts, their geometry, their mass ,etc) must be precisely measured using proper methods.

Finally, the third phase consists in comparing the simulation predictions with the benchmark data (Heydinger et al., 2007; Salaani and Heydinger, 2000; Salaani et al., 1997b, 2001). For this purpose, the simulation parameters of the MB model are the parameters of the second phase of the validation methodology. The inputs of the MB model are obtained by averaging the sensor measures over the repetitions of the maneuver. Each maneuver is repeated with the MB model using these averaged inputs. Then, the predictions of the simulations are compared with the results of the first phase of the validation methodology (i.e. the FT).

The different steps for the application of the methodology to this research are detailed hereafter. For the first phase, the set-up for automatic maneuver repeating on the vehicle prototype is presented in detail in section 2.2. Then, the choice of the control inputs to repeat maneuvers with the vehicle is treated in section 2.2.3. Finally the determination of the confidence interval is addressed in section 4.1. Regarding the second phase, as the vehicle prototype in this research is self-developed, this phase is straight forward. Almost all the simulation parameters are known from computer-aided design (CAD) models and only few identification tests have to be performed. For the third phase, the validation results obtained by comparing experimental data with simulation predictions are presented in Chapter 4.

2.2 The X–by–wire vehicle prototype

2.2.1 Overview

The test vehicle in this research is a self-developed XBW vehicle prototype. The motivations of this choice are explained in section 2.1. An XBW vehicle is a vehicle that is equipped with several electronically controlled systems (throttle, brake, steering system...). Figure 2.2 demostrates the vehicle prototype developed at the Mechanical Engineering Laboratory of the University of La Coruña (Pastorino et al., 2009, 2010). During the development phase, the dominant trends have been flexibility and low cost while complying the requirements. When designing a vehicle for automatic maneuver repeating, the first part to be chosen is

Figure 2.2: Self-developed XBW vehicle prototype

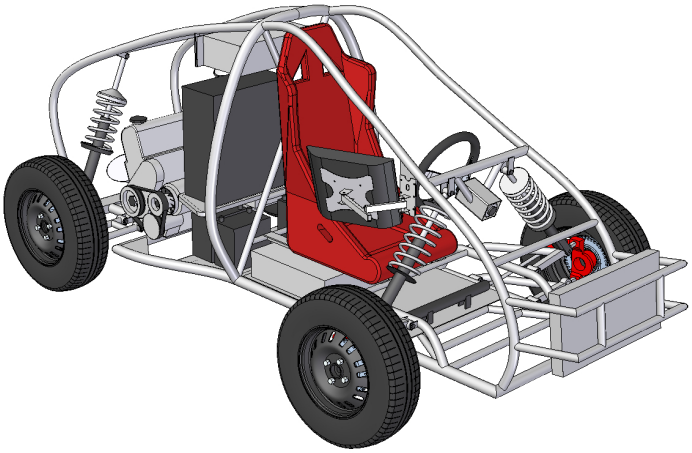

Figure 2.3: CAD model of the vehicle prototype

the engine. In this case, there exist two main options: an internal combustion engine or an electric engine. In this research, an old internal combustion engine with 4 cylinders, a 2-barrel carburetor and an automatic gearbox transmission has been employed in order to maintain low costs. It is essential that the engine can shift gears automatically in order to simplify the vehicle automation. The frame has been made of tubes, the front suspension is of double wishbone type while the rear suspension is of MacPherson type and the tyres are 4 Michelin tyres 155/80 R13. With a view to maneuver repeating, the vehicle prototype has been provided with several by-wire systems: a SBW, a throttle-by-wire (TBW) and a brake-by-wire (BBW) systems. They are latter described in section 2.2.3. As well as the sensors of the by-wire systems, multiple other sensors are necessary to measure the vehicle dynamics of interest. They are presented in section 2.2.4. Figure 2.3 shows the CAD model of the vehicle prototype. The choice of the prototype control inputs for maneuver repeating and the multibody model inputs for simulation are closely dependent. The firsts must control the engine, the braking and the steering of the vehicle prototype. This implies that within the multibody model, each one of the controlled subsystems must be modeled. To facilitate the design process of these subsystems, special sensors that sense the operations of the subsystems can provide useful information. This point will be discussed in sections 2.2.4 and 3.1.2.

2.2.2 The digital acquisition system

A complete on-board data acquisition system (DAS) is essential to gather information of the sensors, to control by-wire systems and to establish communication channels with the on-board computer. Numerous DASs that fulfill part or all these requirements are available on the market. Therefore, it is crucial to define precisely the features that the DAS must have and the tasks it has to accomplish. In turn, this depends a lot on the number and types of the sensors mounted on the vehicle. However, these characteristics are not always known in advance. Moreover, it is also interesting to have the possibility to use both Windows and Linux operating systems. Indeed, most DAS have better end-user applications for rapid developing under Windows while numerous specific applications run in Linux in order to take advantage of the following characteristics: efficiency, open-source, customizability, real-time, etc. The DAS must also allow to create custom user commands that extend the capabilities of the system for special tasks. Therefore, the best DAS for vehicle research purpose is a flexible modular expandable and programmable one.

In accordance with these requirements, a PC-based DAS with PCI host interface has been employed in this work. A connection scheme for the DAS, personal computer (PC), sensors, drivers and actuators is shown in fig. 2.4. A main board (model *DAP4200a* from *Microstar Laboratories*) has been purchased. One of its advantages is that it is installed in a standard computer thus maintaining reduced costs. This system is designed for high speed data transfers and real-time data acquisition. The sample period is specified with a resolution of 100 ns. User-defined processing commands can be created in `C/C++` language for special tasks and a `C++` library is available to interface the main board with computer applications. The on-board computer is powered by a non-standard power supply unit (PSU). A special 250 W PSU (model *M4-ATX* from *mini-box*) has replaced the standard PSU. It is powered directly by the car battery. Designed for vehicle on-board applications, it avoids computer shutdown at the engine start and also gives a good protection against over-voltage situations. PSU monitoring software is available for both Windows and Linux. A screen, a wireless trackball and a wireless keyboard help the driver to control on-board the DAS.

Despite the fact that the main board is already fairly complete, specific signal interfaces for some sensors are usually necessary. Therefore five expansion boards that are connected to the main board complete the DAS. They are located in a separate rack under the driver's seat. The first one (model *MSXB 037*) provides 16 analog inputs with 14-bit A/D converter resolution and has several input voltage configurations. It is connected to an analog backplane (model *MSXB 030*) that in turn is connected to an analog backplane interface board (model *MSXB 029*).

The second and third boards (model *MSXB 056*) have 8 analog outputs with 16-bit D/A converter resolution and have also several input voltage configurations. The fourth board (model *MSXB 036*) is a high speed counting board used for rotational speed (tachometer) measurement. Ten independent counter inputs with 16-bit resolution are available. Two of them have a maximum input frequency of 100 MHz while the rest have a maximum frequency of 6.8 MHz. Finally, the fifth board (model *MSXB 050*) is a quadrature decoder board that is used for high speed angle counting. It has 4 input channels with 16-bit resolution and a maximum frequency of 1 MHz for each counter. The independent counting feature of the last two boards avoids to overload the main board with extensive counting and quadrature-decoding tasks. The last four boards are all connected to a digital backplane (model *MSXB 034*). This

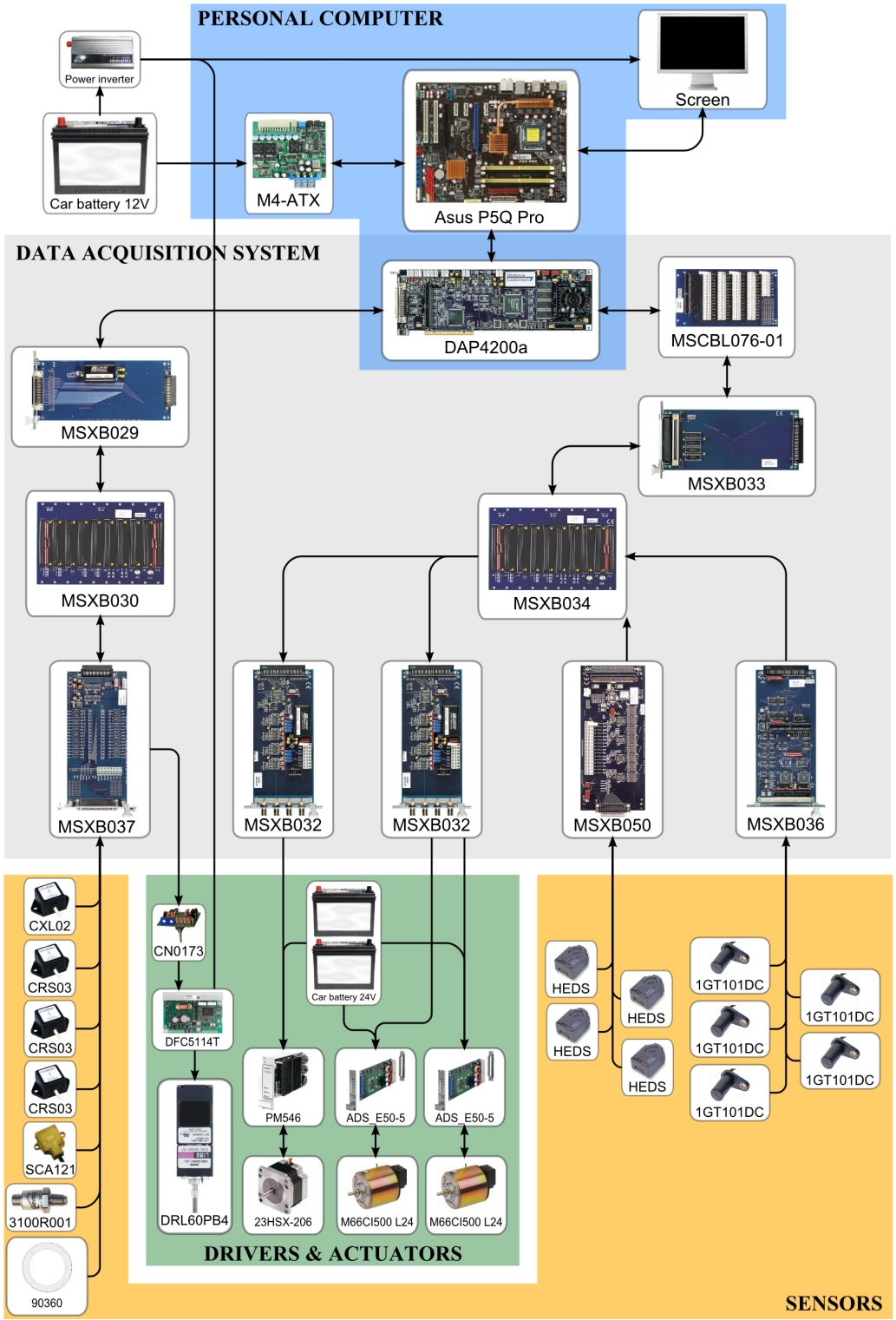

Figure 2.4: Connection scheme: DAS, PC, sensors, actuators, drivers

backplane is then connected to a digital backplane interface (model *MSXB 033*) that in turn is connected to a digital adapter panel (model *MSCBL 076-01*).

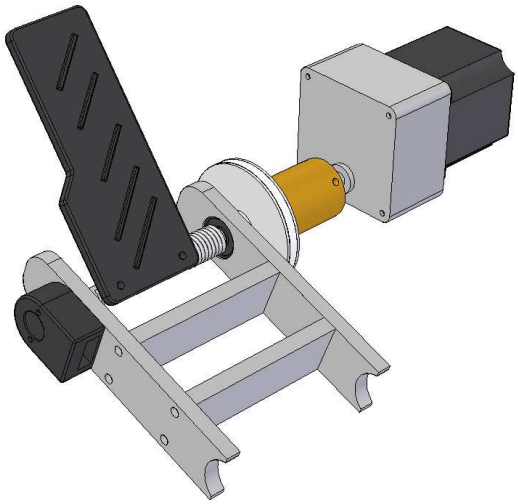

Figure 2.5: CAD model of the TBW

2.2.3 By-wire systems

As previously mentioned, the vehicle prototype has been equipped with three by-wire systems. Their characteristics, presented by Pastorino et al. (2010), are discussed below.

The TBW system

The conventional throttle cable system of the vehicle prototype has been converted into a TBW system, as shown in fig. 2.5. A geared stepper motor has been mounted on the axis of the throttle pedal. The motor (model *23HSX-206* from *Mclennan*) is a hybrid stepper motor that provides 200 $^{\text{steps}}/_{\text{rev}}$ with full step drives. The gearbox (model *MRIG02* from the same manufacturer) has a ratio of 5:1. As a consequence, the output shaft of the geared motor has an angular resolution of 1000 $^{\text{steps}}/_{\text{rev}}$ or 0.36°. The motor is controlled by an economic bipolar drive (model *PM546* from *Mclennan*) that is connected to a 24V battery (two car battery in series). In order to control the throttle pedal position, an encoder (model *HEDS 5540 A06* from *Agilent*) has also been mounted on the shaft of the pedal. Finally, a simple digital closed-loop controller that uses the error between the actual and the reference throttle angle has been programmed in `C` as a custom command of the DAS. The code, as well as the datasheets of the components of the TBW, are available in the appendices A, B and C.

The BBW system

The brake system has also been converted into a by-wire system, as shown in fig. 2.6. Like for the conventional use of a brake, the BBW system actuates on the vacuum servo. The selection of the actuator is a bit more challenging than that of the TBW system, especially when attempting to maintain reduced costs. As the motion of the piston of the vacuum servo is linear, it seems natural to employ a linear actuator. However, linear actuators are most expensive than their rotational counterparts. This is particularly true if the axial force has to be greater than a few hundreds of Newtons. If a rotational actuator is employed, a system has to convert the rotational movement into a linear one. This could be a mechanism, a ball screw...

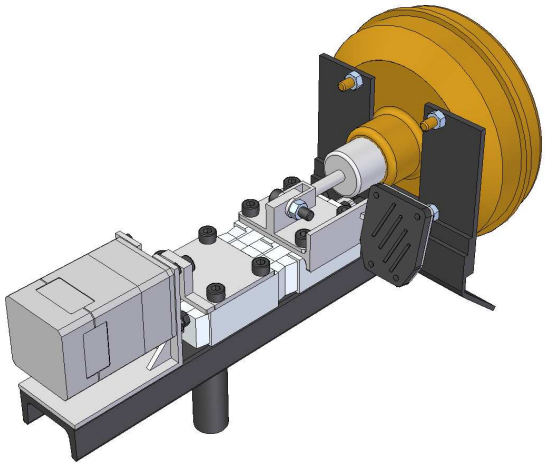

Figure 2.6: CAD model of the BBW

A ball screw system is generally selected when the space is limited. Next, the motor can be a direct current (DC) motor, a stepper motor, etc. The preferred solution in this research has been a 5 phase stepper motor with an integrated ball screw (model *DRL60PB4-05G* from *Oriental motor*). An indexer (model *CN0173* from *Centent*), controlled by the DAS, provides the high frequency step signal to the driver of the motor (model *DFC5114T* from *Oriental motor*). The driver is powered by a power inverter connected to the 12V battery. This indexer avoids to overload the main board of the DAS with extensive output updating tasks. Concerning the control scheme, several experiments have shown that the control of the brake motion based on its positions (measured by a linear encoder) does not guarantee a good accuracy of the brake pressure. This pressure, which is the variable of interest for the BBW, is measured by a pressure sensor (model *3100R0040G0LB00* from *Gems*). Therefore, the digital closed-loop control has been based on the error between the reference and brake pressures. The code, as well as the datasheets of the components of the BBW, are available in the appendices A, B and C.

The SBW system

The steering system is the third and last system that has been converted into a by-wire one. A diagram of the SBW system that equip the XBW vehicle prototype is presented in fig. 2.7. SBW systems have no mechanical linkage (steering column) between the steering wheel and the rack and pinion gear system. Therefore the steering task is performed by two electrical motors. The first, the road wheel motor (RWM) steers the front wheels of the vehicle following the angular position of the steering wheel. The second motor, called the steering wheel motor (SWM), is responsible for generating a reaction torque to the steering wheel. This is the driver's force feedback motor. Figure 2.8 demonstrates the CAD model of the rack system. This system is composed of two identical geared DC motors, three encoders and a torque sensor. The motors (model *M66CI 500 L-24* from *Mclennan*) are low inertia coreless permanent magnet (PM)DC motors. They feature linear speed and torque characteristics combined with rapid acceleration and reversal capabilities. Each motor rear plate is fitted with an encoder (model *HEDS 5500 A06* from *Agilent*) whose resolution is

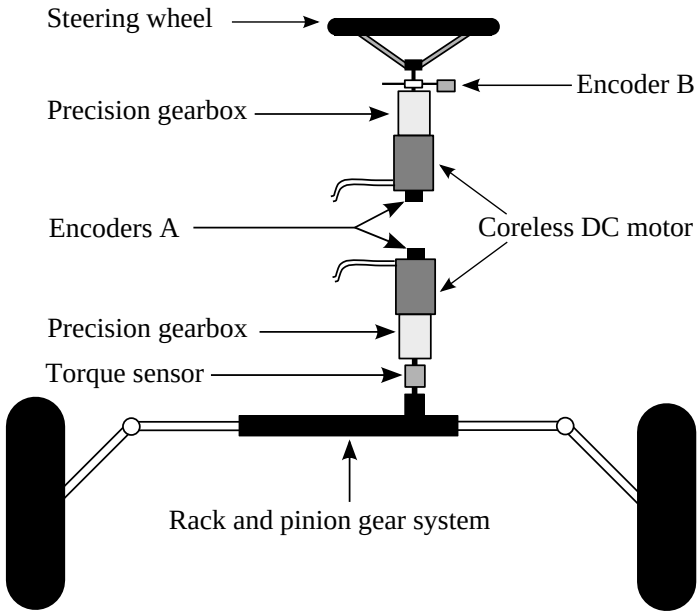

Figure 2.7: Diagram of the SBW system of the XBW vehicle prototype

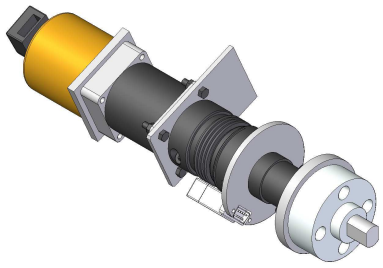

Figure 2.8: CAD model of the rack system for the SBW system

0.18° with 500 cycle per revolution (CPR). They are designated as *encoders A* in fig. 2.7. The motor gearboxes (model *IP57-M2-50* from *Mclennan*) are high strength. They have a two-stage planetary construction that provides high torque in compact dimensions. The backlash angle is small (≤0.5°) and the gearbox ratio is 50 (ω_{in}/ω_{out}). Each motor is controlled by a servo-amplifier(model *ADS E 50-5* from *Maxon motor*) that is connected to the 24V battery. The torque sensor (model *TFF 350 - FSH00646* from *Futek*) has a range of ±17 Nm. It senses the torque in the rack system. A signal conditioner (model *CSG110 - FSH01449* from the same manufacturer) amplifies the measures of the torque sensor and pass them to the DAS. Finally, an encoder (called *encoder B* in fig. 2.7) is connected to the output shaft of the gearbox to sense the steering wheel angle. Since the output shaft turns fifty times slower than the shaft of the motor, this encoder must have a higher resolution (0.0036° with 2500 CPR) than *encoder A*.

In SBW systems, two controllers are necessary. One for the RWM and another for the SWM. Here, the input of the RWM controller is the error between the angles of encoder B (situated under the steering wheel) and encoder A (the one of the rack system). A digital proportional-integral-derivative (PID) controller, that takes as input this error, controls the current of the RWM thus steering the front wheels. Considering the SWM, the steering

torque signal given by the torque sensor is fed back into the servo-amplifier of the SWM. Three controller configurations can be adopted. The first one is a digital current open-loop controller. It directly inputs the steering torque signal to the SWMs servo-amplifier that replicates the steering torque into the steering wheel. This controller configuration has been employed during the FT maneuvers (see section 2.4). The second possible controller would be a closed-loop controller that uses an electrical current sensor to measure the current of the motor. As the current is proportional to the torque of the motor, the input of an electrical current PID controller (i.e. the torque error) can be calculated. Finally, another possible controller would be a closed-loop controller that employs the angular difference between both encoders A and B of the steering wheel system. This angular difference is related to the torque transmitted by the geared motor through its elasticity curve. Using this information, a torque error can be calculated, this time not between the steering torque and the torque of the SWM but rather between the steering torque and the estimated steering wheel torque. The code for the control of the RWM and the code for the control of the SWM, as well as the datasheets of the components of the SBW, are available in the appendices A, B and C.

2.2.4 Extra sensors

The previous section introduced the by-wire systems of the self-developed XBW vehicle prototype: sensors, actuators, controllers, control schemes and source codes. To summarize, the prototype control inputs are the steering wheel angle, the brake pressure and the throttle pedal angle. In addition to the aforementioned sensors, extra sensors are necessary to sense the vehicle dynamics. Also, an appropriate set of sensors that correspond to the control inputs of the MB model must be available. Considering these control inputs, several different sets of inputs can be chosen depending on the level of details of the MB model. The control inputs employed in this research are described hereafter.

Wheel torque sensor – first input of the MB model

Following the order of presentation of the by-wire systems, the first input of the MB model is the torque of the drive wheels. Indeed, if the throttle pedal angle angle would be taken as control input, it would imply the use of an engine model. However, the development of such a model is a difficult task that usually introduces important errors within the MB model and also this is not the objective of this research. For these reasons, only the effects of the engine on the vehicle are measured using a wheel torque sensor (model *90360* from *Sensor Developments*). Figure 2.9 shows the CAD model of the wheel torque sensor fitted with its adapters , the rim and the frequency modulation (FM) transmitter. The full scale load is 790 Nm. This telemetry based sensor features non-contact signal transmission. An 90 MHz FM transmitter sends the torque signal to an FM receiver that in turn transmits an analog signal to the DAS.

Brake pressure – second input of the MB model

The second input is the brake pressure. It is measured using the pressure sensor mentioned in section 2.2.3. The sensor, whose full scale is 40 bar, is connected in place of the bleed screw of the brake caliper of the left front wheel. The selection of this magnitude implies that a model for the brake system has to be built. The model is latter described in eq. (3.175).

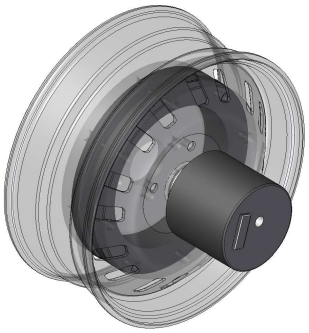

Figure 2.9: CAD model of the wheel torque sensor

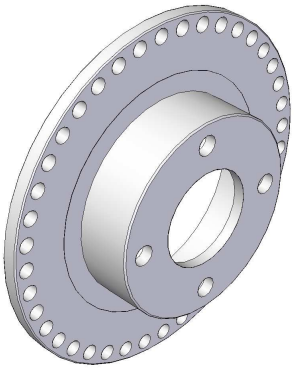

Figure 2.10: CAD model of a front brake disk

Steer angle – third input of the MB model

The last and third input of the MB is the steer angle. As this research focuses only on the vehicle dynamics, the third input needs not to be the steering wheel angle as it would necessary to have a model of the driver's force feedback system. To summarize, the set of control inputs for the MB model are the steer angle, the brake pressure and the rear wheel torque.

Engine speed

To monitor the engine speed, an hall effect sensor (model *1GT101DC* from *Honeywell*) senses the speed of the crankshaft pulley. The sensor is connected to the *MSXB036* high speed counting board mentioned in section 2.2.2. The engine speed together with the throttle pedal angle and the wheel torque allow (if necessary) to develop a basic engine model.

Wheel angles

Four hall effect sensors of the same type than the one of the engine speed are facing the holes of the brake disks to sense the wheel angles. Figure 2.10 shows a front brake disk with the holes for the hall effect sensor. Because each disk has 40 holes, the angular resolution is 9°. These sensors are also connected to the *MSXB036* high speed counting board of the DAS.

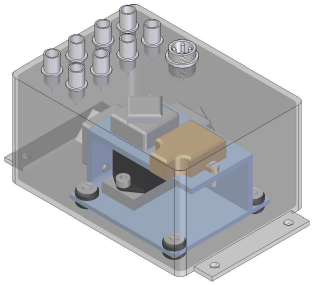

Figure 2.11: CAD model of the IMU

Measured magnitudes	Sensor
Vehicle accelerations (X, Y, Z)	Accelerometers (m/s^2)
Vehicle angular rates (X, Y, Z)	Gyroscopes (rad/s)
Vehicle orientation angles	Inclinometers (rad)
Wheel rotational angles	Hall-effect sensors (rad)
Brake line pressure	Pressure sensor (kPa)
Steering wheel and steer angles	encoders (rad)
Engine speed	Hall-effects sensor(rad/s)
Steering torque	Inline torque sensor (Nm)
Throttle pedal angle	Encoder (rad)
Rear wheel torque	Wheel torque sensor (Nm)

Table 2.1: List of the sensors mounted in the vehicle prototype

Angular velocities – accelerations – pitch and roll angles

A self-developed inertial measurement unit (IMU) features a 3 axis accelerometer (model *CXL02LF3* from *Crossbow*), 3 single axis gyroscopes (model *CRS03-02* from *Silicon Sensing*) and a 2 axis inclinometer (model *SCA121T* from *VTI technologies*). This IMU allows to measure the longitudinal, lateral and vertical accelerations as well as the pitch, roll and yaw angular velocities of the chassis frame. The measures of the inclinometer are only valid when its acceleration is null as the sensor is affected by acceleration. As a consequence, it is used to know the chassis orientation when the vehicle is stationary.

The datasheets of the extra sensors are available in appendix B. Table 2.1 presents a summary of all the sensors mounted in the vehicle prototype.

2.3 Driver's force feedback of the steer–by–wire

SBW systems are widely used in both vehicle prototypes and vehicle simulators. Although SBW systems allow for a wide range of actuator choices, the use of brushless (electronically commutated) motors appears to be the most commonly used. This wide range of actuator choices is reflected in previous research studies. For example, Yih and Gerdes (2005) selected a brushed DC servomotor with a timing belt as the SWM. For Bianchi et al. (2008), the SWM

is a PM synchronous motor in direct drive. The SWM for Iyasere et al. (2007) is a direct drive brushless actuator. Another choice of SWM actuator could be a brushless DC motor coupled with a harmonic-drive gear (Bajçinca et al., 2005) or a worm gear (Heitzer and Seewald, 2004). (Verschuren and Duringhof, 2006) equipped the driver's torque feedback system with a gear set and two alternating current (AC) brushless actuators for redundancy in case of system fault. Gualino and Adounkpé (2006) employed a disturbance observer to estimate the torque in the steering wheel using a brushless synchronous motor and two encoders. Brushless motors are appreciated for their high efficiency, their small size, their low maintenance and even for the high heat capacity of their stators that allows for longer overload time. Despite their superior qualities, brushless motors are less commonly used than brushed types in motion-control applications, mainly due to their higher price.

When designing a SBW system, the choice between a direct drive motor and a geared motor for the SWM is based on a compromise in the motor dimensioning. Selecting a direct drive motor implies a bigger motor size than for a geared motor. Therefore, here, the use of a direct drive motor would imply a high electrical consumption. As mentioned in section 2.2.3, a SBW system using geared coreless DC motors has been installed in the XBW vehicle prototype. The combination of gearboxes and coreless DC motors guarantees low cost SBW systems. The coreless (or ironless) motors are PM brushed DC motors. They have no iron core, therefore no iron losses, low friction and an acceptable level of thermal dissipation. The design of a low-inertia rotor is the key here to rapid acceleration and fast reaction time. Thus coreless motors appear to be a possible low-cost option when designing a SBW system. Precision planetary gearboxes, i.e. with a low backlash angle, are used to increase torque of the motor.

Gearboxes allow for changes in the speed and torque ranges of motors, thus allowing the motor to function at its best operation ranges. As a consequence, smaller and low cost motors can be used in comparison with direct drive motors. Nevertheless, the use of gearboxes has several drawbacks such as friction, backlash, flexibility or additional inertia. To avoid oversized direct drive motors, whilst maintaining good dynamic performances, the use of geared motors requires to compensate for the previously mentioned disadvantages. A controller using a torque sensor or a torque observer is normally required to compensate for the drawbacks associated with the gearbox and the servo-amplifier. The design of such a controller requires the comprehensive knowledge of the dynamics of the system.

Friction, backlash and flexibility were studied separately (Armstrong-Hélouvry et al., 1994; Canudas de Wit et al., 1995; Nordin and Gutman, 2002; Swevers et al., 2000), but more rarely together. Márton and Lantos (2009); Menon and K. (1999) treated friction and backlash together while Wernholt and Gunnarsson (2006) treated friction and flexibility. Inertia is commonly taken into account in the control loop. In this section, a general approach to model accurately amplifier-motor-gearbox assemblies is developed (Pastorino et al., 2011c). This approach that takes into account backlash, flexibility, friction for stiction and sliding, identification procedures, is applicable to a wide range of amplifier-motor-gearbox assemblies. Figure 2.12 shows the CAD assembly of the driver's force feedback system

2.3.1 System description

The actual driver's force feedback system components have already been presented in section 2.2.3. Nevertheless at the time of the study of this system, the amplifier of the motor

Figure 2.12: CAD model of the steering wheel system

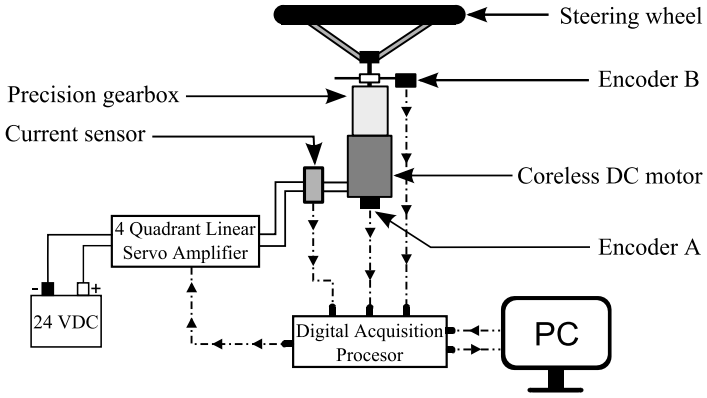

Figure 2.13: Detailed driver's force feedback system

was a four quadrant linear amplifier (model *MSE421* from *Mclennan*). Figure 2.13 shows the block scheme that includes the previously mentioned DAS and an electrical current sensor (model *CSNS300* from *Honeywell*) that measures the amplifier electrical current. The DC motor is powered by a 24 VDC battery. The four quadrant linear amplifier is used as a torque controller. In this control mode, the maximum motor torque is of ±12 Nm. The DAS is used to send the reference current command to the amplifier.

As mentioned before, since the gearbox introduces nonlinearities (friction, backlash, flexibility) into the system, the torque in the steering wheel fails to match the reference torque that is sent by the DAS to the servoamplifier. This problem especially appears in the transient. Consequently, the driver does not receive always an accurate feedback torque. This problem may be solved by installing a sensor torque between the gearbox and the steering wheel (Bajçinca et al., 2005). However this solution implies that additional elasticity is introduced into the mechanical system thus degrading the system performance. Moreover, the stability of force sensing could be improved by replacing the torque sensor with a reaction torque observer (Katsura et al., 2007).

To further understand the system dynamics, a high performance model of the steering wheel system built in Simulink is illustrated hereafter.

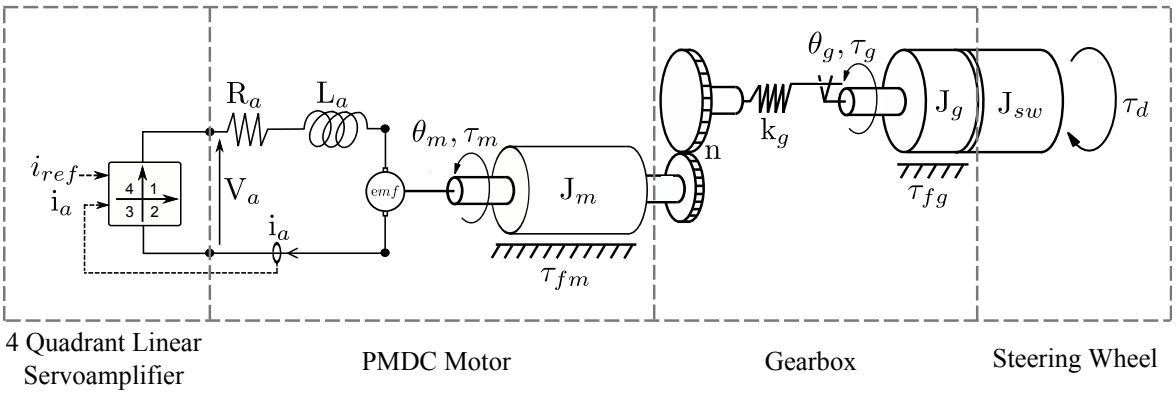

Figure 2.14: Scheme of the driver's force feedback system

2.3.2 Model equations

System modeling

The model of the driver's force feedback system presented in fig. 2.14 is composed, as in the real system, of four parts: the four quadrant linear amplifier, the motor, the gearbox and the steering wheel. Each one of these parts is described below.

Amplifier model – The amplifier is modeled as a current controller which takes into account the four quadrant operating modes. Since the dynamics of the proportional-integral (PI) controller are much faster than the dynamics of the rest of the model, they have been neglected. First the current reference given by the digital acquisition processor, i_{dap}, is bounded by the two values i_{sat}^{-} and i_{sat}^{-} defining the reference current i_{ref} as can be seen in eq. (2.1). These saturation limits are considered constant despite their time fluctuations.

$$i_{ref} = \begin{cases} i_{sat}^{+} & \text{if } i_{sat}^{+} \leq i_{dap} \\ i_{dap} & \text{if } i_{sat}^{-} \leq i_{dap} \leq i_{sat}^{+} \\ i_{sat}^{-} & \text{if } i_{dap} < i_{sat}^{-} \end{cases} \tag{2.1}$$

Next, the voltage of the motor, V_a, is calculated using eq. (2.1) or eq. (2.2) depending on the sign of i_{ref}. Both equations have the same physical interpretation hence only eq. (2.1) is discussed. In this equation, the amplifier changes the voltage to attempt to maintain i_a equal to i_{ref}, the current of the motor. When $i_{ref} < i_a$, as shown in eq. (2.2), the amplifier decreases the voltage of the motor on the base of the difference between the current of the motor i_a and the reference current i_{ref} multiplied by the constant k_1. Then, in eq. (2.2), when $0 < i_a \leq i_{ref}$, the amplifier sets the voltage to its maximum value, V_{sat}^{+}. Finally, when i_{ref} and i_a have different signs, the amplifier increases the voltage of the motor above its maximum value V_{sat}^{+} by a factor using the current of the motor i_a and a constant k_2, eq. (2.2).
If $i_{ref} \geq 0$

$$V_a = \begin{cases} V_{sat}^{+} - k_1 \cdot (i_a - i_{ref}) & \text{if } i_{ref} < i_a \quad (2.2a) \\ V_{sat}^{+} & \text{if } 0 < i_a \leq i_{ref} \quad (2.2b) \\ V_{sat}^{+} - k_2 \cdot i_a & \text{if } i_a \leq 0 \quad (2.2c) \end{cases}$$

Param.	V_{sat}^{+} (V)	V_{sat}^{-} (V)	i_{sat}^{+} (A)	i_{sat}^{-} (A)	k_1 (Ω)	k_2 (Ω)
Value	22.5	-22.5	2.23	-2.38	30000	10000

Table 2.2: Amplifier parameters

Rotor	Ironless
Direction of rotation	Reversible
Nominal voltage	30 VDC
Nominal speed	2120 r/min
Nominal load	100.10^{-3} Nm
No-load speed	2300 r/min
Voltage constant, k_v	10.5 mV/r/min $\pm$10%
Torque constant, $k_{m,avg}$	100.10^{-3} Nm/A $\pm$10%
Terminal resistance, R_a	7.6 Ω $\pm$8%
Rotor inductance at 1 kHz, L_a	3 mH(typical)

Table 2.3: Specification of the DC motors – Electrical data

If $i_{ref}<0$

$$V_a = \begin{cases} V_{sat}^{-} - k_1 \cdot (i_a - i_{ref}) & \text{if } i_a < i_{ref} \quad (2.3a) \\ V_{sat}^{-} & \text{if } i_{ref} \leq i_a < 0 \quad (2.3b) \\ V_{sat}^{-} - k_2 \cdot i_a & \text{if } i_a \geq 0 \quad (2.3c) \end{cases}$$

All the values of the amplifier coefficients are given in table 2.2.

DC motor model – The main characteristics of the DC motor are summarized in table 2.3. The motor is modeled as a rigid body with inertia J_m. The friction torque τ_{fm} models the friction between the shaft and the armature as well as the friction between the inner gears of the first stage and the ring gear of the two stage planetary gearbox. The friction model is later explained in eq. (2.11). The motor shaft elasticity has been included in the gearbox elasticity. The mathematical equation of the PMDC motor is shown in eq. (2.4).

$$V_a = R_a \cdot i_a + L_a \cdot \frac{di_a}{dt} + k_v \cdot \omega_m \quad (2.4)$$

where V_a is the supply voltage to the armature (V), R_a is the resistance of the armature winding (Ω), L_a is the leakage inductance in the armature winding (H), k_v is the motor voltage constant (V/rad/s), ω_m is the motor angular velocity (rad/s) and i_a is the armature current (A). Finally, the torque of the motor τ_m is directly obtained from the current of the motor i_a as stated in eq. (2.5).

$$\tau_m = k_{m,avg} \cdot i_a \quad (2.5)$$

where $k_{m,avg}$ is the motor torque constant. The Simulink model of the DC motor is shown in fig. 2.15.

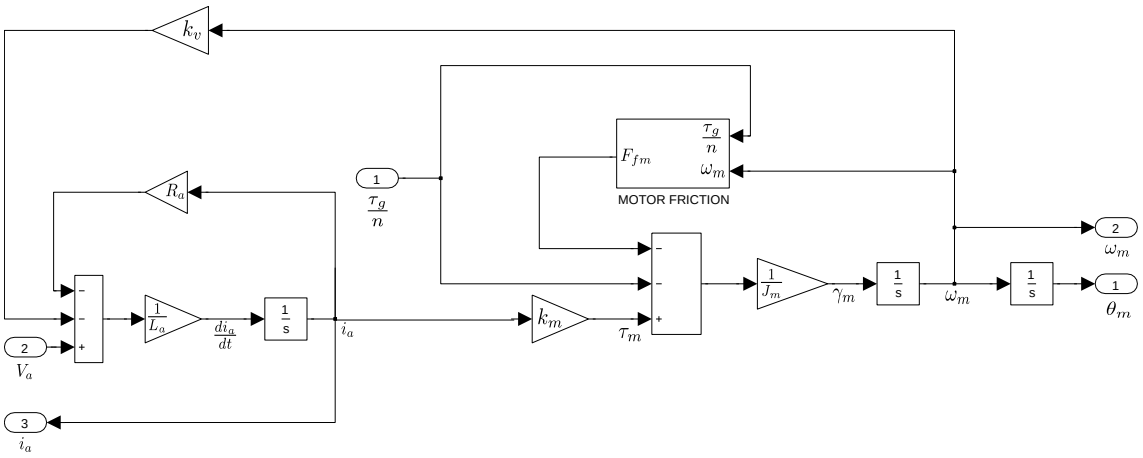

Figure 2.15: Simulink model of the DC motor

Gearbox model – At first approximation, as did Bajçinca et al. (2005), gearbox elasticity is often considered proportional to the twist of the gearbox, θ_a, as stated in eq. (2.7). Nevertheless, Wernholt and Gunnarsson modeled the elasticity of their gearbox by adding a cubic term to the proportional term (Wernholt and Gunnarsson, 2006). If backlash (or gear play) has to be taken into account, the most common models used are the dead zone model and the backlash exact model as explained by Nordin and Gutman (2002). Although these backlash models clearly represent the extent of backlash between two gears, they are less accurate when used with a higher number of gears, as is the case here with the two stage planetary gearbox. In practice, within such a gearbox, there are numerous clearances and, due to gear friction, backlash is not so accurately marked. One way to take backlash into account when using multiple gears is to model the gearbox elasticity and the backlash together as follows. Here, the relation between the twist of the gearbox and the elastic term of the gearbox torque $\tau_{g\_elastic}$ is modeled by adding to the proportional term, a cubic term and another to the fifth power, as shown in eq. (2.6). Only the odd power terms are considered in order to maintain the monotonically increasing shape for positive twist angle and the monotonically decreasing shape for negative twist angle of the backlash-flexibility curve.

$$\tau_{g\_elastic} = \begin{cases} k_{g1}{}^{+} \cdot \theta_a + k_{g3}{}^{+} \cdot \theta_a{}^3 + k_{g5}{}^{+} \cdot \theta_a{}^5 & \text{if } \theta_a > 0 \\ k_{g1}{}^{-} \cdot \theta_a + k_{g3}{}^{-} \cdot \theta_a{}^3 + k_{g5}{}^{-} \cdot \theta_a{}^5 & \text{if } \theta_a < 0 \end{cases} \tag{2.6}$$

$$\theta_a = \left(\frac{\theta_m}{n} - \theta_g \right) \tag{2.7}$$

where $k_{g1}+$, $k_{g3}{}^{+}$, $k_{g5}{}^{+}$, $k_{g1}{}^{-}$, $k_{g3}{}^{-}$, $k_{g5}{}^{-}$ are constant parameters, θ_m is the motor angle, n is the gearbox ratio (ω_{in}/ω_{out}), θ_g is the gearbox angle and θ_a is the twist of the gearbox. One advantage of modeling the elasticity and the backlash together is that the backlash angle is not required as in other models. Later, a viscous term τ_{g_visc} depending on the velocity of the twist angle $\dot{\theta}_a$ is added according to eq. (2.8).

$$\tau_{g\_visc} = b_g \cdot \dot{\theta}_a \tag{2.8}$$

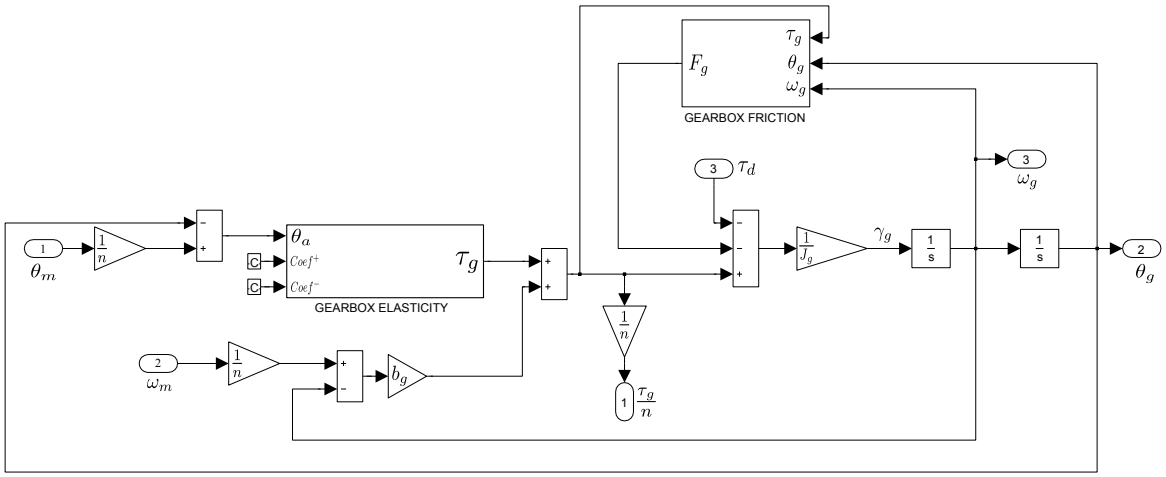

Figure 2.16: Simulink model of the gearbox

where b_g is a constant parameter whose value is given in table 2.8. Therefore the gearbox torque τ_g is the sum of the elastic and viscous terms as stated in eq. (2.9).

$$\tau_g = \tau_{g\_elastic} + \tau_{g\_visc} \tag{2.9}$$

To complete the gearbox model, a friction torque τ_{fg} models the friction between the inner gears of the second stage and the ring gear of the two stage planetary gearbox. The friction model used is explained below in eq. (2.11). The Simulink model of the gearbox is shown in fig. 2.16.

System equations – The dynamics of the system are described by eq. (2.10) and eq. (2.11) corresponding respectively to the dynamics of the motor and the gearbox.

$$\tau_m - J_m \cdot \ddot{\theta}_m - \tau_{fm} - \frac{\tau_g}{n} = 0 \tag{2.10}$$

$$\tau_g - J_{tot} \cdot \ddot{\theta}_g - \tau_{fg} + \tau_d = 0 \tag{2.11}$$

where $J_{tot} = J_g + J_{sw}$, J_m is the motor inertia, J_{sw} is the steering wheel inertia, J_g is the sum of the gearbox inertia and its coupling inertia, τ_d is the driver torque acting on the steering wheel, τ_{fm} is the motor friction torque, τ_{fg} is the gearbox friction torque and τ_g is the output torque of the gearbox. The remaining parameters have been defined previously.

Friction model and friction parameter identification

Friction model – Simple friction models that only account for a relation between velocity and friction force are in this case not suitable, as they do not consider the presliding behaviour, resulting in simulation errors at motion stops and reversals. For these models, at zero velocity, the friction force is constant: zero or F_s (F_c if F_s is not considered) instead of having a spring like behaviour. F_c is the Coulomb friction level and F_s is the level of the stiction force. That is why a bristle friction model, the LuGre model (Canudas de Wit et al., 1995), is used. Some authors have proposed improvements of the latter, especially for the presliding behaviour (Swevers et al., 2000). Nonetheless, here, this behaviour is not crucial to such an extent that an improved LuGre model is necessary. The LuGre model has the

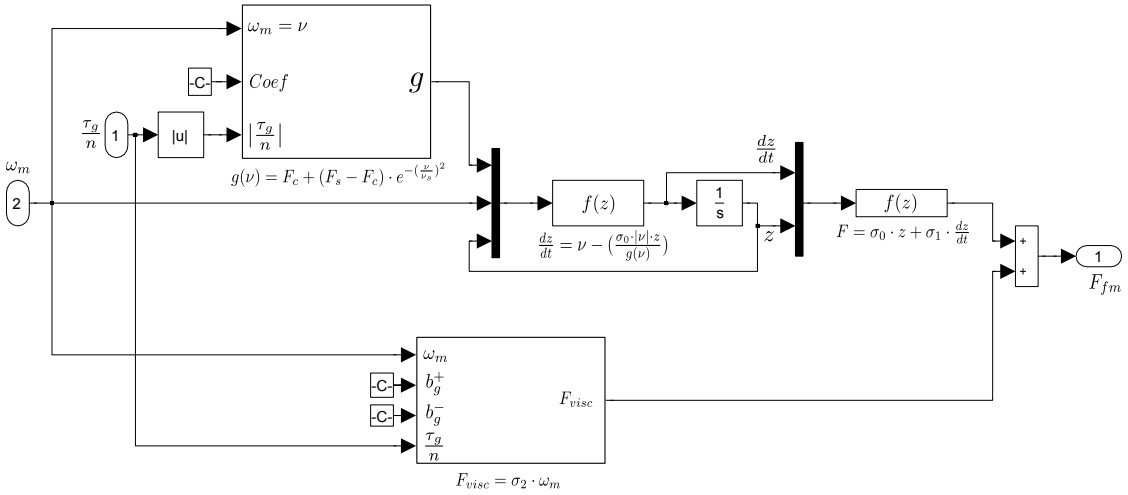

Figure 2.17: Simulink model of the motor friction

following form:

$$\dot{z} = \nu - \sigma_0 \cdot \frac{|\nu|}{g(\nu)} \cdot z \tag{2.12}$$

$$g(\nu) = \mathrm{F_c} + (\mathrm{F_s} - \mathrm{F_c}) \cdot e^{-(\nu/\nu_s)^2} \tag{2.13}$$

$$\mathrm{F} = \sigma_0 \cdot z + \sigma_1 \cdot \dot{z} + \sigma_2 \cdot \nu \tag{2.14}$$

where F is the friction force, ν is the velocity, ν_s is the Stribeck velocity, z is the average deflection of the bristles, σ_0 represents the stiffness of the bristles, σ_1 is the damping coefficient of the bristles and σ_2 is the viscous damping.

Moreover, the friction in the gearbox appears in this case to be load-dependent. When the torque transmitted by the gearbox increases, the friction torque also increases. Load-dependent friction has previously been studied in only a few cases (Dohring et al., 1993) where a load-dependent friction model is presented for a worm gear transmission. Here, the coulomb force, the stiction force and the viscous force are considered load-dependent. The load dependence is modeled as follows:

$$\begin{cases} \mathrm{F_c} = \alpha_1 \cdot \sqrt{\tau_\mathrm{g}} \\ \mathrm{F_s} = \alpha_2 \cdot \sqrt{\tau_\mathrm{g}} \\ \sigma_2 = \alpha_3 \cdot \sqrt{\tau_\mathrm{g}} \end{cases} \quad \text{for the gearbox} \tag{2.15}$$

$$\begin{cases} \mathrm{F_c} = \alpha_1' \cdot \tau_\mathrm{g} \\ \mathrm{F_s} = \alpha_2' \cdot \tau_\mathrm{g} \\ \sigma_2 = \alpha_3' \cdot \tau_\mathrm{g} \end{cases} \quad \text{for the motor} \tag{2.16}$$

where α_1, α_2, α_3 ($\sqrt{Nm}$) and α_1', α_2', α_3' (dimensionless) are positive constants. The Simulink friction model of the DC motor is shown in fig. 2.17. The friction model of the gearbox has exactly the same form.

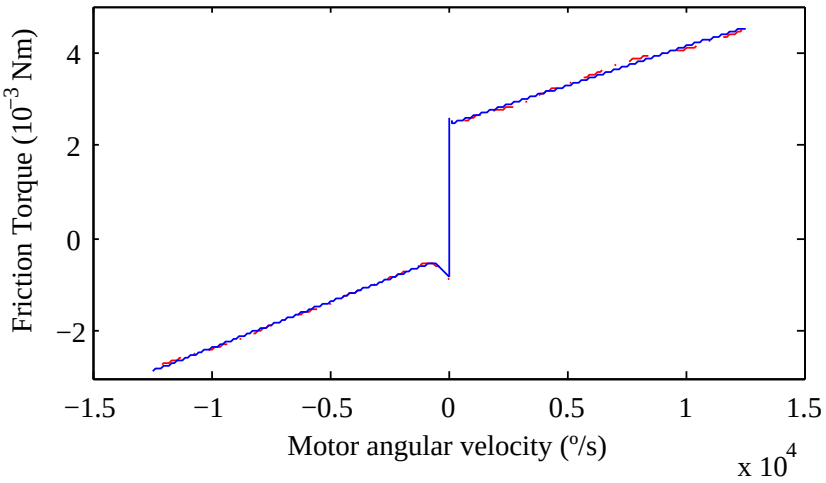

Figure 2.18: No load friction curves

Friction identification – To estimate some parameters of the LuGre model (F_s, F_c, ν_s, σ_0, σ_1, σ_2), the shaft of the geared motor , with no load, is moved at several different speeds. During these tests, the speed is maintained constant in order to avoid exciting dynamic friction components. In this situation, the derivative of the average deflection of the bristles $\dot{z}$ is equal to zero and ν is constant. Therefore eq. (2.14) can written as shown in eq. (2.17).

$$F = F_c + (F_s - F_c) \cdot e^{-(\nu/\nu_s)^2} + \sigma_2 \cdot \nu \tag{2.17}$$

The friction force is measured by means of motor current sensing. Measurements are recorded for 50 different constant speeds on each rotational direction , within a range of $\pm 12000\ °/s$. The friction torque $\tau_{f,no-load}$ is obtained from eq. (2.18).

$$\tau_{f,no-load} = k_{m,avg} \cdot i_{avg} \tag{2.18}$$

where i_{avg} is the average of the current drawn by the motor and $k_{m,avg}$ is the motor torque constant (Nm/A). The average value of $k_{m,avg}$ is given in table 2.3. As in a gearbox the friction is position dependent, the friction torque has an oscillatory behaviour depending on the position. Therefore the motor current is averaged over several turns before calculating the friction torque. After that, a least-squares formulation is used to fit eq. (2.17) to the experimental data. The least-squares method minimizes the summed square of residuals that is given by eq. (2.19).

$$S = \sum_{i=1}^{n} (y_i - \hat{y}_i)^2 \tag{2.19}$$

where y_i is the experimental value and $\hat{y}_i$ is the fitted value. The experimental and model fitted friction curves are shown in fig. 2.18.

The identified friction parameters are shown in table 2.4. These parameters do not correspond directly with τ_{fm} or τ_{fg} as the latter can not be measured separately but they represent the sum (τ_{fm} + τ_{fg}) when the gearbox transmits zero torque. Therefore, these values only give the order of magnitude of the friction parameters. The bristle damping, represented by the coefficient σ_1, is neglected in the motor friction model as well as in the

Rotation	Positive	Negative
$F_{c,noload}$ (10^{-5} Nm)	2.4	0.34
$F_{s,noload}$ (10^{-6} Nm)	2.58	0.84
$\nu_{s,noload}$ (rad/s)	3.49	7.93
$\sigma_{2,noload}$ (10^{-6} Nm/rad/s)	1	1.15

Table 2.4: Identified friction parameters with no load applied

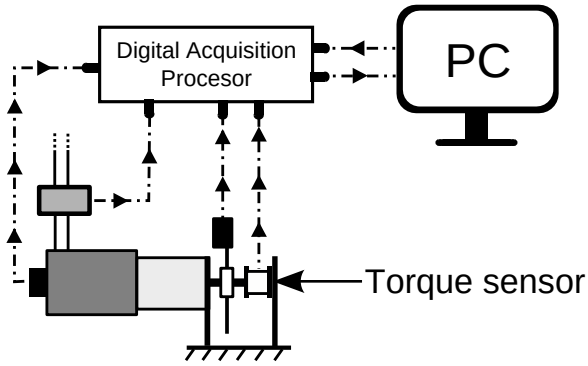

Figure 2.19: Geared motor with the output shaft blocked

gearbox friction model, having verified with simulations that its contribution in this model is not significant. The remaining parameters σ_0 for both the motor and the gearbox, α_1, α_1', α_2, α_2', σ_2 for both the motor and the gearbox and ν_s for the gearbox, were tuned for each rotational direction to best fit the model to the experimental data, as is explained in Section 2.3.3. Further friction identification tests could be done, especially with the output shaft of the gearbox loaded during its movement. Nevertheless, as the friction parameters have a direct physical significance, their tuning to adjust the model to the experimental data has proved to be feasible and intuitive.

Gearbox elasticity and backlash identification

In order to identify the elasticity and backlash parameters, the gearbox output shaft is blocked with a torque sensor, as shown in fig. 2.19. The motor torque is slowly ramped up and down on each rotational direction without stopping. Different maximum values for the motor torque are applied.

Figure 2.20 shows the experimental data when the motor torque is ramped up and down on each rotational direction using full scale torque.

The first observation is that this curve is not linear (as is usually supposed) and presents hysteresis. Actually, this hysteretic behaviour is due to the friction in the gearbox. The torque curve has an inflection point where, for low values of the twist angle, the torque transmitted by the gearbox is almost zero. This is the backlash zone (grey area). Finally the relation between the torque and the twist angle of the gearbox is approximated by two curves (positive and negative twist, solid lines without arrows) using eq. (2.6). The coefficients for each rotational direction are shown in table 2.5.

At this point,the gearbox elasticity parameters are known. The few friction parameters

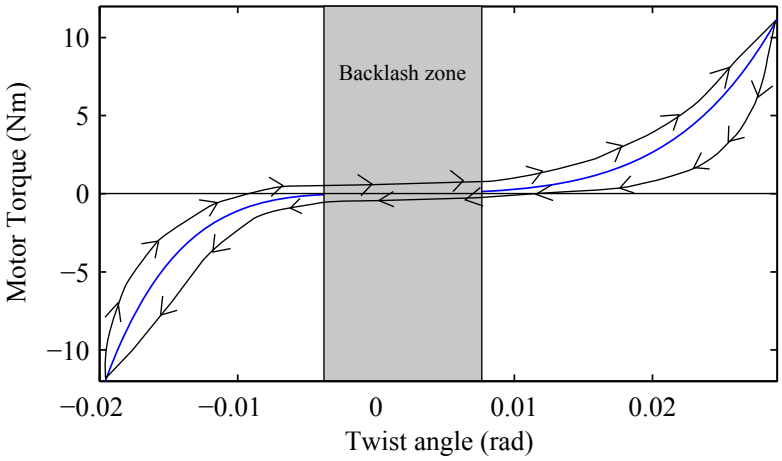

Figure 2.20: Elasticity-backlash curve of the gearbox

Rotation	Positive	Negative
k_{g1} (Nm/rad)	5	1
k_{g3} (Nm/rad^3)	2e5	9e5
k_{g5} (Nm/rad^5)	3e8	18e8

Table 2.5: Gearbox elasticity parameters

	Inertia $(10^{-6}\ kg \cdot m^2)$
J_m	22
J_1	40.5
J_2	294
J_{sw}	17789

Table 2.6: System component inertias

that have been identified will be used as initial conditions for the optimization of all the friction parameters through comparisons between the experimental and the simulated data.

2.3.3 Identification procedures and simulation results

In order to evaluate the accuracy of the model, three different tests corresponding to real situations are performed. In the first test, the steering wheel is blocked as though the driver were holding it tightly, preventing almost any rotation. In the second test, the driver leaves the steering wheel free and, in the third test, the driver holds and turns the steering wheel in both rotational directions while the motor is actuating. Table 2.6 shows the inertia of different components forming part of the system. J_g is the sum of the gearbox inertia J_1 and the coupling inertia J_2. J_m is the inertia of the motor shaft, the sun gear and its adapter. J_{sw} is the steering wheel inertia. Next, to quantify the accuracy of the model, a least mean square criterion is used, eq. (2.19). Then the fit is obtained from eq. (2.20).

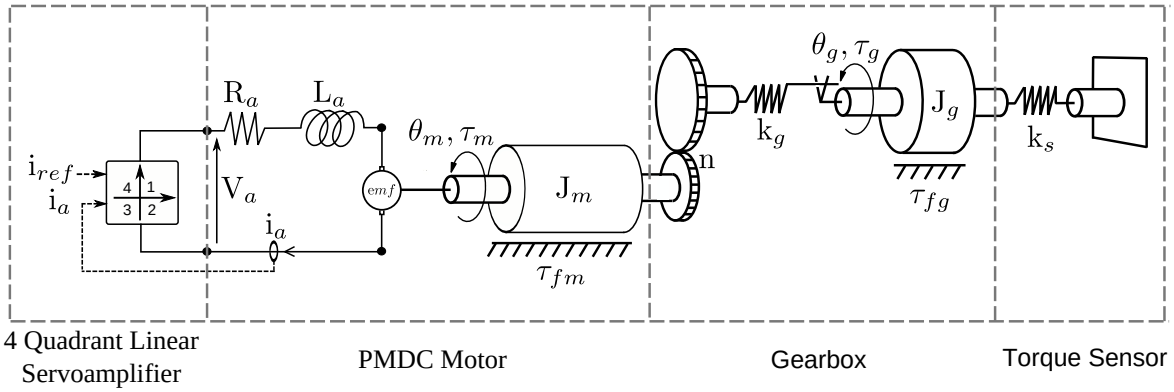

Figure 2.21: Locked steering wheel system

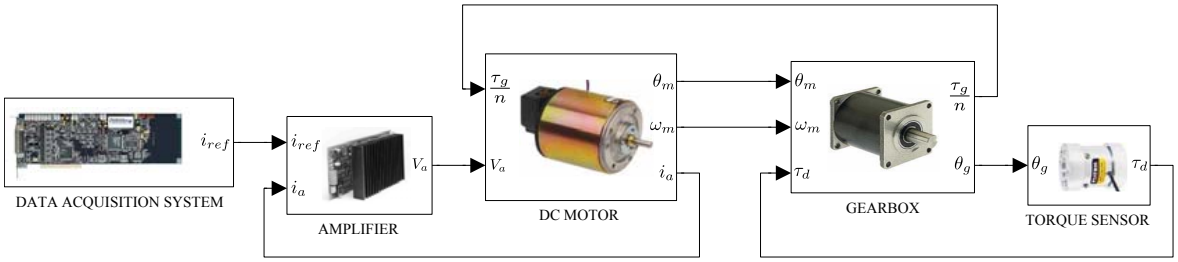

Figure 2.22: Simulink model for the locked steering wheel system

$$Fit = 100 \cdot \left(1 - \frac{\sqrt{S}}{\sqrt{\sum_{i=1}^{N}(y(t) - \bar{y})^2}}\right) \tag{2.20}$$

where $y(t)$ is the measured output, $\bar{y}$ is the mean value of the measured output and S is the summed square of the residuals (see eq. (2.19)).

Locked steering wheel

The first test is conducted with the steering wheel blocked, as shown in fig. 2.19. In order to easily block the output shaft of the gearbox, the steering wheel is replaced by a torque sensor, fixed on one side, thus neglecting the steering wheel coupling elasticity. A scheme of the assembly is shown in fig. 2.21, where k_s (= 4500 N m/rad) is the elasticity of the torque sensor.

The Simulink model of this assembly is shown in Fig. 2.22.

Two different current commands are applied to the DC motor of the real system: a sine wave of period 1 s and a square wave of period 0.27 s. Three different amplitudes are tested: 1/3 of full scale (0.14 Nm), 2/3 of full scale (0.28 Nm) and full scale (0.42 Nm). The amplitude of the steps of the square wave is randomly chosen (white noise distribution) within the selected amplitude. The period of the square wave is chosen so that the system has enough time to reach a steady state between two consecutive steps. The torque of the sensor is shown for a sine wave excitation in fig. 2.23 and for a square wave excitation signal in fig. 2.24.

These figures highlight several important characteristics of the real system. Figure 2.23 shows the current saturation of the servo-amplifier, the delay and the nonlinearities introduced by the gearbox. Figure 2.24 shows the oscillatory behavior of the system and especially the amplitude reached by the system with respect to the reference command. In order to

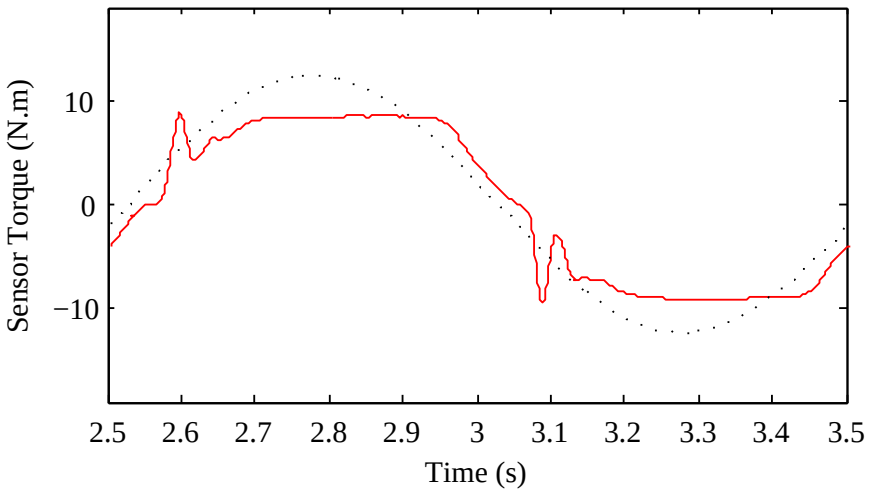

Figure 2.23: Sensor torque, τ_d, for a sine wave excitation signal

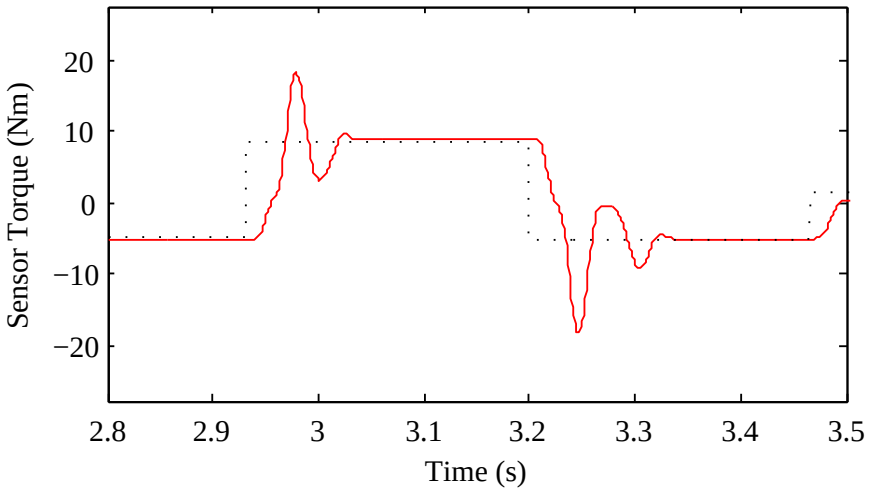

Figure 2.24: Sensor torque, τ_d, for a square wave excitation signal

adjust the model parameters that were either not identified or whose identification value is distant from the real value, several optimizations using comparison between experimental and simulated data are performed.

Tuning of the amplifier parameters – The first parameters to be tuned are those of the amplifier. During the experiments, the current of the motor is recorded by means of the Hall effect sensor. The objective is to match the simulated current to the recorded current of the sensor. Both the model and the real system are excited with the same reference signal. The sine wave is used to adjust the saturation limits of the current. Figure 2.25 shows the experimental and the simulated data for the sine wave reference. The fit, calculated using eq. (2.20), between the experimental and the simulated velocity is of 96.8%.

The tuned parameters of the model are presented in table 2.2. The tuning of the saturation limits of the voltage is addressed in table 2.9.

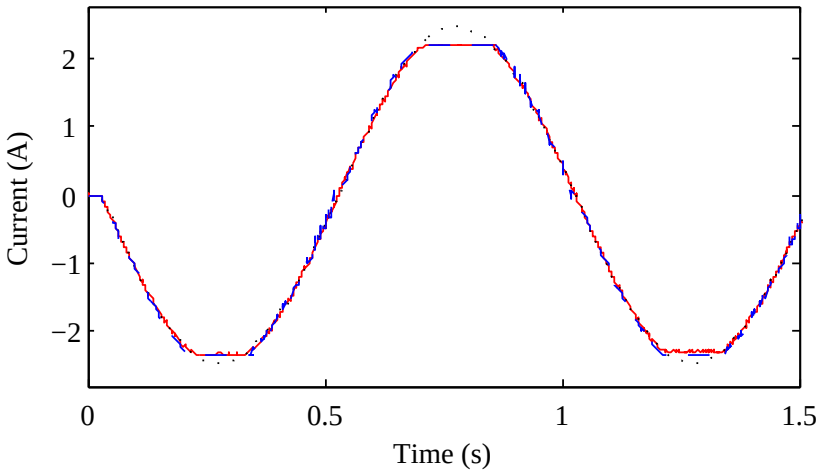

Figure 2.25: Amplifier current, i_a, for a sine wave reference

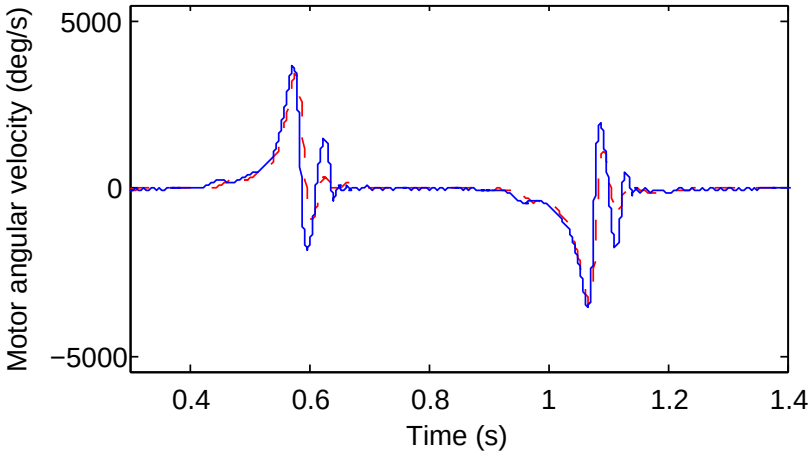

Figure 2.26: Motor angular velocity, ω_m, for a sine wave reference

Tuning of the motor friction parameters – Having found the optimal parameters for the amplifier, the following optimization is that of the friction parameters of the motor. The available data for the motor are the angle θ_m and the angular velocity ω_m. The sine wave reference with an amplitude of 2/3 of full scale is used. As a sine wave contains only one frequency, the influence of each friction parameter is more easily spotted. Here, the tuned parameters are α_1', α_2', α_3' for each rotational direction and σ_0 for the motor. The best results are obtained by tuning the parameters with respect to the motor angular velocity. Figure 2.26 shows the experimental and simulated angular velocity of the motor and fig. 2.27 shows the experimental and simulated angle of the motor.

The fits are of 95.4% for the motor angle and of 76.41% for the motor angular velocity. Although this last fit is not as high as that of the amplifier or the motor angle, the motor dynamics are well matched. Table 2.7 shows the values of the tuned parameters.

Tuning of the gearbox friction parameters – Finally the friction parameters of the gearbox are adjusted. As for the motor, these parameters are ${\alpha_1}^+$, ${\alpha_1}^-$, ${\alpha_2}^+$, ${\alpha_2}^-$, ${\alpha_3}^+$, ${\alpha_3}^-$

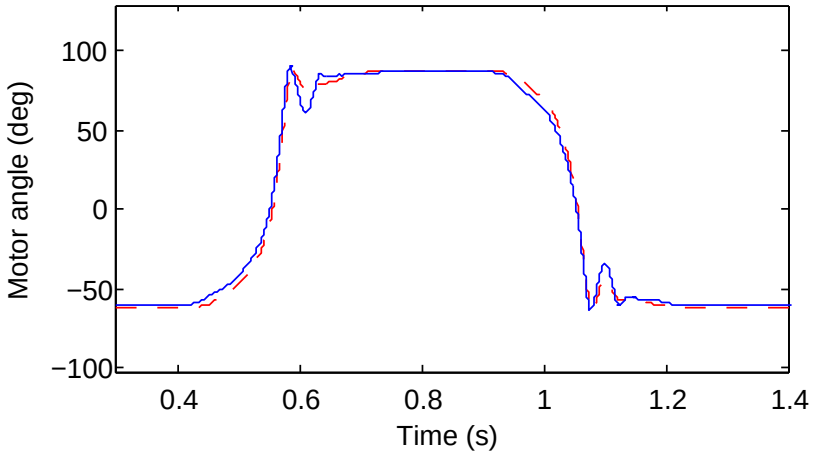

Figure 2.27: Motor angle, θ_{m}, for a sine wave reference

Param.	Value	Unit
σ_0	5	N m
α'_1	0.2	N m^{-1}
α'_2	0.3	N m^{-1}
α'_3	1e-5	s/N m
ν_s	0.174	s

Table 2.7: Motor parameters

Param.	Value	Unit
n	50	-
$\mathrm{b_g}$	0.1	N m/s
σ_0	3000	N m
${\alpha_1}^+$	0.4	N m^{-1}
${\alpha_2}^+$	0.5	N m^{-1}
${\alpha_3}^+$	1e-5	s/N m
${\alpha_1}^-$	0.05	N m^{-1}
${\alpha_2}^-$	0.06	N m^{-1}
${\alpha_3}^-$	1e-5	s/N m
ν_s	43.48	s

Table 2.8: Gearbox parameters

and σ_0. Figure 2.28 and fig. 2.29 show the experimental and simulated torque of the sensor when using the sine wave reference and the random square wave. The values of the tuned parameters are compiled in table 2.8.

The fit is of 88.8% for the sine wave reference and of 82.2% for the square wave reference. These results demonstrate that the model represents with high accuracy the dynamics of the driver's force feedback system when the steering wheel is blocked. The gearbox torque, that is the most important parameter of the model, is especially well represented.

Free steering wheel

When the steering wheel is free (i.e. the driver is not holding it) and a reference current is demanded, the steering wheel begins to turn and rapidly reaches a maximum rotational velocity. This velocity is a little lower than the no-load speed of the motor without the gearbox, as the geared motor has to overcome friction in the gearbox. The amplifier and the DC motor models presented in this paper explain this operating mode. When a reference

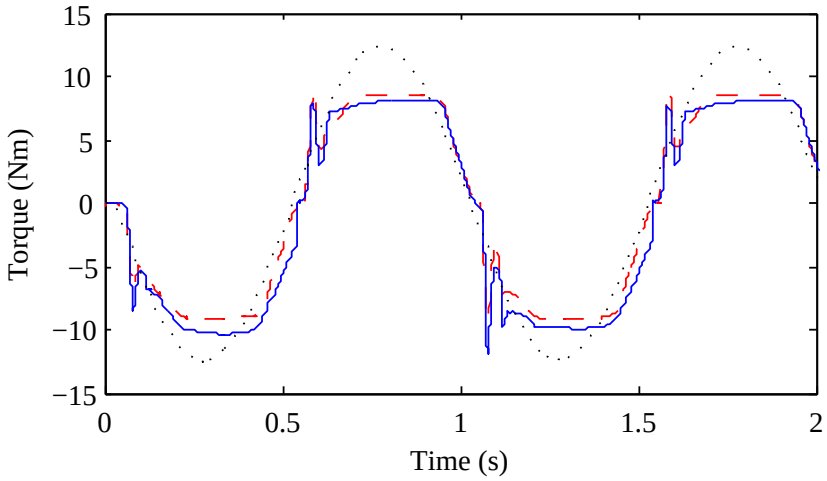

Figure 2.28: Gearbox torque, τ_g, for a sine wave reference

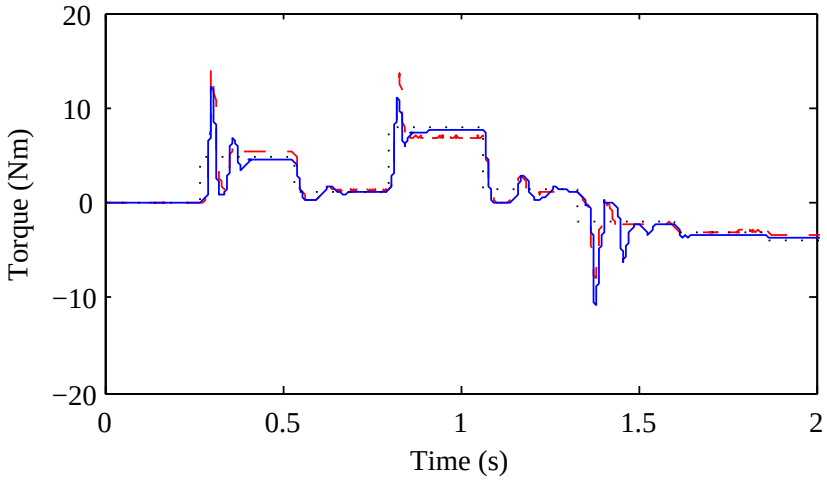

Figure 2.29: Gearbox torque, τ_g, for a square wave reference

current i_{dap} is given by the DAS, first this current is maintained between both saturation bounds as stated in eq. (2.1). Then, the voltage V_a necessary to keep the motor current i_a equal to the reference current i_{ref} is calculated using eq. (2.1) or eq. (2.2) depending on the sign of i_{ref}. Since the motor has no load, the maximum current that can be drawn by the motor is the current necessary to overcome the friction forces. In that particular situation, V_a, obtained from eq. (2.2) or eq. (2.3), is equal to V_{sat}^{+}. Looking now at eq. (2.4), the motor angular velocity ω_m which is the only remaining unknown, must be constant and equal to the no load speed as the rest of the variables are constants as explained above. Figure 2.30 shows the current of the motor while fig. 2.31 shows the angular velocity of the motor during a test in which a constant reference current of 0.64 A is applied to the steering wheel that is free.

The comparison between the experimental and the simulated data demonstrates that the model is accurate enough to represent this operating mode. The transient is not very well represented by the model but it has almost no impact on the accuracy as it is very fast. However the steady state is well matched for both the motor current and the motor angular velocity. The fit is not given as it would not be interesting in this case. Table 2.2 shows the

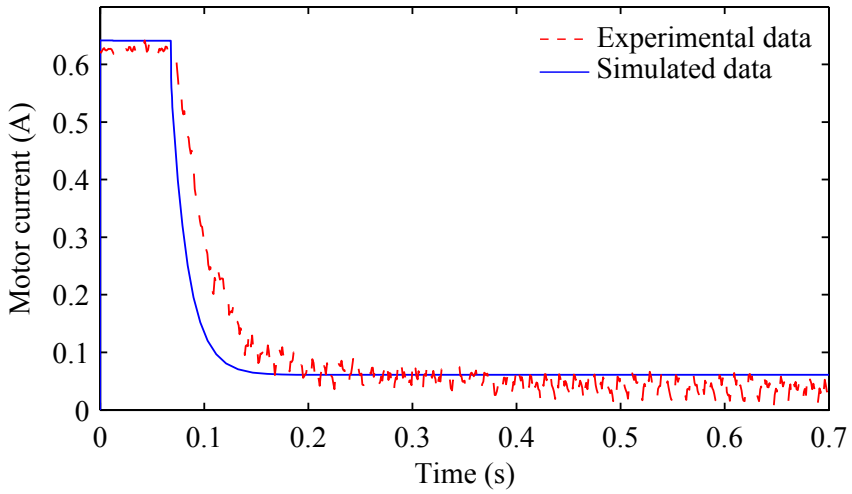

Figure 2.30: Motor current, i_a, for the free steering wheel case

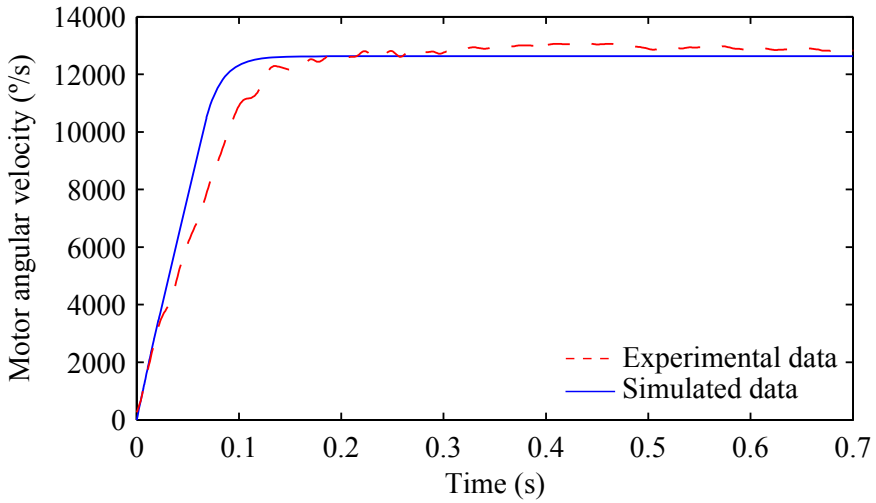

Figure 2.31: Motor angular velocity, ω_m, for the free steering wheel case

$\omega^{max}_{m,real}$ $(°/s)$	12780
$\omega^{max}_{m,simulated}$ $(°/s)$	12631

Table 2.9: Real and simulated rotational velocity

saturation limits of the voltage V_a and table 2.9 shows the maximum speed reached by the geared motor for both real and simulated data.

Held steering wheel

A scheme of this operating mode is shown in fig. 2.14. In this last test, the driver turns the steering wheel in both rotational directions while the amplifier attempts to follow its reference current. In the locked and free steering wheel tests, the motor is always motoring, therefore absorbing electrical energy and producing mechanical work. Nevertheless in this test, the torque applied by the driver to the steering wheel can lead to a regenerative behavior, where the current is inverted and fed back to the amplifier. In quadrants 2 and 4, i.e. when

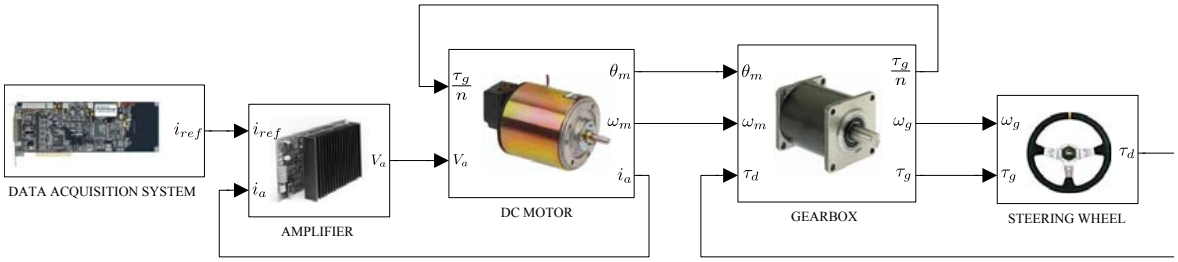

Figure 2.32: Simulink model for the held steering wheel system

Param.	Value	Unit
K_p	200	N
K_i	150	N

Table 2.10: PI controller parameters

the motor acts as a generator, the amplifier actively controls the motor current. If the counter electromotive force (CEMF) is low, power is dissipated within the amplifier in order to maintain the current equal to its reference. In this case there is no regenerative effect of power being fed back to the power supply. If the CEMF created becomes too high, the amplifier begins to return the excess of energy to the power supply via internal diodes.

Considering the operating modes of the driver's force feedback system, the motor can generate energy in three different situations. In the first case, the reference current is zero and the driver turns the steering wheel in any direction. As a torque is normally applied to the motor, this situation does not normally occur. In the second case, the driver turns the steering wheel in the direction that opposes the reference current of the motor (differing from zero). Finally in the third case, the driver turns the steering wheel in the same direction as the reference current of the motor at a velocity higher than the no-load speed. In the three cases, the generated CEMF creates a torque that goes against the driver's movement.

The Simulink model employed here is presented in fig. 2.32. In order to complete the optimization of the model parameters, a last experimental test is realized. A constant reference current is applied to the motor while the driver turns the steering wheel in both directions increasing for each movement its rotational velocity. The objective is that the motor actuates in quadrants 2 and 4.

During this test, the torque in the steering wheel (τ_d), the gearbox angle (θ_g), the motor angle (θ_m), the motor voltage (V_a) and the motor current (i_a) are recorded. To run the simulation, two inputs are necessary: the current applied to the motor (i_a) and the driver's torque acting on the steering wheel (τ_d). Whilst the reference current applied to the motor is known, the driver's torque has to be obtained using a PI controller as there is no torque sensor. The PI error is the difference between the known experimental velocity and the simulated velocity of the steering wheel. The PI coefficients K_p and K_i are tuned until the simulated velocity of the steering wheel matches the experimental velocity (recorded previously). They are compiled in table 2.10. The comparison between the experimental and the simulated data presented in fig. 2.33, shows that the match is very good. The fit is of 98.2%.

The angle of the gearbox during the experimental test is shown in fig. 2.34. As for the gearbox velocity, the simulated gearbox angle (or the steering wheel angle), follows its reference

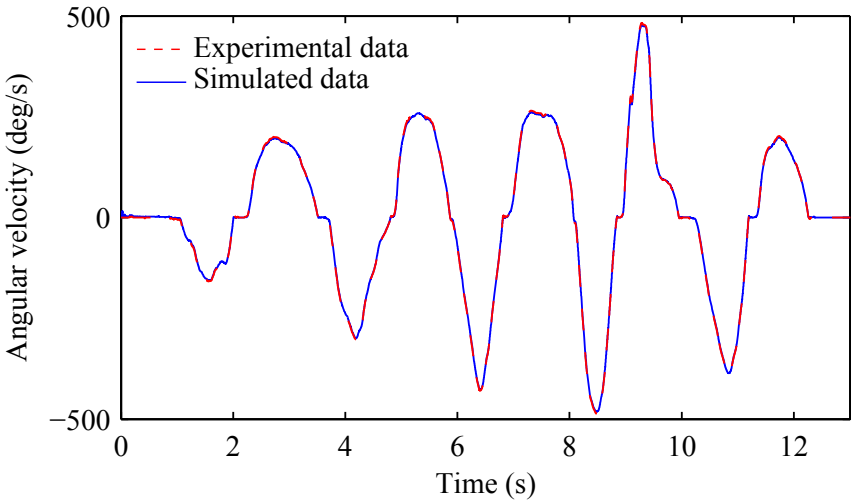

Figure 2.33: Angular velocity of the gearbox, ω_m, for the held steering wheel case

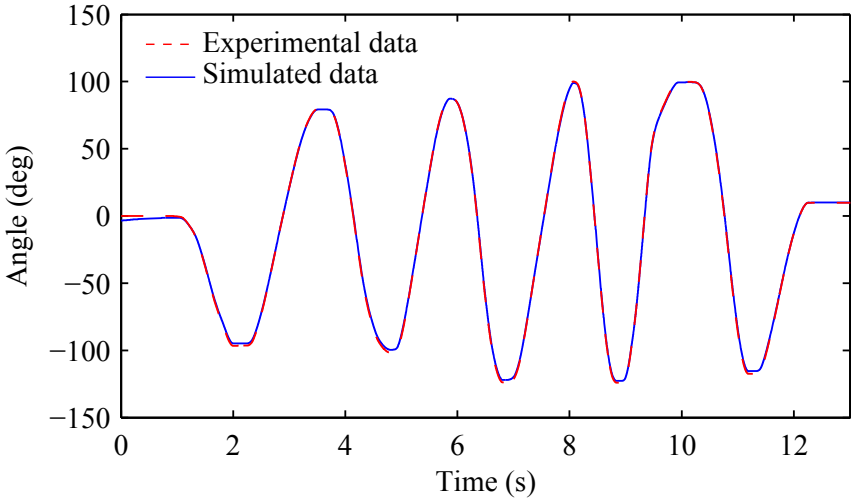

Figure 2.34: Angle of the gearbox, θ_g, for the held steering wheel case

with high accuracy and the fit is of 91.4%.

After that, the friction parameters of the motor are finely tuned to match the simulated data to the experimental data. The three basic variables of the motor model, ω_m, i_a and V_a stated in eq. (2.4), are presented in fig. 2.35, fig. 2.36 and fig. 2.37. The respective values of the fit are 88.6%, 92.6%, 92.6%.

Finally the friction parameters of the gearbox are finely tuned to match the experimental and simulated data. Once all the model parameters have been optimized, the driver's torque of the model matches well the experimental driver's torque recorded during the test, as can be seen in fig. 2.38. Although the fit, 45.7%, is lower than the previous fits, it demonstrates that when a motor torque is applied to the system and the angular velocity of the steering wheel is known, the driver's torque of the model is very similar the experimental driver's torque. The results obtained in this section demonstrate that the model, not only matches the dynamics of the real system with the steering wheel blocked or free, but also represents with high accuracy the dynamics of the system when both input torques, the motor torque

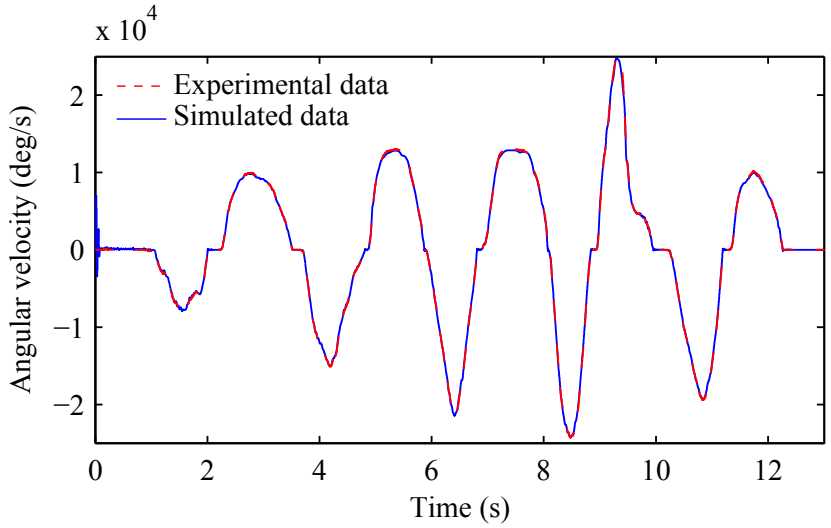

Figure 2.35: Motor velocity, ω_m, for the held steering wheel case

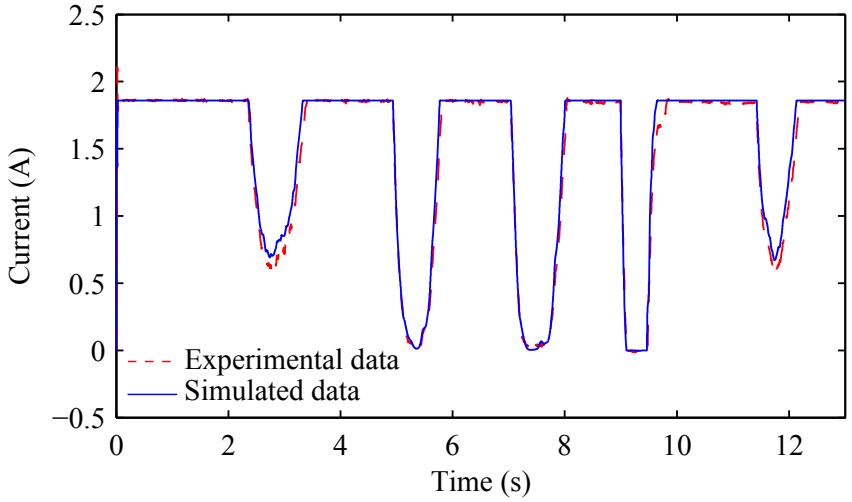

Figure 2.36: Motor current, i_a, for the held steering wheel case

and the driver's torque, are applied to the system.

2.3.4 Discussion

In this section, a general approach to model accurately amplifier-motor-gearbox assemblies has been developed. This approach that takes into account backlash, flexibility, friction for stiction and sliding, identification procedures, is applicable to a wide range of amplifier-motor-gearbox assemblies. It has been presented through an example: the modeling of a low cost driver's torque feedback system of a SBW system that uses a two stage planetary gearbox, a coreless PMDC motor and a four quadrant linear amplifier. All the parameters of this model have a direct physical significance thus making easier the identification procedures. The amplifier has been modeled as a current controller which takes into account the four quadrant operating modes. Then, the PMDC motor has been modeled as a resistor, a coil and a CEMF in series. Friction within both the motor and the gearbox has been taken into account by using a

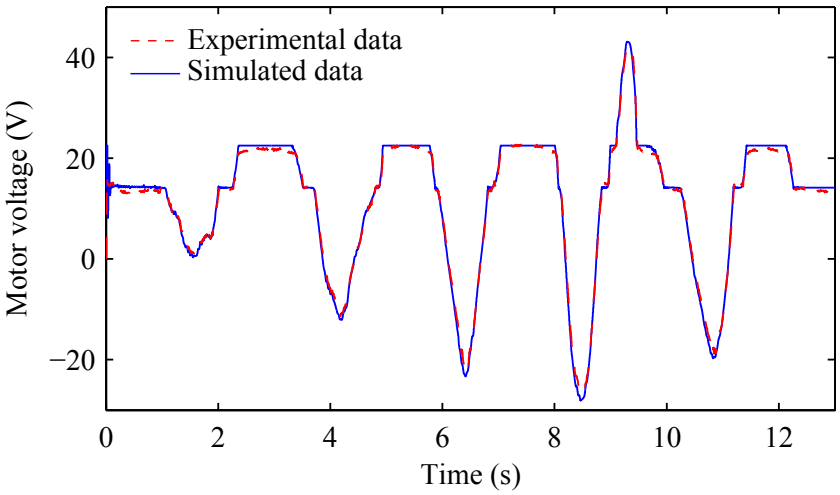

Figure 2.37: Motor voltage, V_a, for the held steering wheel case

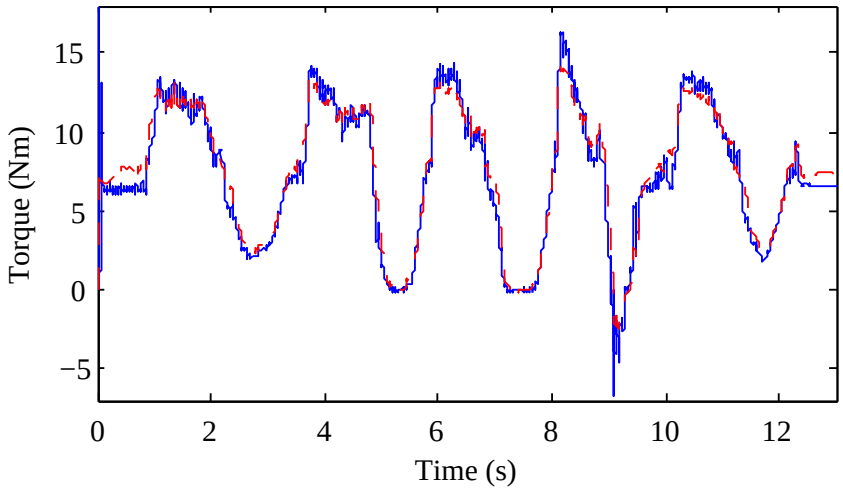

Figure 2.38: Driver's torque, τ_d, for the held steering wheel case

modification of the LuGre model that allows friction to be considered as load-dependent. Backlash and flexibility within the gearbox have been considered together using a fifth order polynomial for each rotational direction.

Comparisons between simulations and experimental data for three typical driving situations show that the model represents the dynamics of the system with high accuracy. Future work regarding this section could focus on the design of a controller employing a torque observer to compensate the gearbox drawbacks using the model developed in this paper.

2.4 Test maneuvers

Two test maneuvers have been repeated about seven times in an almost flat test track of the engineering school's campus. Both maneuvers are presented hereafter as well as the most relevant magnitudes of the vehicle motion for each test maneuver. Extensive experimental data post–processing is necessary to properly condition the data of the sensors. Most of the

post–processing applied to the data of the sensors of the XBW vehicle prototype is described below.

2.4.1 Sensor data post-processing

The data of the sensors are gathered using the DAS presented in section 2.2.2. All analog signals of the sensors are converted to discrete–time. After the conversion, digital signals are saved to disk. In order to visualize the data of the sensors with the scale in the International System of Units, a sequence of conversions is necessary. First the sensitivity of the sensors, that relates measured magnitude to output voltage, is needed. After that, the correspondence between the full voltage range of the DAS pin to which the sensor is connected and the digital precision of the DAS input bus is also required. This is the simplest case of conversions. It can be illustrated with the brake pressure sensor mounted on the XBW vehicle prototype. This pressure sensor, presented in section 2.2.3, has a sensitivity of 8×10^5 Pa/V. The full voltage range of the pin corresponding to the pressure sensor is ± 5 V and the digital precision of the DAS input bus is 16 bits, that gives a range of ± 32767. As a consequence, the data of the sensors saved on disk must be multiply by a factor of 122.072 to be expressed in units of the International System of Units. In some cases it is also necessary to remove sensor offsets. For example an accelerometer measuring zero gravity outputs a value equal to half its voltage range. For other sensors like for instance gyroscopes or inclinometers, sometimes formulae are given in the datasheets to calculate the sensitivity factor. If the output pf the sensors is already in digital form, as it is the case for encoders, it is only necessary to know the sensitivity that in this case relates measured magnitude and digital value.

Experimental data is commonly corrupted by all kind of minor undesirable signals. For that purpose, after having scaled properly all signals of the sensors, they are smoothened to leave out noise and other rapid phenomena like radio interferences from the radio transmission of the wheel torque sensor. Simple moving average with different spans depending on the sensor type proved to be adequate. The data presented in the next two sections have been post–processed as explained.

2.4.2 Low speed straight–line maneuver

The first test maneuver is a low speed straight–line maneuver. It is intended for studying the longitudinal dynamics of the vehicle. At the beginning of the maneuver, the automatic gear was put to go forward and the brake was actuated to held the vehicle steady. Then, the brake pedal was slowly released, allowing the vehicle to start moving. Once the brake pedal was completely released, the throttle pedal was actuated and then released. Finally, the brake pedal was slowly actuated until the vehicle stopped completely. The total distance was 63.5 m and the maximum vehicle speed 23 km/h. The reference maneuver has been repeated seven times using the TBW and the BBW systems. The brake pressure and the position of the throttle pedal are shown in figs. 2.39 and 2.40 for the reference maneuver and the seven repetitions. In the following figures, the reference is always the dashed line.

As observed in both figures, the repeatability of the control inputs is very good and could hardly be improved, meaning that the experimental setup of the vehicle complies with the requirements of this research. The most important magnitudes for the longitudinal dynamics of the vehicle are presented hereafter:

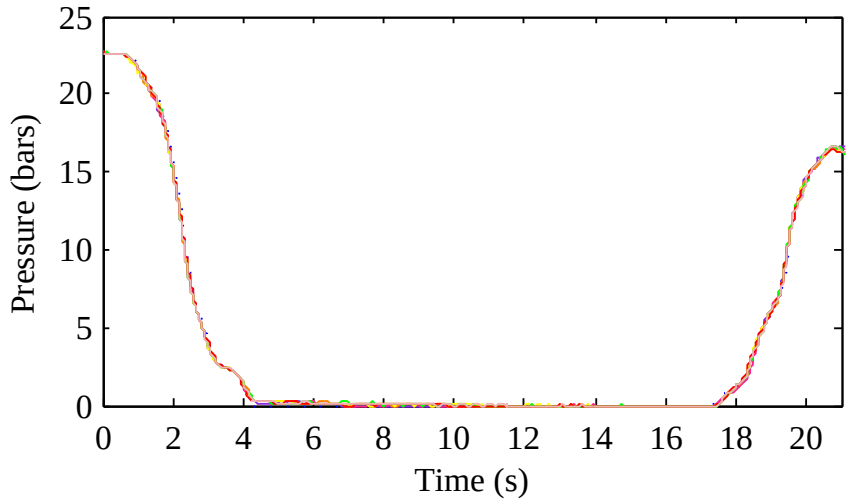

Figure 2.39: Brake pressure (straight–line)

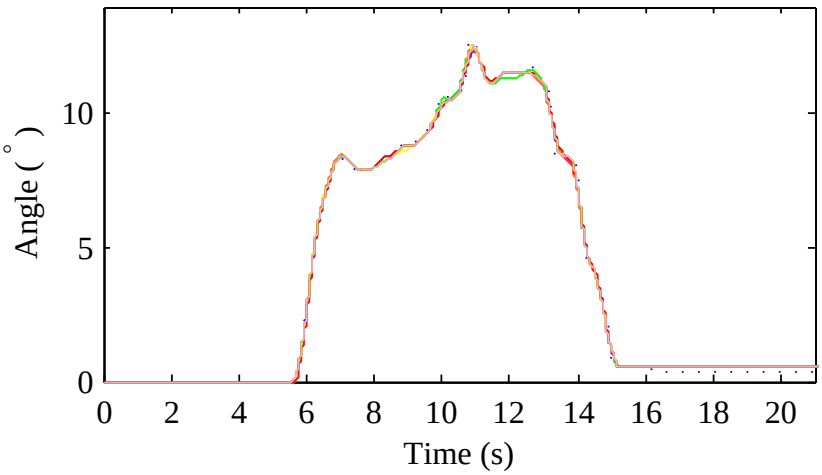

Figure 2.40: Throttle angle (straight–line)

- chassis longitudinal acceleration – fig. 2.41
- pitch angular velocity – fig. 2.42
- right rear wheel torque – fig. 2.43
- left front wheel speed – fig. 2.44. It is calculated using the wheel angles and the loaded tire radius.

2.4.3 Low speed J–turn maneuver

The second test maneuver is a low speed J–turn maneuver. It is intended in this case for studying the lateral dynamics of the vehicle. The beginning of the maneuver is identical to the straight–line maneuver. The driver's actuations on the brake and the throttle pedal are also very similar. During the maneuver, the steering wheel is turned moderately quickly on

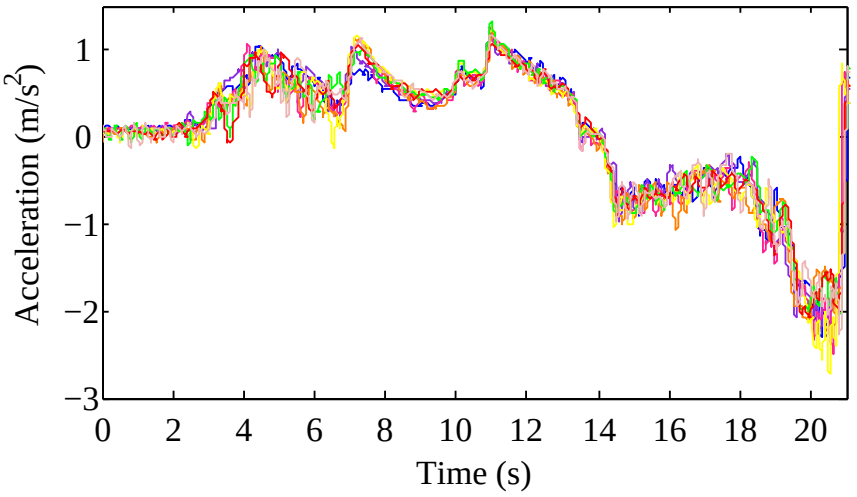

Figure 2.41: Longitudinal acceleration (straight–line)

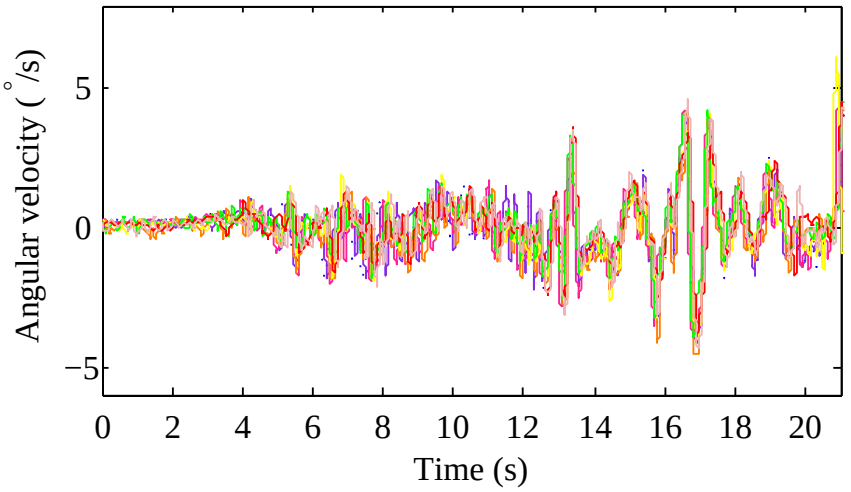

Figure 2.42: Pitch angular velocity (straight–line)

one side before being brought back to its original position to complete the J–turn. The total distance was 59.6 m and the maximum vehicle speed 18 km/h. The reference maneuver has been repeated six times using the TBW, the BBW and the SBW systems. The brake pressure, the position of the throttle pedal and the rack and pinion system angle are shown in figs. 2.45 to 2.47. As for the previous maneuver, the repeatability of the control inputs is very good and the same conclusion as before can be made. The most important magnitudes for the lateral dynamics of the vehicle as well as some for the longitudinal dynamics are presented hereafter:

- chassis longitudinal acceleration – fig. 2.48
- chassis lateral acceleration – fig. 2.49
- right rear wheel torque – fig. 2.50
- left front wheel speed – fig. 2.51

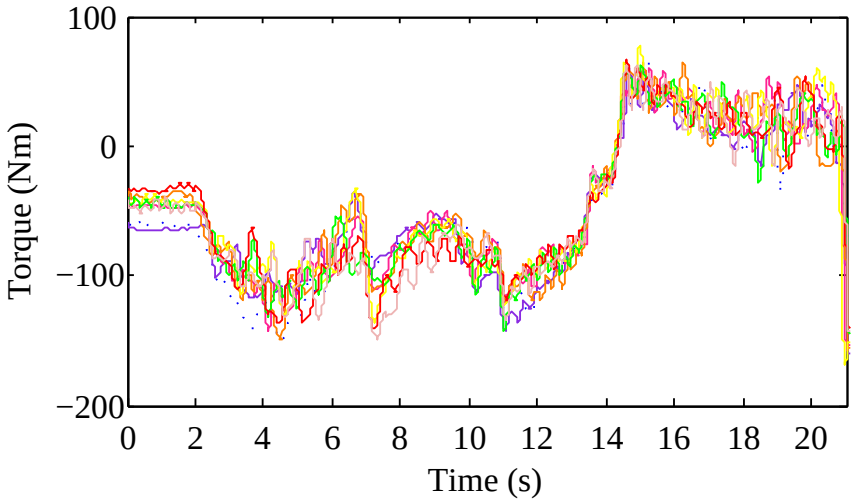

Figure 2.43: Right rear wheel torque (straight–line)

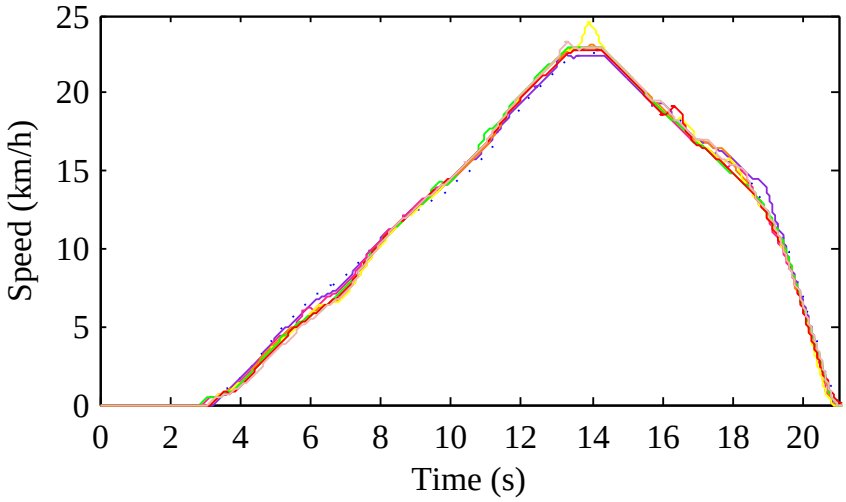

Figure 2.44: Left front wheel speed (straight–line)

- roll angular velocity – fig. 2.52
- pitch angular velocity – fig. 2.53

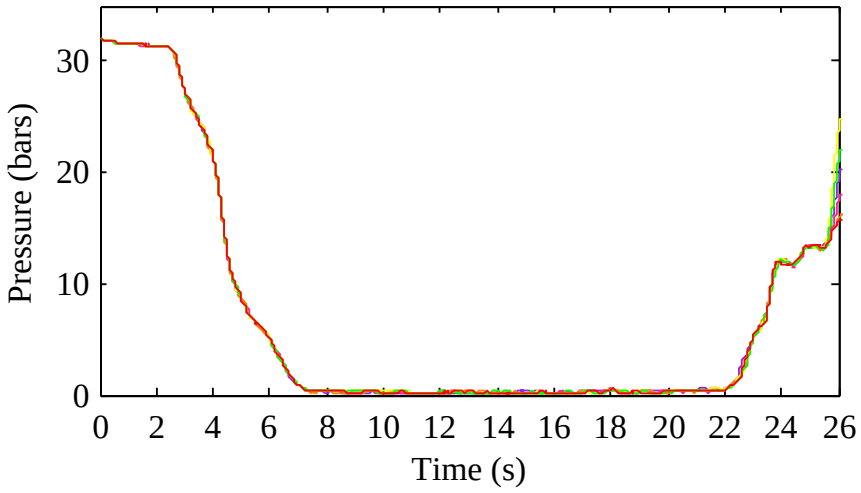

Figure 2.45: Brake pressure (J–turn)

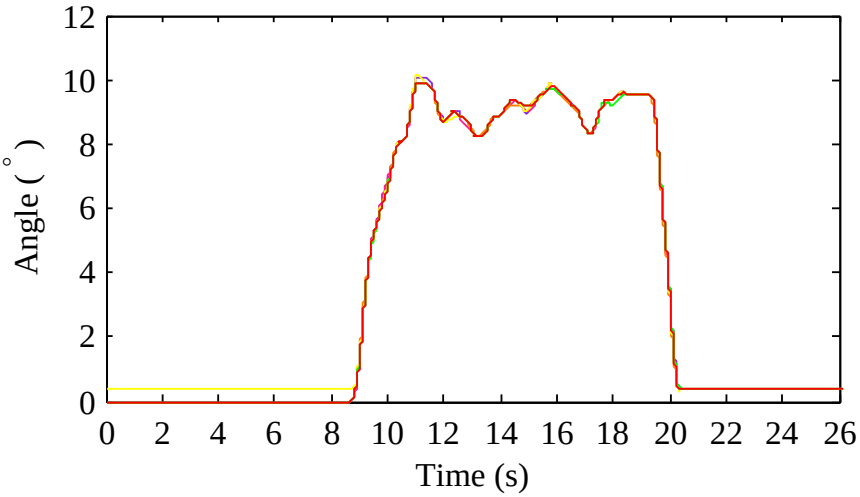

Figure 2.46: Throttle angle (J–turn)

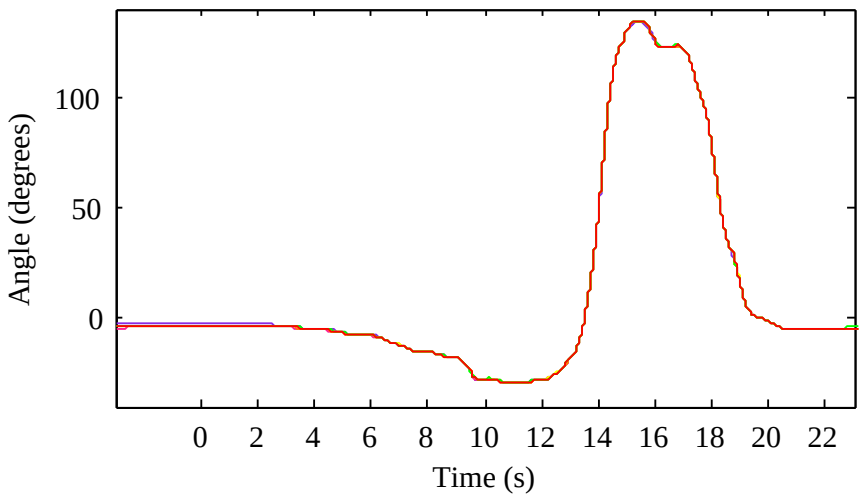

Figure 2.47: Rack and pinion system angle (J–turn)

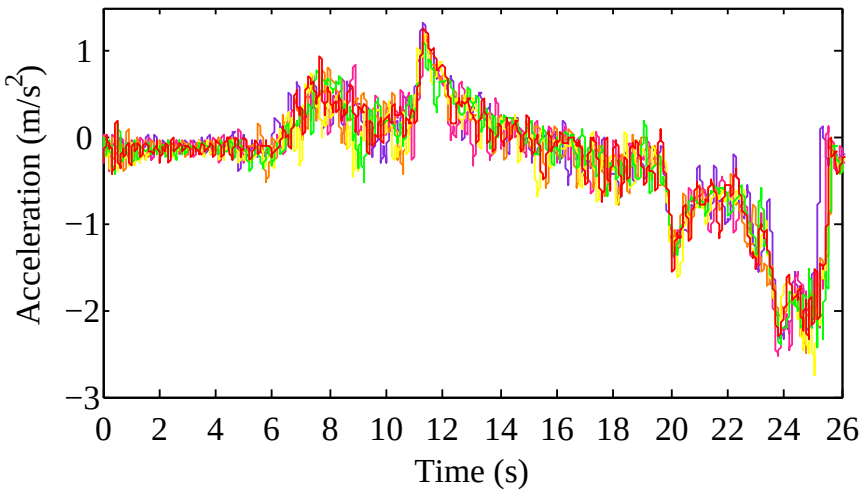

Figure 2.48: Longitudinal acceleration (J–turn)

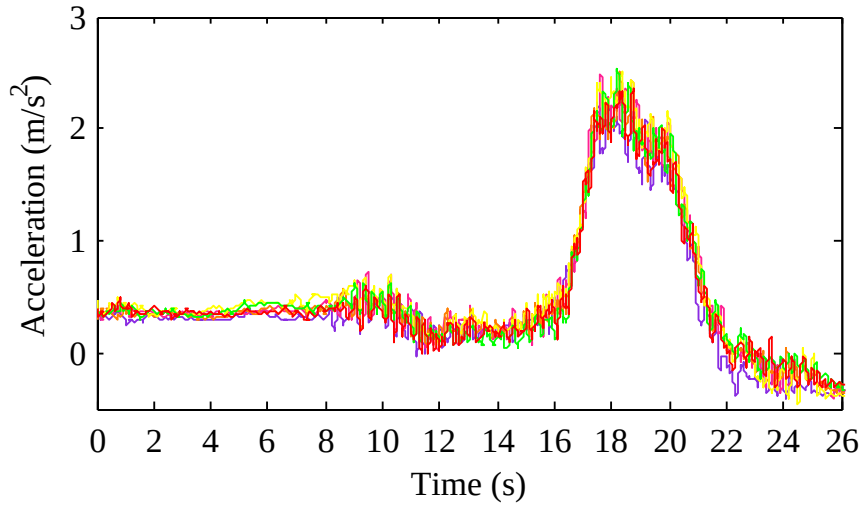

Figure 2.49: Lateral acceleration (J–turn)

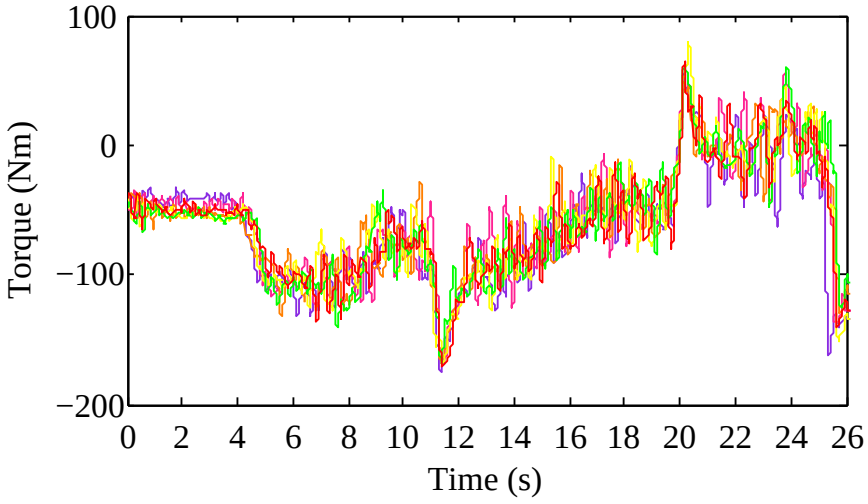

Figure 2.50: Right rear wheel torque (J–turn)

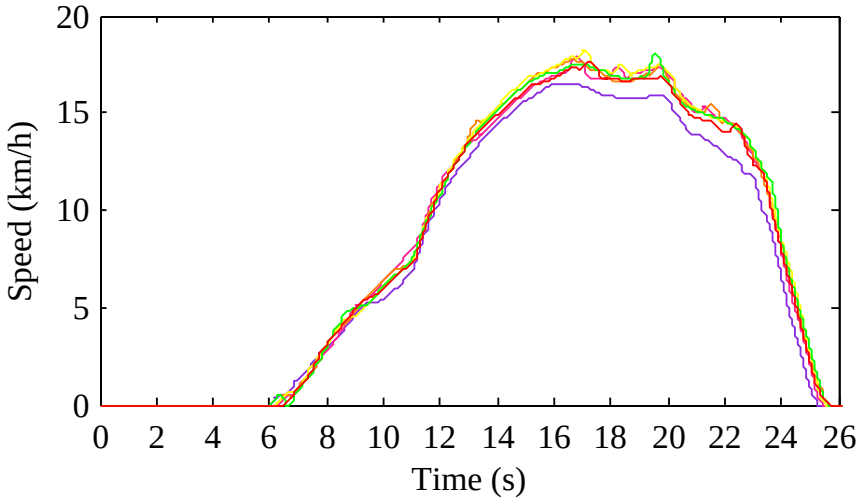

Figure 2.51: Left front wheel speed (J–turn)

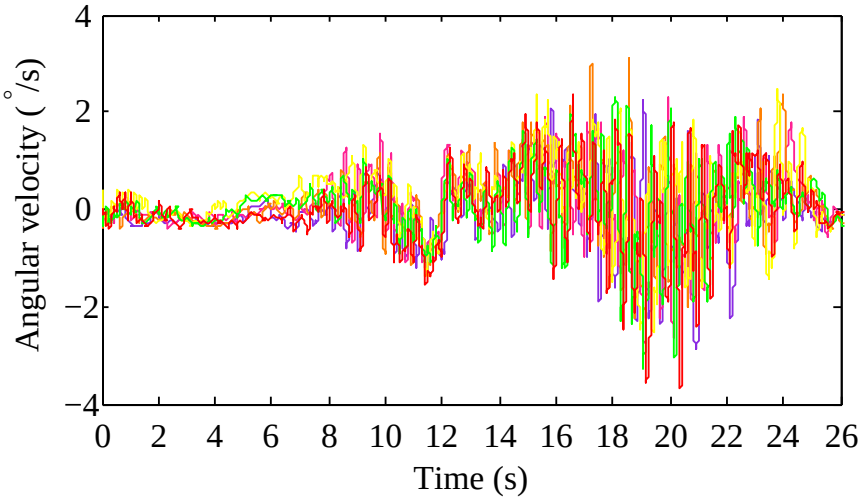

Figure 2.52: Roll angular velocity (J–turn)

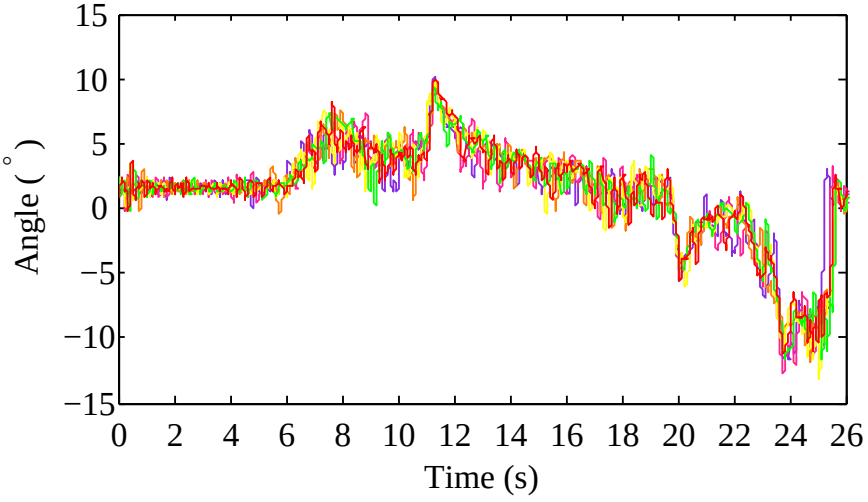

Figure 2.53: Pitch angular velocity (J–turn)

Chapter 3

Vehicle modeling and simulation environment

3.1 Vehicle modeling

3.1.1 Multibody formulation and integrator

As explained in section 1.2, MB vehicle models can be built either employing commercial MB softwares or self-developed MB codes. This work deals with the second option. The XBW vehicle prototype presented in section 2.2 has been modeled using fully Cartesian dependent coordinates, also called natural coordinates (García de Jalón and Bayo, 1994; García de Jalón, 2007). For three dimensional MB systems, these coordinates describe the positions of each element by means of the Cartesian coordinates of *basic points* distributed throughout all the elements and the Cartesian components of several unit vectors. Each element of the system should have a sufficient number of points and vectors linked to it so that their motion completely defines that of the element. The chosen MB formulation is an *index 3 augmented Lagrangian (I3AL) formulation with mass–damping–stiffness–orthogonal projections in velocities and accelerations*. It is explained in detail below.

The constraints that relate the dependent coordinates can first be grouped as shown in eq. (3.1). The Lagrange's equations for a constrained mechanical system are presented in eq. (3.2). Equations (3.1) and (3.2) constitutes a system of DAEs. Its solution yields the values of n_d dependent coordinates as well as the m Lagrange multipliers. Instead of solving the system using this approach, it is possible to introduce some penalty terms following the alternative penalty formulation approach (Bayo et al., 1988). The resulting equations, shown in eq. (3.3) yield the *augmented Lagrangian (AL) formulation* (García de Jalón and Bayo, 1994), where the penalty terms are zero if the constraints are satisfied. In this method, in order to avoid using explicitly eq. (3.1), the Lagrange multipliers are calculated iteratively, as shown in eq. (3.4). This last equation represents the progressive introduction of forces that help to fulfill better the constraints of eq. (3.1). Finally, the iterative process of eq. (3.4) can be introduced in eq. (3.3), leading to eq. (3.5) that is used to iterate until $\|\mathbf{q}_{i+1} - \mathbf{q}_i\| \leq \epsilon$, where ϵ is user–defined.

$$\boldsymbol{\Phi}(\mathbf{q}, t) = \mathbf{0} \tag{3.1}$$

$$\mathbf{M}\ddot{\mathbf{q}} + \boldsymbol{\Phi}_{\mathbf{q}}^{\mathrm{T}}\boldsymbol{\lambda} = \mathbf{Q} \tag{3.2}$$

$$\mathbf{M}\ddot{\mathbf{q}} + \boldsymbol{\Phi}_{\mathbf{q}}^{\mathrm{T}}\boldsymbol{\alpha}(\ddot{\boldsymbol{\Phi}} + 2\boldsymbol{\omega}\boldsymbol{\zeta}\dot{\boldsymbol{\Phi}} + \boldsymbol{\omega}^2\boldsymbol{\Phi}) + \boldsymbol{\Phi}_{\mathbf{q}}^{\mathrm{T}}\boldsymbol{\lambda}^* = \mathbf{Q} \tag{3.3}$$

$$\boldsymbol{\lambda}^*_{i+1} = \boldsymbol{\lambda}^*_i + \boldsymbol{\alpha}(\ddot{\boldsymbol{\Phi}} + 2\boldsymbol{\omega}\boldsymbol{\zeta}\dot{\boldsymbol{\Phi}} + \boldsymbol{\omega}^2\boldsymbol{\Phi}) \quad \text{with } \boldsymbol{\lambda}^*_0 = \mathbf{0} \tag{3.4}$$

$$(\mathbf{M} + \boldsymbol{\Phi}_{\mathbf{q}}^{\mathrm{T}}\boldsymbol{\alpha}\boldsymbol{\Phi}_{\mathbf{q}})\ddot{\mathbf{q}}_{i+1} = \mathbf{M}\ddot{\mathbf{q}}_i - \boldsymbol{\Phi}_{\mathbf{q}}^{\mathrm{T}}\boldsymbol{\alpha}(\dot{\boldsymbol{\Phi}}_{\mathbf{q}}\dot{\mathbf{q}} + \dot{\boldsymbol{\Phi}}_t + 2\boldsymbol{\omega}\boldsymbol{\zeta}\dot{\boldsymbol{\Phi}} + \boldsymbol{\omega}^2\boldsymbol{\Phi}) \tag{3.5}$$

where i is the index for the iterative process (i=0,1,2...), $\boldsymbol{\Phi}$ are the constraints, $\mathbf{q}$ is the vector of dependent coordinates, $\mathbf{M}$ is the mass matrix, $\boldsymbol{\Phi}_{\mathbf{q}}$ is the Jacobian matrix of the constraint equations, $\boldsymbol{\lambda}$ and $\boldsymbol{\lambda}^*$ are the Lagrange multipliers, $\mathbf{Q}$ contains the external forces, the velocity–dependent inertia forces and those obtained from a potential, $\boldsymbol{\Phi}_t$ is the partial derivative of the constraints with respect to time and $\boldsymbol{\alpha}$, $\boldsymbol{\zeta}$ and $\boldsymbol{\omega}$ contain the penalty factors (usually $> 10^7$, its dimension depends on the type of constraints), the dimensionless damping ratios (usually $\simeq 1$) and the natural frequencies (usually $\simeq 10$ rad/s) for each constraint.

The AL formulation yields a solution set of $\mathbf{q}^*$, $\dot{\mathbf{q}}^*$ and $\ddot{\mathbf{q}}^*$ that enforces the penalty system $(\ddot{\boldsymbol{\Phi}} + 2\boldsymbol{\omega}\boldsymbol{\zeta}\dot{\boldsymbol{\Phi}} + \boldsymbol{\omega}^2\boldsymbol{\Phi})$ to be exactly equal to zero (within machine precision) but not each individual constraint. In order to achieve full constraint satisfaction, constraint cleaning through mass–orthogonal projections has been proposed by Bayo and Ledesma

(1996). The main idea of this approach is to force the set of DAE to meet the underlying ordinary differential equation (ODE) by taking the solution to the constraint manifold where $\boldsymbol{\Phi}$, $\dot{\boldsymbol{\Phi}}$ and $\ddot{\boldsymbol{\Phi}}$ are all equal to zero. A modification of the projection method for an index 3 formulation, in which the positions $\mathbf{q}$ are the primary variables in the integration process, has been proposed by Cuadrado et al. (2000). It consists in mass–damping–stiffness–orthogonal projections in velocities and accelerations that improve the computational efficiency of the method. The integration process yields a set of velocities $\dot{\mathbf{q}}^*$ that does not completely satisfy $\dot{\boldsymbol{\Phi}} = \mathbf{0}$. This solution is therefore projected to the velocity constraint manifold to obtain a set of velocities $\dot{\mathbf{q}}$ that satisfy $\dot{\boldsymbol{\Phi}} = 0$. In a similar way, for the accelerations, the solution $\ddot{\mathbf{q}}^*$ is projected to the acceleration constraint manifold to obtain a set of accelerations $\ddot{\mathbf{q}}$ that satisfy $\ddot{\boldsymbol{\Phi}} = 0$. The mass–damping–stiffness–orthogonal projections in velocities and accelerations are obtained through the constrained minimization problems shown in eq. (3.6) and eq. (3.7) respectively. Each minimization problem can be solved for instance using the AL method.

$$\min_{\dot{\mathbf{q}}} \mathrm{V} = \frac{1}{2}(\dot{\mathbf{q}} - \dot{\mathbf{q}}^*)\mathrm{W}(\dot{\mathbf{q}} - \dot{\mathbf{q}}^*) \quad \text{subject to } \dot{\boldsymbol{\Phi}}(\mathbf{q}, \dot{\mathbf{q}}, \mathrm{t}) = \mathbf{0} \tag{3.6}$$

$$\min_{\ddot{\mathbf{q}}} \mathrm{V} = \frac{1}{2}(\ddot{\mathbf{q}} - \ddot{\mathbf{q}}^*)\mathrm{W}(\ddot{\mathbf{q}} - \ddot{\mathbf{q}}^*) \quad \text{subject to } \ddot{\boldsymbol{\Phi}}(\mathbf{q}, \dot{\mathbf{q}}, \ddot{\mathbf{q}}, \mathrm{t}) = \mathbf{0} \tag{3.7}$$

$$\left[\mathrm{W} + \frac{\Delta \mathrm{t}^2}{4}\boldsymbol{\Phi}_{\mathbf{q}}^{\mathrm{T}}\boldsymbol{\alpha}\boldsymbol{\Phi}_{\mathbf{q}}\right]\dot{\mathbf{q}}_{\mathrm{i}} = \mathrm{W}\dot{\mathbf{q}}_{\mathrm{i}}^* - \frac{\Delta \mathrm{t}^2}{4}\boldsymbol{\Phi}_{\mathbf{q}}^{\mathrm{T}}\boldsymbol{\alpha}\boldsymbol{\Phi}_{\mathrm{t}} \tag{3.8}$$

$$\left[\mathrm{W} + \frac{\Delta \mathrm{t}^2}{4}\boldsymbol{\Phi}_{\mathbf{q}}^{\mathrm{T}}\boldsymbol{\alpha}\boldsymbol{\Phi}_{\mathbf{q}}\right]\ddot{\mathbf{q}}_{\mathrm{i}} = \mathrm{W}\ddot{\mathbf{q}}_{\mathrm{i}}^* - \frac{\Delta \mathrm{t}^2}{4}\boldsymbol{\Phi}_{\mathbf{q}}^{\mathrm{T}}\boldsymbol{\alpha}(\dot{\boldsymbol{\Phi}}_{\mathbf{q}}\dot{\mathbf{q}} + \dot{\boldsymbol{\Phi}}_{\mathrm{t}}) \tag{3.9}$$

where $\mathrm{W} = \left(\mathbf{M} + \frac{\Delta \mathrm{t}}{2}\mathbf{C} + \frac{\Delta \mathrm{t}^2}{4}\mathbf{K}\right)$. As the projections in velocities and accelerations enforce the constraints $\dot{\boldsymbol{\Phi}}$ and $\ddot{\boldsymbol{\Phi}}$ to be equal to zero (within machine precision), the equations of motion (eq. (3.3)) and the iterative process of the Lagrange multipliers (eq. (3.4)) can be simplified as can be seen in eq. (3.10) and eq. (3.11).

$$\mathbf{M}\ddot{\mathbf{q}} + \boldsymbol{\Phi}_{\mathbf{q}}^{\mathrm{T}}\boldsymbol{\alpha}^*\boldsymbol{\Phi} + \boldsymbol{\Phi}_{\mathbf{q}}^{\mathrm{T}}\boldsymbol{\lambda}^* = \mathbf{Q} \tag{3.10}$$

$$\boldsymbol{\lambda}_{\mathrm{i}+1}^* = \boldsymbol{\lambda}_{\mathrm{i}}^* + \boldsymbol{\alpha}^*\boldsymbol{\Phi}_{\mathrm{i}+1} \quad \text{with } \boldsymbol{\lambda}_0^* = \boldsymbol{\lambda}_{\mathrm{k}}^* \tag{3.11}$$

where i is the index for the iterative process ($\mathrm{i} = 0, 1, 2\ldots$), $\boldsymbol{\alpha}^*$ are the penalty factors (they do not have the same value than $\boldsymbol{\alpha}$ previously mentioned) and $\boldsymbol{\lambda}_k^*$ are the Lagrange multipliers of the previous time step. As integration scheme, the implicit single-step trapezoidal rule with fixed time step has been employed. The corresponding difference equations for velocities and accelerations are presented in eqs. (3.12) and (3.13).

$$\dot{\mathbf{q}}_{\mathrm{k}+1} = \frac{2}{\Delta \mathrm{t}}\mathbf{q}_{\mathrm{k}+1} + \hat{\dot{\mathbf{q}}}_{\mathrm{k}} \quad \text{with } \hat{\dot{\mathbf{q}}}_{\mathrm{k}} = -\left(\frac{2}{\Delta \mathrm{t}}\mathbf{q}_{\mathrm{k}} + \dot{\mathbf{q}}_{\mathrm{k}}\right) \tag{3.12}$$

$$\ddot{\mathbf{q}}_{\mathrm{k}+1} = \frac{4}{\Delta \mathrm{t}^2}\mathbf{q}_{\mathrm{k}+1} + \hat{\ddot{\mathbf{q}}}_{\mathrm{k}} \quad \text{with } \hat{\ddot{\mathbf{q}}}_{\mathrm{k}} = -\left(\frac{4}{\Delta \mathrm{t}^2}\mathbf{q}_{\mathrm{k}} + \frac{4}{\Delta \mathrm{t}}\dot{\mathbf{q}}_{\mathrm{k}} + \ddot{\mathbf{q}}_{\mathrm{k}}\right) \tag{3.13}$$

The equations of the integrator can be introduced into eq. (3.10) to establish the dynamical equilibrium at time step (k+1). They are shown in eq. (3.14) after having been scaled by a factor of $\Delta \mathrm{t}/4$ for numerical reasons.

$$\begin{aligned} \mathbf{g}(\mathbf{q}_{\mathrm{k}+1}) &\equiv \mathbf{M}\mathbf{q}_{\mathrm{k}+1} + \frac{\Delta \mathrm{t}^2}{4}\boldsymbol{\Phi}_{\mathbf{q}_{\mathrm{k}+1}}^{T}(\boldsymbol{\alpha}\boldsymbol{\Phi}_{\mathrm{k}+1} + \boldsymbol{\lambda}_{\mathrm{k}+1}) - \frac{\Delta \mathrm{t}^2}{4}\mathbf{Q}_{\mathrm{k}+1} + \frac{\Delta \mathrm{t}^2}{4}\mathbf{M}\hat{\ddot{\mathbf{q}}}_{\mathrm{k}} = 0 \\ &\equiv \frac{\Delta \mathrm{t}^2}{4}(\mathbf{M}\ddot{\mathbf{q}} + \boldsymbol{\Phi}_{\mathbf{q}}^{T}\boldsymbol{\alpha}\boldsymbol{\Phi} + \boldsymbol{\Phi}^{T}\boldsymbol{\lambda}^* - \mathbf{Q}) \end{aligned} \tag{3.14}$$

The solution of this nonlinear system can be obtain using for instance the Newton–Raphson method. This method is based on a linearization of $\mathbf{g}$ that consists in replacing the function by the first two terms of its expansion in Taylor series around a certain approximation $\mathbf{q}_i$ to the desired solution, as described in eq. (3.15). To accurately approximate vector $\mathbf{q}_{k+1}$, an initial approximation of it (i.e. $\mathbf{q}_0$) is calculated using an explicit integrator and then the iterative formula shown eq. (3.15) is used until the approximation error becomes insignificant, as demonstrated eq. (3.16). The tangent matrix, shown in eq. (3.17), has been approximated by removing the negligible terms $\mathbf{\Phi_{qq}}$.

$$\mathbf{g}(\mathbf{q}_{i+1}) \simeq \mathbf{g}(\mathbf{q}_i) + \frac{\partial \mathbf{g}(\mathbf{q}_i)}{\partial \mathbf{q}_i}(\mathbf{q}_{i+1} - \mathbf{q}_i) = \mathbf{0} \tag{3.15}$$

$$\mathbf{q}_{k+1} = \mathbf{q}_{i+1} \quad \text{when } (\mathbf{q}_{i+1} - \mathbf{q}_i) \simeq 0 \tag{3.16}$$

$$\frac{\partial \mathbf{g}(t, \mathbf{q})}{\partial \mathbf{q}} \simeq W + \frac{\Delta t^2}{4}\mathbf{\Phi}_\mathbf{q}^T \boldsymbol{\alpha} \mathbf{\Phi_q} \tag{3.17}$$

After convergence has been achieved in the Newton–Raphson method, the resulting velocities $\dot{\mathbf{q}}^*$ and the accelerations $\ddot{\mathbf{q}}^*$ are projected using eqs. (3.8) and (3.9) to get their cleaned counterparts $\dot{\mathbf{q}}$ and $\ddot{\mathbf{q}}$.

3.1.2 Details of the multibody model

The vehicle prototype has been modeled with natural coordinates plus some relative coordinates (angles and distances added for convenience), which are usually referred as mixed coordinates. An integration time step of 5 ms has been used. All the 18 bodies of the prototype have been modeled as rigid bodies. Each element or body of the system should have a sufficient number of points and vectors rigidly attached to it, so that their motion completely defines that of the element. All the points employed in the modeling of the vehicle prototype plus some vectors are presented in fig. 3.1. The rest of vectors and relative coordinates are presented in the following subsections for every body. After having defined the set of natural coordinates as well as the set of relative coordinates, constraint equations are necessary to define the relations between points and vectors. The first constraint equations that have been employed are those of rigid bodies: unit vector – eq. (3.18), constant distance – eq. (3.19) and constant angle – eq. (3.20).

$$\mathbf{u}_n \cdot \mathbf{u}_n - 1 = 0 \tag{3.18}$$

$$\mathbf{r}_{i,j} \cdot \mathbf{r}_{i,j} - L_{i,j}^2 = 0 \tag{3.19}$$

$$\mathbf{r}_{i,j} \cdot \mathbf{u}_n - L_{i,j}^2 \, cos\phi = 0 \tag{3.20}$$

where i and j refer to the basic point numbers and n to the unit vector numbers. Some other constraints have been defined as linear combination of previously defined vectors. For instance the unit vector $\mathbf{u}_n$ can be defined as a linear combination of the unit vector $\mathbf{u}_m$ and the segment $(i - j)$ as shown in eq. (3.21).

$$\mathbf{u}_n - \alpha \mathbf{r}_{i,j} - \beta \cdot \mathbf{u}_m = 0 \tag{3.21}$$

where α_1 and α_2 are constant scalar coefficients. Joint constraints have also been used as the one to maintain two vectors aligned (for example $\mathbf{u}_n$ and $\mathbf{r}_{i,j}$) eq. (3.22).

$$\mathbf{u}_n \wedge \mathbf{r}_{i,j} = 0 \tag{3.22}$$

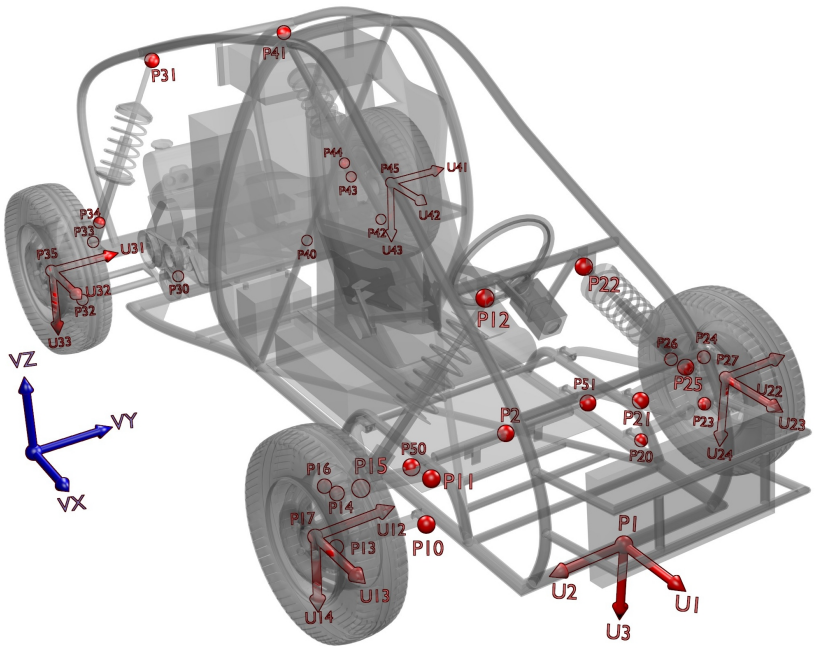

Figure 3.1: All the points and some vectors of the modeling

Varying distance constraint equations have been introduced in relation with the use of mixed coordinates eq. (3.23).

$$\mathbf{r}_{i,j} \cdot \mathbf{r}_{i,j} - \mathrm{s}^2 = 0 \tag{3.23}$$

Finally angle definitions have also been necessary. The equation corresponding to the angle between segments $(i-k)$ and $(k-j)$ when the angle, whose direction is defined by the unit vector $\mathbf{u}$, is not close to 0 nor 180 is shown in eq. (3.24). Otherwise eq. (3.25) is taken.

$$\mathbf{r}_{k,i} \cdot \mathbf{r}_{k,j} - (\mathbf{r}_{k,i} \cdot \mathbf{u})(\mathbf{r}_{k,j} \cdot \mathbf{u}) - \mathrm{L}_{i',i}\mathrm{L}_{j',j} cos\phi = 0 \tag{3.24}$$

$$\mathbf{r}_{k,i} \wedge \mathbf{r}_{k,j} - (\mathbf{r}_{k,i} \cdot \mathbf{u})\mathbf{u} \wedge \mathbf{r}_{k,j} - (\mathbf{r}_{k,j} \cdot \mathbf{u})\mathbf{r}_{k,i} \wedge \mathbf{u} - \mathbf{u}\,\mathrm{L}_{i',i}\mathrm{L}_{j',j} sin\phi = 0 \tag{3.25}$$

Rigid bodies

Chassis – The chassis has been modeled as one rigid body. This element is defined by point p_1 and unit vectors $\mathbf{u}_1$, $\mathbf{u}_2$ and $\mathbf{u}_3$. $\mathbf{u}_1$, $\mathbf{u}_2$ and $\mathbf{u}_3$ form the coordinate system of the element with origin in p_1. Extra basic points (p_2, p_{10}, p_{11}, p_{12}, p_{20}, p_{21}, p_{22}, p_{30}, p_{31}, p_{40}, p_{41}) have been defined in order to automatically consider the joints with the bodies connected to the chassis. As a consequence, the total number of variables for the chassis is 45. All the aforementioned points and vectors are demonstrated in fig. 3.2. The restrictions for the chassis are presented below. The rigid bodies constraints are shown in eqs. (3.26) to (3.31).

$$\mathbf{u}_1 \cdot \mathbf{u}_1 - 1 = 0 \tag{3.26}$$

$$\mathbf{u}_2 \cdot \mathbf{u}_2 - 1 = 0 \tag{3.27}$$

$$\mathbf{u}_3 \cdot \mathbf{u}_3 - 1 = 0 \tag{3.28}$$

$$\mathbf{u}_1 \cdot \mathbf{u}_2 = 0 \tag{3.29}$$

$$\mathbf{u}_1 \cdot \mathbf{u}_3 = 0 \tag{3.30}$$

$$\mathbf{u}_2 \cdot \mathbf{u}_3 = 0 \tag{3.31}$$

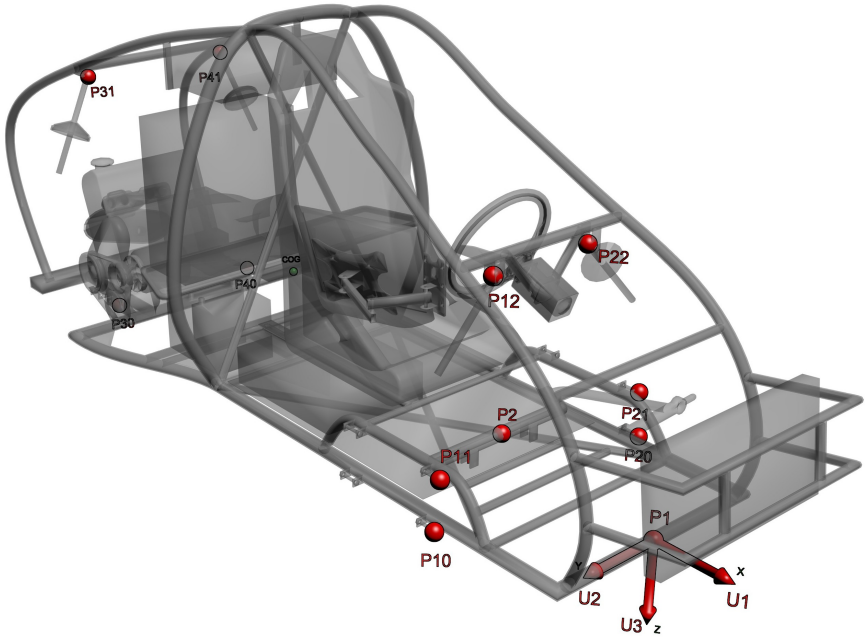

Figure 3.2: Points, vectors, COG, reference set of the chassis

The rest of constraints define the extra points as linear combination of $\mathbf{u}_1$, $\mathbf{u}_2$ and $\mathbf{u}_3$. They are presented in eqs. (3.32) to (3.42).

$$\mathbf{r}_{1,2} - \alpha_2 \cdot \mathbf{u}_1 - \beta_2 \cdot \mathbf{u}_2 - \gamma_2 \cdot \mathbf{u}_3 = 0 \tag{3.32}$$
$$\mathbf{r}_{1,10} - \alpha_{10} \cdot \mathbf{u}_1 - \beta_{10} \cdot \mathbf{u}_2 - \gamma_{10} \cdot \mathbf{u}_3 = 0 \tag{3.33}$$
$$\mathbf{r}_{1,11} - \alpha_{11} \cdot \mathbf{u}_1 - \beta_{11} \cdot \mathbf{u}_2 - \gamma_{11} \cdot \mathbf{u}_3 = 0 \tag{3.34}$$
$$\mathbf{r}_{1,12} - \alpha_{12} \cdot \mathbf{u}_1 - \beta_{12} \cdot \mathbf{u}_2 - \gamma_{12} \cdot \mathbf{u}_3 = 0 \tag{3.35}$$
$$\mathbf{r}_{1,20} - \alpha_{20} \cdot \mathbf{u}_1 - \beta_{20} \cdot \mathbf{u}_2 - \gamma_{20} \cdot \mathbf{u}_3 = 0 \tag{3.36}$$
$$\mathbf{r}_{1,21} - \alpha_{21} \cdot \mathbf{u}_1 - \beta_{21} \cdot \mathbf{u}_2 - \gamma_{21} \cdot \mathbf{u}_3 = 0 \tag{3.37}$$
$$\mathbf{r}_{1,22} - \alpha_{22} \cdot \mathbf{u}_1 - \beta_{22} \cdot \mathbf{u}_2 - \gamma_{22} \cdot \mathbf{u}_3 = 0 \tag{3.38}$$
$$\mathbf{r}_{1,30} - \alpha_{30} \cdot \mathbf{u}_1 - \beta_{30} \cdot \mathbf{u}_2 - \gamma_{30} \cdot \mathbf{u}_3 = 0 \tag{3.39}$$
$$\mathbf{r}_{1,31} - \alpha_{31} \cdot \mathbf{u}_1 - \beta_{31} \cdot \mathbf{u}_2 - \gamma_{31} \cdot \mathbf{u}_3 = 0 \tag{3.40}$$
$$\mathbf{r}_{1,40} - \alpha_{40} \cdot \mathbf{u}_1 - \beta_{40} \cdot \mathbf{u}_2 - \gamma_{40} \cdot \mathbf{u}_3 = 0 \tag{3.41}$$
$$\mathbf{r}_{1,41} - \alpha_{41} \cdot \mathbf{u}_1 - \beta_{41} \cdot \mathbf{u}_2 - \gamma_{41} \cdot \mathbf{u}_3 = 0 \tag{3.42}$$

The total number of constraints for the chassis is 39 (6 for the rigid body constraints and 33 for the linear combinations). Therefore the number of degrees of freedom (DOF) of the chassis is 6. Regarding the chassis mass properties, all the elements fixed to it should be taken into account to calculate its weight and its inertia. On the one hand, it is only necessary to sum the mass of each element for calculating the total mass of the chassis. However, if the heaviest elements were easily taken into account, the mass of smaller elements (wires, fixing elements, etc.) is more difficult to account for. The approach has been to compare the mass of the real chassis with the calculated mass and to sum the difference to the chassis frame mass. Table 3.1 summarizes these masses. On the other hand, the correct mass distribution must be used to calculate the total inertia. In this work, all the chassis elements were assembled in a

Body	Number	Unit mass (kg)	Mass (kg)
chassis frame	1	–	169.3
steering wheel assembly	1	–	1.6
monitor and support	1	–	6.2
seat	1	–	8.4
driver	1	–	75
rack of the amplifier	1	–	7
computer	1	–	10.1
engine and gearbox	1	–	180.4
exhaust system	1	–	10.1
batteries	3	11	33
DAS expansion board rack	1	–	8.1
brake system	1	–	10.3
radiator	1	–	12.1
upper part of the front dampers	2	2.7	5.4
upper part of the rear dampers	2	2	4
Total			541

Table 3.1: Chassis mass properties

COG position (m)		moments of inertia (kg m^2)			
X	-1.489	I_{xx}	+64.571	I_{xy}	-0.900
Y	+0.026	I_{yy}	+306.849	I_{xz}	-2.403
Z	-0.285	I_{zz}	+297.270	I_{yz}	-1.722

Table 3.2: COG coordinates and inertia tensor for the chassis

CAD software to calculate this inertia. Average positions for the upper parts of the front and rear dampers have been used. The position of the center of gravity (COG) and the inertia tensor of this element, expressed in the reference set shown in fig. 3.2, are summarized in table 3.2.

Front right lower wishbone arm – This element is defined by points p_{10}, p_{13} and unit vectors $\mathbf{u}_1$ and $\mathbf{u}_{10}$, as shown in fig. 3.3. $\mathbf{u}_{10}$, $\mathbf{u}_1$ and segment (10–13) form the coordinate system of the element with origin in p_{10}. 6 new variables (p_{13} and $\mathbf{u}_{10}$) are added. It is worth mentioning that as point p_{10} and vector $\mathbf{u}_1$ have been previously defined during the chassis modeling, a revolute joint between the chassis and the front right lower wishbone arm is automatically considered. The constraints for this element are rigid body constraints, eqs. (3.43) to (3.47). As 6 new variables and 5 constraints are added, a new DOF is defined. Considering the previously defined DOFs, the DOF number is at this stage of the modeling is 7. The body mass is 4.2 kg. The position of the COG and the inertia tensor of this element,

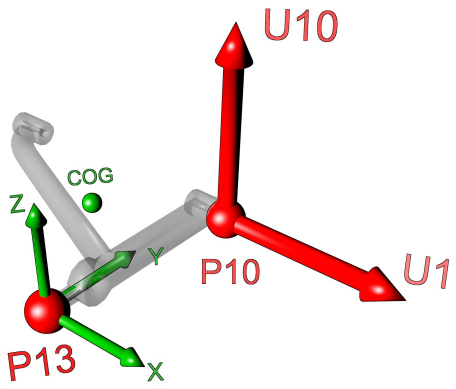

Figure 3.3: Points, vectors, COG, reference set of the front right lower wishbone arm

COG position (m)		moments of inertia (kg m^2)			
X	-0.109	I_{xx}	+0.020	I_{xy}	-0.017
Y	+0.182	I_{yy}	+0.061	I_{xz}	+0.000
Z	+0.0	I_{zz}	+0.081	I_{yz}	+0.000

Table 3.3: COG coordinates and inertia tensor for the front right lower wishbone arm

expressed in the reference set shown in fig. 3.3, are summarized in table 3.3.

$$\mathbf{u}_{10} \cdot \mathbf{u}_{10} - 1 = 0 \tag{3.43}$$

$$\mathbf{u}_{1} \cdot \mathbf{u}_{10} - \cos\phi_{1,10} = 0 \tag{3.44}$$

$$\mathbf{u}_{1} \cdot \mathbf{r}_{10,13} - \mathrm{L}_{10,13} = 0 \tag{3.45}$$

$$\mathbf{u}_{10} \cdot \mathbf{r}_{10,13} = 0 \tag{3.46}$$

$$\mathbf{r}_{10,13} \cdot \mathbf{r}_{10,13} - \mathrm{L}^2_{10,13} = 0 \tag{3.47}$$

Front right upper wishbone arm – This element is defined by points p_{11}, p_{14} and unit vectors $\mathbf{u}_1$ and $\mathbf{u}_{11}$, as shown in fig. 3.4. $\mathbf{u}_{11}$, $\mathbf{u}_1$ and segment (11–14) form the coordinate system of the element with origin in p_{11}. An extra point, p_{15}, is defined to consider the spherical joint between this element and the front right damper. 9 new variables (p_{14}, p_{15} and $\mathbf{u}_{11}$) are added. It is worth mentioning that as point p_{11} and vector $\mathbf{u}_1$ have been previously defined during the chassis modeling, a revolute joint between the chassis and the front right upper wishbone arm is automatically considered. The constraints for this element are rigid body constraints, eqs. (3.48) to (3.52) and a linear combination, eq. (3.53). As 9 new variables and 8 constraints (5 scalar and one vectorial) are added, a new DOF is defined. Considering the previously defined DOFs, the DOF number at this stage of the modeling is 8. The body mass is 9.5 kg. It is composed of the mass of the wishbone arm (4.2 kg) as well as the mass of the damper (5.3 kg), which is considered to be a point mass applied at p_{15}. This approximation allows to take into the damper mass as the damper is not a body of the MB model. The position of the COG and the inertia tensor of this element, expressed in the

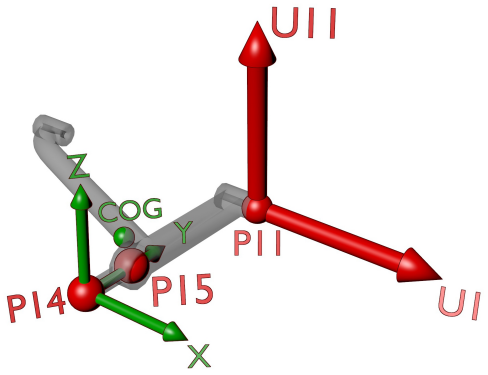

Figure 3.4: Points, vectors, COG, reference set of the front right upper wishbone arm

COG position (m)		moments of inertia (kg m^2)			
X	-0.048	I_{xx}	0.05	I_{xy}	-0.017
Y	0.119	I_{yy}	0.09	I_{xz}	0.000
Z	0.000	I_{zz}	0.139	I_{yz}	0.000

Table 3.4: COG coordinates and inertia tensor for the front right upper wishbone arm

reference set shown in fig. 3.4, are summarized in table 3.4.

$$\mathbf{u}_{11} \cdot \mathbf{u}_{11} - 1 = 0 \tag{3.48}$$

$$\mathbf{u}_{1} \cdot \mathbf{u}_{11} - \cos\phi_{1,11} = 0 \tag{3.49}$$

$$\mathbf{u}_{1} \cdot \mathbf{r}_{11,14} - \cos\phi_{1,11-14} = 0 \tag{3.50}$$

$$\mathbf{u}_{11} \cdot \mathbf{r}_{11,14} - \cos\phi_{11,11-14} = 0 \tag{3.51}$$

$$\mathbf{r}_{11,14} \cdot \mathbf{r}_{11,14} - \mathrm{L}^2_{11,14} = 0 \tag{3.52}$$

$$\mathbf{r}_{11,15} - \alpha_{15} \cdot \mathbf{r}_{11,14} - \beta_{15} \cdot \mathbf{u}_{1} - \gamma_{15} \cdot \mathbf{u}_{11} = 0 \tag{3.53}$$

Front right wheel knuckle – This element is defined by points p_{13}, p_{14}, p_{16}, p_{17} and unit vector $\mathbf{u}_{12}$, as shown in fig. 3.5. $\mathbf{u}_{12}$, segments (14–13) and (14–16) form the coordinate system of the element with origin in p_{14}. An extra point (p_{17}) is defined to consider the revolute joint between this element and the front right wheel. 9 new variables (p_{16}, p_{17} and $\mathbf{u}_{12}$) are added. It is worth mentioning that as points p_{13} and p_{14} have been previously defined during the modeling of the wishbone arms, two spherical joints between the wishbone arms and the front right wheel knuckle are automatically considered. The constraints for this element are rigid body constraints, eqs. (3.54) to (3.59) and a linear combination, eq. (3.60). As 9 new variables and 9 constraints (6 scalar and one vectorial) are added, the number of DOF remains unchanged. In fact, the rotation of the knuckle due to the steering system has been added but the distance between p_{13} and p_{14} has been set constant.

This element is composed of the wheel knuckle and the brake caliper that is rigidly attached to it. The body mass is 7.4 kg. The position of the COG and the inertia tensor of

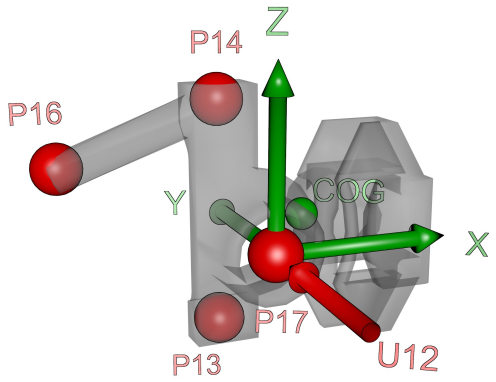

Figure 3.5: Points, vectors, COG, reference set of the front right wheel knuckle

COG position (m)		moments of inertia (kg m^2)			
X	+0.043	I_{xx}	+0.023	I_{xy}	-0.005
Y	+0.055	I_{yy}	+0.044	I_{xz}	-0.007
Z	+0.011	I_{zz}	+0.036	I_{yz}	+0.002

Table 3.5: COG coordinates and inertia tensor for the front right wheel knuckle

this element, expressed in the reference set shown in fig. 3.5, are summarized in table 3.5.

$$\mathbf{u}_{12} \cdot \mathbf{u}_{12} - 1 = 0 \tag{3.54}$$
$$\mathbf{r}_{14,13} \cdot \mathbf{r}_{14,13} - \mathrm{L}_{14,13}^2 = 0 \tag{3.55}$$
$$\mathbf{r}_{14,16} \cdot \mathbf{r}_{14,16} - \mathrm{L}_{14,16}^2 = 0 \tag{3.56}$$
$$\mathbf{r}_{14,13} \cdot \mathbf{r}_{14,16} - \cos\phi_{14-13,14-16} = 0 \tag{3.57}$$
$$\mathbf{r}_{14,13} \cdot \mathbf{u}_{12} - \cos\phi_{14-13,12} = 0 \tag{3.58}$$
$$\mathbf{r}_{14,16} \cdot \mathbf{u}_{12} - \cos\phi_{14-16,12} = 0 \tag{3.59}$$
$$\mathbf{r}_{14,17} - \alpha_{17} \cdot \mathbf{r}_{14,13} - \beta_{17} \cdot \mathbf{r}_{14,16} - \gamma_{17} \cdot \mathbf{u}_{12} = 0 \tag{3.60}$$

Front left lower wishbone arm – This element is defined by points p_{20}, p_{23} and unit vectors $\mathbf{u}_1$ and $\mathbf{u}_{20}$, as shown in fig. 3.6. $\mathbf{u}_1$, $\mathbf{u}_{20}$ and segment (20–23) form the coordinate system of the element with origin in p_{20}. 6 new variables (p_{23} and $\mathbf{u}_{20}$) are added. It is worth mentioning that as point p_{20} and vector $\mathbf{u}_1$ have been previously defined during the chassis modeling, the revolute joint between the chassis and the front left lower wishbone arm is automatically considered. The constraints for this element are rigid body constraints, eqs. (3.61) to (3.65). As 6 new variables and 5 constraints are added, a new DOF is defined. Considering the previously defined DOFs, the DOF number at this stage of the modeling is 9. The body mass is 4.2 kg. The position of the COG and the inertia tensor of this element,

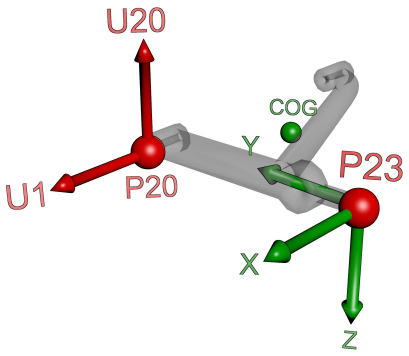

Figure 3.6: Points, vectors, COG, reference set of the front left lower wishbone arm

COG position (m)		moments of inertia (kg m^2)			
X	-0.109	I_{xx}	+0.020	I_{xy}	-0.017
Y	+0.182	I_{yy}	+0.061	I_{xz}	+0.000
Z	+0.0	I_{zz}	+0.081	I_{yz}	+0.000

Table 3.6: COG coordinates and inertia tensor for the front left lower wishbone arm

expressed in the reference set shown in fig. 3.6, are summarized in table 3.6.

$$\mathbf{u}_{20} \cdot \mathbf{u}_{20} - 1 = 0 \tag{3.61}$$

$$\mathbf{r}_{20,23} \cdot \mathbf{r}_{20,23} - \mathrm{L}_{20,23}^2 = 0 \tag{3.62}$$

$$\mathbf{u}_1 \cdot \mathbf{u}_{20} - \cos\phi_{1,20} = 0 \tag{3.63}$$

$$\mathbf{r}_{20,23} \cdot \mathbf{u}_1 - \cos\phi_{20-23,1} = 0 \tag{3.64}$$

$$\mathbf{r}_{20,23} \cdot \mathbf{u}_{20} - \cos\phi_{20-23,20} = 0 \tag{3.65}$$

Front left upper wishbone arm – This element is defined by points p_{21}, p_{24} and unit vectors $\mathbf{u}_1$ and $\mathbf{u}_{21}$, as shown in fig. 3.7. $\mathbf{u}_{21}$, $\mathbf{u}_1$ and segment (21–24) form the coordinate system of the element with origin in p_{21}. An extra point, p_{25}, is defined to consider the spherical joint between this element and the front left damper. 9 new variables (p_{24}, p_{25} and $\mathbf{u}_{21}$) are added. It is worth mentioning that as point p_{21} and vector $\mathbf{u}_1$ have been previously defined during the chassis modeling, a revolute joint between the chassis and the front left upper wishbone arm is automatically considered. The constraints for this element are rigid body constraints, eqs. (3.66) to (3.70) and a linear combination, eq. (3.71). As 9 new variables and 8 constraints (5 scalar and one vectorial) are added, a new DOF is defined. Considering the previously defined DOFs, the DOF number at this stage of the modeling is 10. The body mass is 4.2 kg. It is composed of the mass of the wishbone arm (4.2 kg) as well as the mass of the damper (5.3 kg), which is considered to be a point mass applied at p_{15}. This approximation allows to take into the damper mass as the damper is not a body of the MB model. The position of the COG and the inertia tensor of this element, expressed in the

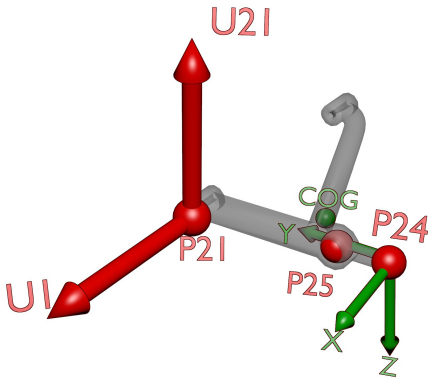

Figure 3.7: Points, vectors, COG, reference set of the front left upper wishbone arm

COG position (m)		moments of inertia (kg m^2)			
X	-0.048	I_{xx}	0.05	I_{xy}	-0.017
Y	0.119	I_{yy}	0.09	I_{xz}	0.000
Z	0.000	I_{zz}	0.139	I_{yz}	0.000

Table 3.7: COG coordinates and inertia tensor for the front left upper wishbone arm

reference set shown in fig. 3.7, are summarized in table 3.7.

$$\mathbf{u}_{21} \cdot \mathbf{u}_{21} - 1 = 0 \tag{3.66}$$

$$\mathbf{u}_{1} \cdot \mathbf{u}_{21} - \cos\phi_{1,21} = 0 \tag{3.67}$$

$$\mathbf{u}_{1} \cdot \mathbf{r}_{21,24} - \cos\phi_{1,21-24} = 0 \tag{3.68}$$

$$\mathbf{u}_{21} \cdot \mathbf{r}_{21,24} - \cos\phi_{21,21-24} = 0 \tag{3.69}$$

$$\mathbf{r}_{21,24} \cdot \mathbf{r}_{21,24} - \mathrm{L}^2_{21,24} = 0 \tag{3.70}$$

$$\mathbf{r}_{21,25} - \alpha_{25} \cdot \mathbf{r}_{21,25} - \beta_{25} \cdot \mathbf{u}_{1} - \gamma_{25} \cdot \mathbf{u}_{21} = 0 \tag{3.71}$$

Front left wheel knuckle – This element is defined by points p_{23}, p_{24}, p_{26}, p_{27} and unit vector $\mathbf{u}_{22}$, as shown in fig. 3.8. $\mathbf{u}_{22}$, segments (24–23) and (24–26) form the coordinate system of the element with origin in p_{24}. An extra point (p_{27}) is defined to consider the revolute joint between this element and the front left wheel. 9 new variables (p_{26}, p_{27} and $\mathbf{u}_{22}$) are added. It is worth mentioning that as points p_{23} and p_{24} have been previously defined during the modeling of the wishbone arms, two spherical joints between the wishbone arms and the front left wheel knuckle are automatically considered. The constraints for this element are rigid body constraints, eqs. (3.72) to (3.77) and a linear combination, eq. (3.60). As 9 new variables and 9 constraints (6 scalar and one vectorial) are added, the number of DOF remains unchanged. In fact, the rotation of the knuckle due to the steering system has been added but the distance between p_{23} and p_{24} has been set constant.

This element is composed of the wheel knuckle and the brake caliper that is rigidly attached to it. The body mass is 7.4 kg. The position of the COG and the inertia tensor of

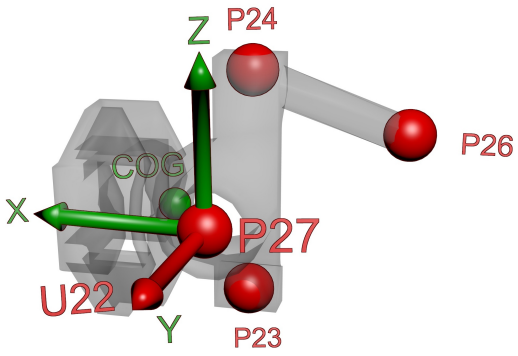

Figure 3.8: Points, vectors, COG, reference set of the front left wheel knuckle

COG position (m)		moments of inertia (kg m^2)			
X	+0.043	I_{xx}	+0.023	I_{xy}	+0.005
Y	-0.055	I_{yy}	+0.044	I_{xz}	-0.007
Z	+0.011	I_{zz}	+0.036	I_{yz}	-0.002

Table 3.8: COG coordinates and inertia tensor for the front left wheel knuckle

this element, expressed in the reference set shown in fig. 3.8, are summarized in table 3.8.

$$\mathbf{u}_{22} \cdot \mathbf{u}_{22} - 1 = 0 \tag{3.72}$$
$$\mathbf{r}_{24,23} \cdot \mathbf{r}_{24,23} - \mathrm{L}^2_{24,23} = 0 \tag{3.73}$$
$$\mathbf{r}_{24,26} \cdot \mathbf{r}_{24,26} - \mathrm{L}^2_{24,26} = 0 \tag{3.74}$$
$$\mathbf{r}_{24,23} \cdot \mathbf{r}_{24,26} - \cos\phi_{24-23,24-26} = 0 \tag{3.75}$$
$$\mathbf{r}_{24,23} \cdot \mathbf{u}_{22} - \cos\phi_{24-23,22} = 0 \tag{3.76}$$
$$\mathbf{r}_{24,26} \cdot \mathbf{u}_{22} - \cos\phi_{24-26,22} = 0 \tag{3.77}$$
$$\mathbf{r}_{24,27} - \alpha_{27} \cdot \mathbf{r}_{24,23} - \beta_{27} \cdot \mathbf{r}_{24,26} - \gamma_{27} \cdot \mathbf{u}_{22} = 0 \tag{3.78}$$

Steering system – This element is defined by points p_{50}, p_{51} and unit vectors $\mathbf{u}_1$ and $\mathbf{u}_3$, as shown in fig. 3.9. $\mathbf{u}_1$, $\mathbf{u}_3$ and segment (50–51) form the coordinate system of the element with origin in p_{50}. 6 new variables (p_{50} and p_{51}) are added. The constraints for this element are rigid body constraints, eqs. (3.79) to (3.81) and a cylindrical joint constraint, eq. (3.82) of which only two are independent. As 6 new variables and 5 constraints are added, a new DOF is defined. Considering the previously defined DOFs, the DOF number at this stage of the modeling is 11. The body mass is 0.57 kg. The position of the COG and the inertia tensor of this element, expressed in the reference set shown in fig. 3.9, are summarized in table 3.9.

$$\mathbf{r}_{50,51} \cdot \mathbf{r}_{50,51} - \mathrm{L}^2_{50,51} = 0 \tag{3.79}$$
$$\mathbf{r}_{50,51} \cdot \mathbf{u}_1 - \cos\phi_{50-51,1} = 0 \tag{3.80}$$
$$\mathbf{r}_{50,51} \cdot \mathbf{u}_3 - \cos\phi_{50-51,3} = 0 \tag{3.81}$$
$$\mathbf{r}_{50,2} \wedge \mathbf{r}_{51,2} = 0 \tag{3.82}$$

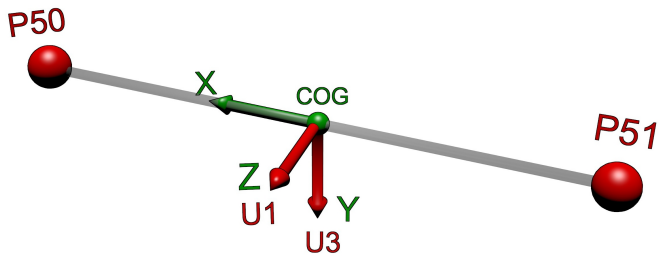

Figure 3.9: Points, vectors, COG, reference set of the steering system

COG position (m)		moments of inertia (kg m^2)		
X	+0.000	I_{xx}	0.00001	I_{xy}
Y	+0.000	I_{yy}	0.0198	I_{xz}
Z	+0.000	I_{zz}	0.0198	I_{yz}

Table 3.9: COG coordinates and inertia tensor for the steering system

Figure 3.10: Points, vectors, COG, reference set of the right tie rod

Right tie rod – This element is defined by points p_{50} and p_{16} as shown in fig. 3.10. No new variables are added. The only constraint for this element is a rigid body constraint, eq. (3.83). As no new variables and 1 constraint are added, a DOF disappears. In fact, the rotation of the right wheel knuckle is now constrained by the translation of the steering system. Considering the previously defined DOFs, the DOF number at this stage of the modeling is 10. The body mass is 0.29 kg. The inertia of this element is one of a bar. For example, at point 50, this inertia is 0.030 kg m^2 as the tie rod length is 0.32 m.

$$\mathbf{r}_{50,16} \cdot \mathbf{r}_{50,16} - \mathrm{L}_{50,16}^2 = 0 \tag{3.83}$$

Left tie rod – This element is defined by points p_{51} and p_{26} as shown in fig. 3.11. No new variables are added. The only constraint for this element is a rigid body constraint, eq. (3.84). As no new variables and 1 constraint are added, a DOF disappears. In fact, the rotation of the left wheel knuckle is now constrained by the translation of the steering system. Considering the previously defined DOFs, the DOF number at this stage of the modeling is 9. The body mass is 0.29 kg. For example, at point 51, this inertia is 0.030 kg m^2 as the tie rod

Figure 3.11: Points, vectors, COG, reference set of the left tie rod

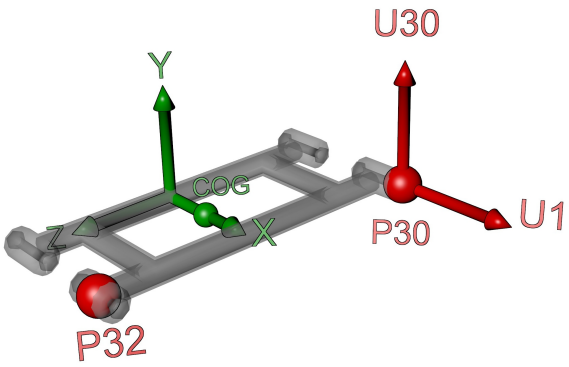

Figure 3.12: Points, vectors, COG, reference set of the rear right wishbone arm

length is 0.32 m.

$$\mathbf{r}_{51,26} \cdot \mathbf{r}_{51,26} - \mathrm{L}^2_{51,26} = 0 \tag{3.84}$$

Rear right wishbone arm – This element is defined by points p_{30}, p_{32} and unit vectors $\mathbf{u}_1$ and $\mathbf{u}_{30}$, as shown in fig. 3.12. $\mathbf{u}_1$, $\mathbf{u}_{30}$ and segment (30–32) form the coordinate system of the element with origin in p_{30}. 6 new variables (p_{32} and $\mathbf{u}_{30}$) are added. It is worth mentioning that as point p_{30} and vector $\mathbf{u}_1$ have been previously defined during the chassis modeling, the revolute joint between the chassis and the rear right wishbone arm is automatically considered. The constraints for this element are rigid body constraints, eqs. (3.85) to (3.89). As 6 new variables and 5 constraints are added, a new DOF is defined. Considering the previously defined DOFs, the DOF number at this stage of the modeling is 10. The body mass is 2.7 kg. The position of the COG and the inertia tensor of this element, expressed in the reference set shown in fig. 3.12, are summarized in table 3.10.

$$\mathbf{u}_{30} \cdot \mathbf{u}_{30} - 1 = 0 \tag{3.85}$$
$$\mathbf{r}_{30,32} \cdot \mathbf{r}_{30,32} - \mathrm{L}^2_{30,32} = 0 \tag{3.86}$$
$$\mathbf{u}_1 \cdot \mathbf{u}_{30} - \cos\phi_{1,30} = 0 \tag{3.87}$$
$$\mathbf{r}_{30,32} \cdot \mathbf{u}_1 - \cos\phi_{30-32,1} = 0 \tag{3.88}$$
$$\mathbf{r}_{30,32} \cdot \mathbf{u}_{30} - \cos\phi_{30-32,30} = 0 \tag{3.89}$$

Rear left wishbone arm – This element is defined by points p_{40}, p_{42} and unit vectors $\mathbf{u}_1$ and $\mathbf{u}_{40}$, as shown in fig. 3.13. $\mathbf{u}_1$, $\mathbf{u}_{40}$ and segment (40–42) form the coordinate system of the element with origin in p_{40}. 6 new variables (p_{42} and $\mathbf{u}_{40}$) are added. It is worth mentioning

COG position (m)		moments of inertia (kg m^2)			
X	+0.060	I_{xx}	+0.055	I_{xy}	+0.000
Y	+0.000	I_{yy}	+0.064	I_{xz}	+0.000
Z	+0.000	I_{zz}	+0.009	I_{yz}	+0.000

Table 3.10: COG coordinates and inertia tensor for the rear right wishbone arm

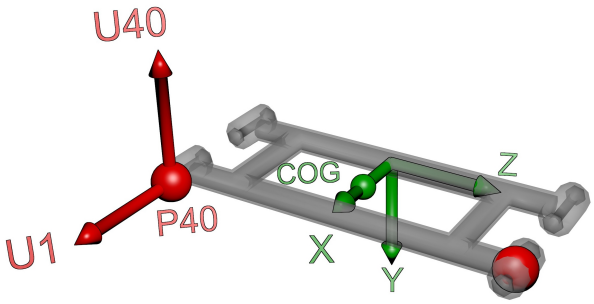

Figure 3.13: Points, vectors, COG, reference set of the rear left wishbone arm

COG position (m)		moments of inertia (kg m^2)			
X	+0.060	I_{xx}	+0.055	I_{xy}	+0.000
Y	+0.000	I_{yy}	+0.064	I_{xz}	+0.000
Z	+0.000	I_{zz}	+0.009	I_{yz}	+0.000

Table 3.11: COG coordinates and inertia tensor for the rear left wishbone arm

that as point p_{40} and vector $\mathbf{u}_1$ have been previously defined during the chassis modeling, the revolute joint between the chassis and the rear left wishbone arm is automatically considered. The constraints for this element are rigid body constraints, eqs. (3.90) to (3.94). As 6 new variables and 5 constraints are added, a new DOF is defined. Considering the previously defined DOFs, the DOF number at this stage of the modeling is 11. The body mass is 2.7 kg. The position of the COG and the inertia tensor of this element, expressed in the reference set shown in fig. 3.13, are summarized in table 3.11.

$$\mathbf{u}_{40} \cdot \mathbf{u}_{40} - 1 = 0 \tag{3.90}$$

$$\mathbf{r}_{40,42} \cdot \mathbf{r}_{40,42} - \mathrm{L}_{40,42}^2 = 0 \tag{3.91}$$

$$\mathbf{u}_1 \cdot \mathbf{u}_{40} - \cos\phi_{1,40} = 0 \tag{3.92}$$

$$\mathbf{r}_{40,42} \cdot \mathbf{u}_1 - \cos\phi_{40-42,1} = 0 \tag{3.93}$$

$$\mathbf{r}_{40,42} \cdot \mathbf{u}_{40} - \cos\phi_{40-42,40} = 0 \tag{3.94}$$

Rear right wheel knuckle – This element is defined by points p_{32}, p_{34} and unit vectors $\mathbf{u}_1$, $\mathbf{u}_{31}$ as shown in fig. 3.14. $\mathbf{u}_1$, $\mathbf{u}_{31}$ and (32–34) form the coordinate system of the element with origin in p_{32}. Two extra point (p_{33} and p_{35}) are defined. The first one is used to define

COG position (m)		moments of inertia (kg m^2)			
X	-0.117	I_{xx}	+0.284	I_{xy}	-0.156
Y	+0.080	I_{yy}	+0.169	I_{xz}	-0.032
Z	-0.031	I_{zz}	+0.370	I_{yz}	+0.035

Table 3.12: COG coordinates and inertia tensor for the rear right wheel knuckle

automatically the revolute joint between this element and the rear right wheel while the second one is employed to define the cylindrical joint of the rear right damper. 12 new variables (p_{33}, p_{34}, p_{35} and $\mathbf{u}_{31}$) are added. It is worth mentioning that as point p_{32} and unit vector u_1 have been previously defined during the rear right wishbone arm modeling, a revolute joint between this wishbone arm and the rear right wheel knuckle is automatically considered. The constraints for this element are rigid body constraints, eqs. (3.95) to (3.99), linear combinations, eqs. (3.100) and (3.101), and a cylindrical joint constraint, eq. (3.102). As 12 new variables and 12 constraints (5 scalar and 7 vectorial) are added, the number of DOF remains unchanged (i.e 11). In fact, only 12 of the 14 constraint equations are independent. Two of the three equations in eq. (3.102) are independent and p_{33} is first defined as a linear combination of the coordinate set and then aligned with p_{31} and p_{34}. To give a physical significance to these constraints, it can be said that before the definition of the rear right wheel knuckle, the rear right wishbone arm had one DOF. After this definition, a revolute joint between the wheel knuckle and the wishbone arm appears but the motion of this joint is constrained by the motion of the damper attached to the chassis. As a consequence, the DOF number remains unchanged despite the definition of new bodies and constraints.

This element is composed of the wheel knuckle, the damper and the brake caliper that are rigidly interconnected. The body mass is 14.1 kg. The position of the COG and the inertia tensor of this element, expressed in the reference set shown in fig. 3.14, are summarized in table 3.12.

$$\mathbf{u}_{31} \cdot \mathbf{u}_{31} - 1 = 0 \tag{3.95}$$
$$\mathbf{r}_{32,34} \cdot \mathbf{r}_{32,34} - \mathrm{L}^2_{32,34} = 0 \tag{3.96}$$
$$\mathbf{u}_1 \cdot \mathbf{u}_{31} - \cos\phi_{1,31} = 0 \tag{3.97}$$
$$\mathbf{r}_{32,34} \cdot \mathbf{u}_1 - \cos\phi_{32-34,1} = 0 \tag{3.98}$$
$$\mathbf{r}_{32,34} \cdot \mathbf{u}_{31} - \cos\phi_{32-34,31} = 0 \tag{3.99}$$
$$\mathbf{r}_{32,33} - \alpha_{33} \cdot \mathbf{r}_{32,34} - \beta_{33} \cdot \mathbf{u}_1 - \gamma_{33} \cdot \mathbf{u}_{31} = 0 \tag{3.100}$$
$$\mathbf{r}_{32,35} - \alpha_{35} \cdot \mathbf{r}_{32,34} - \beta_{35} \cdot \mathbf{u}_1 - \gamma_{35} \cdot \mathbf{u}_{31} = 0 \tag{3.101}$$
$$\mathbf{r}_{33,34} \wedge \mathbf{r}_{33,31} = 0 \tag{3.102}$$

Rear left wheel knuckle – This element is defined by points p_{42}, p_{44} and unit vectors $\mathbf{u}_1$, $\mathbf{u}_{41}$ as shown in fig. 3.15. $\mathbf{u}_1$, $\mathbf{u}_{41}$ and (42–44) form the coordinate system of the element with origin in p_{42}. Two extra point (p_{43} and p_{45}) are defined. The first one is used to define automatically the revolute joint between this element and the rear left wheel while the second one is employed to define the cylindrical joint of the rear left damper. 12 new variables (p_{43}, p_{44}, p_{45} and $\mathbf{u}_{41}$) are added. It is worth mentioning that as point p_{42} and unit vector

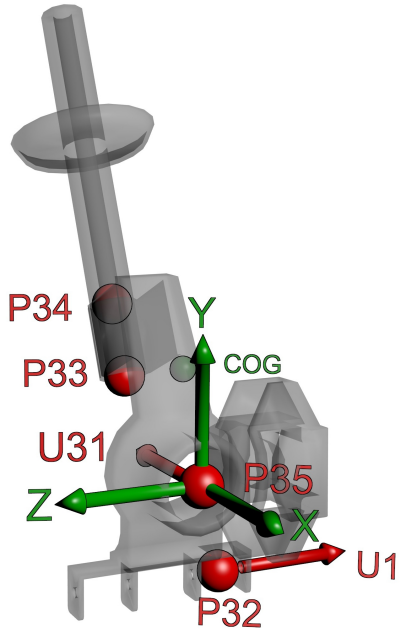

Figure 3.14: Points, vectors, COG, reference set of the rear right wheel knuckle

u_1 have been previously defined during the rear left wishbone arm modeling, a revolute joint between this wishbone arm and the rear left wheel knuckle is automatically considered. The constraints for this element are rigid body constraints, eqs. (3.103) to (3.107), linear combinations, eqs. (3.108) and (3.109), and a cylindrical joint constraint, eq. (3.110). As 12 new variables and 12 constraints (5 scalar and 7 vectorial) are added, the number of DOF remains unchanged (i.e 11). In fact, only 12 of the 14 constraint equations are independent. Two of the three equations in eq. (3.110) are independent and p_{43} is first defined as a linear combination of the coordinate set and then aligned with p_{41} and p_{44}. To give a physical significance to these constraints, it can be said that before the definition of the rear left wheel knuckle, the rear left wishbone arm had one DOF. After this definition, a revolute joint between the wheel knuckle and the wishbone arm appears but the motion of this joint is constrained by the motion of the damper attached to the chassis. As a consequence, the DOF number remains unchanged despite the definition of new bodies and constraints.

This element is composed of the wheel knuckle, the damper and the brake caliper that are rigidly interconnected. The body mass is 14.1 kg. The position of the COG and the inertia tensor of this element, expressed in the reference set shown in fig. 3.15, are summarized in

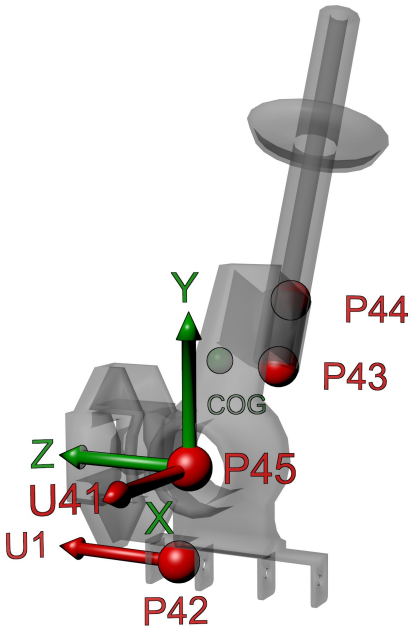

Figure 3.15: Points, vectors, COG, reference set of the rear left wheel knuckle

COG position (m)		moments of inertia (kg m^2)			
X	-0.117	I_{xx}	+0.284	I_{xy}	-0.156
Y	+0.080	I_{yy}	+0.169	I_{xz}	+0.032
Z	+0.031	I_{zz}	+0.370	I_{yz}	-0.035

Table 3.13: COG coordinates and inertia tensor for the rear left wheel knuckle

table 3.13.

$$\mathbf{u}_{41} \cdot \mathbf{u}_{41} - 1 = 0 \tag{3.103}$$
$$\mathbf{r}_{42,44} \cdot \mathbf{r}_{42,44} - \mathrm{L}^2_{42,44} = 0 \tag{3.104}$$
$$\mathbf{u}_1 \cdot \mathbf{u}_{41} - \cos\phi_{1,41} = 0 \tag{3.105}$$
$$\mathbf{r}_{42,44} \cdot \mathbf{u}_1 - \cos\phi_{42-44,1} = 0 \tag{3.106}$$
$$\mathbf{r}_{42,44} \cdot \mathbf{u}_{41} - \cos\phi_{42-44,41} = 0 \tag{3.107}$$
$$\mathbf{r}_{42,43} - \alpha_{43} \cdot \mathbf{r}_{42,44} - \beta_{43} \cdot \mathbf{u}_1 - \gamma_{43} \cdot \mathbf{u}_{41} = 0 \tag{3.108}$$
$$\mathbf{r}_{42,45} - \alpha_{45} \cdot \mathbf{r}_{42,44} - \beta_{45} \cdot \mathbf{u}_1 - \gamma_{45} \cdot \mathbf{u}_{41} = 0 \tag{3.109}$$
$$\mathbf{r}_{43,44} \wedge \mathbf{r}_{43,41} = 0 \tag{3.110}$$

Front right wheel – This element is defined by points p_{17} and unit vectors $\mathbf{u}_{12}$, $\mathbf{u}_{13}$ and $\mathbf{u}_{14}$, as shown in fig. 3.16. $\mathbf{u}_{12}$, $\mathbf{u}_{13}$ and $\mathbf{u}_{14}$ form the coordinate system of the element with origin in p_{17}. 6 new variables ($\mathbf{u}_{13}$ and $\mathbf{u}_{14}$) are added. It is worth mentioning that as point p_{17} and vector $\mathbf{u}_{12}$ have been previously defined during the front right wheel knuckle modeling, the revolute joint between the wheel and the wheel knuckle is automatically considered. The constraints for this element are rigid body constraints, eqs. (3.111) to (3.115). As 6 new

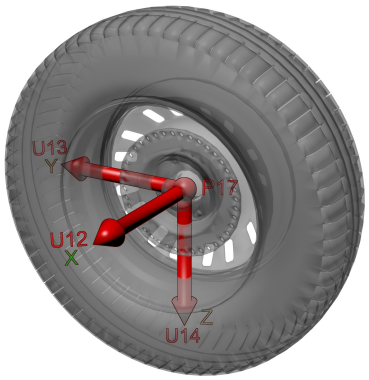

Figure 3.16: Points, vectors, COG, reference set of the front right wheel assembly

COG position (m)		moments of inertia (kg m^2)			
X	+0.065	I_{xx}	+0.534	I_{xy}	+0.000
Y	+0.000	I_{yy}	+0.300	I_{xz}	+0.000
Z	+0.000	I_{zz}	+0.300	I_{yz}	+0.000

Table 3.14: COG coordinates and inertia tensor for the front right wheel

variables and 5 constraints are added, a new DOF is defined. Considering the previously defined DOFs, the DOF number at this stage of the modeling is 12.

This element is composed of the wheel rim, the tire, the wheel hub, the brake disc and the drive flange that are rigidly interconnected. The body mass is 15.1 kg. The position of the COG and the inertia tensor of this element, expressed in the reference set shown in fig. 3.16, are summarized in table 3.14.

$$\mathbf{u}_{13} \cdot \mathbf{u}_{13} - 1 = 0 \tag{3.111}$$
$$\mathbf{u}_{14} \cdot \mathbf{u}_{14} - 1 = 0 \tag{3.112}$$
$$\mathbf{u}_{12} \cdot \mathbf{u}_{13} - \cos\phi_{12,13} = 0 \tag{3.113}$$
$$\mathbf{u}_{12} \cdot \mathbf{u}_{14} - \cos\phi_{12,14} = 0 \tag{3.114}$$
$$\mathbf{u}_{13} \cdot \mathbf{u}_{14} - \cos\phi_{13,14} = 0 \tag{3.115}$$

Front left wheel – This element is defined by points p_{27} and unit vectors $\mathbf{u}_{22}$, $\mathbf{u}_{23}$ and $\mathbf{u}_{24}$, as shown in fig. 3.17. $\mathbf{u}_{22}$, $\mathbf{u}_{23}$ and $\mathbf{u}_{24}$ form the coordinate system of the element with origin in p_{27}. 6 new variables ($\mathbf{u}_{23}$ and $\mathbf{u}_{24}$) are added. It is worth mentioning that as point p_{27} and vector $\mathbf{u}_{22}$ have been previously defined during the front left wheel knuckle modeling, the revolute joint between the wheel and the wheel knuckle is automatically considered. The constraints for this element are rigid body constraints, eqs. (3.116) to (3.120). As 6 new variables and 5 constraints are added, a new DOF is defined. Considering the previously defined DOFs, the DOF number at this stage of the modeling is 13.

This element is composed of the wheel rim, the tire, the wheel hub and the brake disc that are rigidly interconnected whose masses are presented in table 3.15. The position of the COG and the inertia tensor of this element, expressed in the reference set shown in fig. 3.17,

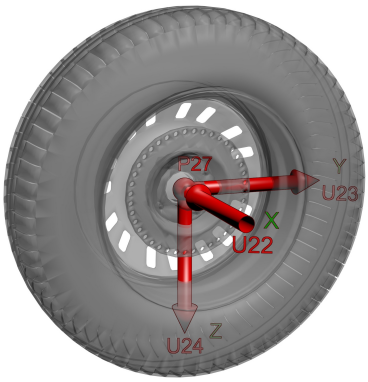

Figure 3.17: Points, vectors, COG, reference set of the front left wheel assembly

Body	number	mass (kg)
rim	1	6
tire	1	5.1
disk brake	1	2.7
hub	1	1.3
Total		15.1

Table 3.15: Front left wheel mass properties

COG position (m)		moments of inertia (kg m^2)			
X	+0.065	I_{xx}	+0.534	I_{xy}	+0.000
Y	+0.000	I_{yy}	+0.300	I_{xz}	+0.000
Z	+0.000	I_{zz}	+0.300	I_{yz}	+0.000

Table 3.16: COG coordinates and inertia tensor for the front left wheel

are summarized in table 3.16.

$$\mathbf{u}_{23} \cdot \mathbf{u}_{23} - 1 = 0 \tag{3.116}$$

$$\mathbf{u}_{24} \cdot \mathbf{u}_{24} - 1 = 0 \tag{3.117}$$

$$\mathbf{u}_{22} \cdot \mathbf{u}_{23} - \cos\phi_{22,23} = 0 \tag{3.118}$$

$$\mathbf{u}_{22} \cdot \mathbf{u}_{24} - \cos\phi_{22,24} = 0 \tag{3.119}$$

$$\mathbf{u}_{23} \cdot \mathbf{u}_{24} - \cos\phi_{23,24} = 0 \tag{3.120}$$

Rear right wheel – This element is defined by points p_{35} and unit vectors $\mathbf{u}_{31}$, $\mathbf{u}_{32}$ and $\mathbf{u}_{33}$, as shown in fig. 3.18. $\mathbf{u}_{31}$, $\mathbf{u}_{32}$ and $\mathbf{u}_{33}$ form the coordinate system of the element with origin in p_{35}. 6 new variables ($\mathbf{u}_{32}$ and $\mathbf{u}_{33}$) are added. It is worth mentioning that as point p_{35} and vector $\mathbf{u}_{31}$ have been previously defined during the rear right wheel knuckle modeling, the revolute joint between the wheel and the wheel knuckle is automatically considered. The constraints for this element are rigid body constraints, eqs. (3.121) to (3.125). As 6 new

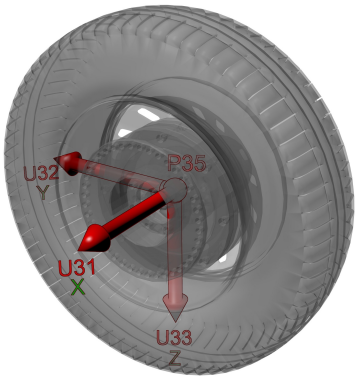

Figure 3.18: Points, vectors, COG, reference set of the rear right wheel

Body	mass (kg)
rim	6
tire	5.1
disk brake	3.2
hub	1.7
torque sensor	14
Total	30

Table 3.17: Rear right wheel mass properties

variables and 5 constraints are added, a new DOF is defined. Considering the previously defined DOFs, the DOF number at this stage of the modeling is 14.

This element is composed of the wheel rim, the tire, the wheel hub, the brake disc and the torque sensor that are rigidly interconnected and whose masses are presented in table 3.17. The position of the COG and the inertia tensor of this element, expressed in the reference set shown in fig. 3.18, are summarized in table 3.18.

$$\mathbf{u}_{32} \cdot \mathbf{u}_{32} - 1 = 0 \tag{3.121}$$

$$\mathbf{u}_{33} \cdot \mathbf{u}_{33} - 1 = 0 \tag{3.122}$$

$$\mathbf{u}_{31} \cdot \mathbf{u}_{32} - \cos\phi_{31,32} = 0 \tag{3.123}$$

$$\mathbf{u}_{31} \cdot \mathbf{u}_{33} - \cos\phi_{31,33} = 0 \tag{3.124}$$

$$\mathbf{u}_{32} \cdot \mathbf{u}_{33} - \cos\phi_{32,33} = 0 \tag{3.125}$$

Rear left wheel – This element is defined by points p_{45} and unit vectors $\mathbf{u}_{41}$, $\mathbf{u}_{42}$ and $\mathbf{u}_{43}$, as shown in fig. 3.19. $\mathbf{u}_{41}$, $\mathbf{u}_{42}$ and $\mathbf{u}_{43}$ form the coordinate system of the element with origin in p_{45}. 6 new variables ($\mathbf{u}_{42}$ and $\mathbf{u}_{43}$) are added. It is worth mentioning that as point p_{45} and vector $\mathbf{u}_{41}$ have been previously defined during the rear left wheel knuckle modeling, the revolute joint between the wheel and the wheel knuckle is automatically considered. The constraints for this element are rigid body constraints, eqs. (3.126) to (3.130). As 6 new variables and 5 constraints are added, a new DOF is defined. Considering the previously defined DOFs, the DOF number at this stage of the modeling is 15.

COG position (m)		moments of inertia (kg m^2)			
X	+0.077	I_{xx}	+0.647	I_{xy}	+0.000
Y	+0.000	I_{yy}	+0.393	I_{xz}	+0.000
Z	+0.000	I_{zz}	+0.393	I_{yz}	+0.000

Table 3.18: COG coordinates and inertia tensor for the rear right wheel

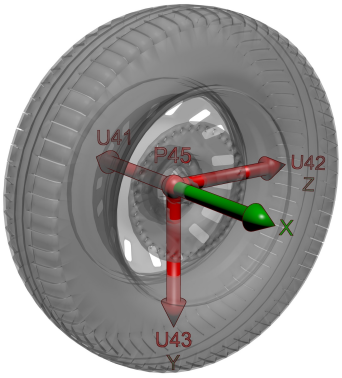

Figure 3.19: Points, vectors, COG, reference set of the rear left wheel

Body	mass (kg)
rim	6
tire	5.1
disk brake	3.2
hub	1.7
Total	16

Table 3.19: Rear left wheel mass properties

This element is composed of the wheel rim, the tire, the wheel hub and the brake disc that are rigidly interconnected and whose masses are presented in table 3.19. The position of the COG and the inertia tensor of this element, expressed in the reference set shown in fig. 3.19, are summarized in table 3.20.

$$\mathbf{u}_{42} \cdot \mathbf{u}_{42} - 1 = 0 \tag{3.126}$$

$$\mathbf{u}_{43} \cdot \mathbf{u}_{43} - 1 = 0 \tag{3.127}$$

$$\mathbf{u}_{41} \cdot \mathbf{u}_{42} - \cos\phi_{41,42} = 0 \tag{3.128}$$

$$\mathbf{u}_{41} \cdot \mathbf{u}_{43} - \cos\phi_{41,43} = 0 \tag{3.129}$$

$$\mathbf{u}_{42} \cdot \mathbf{u}_{43} - \cos\phi_{42,43} = 0 \tag{3.130}$$

COG position (m)		moments of inertia (kg m^2)			
X	+0.065	I_{xx}	+0.534	I_{xy}	+0.000
Y	+0.000	I_{yy}	+0.300	I_{xz}	+0.000
Z	+0.000	I_{zz}	+0.300	I_{yz}	+0.000

Table 3.20: COG coordinates and inertia tensor for the rear left wheel

Extra variables

The set of natural coordinates has been supplemented with angles and distances that describe the relative motion of some kinematic joints. This information allows for a better understanding of the model and provides some parameters required by the brake model and the tire model.

Distances – Four variables, s_{10}, s_{20}, s_{30} and s_{40}, have been introduced to define the strokes of the dampers and one more, s_{50} to define the steering translation. Four equations have been added for the dampers, eqs. (3.131) to (3.134), and another for the steering, eq. (3.135). The definition of these five distances has not affected the number of DOF as five equations have been introduced.

$$s_{10} = |\mathbf{r}_{12,15}| \tag{3.131}$$
$$s_{20} = |\mathbf{r}_{22,25}| \tag{3.132}$$
$$s_{30} = |\mathbf{r}_{31,34}| \tag{3.133}$$
$$s_{40} = |\mathbf{r}_{41,44}| \tag{3.134}$$
$$s_{50} = |\mathbf{r}_{50,2}| \tag{3.135}$$

Angles – Four angles, ϕ_{10}, ϕ_{20}, ϕ_{30} and ϕ_{40}, have been introduced to define the wheel angles. For each one, two equations, never enabled at the same time, are necessary as explained in section 3.1.2. For the front wheels, the angles have been defined between the projection of two points of the knuckle onto the wheel plane and a vector contained in the latter, eqs. (3.136) to (3.139). For the rear wheels, the angles have been defined between the projection of a vector of the chassis onto the wheel plane and a vector contained in the latter, eqs. (3.140) to (3.143). The definition of these four angles has not affected the number of DOF as four equations have been introduced.

$$\mathbf{u}_{14} \cdot \mathbf{r}_{13,14} - (\mathbf{u}_{14} \cdot \mathbf{u}_{12})(\mathbf{r}_{13,14} \cdot \mathbf{u}_{12}) - L_{14',14}\, cos\phi_{10} = 0 \tag{3.136}$$
$$\mathbf{u}_{14} \wedge \mathbf{r}_{13,14} - (\mathbf{u}_{14} \cdot \mathbf{u}_{12})\mathbf{u}_{12} \wedge \mathbf{r}_{13,14} - (\mathbf{r}_{13,14} \cdot \mathbf{u}_{12})\mathbf{u}_{12} \wedge \mathbf{u}_{12} - \mathbf{u}_{12}\, L_{14',14}\, sin\phi_{10} = 0 \tag{3.137}$$
$$\mathbf{u}_{24} \cdot \mathbf{r}_{23,24} - (\mathbf{u}_{24} \cdot \mathbf{u}_{22})(\mathbf{r}_{23,24} \cdot \mathbf{u}_{22}) - L_{24',24}\, cos\phi_{20} = 0 \tag{3.138}$$
$$\mathbf{u}_{24} \wedge \mathbf{r}_{23,24} - (\mathbf{u}_{24} \cdot \mathbf{u}_{22})\mathbf{u}_{22} \wedge \mathbf{r}_{23,24} - (\mathbf{r}_{23,24} \cdot \mathbf{u}_{22})\mathbf{u}_{22} \wedge \mathbf{u}_{22} - \mathbf{u}_{22}\, L_{24',24}\, sin\phi_{20} = 0 \tag{3.139}$$
$$\mathbf{u}_{32} \cdot \mathbf{u}_1 - (\mathbf{u}_{32} \cdot \mathbf{u}_{31})(\mathbf{u}_1 \cdot \mathbf{u}_{31}) - L_{u_{1'},u_1}\, cos\phi_{30} = 0 \tag{3.140}$$
$$\mathbf{u}_{32} \wedge \mathbf{u}_1 - (\mathbf{u}_{32} \cdot \mathbf{u}_{31})\mathbf{u}_{31} \wedge \mathbf{u}_1 - (\mathbf{u}_1 \cdot \mathbf{u}_{31})\mathbf{u}_{31} \wedge \mathbf{u}_{31} - \mathbf{u}_{31}\, L_{u_{1'},u_1}\, sin\phi_{30} = 0 \tag{3.141}$$
$$\mathbf{u}_{42} \cdot \mathbf{u}_1 - (\mathbf{u}_{42} \cdot \mathbf{u}_{41})(\mathbf{u}_1 \cdot \mathbf{u}_{41}) - L_{u_{1'},u_1}\, cos\phi_{40} = 0 \tag{3.142}$$
$$\mathbf{u}_{42} \wedge \mathbf{u}_1 - (\mathbf{u}_{42} \cdot \mathbf{u}_{41})\mathbf{u}_{41} \wedge \mathbf{u}_1 - (\mathbf{u}_1 \cdot \mathbf{u}_{41})\mathbf{u}_{41} \wedge \mathbf{u}_{41} - \mathbf{u}_{41}\, L_{u_{1'},u_1}\, sin\phi_{40} = 0 \tag{3.143}$$

Kinematic guidance of the steering system – The steering system has been kinematically guided as the behavior of the steering wheel system is not of interest in this research. Moreover, for maneuver repeating with the XBW vehicle prototype, the steering system angle is controlled using the steering wheel angle recorded during the reference maneuver. As a consequence, the mean of the steering angles of the maneuvers can be employed to control the behavior of the steering system of the model when repeating the real test maneuvers with the MB model. The steering system displacement is calculated using the mean steering angle and the rack and pinion ratio. The general equations that relate the mean steering displacement (i.e. the reference displacement) and the steering displacement of the model are shown in eqs. (3.144) to (3.146).

$$\mathrm{s}_{50} - \mathrm{s}_{50,ref} \tag{3.144}$$

$$\dot{\mathrm{s}}_{50} - \dot{\mathrm{s}}_{50,ref} \tag{3.145}$$

$$\ddot{\mathrm{s}}_{50} - \ddot{\mathrm{s}}_{50,ref} \tag{3.146}$$

where $\mathrm{s}_{50,ref}$, $\dot{\mathrm{s}}_{50,ref}$ and $\ddot{\mathrm{s}}_{50,ref}$ are the reference variables (means of the repetition maneuvers or others if the MB model is controlled with a pad). As a rheonomic constraint is defined and no variables are created, the DOF number decreases by one.

Summary of variables and constraints

All the variables and constraints previously defined have been summarized in table 3.21 allowing for a better understanding of the modeling of the vehicle. In this table, the new variables (names and number), the constraints and the number of DOF introduced by each body are listed. The MB model has a total of 168 variables and 154 constraints without counting the ones of the subsystems. It is possible to give a physical interpretation to the 14 aforementioned DOFs: 6 DOFs go to the 3 rotations and the 3 translations of a free body, 4 DOFs to the 4 suspension deflections and 4 DOFs to the rotation of each wheel. There is no additional DOF for the steering system as it is kinematically guided.

Forces

Different kinds of forces can be considered depending on the type of maneuver. As the two maneuvers considered in this research are low speed maneuvers, the following forces have been taken into account:

- gravitational forces
- driving and braking torques of the rear wheels
- braking torques of the front wheels
- suspension forces
- tire forces

The tire and brake model are described later in section 3.1.3.

Gravitational forces – The gravitational forces have been applied in the opposite direction of unit vector $\mathbf{u}_z$ that is shown in fig. 3.1. The gravity has been taken as 9.81 m/s^2. Every body has a gravitational force applied in its COG.

Body	names of the variable	number	constraints	DOFs
chassis	$\mathbf{u}_1$, $\mathbf{u}_2$, $\mathbf{u}_3$, p_1, p_2, p_{10}, p_{11}, p_{12}, p_{20}, p_{21}, p_{22}, p_{30}, p_{31}, p_{40}, p_{41}	45	39	6
front right lower wishbone arm	$\mathbf{u}_{10}$, p_{13}	6	5	1
front right upper wishbone arm	$\mathbf{u}_{11}$, p_{14}, p_{15}	9	8	1
front right wheel knuckle	$\mathbf{u}_{12}$, p_{16}, p_{17}	9	9	0
front left lower wishbone arm	$\mathbf{u}_{20}$, p_{23}	6	5	1
front left upper wishbone arm	$\mathbf{u}_{21}$, p_{24}, p_{25}	9	8	1
front left wheel knuckle	$\mathbf{u}_{22}$, p_{26}, p_{27}	9	9	0
steering system	p_{50}, p_{51}	6	5	1
right tie rod	-	0	1	-1
left tie rod	-	0	1	-1
rear right wishbone arm	$\mathbf{u}_{30}$, p_{32}	6	5	1
rear left wishbone arm	$\mathbf{u}_{40}$, p_{42}	6	5	1
rear right wheel knuckle	$\mathbf{u}_{31}$, p_{33}, p_{34}, p_{35}	12	12	0
rear left wheel knuckle	$\mathbf{u}_{41}$, p_{43}, p_{44}, p_{45}	12	12	0
front right wheel	$\mathbf{u}_{13}$, $\mathbf{u}_{14}$	6	5	1
front left wheel	$\mathbf{u}_{23}$, $\mathbf{u}_{24}$	6	5	1
rear right wheel	$\mathbf{u}_{32}$, $\mathbf{u}_{33}$	6	5	1
rear left wheel	$\mathbf{u}_{42}$, $\mathbf{u}_{43}$	6	5	1
front right suspension distance	$\mathbf{s}_{10}$	1	1	0
front left suspension distance	$\mathbf{s}_{20}$	1	1	0
rear right suspension distance	$\mathbf{s}_{30}$	1	1	0
rear left suspension distance	$\mathbf{s}_{40}$	1	1	0
steering distance	$\mathbf{s}_{50}$	1	1	0
front right wheel angle	ϕ_{10}	1	1	0
front left wheel angle	ϕ_{20}	1	1	0
rear right wheel angle	ϕ_{30}	1	1	0
rear left wheel angle	ϕ_{40}	1	1	0
kinematic guidance of the steering system	-	0	1	-1
Total	-	168	154	14

Table 3.21: Summary of variables and constraints

Driving and braking torques of the rear wheels – The driving and braking torques acting on the rear wheels of the MB model are inputs either given by the wheel torque sensor or by the user (predefined maneuver or pad commands). The driving torque is not given by an engine model as not being an objective of this research. Indeed, the development of a engine model is a hard task that here would not be worth. The wheel torque sensor measures both driving and braking torques of the rear right wheel thus eliminating the necessity of using a brake model. Both rear right and left torques have been supposed to be identical as the engine gearbox is outfitted with a non-locked differential. The torques for both rear wheels have to be introduced in the vector of generalized forces at the positions corresponding to angles ϕ_{30} and ϕ_{40}.

3.1.3 Models of the subsystems

A vehicle model not only includes the dynamics of its bodies but also the behavior of several subsystems like brakes, tires, steering system, engine, etc. In this thesis, the models of two subsystems have been considered: the tire and brake models. Both have been implemented according to the characteristics of the test maneuvers.

Tire model

Apart from the aerodynamic and gravitational forces, the rest of major forces and moments acting on a vehicle are transferred by the tires to the wheel rims. Consequently, the tire behavior and characteristics play a crucial role in the evaluation of vehicle dynamics. Over the last 60 years, the tire characteristics have been extensively and qualitatively described by many authors (Gillespie, 1992; Jazar, 2008; Popp and Schielhen, 2010; Wong, 2001). Numerous mathematical models have been developed (Chang et al., 2004; Pacejka, 2005; Pacejka and Sharp, 1991). They differ in accuracy and complexity depending on the areas of application discussed in section 1.2. As described in (Kuiper and Van Oosten, 2007), they can be classified in the following four different groups:

- *simple tire models* – They are aimed at static and quasi-static vehicle dynamics analysis and at the design of vehicle control systems. The vertical behavior consists of a linear or non-linear spring-damper model. The horizontal tire forces are accounted for by linear relationships between slip and resulting forces, and combined slip is not taken into account.

- *empirical models* –They are based on non-linear mathematical approximations of tire forces and moments or interpolation of test data, like the famous versions (1987, 1989, 1993, 1996, 2002) of the *Magic formula* (Bakker et al., 1987, 1989; Pacejka, 2002; Pacejka and Bakker, 1993; Pacejka and Besselink, 1997). Empirical tire models require full-scale tire measurements, data processing and parameter identification. These tire models are in general very accurate, and are used for vehicle dynamics analysis in a broad sense, ranging from non-linear handling to ride simulations.

- *physical models* – These models, which describe the kinematics and dynamics of the tire contact patch in detail, can be very complex. The parameters that describe the tire behavior have physical and/or geometrical significance, and extended tire measurements are not necessary. They are often tailored for a specific area of application

almost unlimited: quasi-static behavior, non-linear handling, ride, comfort, durability, Noise Vibration and Harshness (NVH) and acoustics.

- *finite-element tire models* – The tire is modeled by a detailed finite element (FE) mesh for the complete tire structure including the compressed air. Almost any physical phenomenon can be taken into account and the resulting computational effort is very high. Their use is mostly restricted to detailed structural analysis with high non-linear deformations, hydroplaning and acoustic analysis. For vehicle dynamics analysis, the computational effort is yet too high for application on a regular basis.

The area of application of the tire model in this thesis is related to nonlinear vehicle handling in real–time. As a consequence, the model should be as simple as possible in order to maintain low computational cost while fulfilling the requirements imposed by the test maneuvers. As can be verified in fig. 3.28, the test track is slightly inclined (about 1.5°) and has also some bank angle in specific areas. Therefore, the tire model has to consider precisely situations where the vehicle stands still, starts or stops on an inclined test track. Then, some dynamics behaviors of the tire, like longitudinal and lateral deflections, are necessary in order to assess easily the equilibrium position of the vehicle at the beginning of the simulation while standing still. If the tire model does not manage these situations, any effort to validate the vehicle MB model would be worthless. A common difficulty in the modeling of tires is the calculation of the set of parameters that relate the longitudinal and lateral tire forces and moments to the longitudinal and lateral slips. Very few tire manufacturers sell these parameters (normally for a huge amount of money) and individual tire testing is even more expensive. Subsequently, most researchers employ tire parameters available in the literature if they correspond to their tires and, if this is not the case they extrapolate the tire parameters from tires with similar dimensions and characteristics.

In this research, part of the tire model *TMeasy* has been applied (Hirschberg et al., 2007; Rill, 2006a, 2007, 2009). This is an empirical and physical tire model, in the sense that first, curve fitting using few parameters is necessary to adjust the tire characteristic curves and then, dynamical behaviors of the tire are considered. It is similar to another recent empirical and physical tire model used in *ADAMS*: the `PAC2002` (Kuiper and Van Oosten, 2007). Both are used for low frequency applications. The basics of *TMeasy* and the extra characteristics that have been used in this work are reminded hereafter.

Geometric contact point – To calculate the geometric point of contact $\mathbf{P}$, it is first necessary to assess the contact normal for each tire. The collision detection algorithm that calculates the contact normals $\mathbf{e_n}$ is presented in section 3.2.2.

A scheme of the wheel with the points and vectors used for the tire modeling as well as the triangular face in contact with the tire, are shown in fig. 3.20. The unit vector $\mathbf{e_{yR}}$ defines the wheel center plane and is orientated positively regarding the rotation of the wheel. On the one hand, the unit vector $\mathbf{e_x}$, which is defined as the intersection between the wheel center plane and the stepped triangular face, gives the direction of the longitudinal tire force. On the other hand, the unit vector $\mathbf{e_y}$ gives the direction of the lateral tire forces and is defined as being perpendicular to the contact normal $\mathbf{e_n}$ and the unit vector $\mathbf{e_x}$. The unit vector $\mathbf{e_{zR}}$ is obtained from the scalar product of $\mathbf{e_x}$ and $\mathbf{e_{yR}}$, as can be seen in

$$\mathbf{e_{zR}} = \mathbf{e_x} \wedge \mathbf{e_{yR}} \tag{3.147}$$

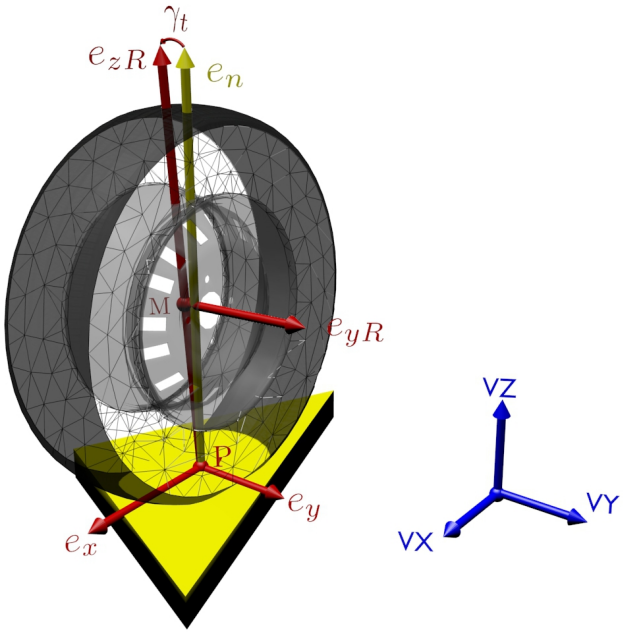

Figure 3.20: Points and vectors for the tire model

The geometric contact point **P** is located at the shortest distance from the wheel center **M** to the intersection between the wheel plane and the triangular face. The tire camber angle is defined as shown in eq. (3.148).

$$\gamma^* = \arcsin(\mathbf{e_{yR}}^{\mathrm{T}} \mathbf{e_n}) \tag{3.148}$$

When the tire has a camber angle, the geometric contact point **P** does not coincide with the effective point of the resulting vertical tire force. However, here, as the camber angle of the wheels of the XBW vehicle prototype is almost zero and as the maneuvers are performed at low speed thus avoiding the camber angle due to suspension kinematics, the effective point has been assumed to be the geometric contact point.

Velocity of the contact point – The velocity of the contact point $\dot{\mathbf{P}}$ is a basic magnitude for the calculation of the tire forces. This velocity is the one of the wheel center $\dot{\mathbf{M}}$ projected onto the contact triangular face, or said in another way, it is the velocity of the wheel center without the component oriented in the direction of the contact normal $\mathbf{e_n}$. As the four wheel centers are points of the vehicle MB model ($p_{17}, p_{27}, p_{35}, p_{45}$), their velocities are easily calculated. Then, the projection onto the contact triangular face is shown in eq. (3.149).

$$\dot{\mathbf{P}} = \dot{\mathbf{M}} - \left(\dot{\mathbf{M}} \cdot \mathbf{e_n}\right) \mathbf{e_n} \tag{3.149}$$

Finally, the velocity of the contact point can be projected on the longitudinal unit vector $\mathbf{e_x}$ and the lateral unit vector $\mathbf{e_y}$ as demonstrated in eqs. (3.150) and (3.151).

$$\nu_{\mathrm{x}} = \dot{\mathbf{P}} \cdot \mathbf{e_x} \tag{3.150}$$

$$\nu_{\mathrm{y}} = \dot{\mathbf{P}} \cdot \mathbf{e_y} \tag{3.151}$$

Wheel vertical load – The vertical tire force $\mathrm{F_z}$ has been calculated as a function of the normal tire deflection $\Delta \mathrm{z}$ and its velocity $\Delta \dot{\mathrm{z}}$, as shown in

$$\mathrm{F_z} = \mathrm{a}\Delta \mathrm{z} + \mathrm{d}_R \Delta \dot{\mathrm{z}} \tag{3.152}$$

where a and d_R are constants.

Generalized tire force – The longitudinal and lateral slips are demonstrated in eqs. (3.153) and (3.154).

$$\mathrm{s_x} = \frac{-(\nu_\mathrm{x} - \mathrm{r_D}\Omega)}{\mathrm{r_D}|\Omega|\hat{\mathrm{s}}_\mathrm{x} + \nu_n} \tag{3.153}$$

$$\mathrm{s_y} = \frac{-\nu_\mathrm{y}}{\mathrm{r_D}|\Omega|\hat{\mathrm{s}}_\mathrm{y} + \nu_n} \tag{3.154}$$

where $\mathrm{r_D}$ is the dynamic rolling radius of the tire, Ω is the angular velocity of the wheel, ν_n is a small fictitious velocity and finally $\hat{\mathrm{s}}_\mathrm{x}$ and $\hat{\mathrm{s}}_\mathrm{y}$ are two coefficients that allow to give more weight to the longitudinal or to the lateral slips for the calculation of the generalized slip presented hereafter. The small fictitious velocity ν_n is necessary to cover situations in which the wheel locks. Indeed, in this particular situation, $\mathrm{r_D}|\Omega| = 0$ and, without ν_n the slips ${\mathrm{s_x}}^N$ and ${\mathrm{s_y}}^N$ would tend to infinity, which is not acceptable from a numerical point of view. When choosing small values of ν_n ($\nu_n > 0$), the singularity is avoided, and the generalized slip points in the direction of the sliding velocity when the wheel is locked. Lastly, in normal driving conditions, ν_n does not affect the tire model behavior as $\mathrm{r_D}|\Omega| >> \nu_n$. In this research, $\nu_n = 10^{-7}$ has been taken.

Both slips can be combined to get the generalized slip, as shown in eq. (3.155). Up to this point of the description of the tire model, no characteristic curves that relate the slip to the tire forces have been assumed. Several approximations can be considered, like for instance the one proposed by the authors of this tire model (Hirschberg et al., 2007) or those of the *Magic Formula*. For the sake of simplicity, in this work, a simple linearized model, shown in fig. 3.21, has been chosen. In this figure μ is the road–tire friction coefficient, F is the generalized tire force, F_z is the vertical tire force and $\mathrm{s_c}$ is the critical slip. First, this choice has been motivated by the fact that the tire behavior for low speed maneuvers is well approximated by means of a linear function. Then, as the tire parameters have been approximated thanks to similar tires, precise approximations of the tire characteristics would not be justified. The longitudinal and lateral tire forces are finally obtained from

$$\mathrm{s_g} = \sqrt{(\mathrm{s_x})^2 + (\mathrm{s_y})^2} \tag{3.155}$$

$$F_\mathrm{x} = F\frac{\mathrm{s_x}}{\mathrm{s_g}} \tag{3.156}$$

$$F_\mathrm{y} = F\frac{\mathrm{s_y}}{\mathrm{s_g}} \tag{3.157}$$

First order tire dynamics – As mentioned before, in this research, the first order tire dynamics are vital to model properly the tire behavior when the vehicle stands still, starts or stops on an inclined test track or when the wheels lock. The forces acting in the contact patch deflect longitudinally and laterally the tire as shown in fig. 3.23. According to the *TMeasy* model, the tire forces F_x and F_y can be reasonably represented by the first order

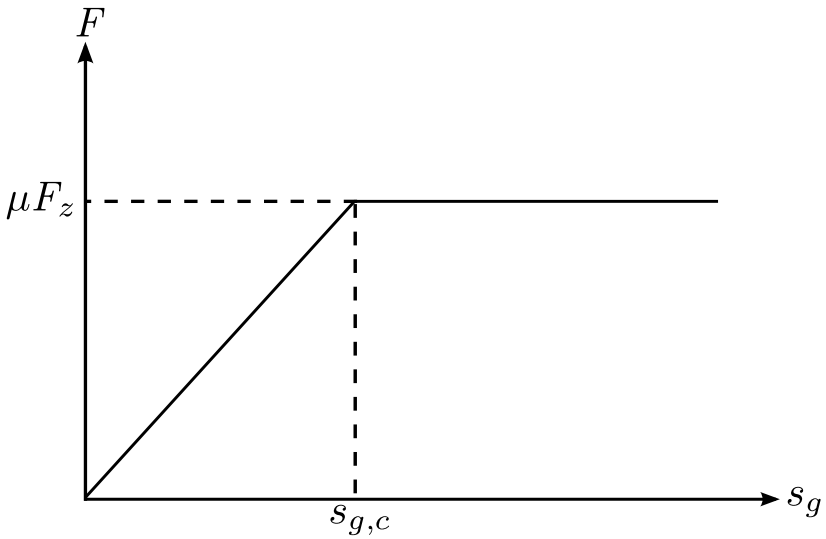

Figure 3.21: Approximations of the generalized tire characteristics

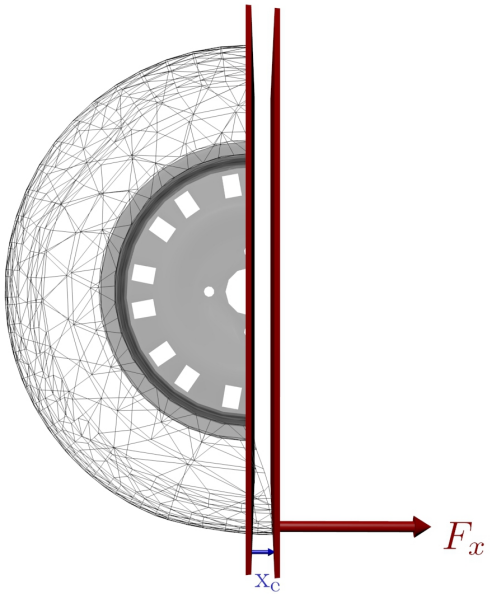

Figure 3.22: Longitudinal tire deflection due to the contact forces

approximations shown in eqs. (3.158) and (3.159).

$$\underbrace{F_x(\nu_\mathrm{x}+\dot{\mathrm{x}}_\mathrm{e})}_{F_x^D} \simeq F_\mathrm{x}(\nu_\mathrm{x}) + \frac{\partial F_\mathrm{x}}{\partial \nu_\mathrm{x}}\left[(\nu_\mathrm{x}+\dot{\mathrm{x}}_\mathrm{e})+\nu_\mathrm{x}\right] = \underbrace{F_x(\nu_\mathrm{x})}_{F_x^S} + \frac{\partial F_\mathrm{x}}{\partial \nu_\mathrm{x}}\,\dot{\mathrm{x}}_\mathrm{e} \tag{3.158}$$

$$\underbrace{F_y(\nu_\mathrm{y}+\dot{\mathrm{y}}_\mathrm{e})}_{F_y^D} \simeq F_\mathrm{y}(\nu_\mathrm{y}) + \frac{\partial F_\mathrm{y}}{\partial \nu_\mathrm{y}}\left[(\nu_\mathrm{y}+\dot{\mathrm{y}}_\mathrm{e})+\nu_\mathrm{y}\right] = \underbrace{F_y(\nu_\mathrm{y})}_{F_y^S} + \frac{\partial F_\mathrm{y}}{\partial \nu_\mathrm{y}}\,\dot{\mathrm{y}}_\mathrm{e} \tag{3.159}$$

where $\dot{\mathrm{x}}_\mathrm{e}$ and $\dot{\mathrm{y}}_\mathrm{e}$ are the longitudinal and lateral tire deflections, F_x^D and F_y^D are the dynamic tire forces and, F_x^S and F_y^S are the steady–state tire forces. In steady–state, that is when $\dot{\mathrm{x}}_\mathrm{e}=0$ and $\dot{\mathrm{y}}_\mathrm{e}=0$, the tire forces F_x^S and F_y^S are given by eqs. (3.156) and (3.157) respectively.

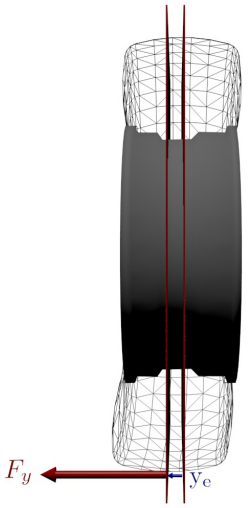

Figure 3.23: Lateral tire deflection due to the contact forces

Their derivatives with respect to the contact point velocity are given in

$$\frac{\partial F_{\mathrm{x}}^{\mathrm{S}}}{\partial \nu_{\mathrm{x}}} = \frac{\partial F_{\mathrm{x}}^{\mathrm{S}}}{\partial s_{\mathrm{x}}} \frac{\partial s_{\mathrm{x}}}{\partial \nu_{\mathrm{x}}} = \frac{\partial F_{\mathrm{x}}^{\mathrm{S}}}{\partial s_{\mathrm{x}}} \frac{-1}{r_{\mathrm{D}} |\Omega| \hat{s}_{\mathrm{x}} + \nu_n} \tag{3.160}$$

$$\frac{\partial F_{\mathrm{x}}^{\mathrm{S}}}{\partial \nu_{\mathrm{x}}} = \frac{\partial F_{\mathrm{y}}^{\mathrm{S}}}{\partial s_{\mathrm{y}}} \frac{\partial s_{\mathrm{y}}}{\partial \nu_{\mathrm{y}}} = \frac{\partial F_{\mathrm{y}}^{\mathrm{S}}}{\partial s_{\mathrm{y}}} \frac{-1}{r_{\mathrm{D}} |\Omega| \hat{s}_{\mathrm{y}} + \nu_n} \tag{3.161}$$

Subsequently, eqs. (3.160) and (3.161) can be substituted into eqs. (3.158) and (3.159), as shown in eqs. (3.162) and (3.163).

$$F_{\mathrm{x}}^{\mathrm{D}} \simeq \frac{F}{s_{\mathrm{g}}} s_{\mathrm{x}} + \frac{\partial F_{\mathrm{x}}^{\mathrm{S}}}{\partial s_{\mathrm{x}}} \frac{-1}{r_{\mathrm{D}} |\Omega| \hat{s}_{\mathrm{x}} + \nu_n} \dot{x}_{\mathrm{e}} = \frac{F}{s_{\mathrm{g}}} \frac{-(\nu_{\mathrm{x}} - r_{\mathrm{D}} \Omega)}{\nu_{\mathrm{x}}^*} + \frac{\partial F_{\mathrm{x}}^{\mathrm{S}}}{\partial s_{\mathrm{x}}} \frac{-1}{\nu_{\mathrm{x}}^*} \dot{x}_{\mathrm{e}} \tag{3.162}$$

$$F_{\mathrm{y}}^{\mathrm{D}} \simeq \frac{F}{s_{\mathrm{g}}} s_{\mathrm{y}} + \frac{\partial F_{\mathrm{y}}^{\mathrm{S}}}{\partial s_{\mathrm{y}}} \frac{-1}{r_{\mathrm{D}} |\Omega| \hat{s}_{\mathrm{y}} + \nu_n} \dot{y}_{\mathrm{e}} = \frac{F}{s_{\mathrm{g}}} s_{\mathrm{y}} + \frac{\partial F_{\mathrm{y}}^{\mathrm{S}}}{\partial s_{\mathrm{y}}} \frac{-1}{\nu_{\mathrm{y}}^*} \dot{y}_{\mathrm{e}} \tag{3.163}$$

where $\nu_{\mathrm{x}}^* = r_{\mathrm{D}} |\Omega| \hat{s}_{\mathrm{x}} + \nu_n$ and $\nu_{\mathrm{y}}^* = r_{\mathrm{D}} |\Omega| \hat{s}_{\mathrm{y}} + \nu_n$. The tire dynamic forces can also be calculated by considering that the tire consists of two spring–damper elements, one in the longitudinal direction and the other in the lateral direction. Both equations are presented in eqs. (3.164) and (3.165).

$$F_{\mathrm{x}}^{\mathrm{D}} \simeq c_{\mathrm{x}} x_{\mathrm{e}} + d_{\mathrm{x}} \dot{x}_{\mathrm{e}} \tag{3.164}$$

$$F_{\mathrm{y}}^{\mathrm{D}} \simeq c_{\mathrm{y}} y_{\mathrm{e}} + d_{\mathrm{y}} \dot{y}_{\mathrm{e}} \tag{3.165}$$

where c_{x}, c_{y}, d_{x}, d_{y} are the stiffness and damping parameters for the longitudinal and lateral tire deflections. After that, eq. (3.162) can be combined with eq. (3.164) to yield a first order differential equation, shown in eq. (3.166) for the longitudinal deflection of the tire. The first order differential equation for the lateral deflection, shown in eq. (3.167) is obtained using eqs. (3.163) and (3.165).

$$\left(\nu_{\mathrm{x}}^* d_{\mathrm{x}} + \frac{\partial F_{\mathrm{x}}^{\mathrm{S}}}{\partial s_{\mathrm{x}}} \right) \dot{x}_{\mathrm{e}} = -\frac{F}{s_{\mathrm{g}}} (\nu_{\mathrm{x}} - r_{\mathrm{D}} \Omega) - \nu_{\mathrm{x}}^* c_{\mathrm{x}} x_{\mathrm{e}} \tag{3.166}$$

$$\left(\nu_{\mathrm{y}}^* d_{\mathrm{y}} + \frac{\partial F_{\mathrm{y}}^{\mathrm{S}}}{\partial s_{\mathrm{y}}} \right) \dot{y}_{\mathrm{e}} = -\frac{F}{s_{\mathrm{g}}} \nu_{\mathrm{y}} - \nu_{\mathrm{y}}^* c_{\mathrm{y}} y_{\mathrm{e}} \tag{3.167}$$

Both differential equations have to be integrated at each time step to calculate the tire forces by means of eqs. (3.164) and (3.165). To this end, in this research, both differential equations are solved for every iteration (corresponding to a time step) of the Newton–Raphson method shown in eq. (3.15). As the variables of eqs. (3.166) and (3.167) are constant during each iteration, both equations become first order differential equations with constant coefficients. Their analytical solutions are presented in eqs. (3.168) and (3.169).

$$
\begin{aligned}
&\mathrm{x_e} = \frac{\mathrm{a_2}}{\mathrm{a_1}} + \mathrm{a_3}\,\mathrm{e}^{-\mathrm{a_1}\Delta \mathrm{t_i}} \\
&\mathrm{a_1} = \frac{\nu_\mathrm{x}^* \mathrm{c_x}}{\left(\nu_\mathrm{x}^* \mathrm{d_x} + \dfrac{\partial F_x}{\partial \mathrm{s_x}}\right)} \qquad \mathrm{a_2} = -\frac{{}^{F}\!/_{\mathrm{s_g}}(\nu_\mathrm{x} - \mathrm{r_D}\Omega)}{\left(\nu_\mathrm{x}^* \mathrm{d_x} + \dfrac{\partial F_x}{\partial \mathrm{s_x}}\right)} \qquad \mathrm{a_3} = \mathrm{x_{e0}} - \frac{\mathrm{a_2}}{\mathrm{a_1}}
\end{aligned}
\tag{3.168}
$$

$$
\begin{aligned}
&\mathrm{y_e} = \frac{\mathrm{b_2}}{\mathrm{b_1}} + \mathrm{b_3}\,\mathrm{e}^{-\mathrm{b_1}\Delta \mathrm{t_i}} \\
&\mathrm{b_1} = \frac{\nu_\mathrm{y}^* \mathrm{c_y}}{\left(\nu_\mathrm{y}^* \mathrm{d_y} + \dfrac{\partial F_y}{\partial \mathrm{s_y}}\right)} \qquad \mathrm{b_2} = -\frac{{}^{F}\!/_{\mathrm{s_g}}\,\nu_\mathrm{y}}{\left(\nu_\mathrm{y}^* \mathrm{d_y} + \dfrac{\partial F_y}{\partial \mathrm{s_y}}\right)} \qquad \mathrm{b_3} = \mathrm{y_{e0}} - \frac{\mathrm{b_2}}{\mathrm{b_1}}
\end{aligned}
\tag{3.169}
$$

where $\mathrm{x_{e0}}$ and $\mathrm{y_{e0}}$ are the initial longitudinal and lateral tire deflection for each integration time step. Consequently, for each iteration of an integration time step, $\mathrm{x_e}$ and $\mathrm{y_e}$ are calculated using eqs. (3.168) and (3.169), and $\dot{\mathrm{x}}_\mathrm{e}$ and $\dot{\mathrm{y}}_\mathrm{e}$ are obtained by means of eqs. (3.166) and (3.167). When the integration time step changes, $\mathrm{x_{e0}}$ and $\mathrm{y_{e0}}$ must be updated with the latest values of $\mathrm{x_e}$ and $\mathrm{y_e}$. Solving the differential equations analytically at each iteration allows calculating efficiently and accurately the tire forces.

Locked wheel with tire sliding – A small modification has to be made to the previous equations to allow the tire model to take into account situations in which the wheel is locked but the tire is sliding. Although this situation is not common in normal driving conditions, it occurs much more frequently in simulation. For example, at the beginning of a simulation, an initial location and orientation are given to the vehicle and then, it is dropped on the test track. Subsequently, the wheel rotation velocities are zero and, longitudinal and lateral slips appear due to the suspension deflections and the test track inclination. When a tire is sliding, for example laterally, $\mathrm{y_e}$ increases until reaching a maximum value which should be maintain during all the sliding.

In such a situation, as $\Omega = 0$, eq. (3.169) becomes eq. (3.170). It can be seen from eq. (3.170) that $\mathrm{e}^{-\mathrm{b_1}\Delta \mathrm{t_i}}$ should be equal to one to get $\mathrm{y_e} = \mathrm{y_{e0}}$. This means that the tire lateral deflection during the iterations of the Newton–Raphson method $\mathrm{y_e}$ is equal to the tire lateral deflection at the beginning of the corresponding integration time step $\mathrm{y_{e0}}$, and so on for the next integration time steps until the tire stops to slide. $\mathrm{e}^{-\mathrm{b_1}\Delta \mathrm{t_i}} \simeq 1$ implies that $-\mathrm{b_1}\Delta \mathrm{t_i} \simeq 0$. As $\left.\dfrac{\partial F_y}{\partial \mathrm{s_y}}\right|_{\mathrm{s_g} > \mathrm{s_c}} = 0$, it follows that $\mathrm{b_1} = \dfrac{\mathrm{c_y}}{\mathrm{d_y}}$. Unfortunately, after having substituted $\mathrm{c_y}$, $\mathrm{d_y}$ and $\Delta \mathrm{t_i}$, $-\mathrm{b_1}\Delta \mathrm{t_i} \neq 0$. Therefore, eqs. (3.168) and (3.169) have to be modified in order to maintain $\mathrm{y_e}$ constant during the sliding. In the *TMeasy* model, it has been chosen to change the derivative as shown in eq. (3.171). In this way, when $\mathrm{s_g} < \mathrm{s_c}$, the correct derivative is well approximated (if linear tire curves are used, the derivative is exact) and, when $\mathrm{s_g} > \mathrm{s_c}$, the derivative is largely greater than zero, thus making $-\mathrm{b_1}\Delta \mathrm{t_i} \simeq 0$. The

same modification has to be made to the derivative of the longitudinal tire forces.

$$
\begin{aligned}
&\mathrm{y_e} = \frac{\mathrm{b_2}}{\mathrm{b_1}} + \left(\mathrm{y_{e0}} - \frac{\mathrm{b_2}}{\mathrm{b_1}}\right) \mathrm{e}^{-\mathrm{b_1}\Delta \mathrm{t_i}} \\
&\mathrm{b_1} = \frac{\nu_n \mathrm{c_y}}{\left(\nu_n \mathrm{d_y} + \left.\dfrac{\partial F_y}{\partial \mathrm{s_y}}\right|_{\mathrm{s_g}>\mathrm{s_c}}\right)} \qquad \mathrm{b_2} = -\frac{{}^{F}\!/_{\mathrm{s_g}}\, \nu_\mathrm{y}}{\left(\nu_n \mathrm{d_y} + \left.\dfrac{\partial F_y}{\partial \mathrm{s_y}}\right|_{\mathrm{s_g}>\mathrm{s_c}}\right)}
\end{aligned} \tag{3.170}
$$

$$
\frac{\partial F_\mathrm{y}}{\partial \mathrm{s_y}} \rightarrow \frac{F_\mathrm{y}}{\mathrm{s_y}} = F_\mathrm{y} \frac{1}{\mathrm{s_y}} = \frac{F}{\mathrm{s_g}} \mathrm{s_y} \frac{1}{\mathrm{s_y}} = \frac{F}{\mathrm{s_g}} \tag{3.171}
$$

Transition to stand–still – The *TMeasy* model is able to handle situations where the vehicle stands still. In such situations, $\nu_\mathrm{x} = 0$, $\nu_\mathrm{y} = 0$, $\Omega = 0$ and $\mathrm{s_g} = 0$· Subsequently, eqs. (3.166) to (3.169) become eqs. (3.172) to (3.175) respectively.

$$
\left(\nu_n \mathrm{d_x} + \left.\frac{\partial F_\mathrm{x}^\mathrm{S}}{\partial \mathrm{s_x}}\right|_{\mathrm{s_g}=0}\right) \dot{\mathrm{x}}_\mathrm{e} = -\nu_n \mathrm{c_x} \mathrm{x_e} \tag{3.172}
$$

$$
\left(\nu_n \mathrm{d_y} + \left.\frac{\partial F_\mathrm{y}^\mathrm{S}}{\partial \mathrm{s_y}}\right|_{\mathrm{s_g}=0}\right) \dot{\mathrm{y}}_\mathrm{e} = -\nu_n \mathrm{c_x} \mathrm{y_e} \tag{3.173}
$$

$$
\begin{aligned}
&\mathrm{x_e} = \mathrm{a_3}\, \mathrm{e}^{-\mathrm{a_1}\Delta \mathrm{t_i}} \\
&\mathrm{a_1} = \frac{\nu_n \mathrm{c_x}}{\left(\nu_n \mathrm{d_x} + \left.\dfrac{\partial F_x}{\partial \mathrm{s_x}}\right|_{\mathrm{s_g}=0}\right)} \qquad \mathrm{a_3} = \mathrm{x_{e0}}
\end{aligned} \tag{3.174}
$$

$$
\begin{aligned}
&\mathrm{y_e} = \mathrm{b_3}\, \mathrm{e}^{-\mathrm{b_1}\Delta \mathrm{t_i}} \\
&\mathrm{b_1} = \frac{\nu_n \mathrm{c_y}}{\left(\nu_\mathrm{y}^* \mathrm{d_y} + \left.\dfrac{\partial F_y}{\partial \mathrm{s_y}}\right|_{\mathrm{s_g}=0}\right)} \qquad \mathrm{b_3} = \mathrm{y_{e0}}
\end{aligned} \tag{3.175}
$$

At stand–still, $\mathrm{x_e}$ and $\mathrm{y_e}$ will decay in time according to eqs. (3.174) and (3.175). This implies that F_x and F_y are never completely constant but small values of ν_n yield large time constants. In this way, the tire model considers the stick–slip phenomena.

Brake model

Similarly to the tire model, the brake model must be able to manage situations where the vehicle stands still, starts or stops on an inclined test track. To this end, the tangential force model developed in (Dopico et al., 2011) has been used since it takes into account stiction and sliding. The parameters of the model have been obtained from experimental data.

3.2 Simulation environment

A self-developed driving simulator has been setup to make the use of the vehicle model easier. Indeed, the vehicle MB model is programmed in `Fortan` and has no convenient graphical output. For that purpose, an open–source 3D graphics toolkit, *OpenSceneGraph*, has been used to provide the simulator with realistic 3D graphics. As a consequence, the simulation code has two different parts: one in `Fortan` containing the vehicle MB model and another in `C++` that covers the 3D outputs, the collision detection and in a near future the communication

Figure 3.24: Topographical survey with the total station

with the DAS. Hereafter the road profile, the collision detection algorithm and the graphical environment are presented.

3.2.1 Road profile

In order to properly validate any vehicle model through field testing, a true road profile is vital for the simulation. In this research, the test track is an almost flat area of the campus of the engineering school. The information about the road profile has been obtained through a topographical survey of the test track using a total station (model *SET530R* from *Sokkia*). Figure 3.24 shows a photo of the use of the total station for the topographical survey. About three hundred points spaced out, on average, every 1.5 m have been collected. The 3D scattered points are shown in fig. 3.25 where the vertical scale has been magnified in order to visualize better the surface. These points have then been interpolated using the natural neighbor interpolation method and regular spacing, as can be seen in fig. 3.26. A drawback inherent to this method is that the convex hull of the 3D scattered points is used by the interpolation method. As a result, undesirable new points that lie outside the limits of the actual test track are created. To solve this problem, the projections of the 3D scattered points on the horizontal plane are used to identify the points that define the contour of the 2D point set. An 2D alpha shape algorithm has been employed to detect this contour as shown in fig. 3.27. As the 3D point set is an almost flat surface, the points that lie in its contour will be the same as the ones of the 2D contour. Once the contour has been defined, a Delaunay triangulation constrained into the alpha shape is performed on the interpolated and regularly spaced points. The result is similar to the one using only the interpolation method except that now undesirable points outside the test track are no more generated. Finally the points and triangles set is saved in *Wavefront* format in order to be passed to the simulation environment. The triangle mesh of the test track surface is shown in fig. 3.28.

3.2.2 Collision detection

The collision detection strategy and algorithms employed in this work are based on the ones developed in the LIM for the real–time simulation of an excavator (Dopico et al., 2011). These methods have been specially tailored for real–time simulations where the MB models have

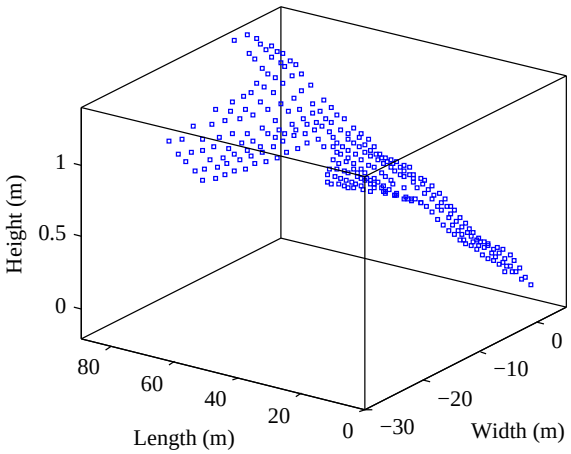

Figure 3.25: 3D scattered points collected during the topographical survey

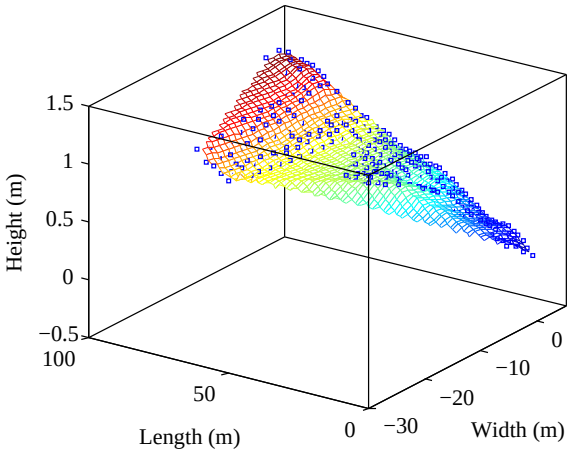

Figure 3.26: Interpolation of the 3D scattered points

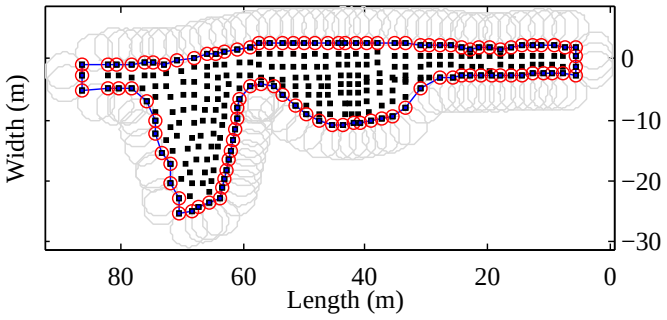

Figure 3.27: Contour detection using the alpha shape algorithm

to interact potentially with a high number of bodies. To this end, the geometry of complex CAD environment and bodies (like the test track) has been approximated by meshes of triangular faces and the geometry of the bodies of the MB systems (like the wheels) by spheres of different sizes. Figure 3.29 shows the four identical spheres that have been employed to approximate the geometry of the tires. It can be noted that if the vehicle would laterally enter in contact with some body, the approximation of the tire geometry would not be valid.

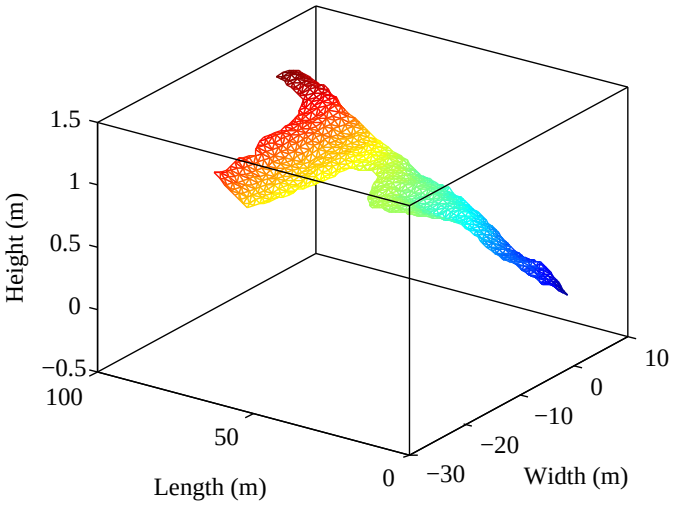

Figure 3.28: 3D model of the test track

However, as this situation can never occur in this work, it has not been necessary to further detailed this geometry. Then, each triangular face of a CAD environment or body has its own normal vector and its own properties of stiffness and friction and each sphere is characterized also depending on the material properties and curvature of the MB model.

After having defined the contact geometry of the different bodies, the detection of the triangular faces that are in contact with the primitive spheres has to be carried out. The most likely contact scenarios are presented in (Dopico et al., 2011) for spheres, yielding to the normal vector of the contact and, in the same paper, the normal forces are calculated. This vector is then used by the tire subroutine to compute the tire forces and moments. It is worth mentioning that as the test track shown in fig. 3.28 is a smooth and almost flat surface, only one contact point exist for each tire. At each time step, the contacts taking place have to be determined efficiently. This involves checking all the spheres against all the faces and their edges leading to intensive computational loads at each time step for realistic environments. In order to speed up this process, the collision detection algorithm uses an octree-based hierarchical decomposition of the entire scene mesh whose principal idea is to generate a tree-based hierarchical structure that is used to quickly reject the polygons not involved in potential collisions, in order to reduce the number of polygons tested against contact with the primitive objects that represent the geometry of the models.

3.2.3 Graphical environment

The 3D graphical environment is intended to reproduce the real environment where the test maneuvers have been realized, as well as the vehicle itself. First, a 2D map in *AutoCAD* of the campus of the engineering school has been used to locate the buildings and the roads. After that, the campus buildings have been extruded outwards in their right places using an open–source 3D content creation software, *Blender*. The road profile obtained in section 3.2.1 has been merged into the 3D objects of the roads. Textures have been applied to roads, buildings, sidewalks, etc, using photos taken on the campus. Lastly, a sky dome and a sun have been added to reproduce the sky and to give lighting to the whole scene. A general view of the 3D objects of the campus is shown in fig. 3.30. Figures 3.31 and 3.32 show the real

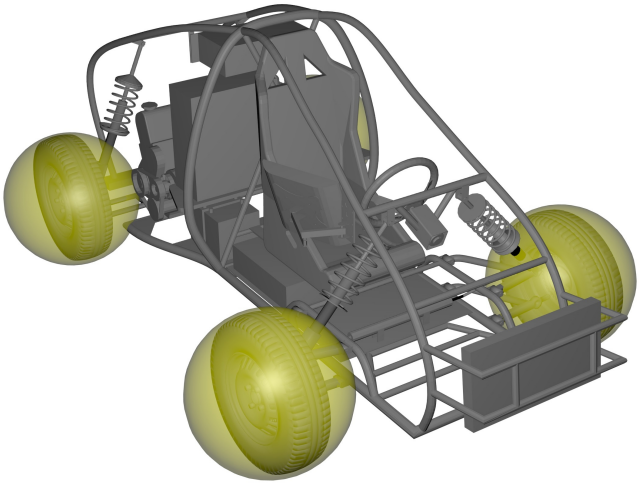

Figure 3.29: Spheres used for the collision detection of the tires

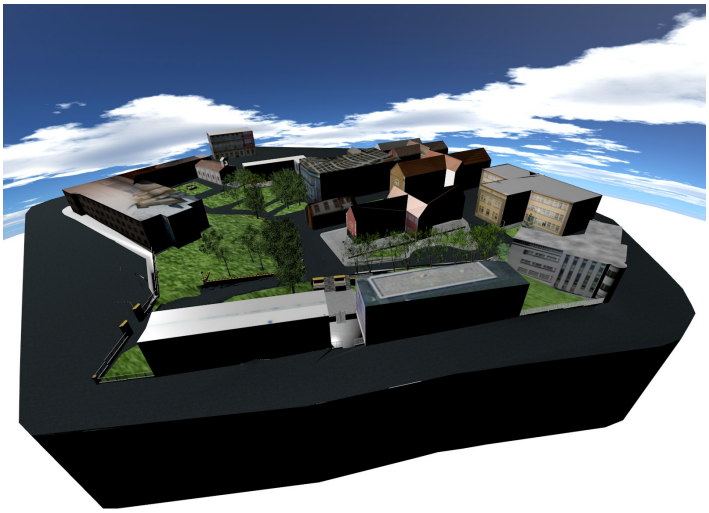

Figure 3.30: 3D model of the campus with the skydome in the background

and virtual surroundings of the test track.

The geometry of the 3D objects for the vehicle have been obtained from the CAD objects, which have been later textured. In order to animate these objects, the vehicle MB model passes to the *OpenSceneGraph* library the position and orientation of each body at each diplay time step.

Figure 3.31: Photo of the test track

Figure 3.32: 3D surroundings of the test track

Chapter 4

Validation results

4.1 Confidence interval and mean values

To validate the vehicle MB model presented in section 3.1, the experimental data shown in section 2.4 and the predictions of the simulations given by the vehicle simulator have to be compared. To this end, as explained in section 2.1, the reference test maneuvers must be repeated several times with the XBW vehicle prototype in order to calculate the control inputs of the model from the average over the repetitions of the sensor data. After that, each test maneuver has to be repeated using the MB model provided with its control inputs. To discard any error due to sensor noises and errors, external disturbances, filtering, post-processing, etc, during vehicle dynamic responses measuring, the sensor data have also been averaged to be compared with the predictions of the simulations. As mentioned in section 2.1, aside from the improvement of the experimental benchmark data through data averaging over the repetition maneuvers, it is also possible to determine a confidence interval (CI) that characterizes the uncertainty of the experimental testing and measurement process. Here it is supposed that the uncertainty follows a normal distribution, first because no other information is available and then for the sake of simplicity. As the number of samples (i.e. the repetition maneuvers) is small, the Student's t-distribution has been employed to calculate the CI as stated in eq. (4.1). The interval employed here is a 95% CI with (n-1) degrees of freedom.

$$\mathrm{CI} = \bar{\mathrm{x}} \pm t^{\mathrm{n}-1}_{(1-\alpha/2)} \cdot \frac{\mathrm{S}}{\sqrt{\mathrm{n}}} \tag{4.1}$$

where $\bar{\mathrm{x}} = \frac{1}{\mathrm{n}}\Sigma^{\mathrm{n}}_{i=1}\mathbf{x}_i$ is the sample mean, $t^{\mathrm{n}-1}_{(1-\alpha/2)}$ is the upper $(1-\alpha/2)$ critical value for the t distribution with (n-1) degrees of freedom, $\mathrm{S}^2 = \frac{1}{\mathrm{n}-1}\Sigma^{\mathrm{n}}_{i=1}(\mathbf{x}_i - \bar{\mathbf{x}})^2$ is the sample variance and n is the sample number. The calculated CI means that a CI in which the true mean is included between the lower and upper bounds, can be found with probability 0.95, for each time step. It is worthwhile pointing out that it reduces when increasing the number of samples (i.e. the number of repetition maneuvers) and that it is centered at the sample mean. According to the definition of simulation validity given in section 2.1.1, this CI defines the maximum accuracy that the predictions of the simulations can reach. If the predictions of the simulations are inside the CI bounds, the vehicle model can not be further improved with this set of experimental data. A data set with lower uncertainty would be necessary.

The predictions of the simulations for both test maneuvers are presented and compared to their corresponding experimental data below.

4.2 Simulation of the low speed straight-line maneuver

For this test maneuver, the inputs of the model were the rear wheel torque and the brake pressure despite the fact that the prototype control inputs were the throttle angle and the brake pressure. Indeed, as mentioned in section 2.2.4, the throttle angle can not be a control input of the MB model if the engine is not modeled. As the development of such a model is not an objective of this work, the rear wheel torque has been chosen instead. The rack and pinion system has been guided so that the model follows the straight–line defined during the test maneuver. Figure 4.1 shows the mean of the rear wheel torques (black line) and the 95% CI (gray area) corresponding to the 7 repetitions shown in fig. 2.43. Similarly, fig. 4.2 presents the mean of the brake pressures (black line) and its 95% CI (gray area) calculated from the 7 repetitions shown in fig. 2.39 After that, the straight–line maneuver has been repeated with

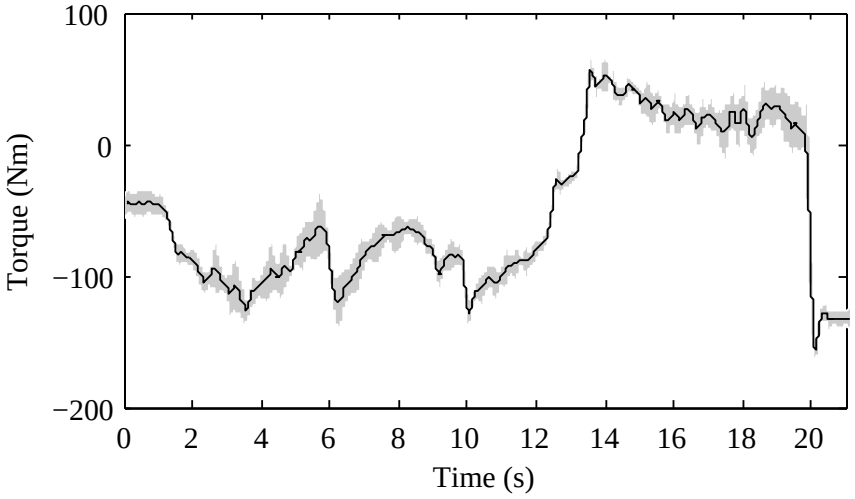

Figure 4.1: Mean and CI of the rear wheel torques (straight–line)

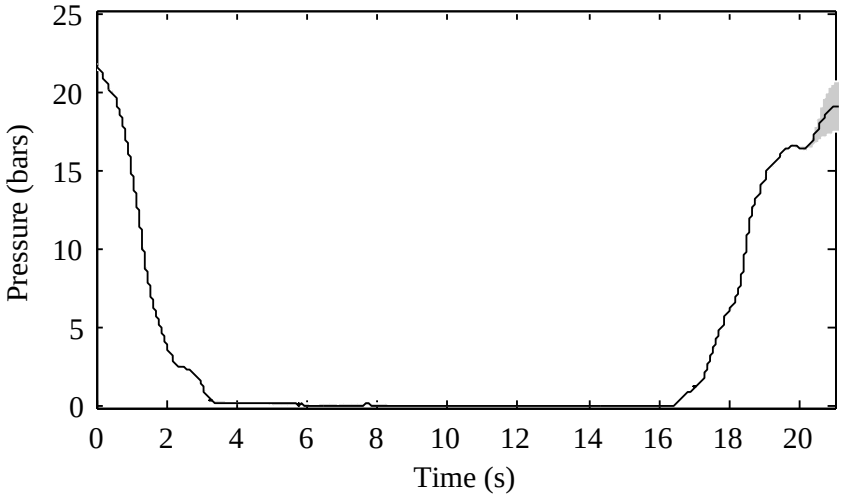

Figure 4.2: Mean and CI of the brake pressures (straight–line)

the MB model provided with the mean of the rear wheel torques and the mean of the brake pressures. Only the most relevant magnitudes for this maneuver are presented below. First, fig. 4.3 compares the 95 % CI of the front left wheel speed, calculated from the hall effect sensor information, to its simulated counterpart. Then, similar comparisons are presented for the longitudinal acceleration of the vehicle, given by the tri–axial accelerometer of the chassis, in fig. 4.4 and for the roll angle rate, given by the corresponding gyroscope, in fig. 4.5.

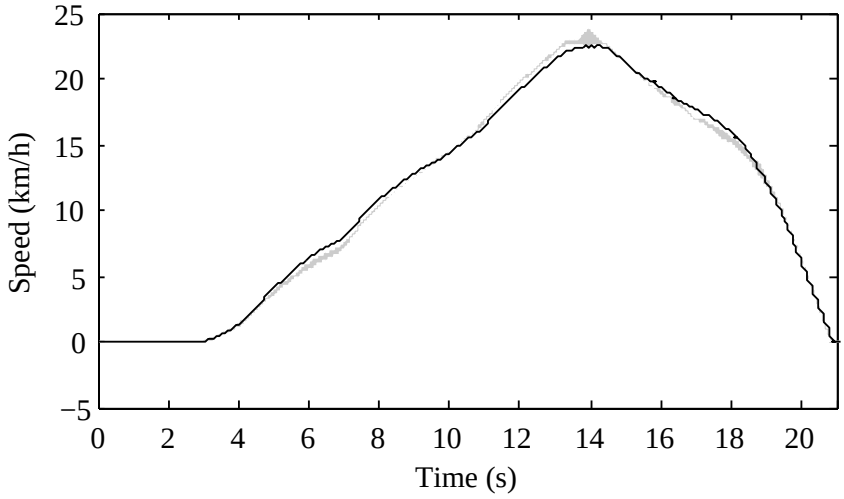

Figure 4.3: CI and MB model prediction of the left front wheel speed (straight–line)

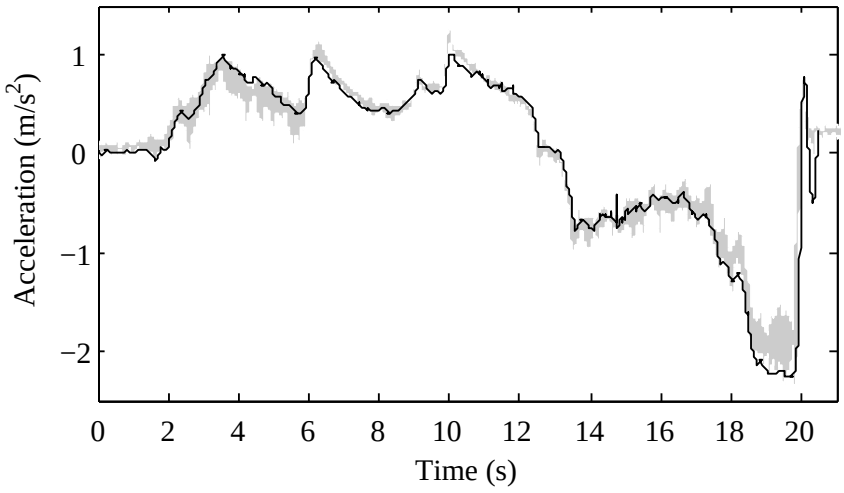

Figure 4.4: CI and MB model prediction of the longitudinal acceleration (straight–line)

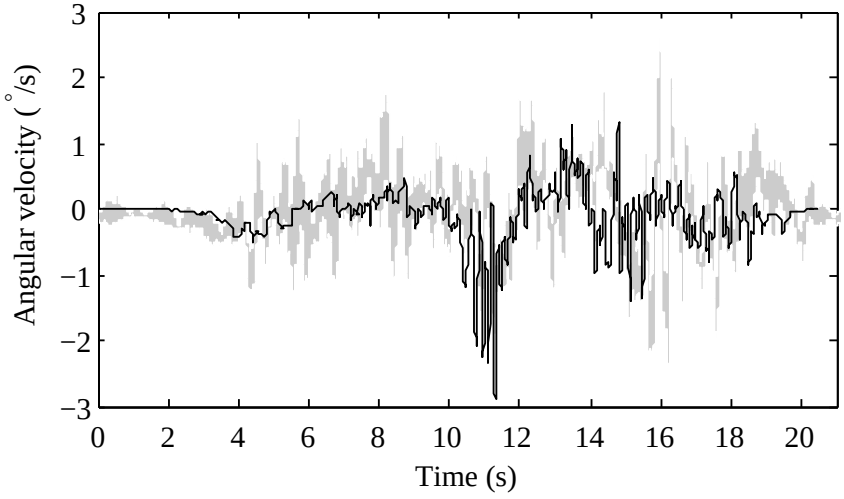

Figure 4.5: CI and MB model prediction of the roll angle rate (straight–line)

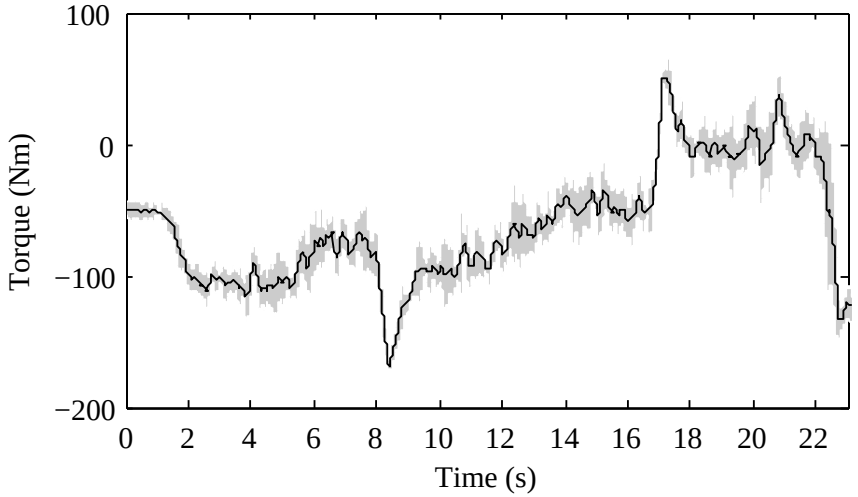

Figure 4.6: Mean and CI of the rear wheel torque (J–turn)

4.3 Simulation of the low speed J-turn maneuver

Similarly to the straight–line maneuver, for the longitudinal dynamics, the control inputs were the torque of the rear right wheel and the brake pressure. Then, for the lateral dynamics, the rack and pinion system angle was used. The mean (black line) and the 95% CI (gray area) for the three control inputs are shown in figs. 4.6 to 4.8. The corresponding 7 repetitions have previously been presented in figs. 2.45, 2.47 and 2.50.

The J–turn maneuver has been repeated with the MB model provided with the mean of the control inputs. The most relevant magnitudes for this maneuver are presented hereafter.

- chassis longitudinal acceleration – fig. 4.9
- chassis lateral acceleration – fig. 4.10
- left front wheel speed – fig. 4.11
- roll angular velocity – fig. 4.12
- pitch angular velocity – fig. 4.13
- yaw angular velocity – fig. 4.14

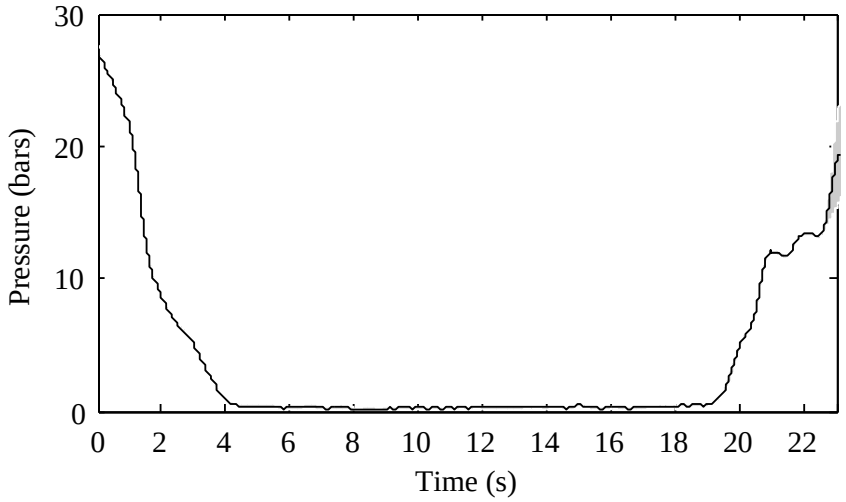

Figure 4.7: Mean and CI of the brake pressure (J–turn)

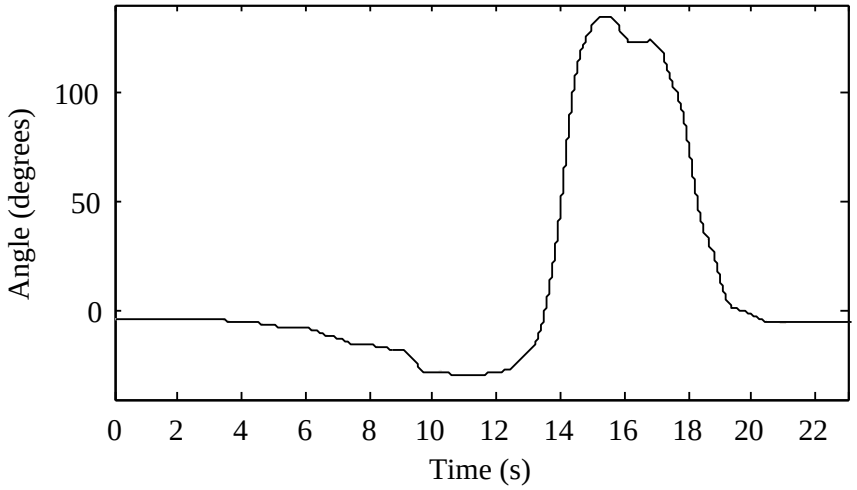

Figure 4.8: Mean and CI of the rack and pinion system angle (J–turn)

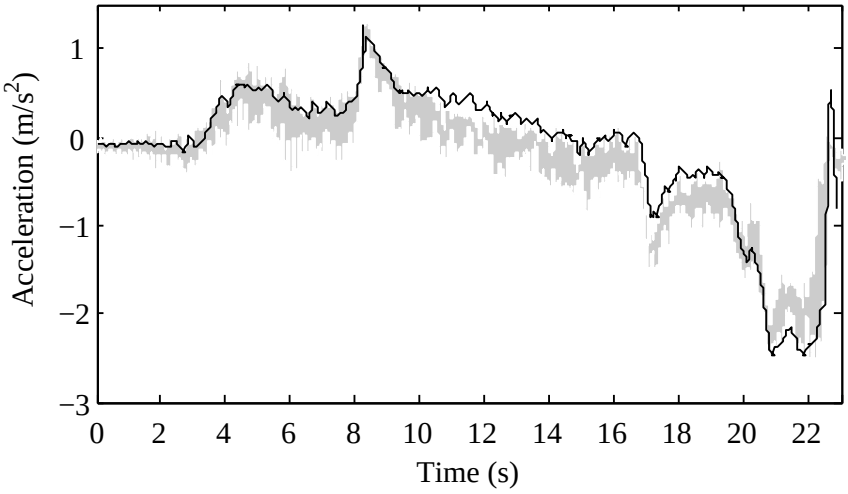

Figure 4.9: CI and MB model prediction for the longitudinal acceleration (J–turn)

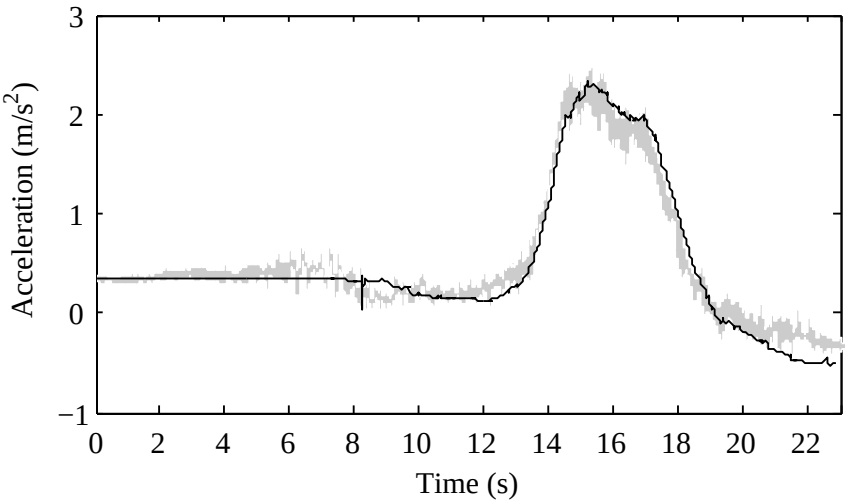

Figure 4.10: CI and MB model prediction for the lateral acceleration (J–turn)

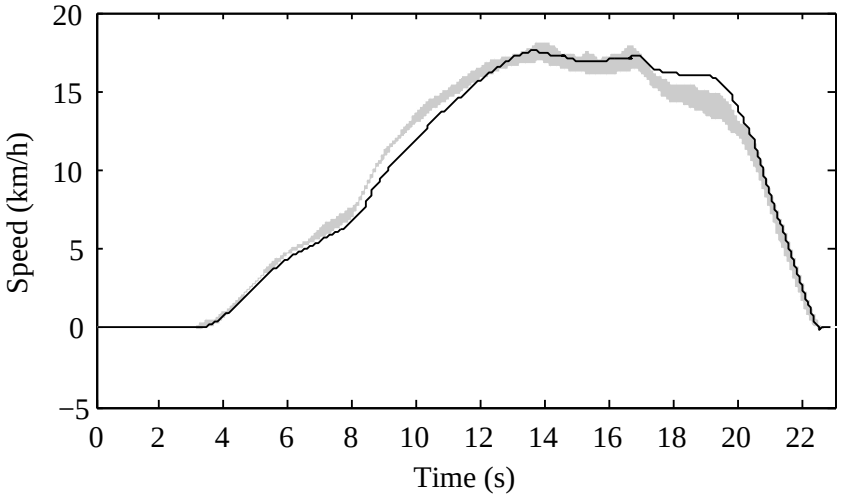

Figure 4.11: CI and MB model prediction for the left front wheel speed (J–turn)

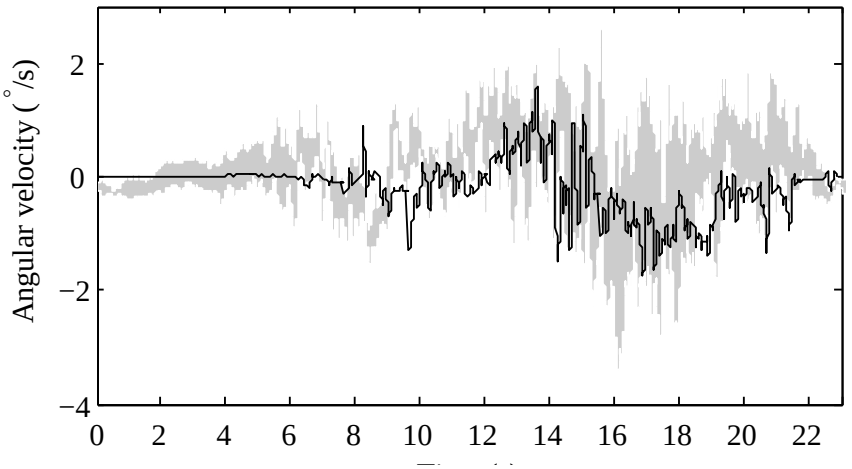

Figure 4.12: CI and MB model prediction for the roll angular velocity (J–turn)

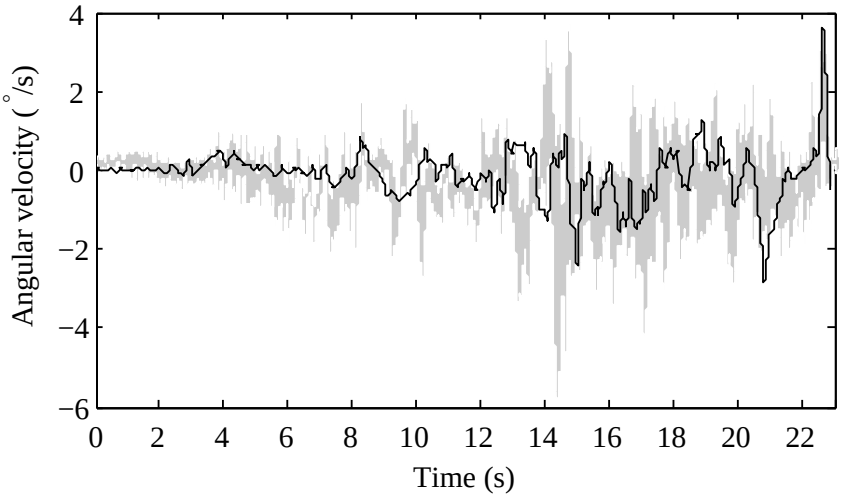

Figure 4.13: CI and MB model prediction for the pitch angular velocity (J–turn)

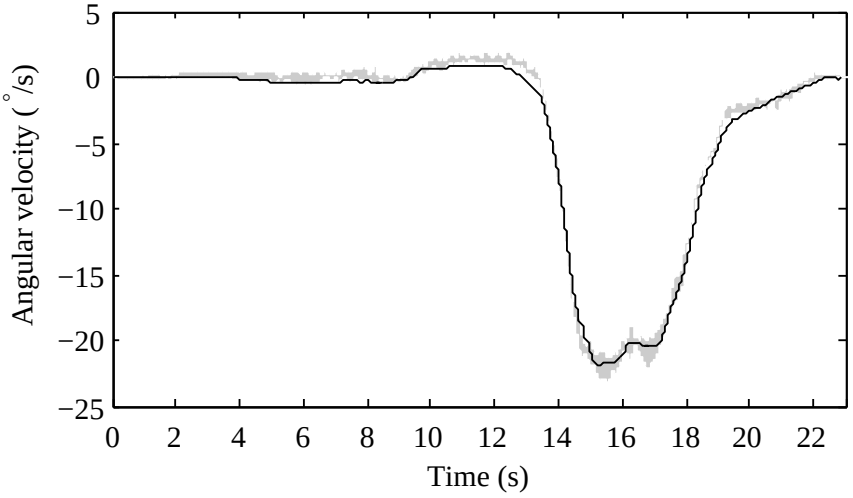

Figure 4.14: CI and MB model prediction for the yaw angular velocity (J–turn)

4.4 Discussion

One of the first comment that can be made regarding both test maneuvers is that the vehicle MB model has repeated the maneuvers with accuracy. Indeed, the main dynamical phenomena of the vehicle prototype have been properly modeled as demonstrated in the previous figures. Discrepancies still exist between the model predictions and the corresponding CIs, indicating that the model can further be improved using the available experimental data. As mentioned in section 4.1, the CIs define the accuracy of the measurement process. At each instant, the true value of a variable is not necessarily inside its CI. Consequently, different validation criteria could be defined to determine if the model discrepancies are acceptable or not, but these criteria are always, in some way, subjectively defined and are not of interest in this research. Instead, this work has focused on particular discrepancies to improve the MB model and the subsystem models. Hereafter, the main parts of the model that contribute to its accuracy are discussed one by one.

- *Test track* – The topographical survey has largely helped to improve the accuracy of the simulations. It can be claimed that without the precise profile of the road, any effort to match the model predictions to the corresponding CIs would be useless. As can be seen in figs. 4.5, 4.12 and 4.13, the topographical survey has smoothened the true road profile as the distance between the points is about 1m.

- *Tire model* – A tire model, which takes into account situations where the vehicle stands still, starts or stops on an inclined road and where the wheels lock, is of vital importance for the maneuvers considered in this research. If the tire model does not consider these situations, the vehicle MB model can not stand still and consequently it should start the simulation with a small longitudinal velocity and stop the simulation before this velocity becomes zero. Such limitations, which are not acceptable in this work, would lead to important discrepancies between the experimental data and the simulation results. Moreover, the tire equations must be integrated at each iteration of the Newton–Raphson method to get the right solution.

- *Brake model* – Similarly to the tire model, the brake model must be able to deal with the same type of situations, implying that it has to model properly the stick–slip phenomena. Any attempt to improve the vehicle MB model accuracy without taking into account this phenomena in the brake model would be worthless.

- *Vehicle geometry* – It has been noted that, as expected, small errors in certain vehicle parameters such as the wheel angles, greatly influence the model accuracy. Measuring the geometry of a vehicle is an error–prone process that requires special test benches. However, as such benches were not available in this work, part of the discrepancies of the simulation predictions can be attributed to geometry errors.

Other parts or parameters of the model, such as inertias, tire curves, etc, are also important but their contribution to the model accuracy is less crucial. The aforementioned guidelines are valid to model accurately maneuvers with the following characteristics:

- low speed

- standing still on an inclined road

- starting and stopping on an inclined road
- longitudinal and lateral dynamics

As expected, the MB model does not predict correctly the high frequency motions. For instance, the low frequencies in figs. 4.12 to 4.14 are well matched but not the high ones. Then, it seems reasonable to think that if test maneuvers at higher speeds are considered, the model discrepancies will increase and new nonlinearities will have to be taken into account: bushings in the suspension joints, accurate tire curves for the longitudinal, lateral and vertical behaviors, flexible bodies, etc.

Chapter 5

State observers using multibody models in the automotive field

5.1 Background and state of the art

In recent years, the interest in state estimation in mechanical systems, and in particular in MB systems, has increased. A state observer is a dynamical system that employs the model of a real system in order to provide estimates of its internal states, given measurements of the inputs and outputs of the real system. This allows to extract otherwise unmeasurable variables of the real system (Radke and Gao, 2006). It is typically a computer-implemented mathematical model. In practice, the knowledge of the system state allows synthesizing effective state controllers, replacing expensive sensors with virtual sensors, improving reliability by making the controlled system robust in relation to sensor fault. On the one hand, many works in the literature address the synthesis of optimal observers for linear mechanical systems through the Kalman filter (KF) (Grewal and Andrews, 2008; Kalman, 1960). On the other hand, when nonlinear mechanical systems are considered, only sub-optimal approaches based on the linearized Kalman Filter (LKF) have usually been adopted to ensure high-frequency and hard real-time estimation (Caracciolo et al., 2008). Indeed, up to now, the use of other types of nonlinear observers in MB systems has only been investigated marginally. This lack of use is mainly due to the difficulties in performing fast integration of the nonlinear equations of motion, which usually involve high frequency dynamics and severe nonlinearities. In (Barreiro et al., 2008; Cuadrado et al., 2008, 2009a,b), it is shown how the recent improvements in MB dynamics raise the possibility of employing complex real-time models in state observers. In these papers, the estimation was performed through the EKF in its continuous form (Kalman and Bucy, 1961). Generally speaking, the EKF is the most widely used algorithm for nonlinear estimation. However, when nonlinearities are severe, EKF often gives unreliable or divergent estimates. In addition, the linearization requires a Jacobian matrix which could either be difficult to calculate or not exist. Implementation difficulties are particularly relevant if the system model is represented by DAE, as it is common in the MB field.

Recent developments in Kalman filtering algorithms make possible to overcome part of the aforementioned EKF shortcomings. The sigma-point Kalman filters (SPKFs), also called Linear Regression Kalman Filters (LRKFs), take advantage of a set of deterministically calculated weighted samples (referred to as sigma-points, or regression points (Julier and Uhlmann, 2004)) to capture at least the first and second order moments of the actual state probability distribution. They are described in detail in section 5.4.2. The approximation made by the SPKFs is more accurate than the EKF linearization, and it does not require the calculation of Jacobian matrices. Different sigma-point set definitions lead to different filter characteristics, allowing priority to be given to either estimation accuracy or computational efficiency. The most relevant variants are the unscented Kalman filter (UKF) (Julier and Uhlmann, 1997, 2004; Julier et al., 1995), the central difference Kalman filter (CDKF) (Nørgaard et al., 2000), the spherical simplex unscented Kalman filter (SSUKF) (Julier, 2003; Julier and Uhlmann, 2002) and their respective numerically stable forms or square-root forms (Van der Merwe and Wan, 2001; Van der Merwe et al., 2004). Therefore, a natural approach to overcome the EKF problems and to improve the estimation in MB systems would be to use SPKFs. To the best of the authors' knowledge, SPKFs have never been applied to the estimation of MB models.

The structure of this chapter is explained hereafter. First, in section 5.2, the equations of the Kalman filter in its continuous–time and discrete–time forms are reminded. Then, section 5.3 includes the presentation of several MB formulations and integrators employed in this work for state estimation. After that, different ways to use MB models with nonlinear

observers are discussed in section 5.4 and finally their performances are compared in section 5.5.

5.2 The Kalman filter

The estimation problem for this filter consists in estimating the state of a linear stochastic system[1]. Both continuous–time and discrete–time forms of the equations are described below. First, the continuous–time equations for the system dynamics and the measurement model are presented in eqs. (5.1) and (5.2) respectively. In this filter, the system dynamics are described by *first order ODEs with independent states*. For the sake of simplicity, the process noises $\boldsymbol{w}(t)$ and the measurement noises $\boldsymbol{v}(t)$ have been considered additive white zero–mean Gaussian noises[2] with covariances $\boldsymbol{\mathcal{Q}}(t)$ and $\boldsymbol{\mathcal{R}}(t)$ respectively.

$$\dot{\mathbf{x}}(t) = \mathbf{f}(\mathbf{x}(t), t) + \boldsymbol{w}(t) \qquad \boldsymbol{w}(t) \sim \mathcal{N}(\mathbf{0}, \boldsymbol{\mathcal{Q}}(t)) \tag{5.1}$$

$$\mathbf{y}(t) = \mathbf{h}(\mathbf{x}(t)) + \boldsymbol{v}(t) \qquad \boldsymbol{v}(t) \sim \mathcal{N}(\mathbf{0}, \boldsymbol{\mathcal{R}}(t)) \tag{5.2}$$

where $\mathbf{x}(t)$ represents the states of the system, $\dot{\mathbf{x}}(t)$ is the time derivative of the state vector, $\mathbf{f}$ is the system dynamics function, $\mathbf{y}(t)$ contains the measurements and $\mathbf{h}$ is the measurement sensitivity matrix. The differential equation for the recursive estimation of the states is presented in eq. (5.3).

$$\dot{\hat{\mathbf{x}}} = \mathrm{E}[\mathbf{f}(\hat{\mathbf{x}}(t), t) + \boldsymbol{w}(t)] + \bar{\mathbf{K}}(t)[\mathbf{y}(t) - \hat{\mathbf{y}}(t)] = \mathbf{F}\hat{\mathbf{x}}(t) + \bar{\mathbf{K}}(t)[\mathbf{y}(t) - \hat{\mathbf{y}}(t)] \tag{5.3}$$

where E is the expectation, $\bar{\mathbf{K}}(t)$ is the Kalman gain matrix, $\hat{\mathbf{y}}(t)$ are the predicted measurements and $\mathbf{F}(t)$ is the linearization of $\mathbf{f}(t)$ (here $\mathbf{f}(t, \mathbf{x}) = \mathbf{F}\mathbf{x}(t)$ as $\mathbf{f}(t)$ is linear). The Kalman gain and the predicted measurements are calculated using eqs. (5.4) and (5.5).

$$\bar{\mathbf{K}}(t) = \mathbf{P}(t)^{\mathrm{T}}(t)\boldsymbol{\mathcal{R}}^{-1}(t) \tag{5.4}$$

$$\hat{\mathbf{y}}(t) = \mathrm{E}[\mathbf{h}(\hat{\mathbf{x}}(t), t) + \boldsymbol{v}(t)] = \mathbf{H}\hat{\mathbf{x}}(t) \tag{5.5}$$

where $\mathbf{H}$ is the linearization of $\mathbf{h}$ (here $\mathbf{h}(t, \mathbf{x}) = \mathbf{H}\mathbf{x}(t)$ as $\mathbf{h}(t)$ is linear) and $\mathbf{P}(t)$ is the covariance matrix of state estimation uncertainty which is obtained using eq. (5.6), also called *Riccati equation*.

$$\dot{\mathbf{P}} = \mathbf{F}\mathbf{P} + \mathbf{P}\mathbf{F}^{\mathrm{T}} - \bar{\mathbf{K}}\boldsymbol{\mathcal{R}}\bar{\mathbf{K}}^{\mathrm{T}} + \mathbf{G}(t)\boldsymbol{\mathcal{Q}}\mathbf{G}^{\mathrm{T}}(t) \tag{5.6}$$

where $\mathbf{G}(t)$ is the coupling matrix between the process noises and the states of the system. The case in which $\mathbf{f}$ is a nonlinear function will be treated in 5.4.1.

The estimation problem can also be formulated in discrete–time form which is the most suitable form for hardware implementation as the estimation is divided in two parts depending on the availability of sensor information. The system dynamics and measurement model, which are now *linear difference equations with independent states*, are shown in eqs. (5.7) and (5.8). The same assumptions mentioned above have been made for the process and measurement noises.

$$\mathbf{x}_{k+1} = \boldsymbol{\phi}_k(\mathbf{x}_k) + \boldsymbol{w}_k \qquad \boldsymbol{w}_k \sim \mathcal{N}(\mathbf{0}, \boldsymbol{\mathcal{Q}}_k) \tag{5.7}$$

$$\mathbf{y}_k = \mathbf{h}_k(\mathbf{x}_k) + \boldsymbol{v}_k \qquad \boldsymbol{v}_k \sim \mathcal{N}(\mathbf{0}, \boldsymbol{\mathcal{R}}_k) \tag{5.8}$$

[1] *Stochastic* refers to systems whose behavior is aleatory or non–deterministic.

[2] *Additive* refers to the fact that the noise is linearly added, *white noise* is a random signal with flat power spectral density (i.e. the noise is uncorrelated in time), *Gaussian* means that the noise follows a normal distribution.

where k represents the time step and $\boldsymbol{\phi}_k$ is the state transition matrix. The estimates of the states and the covariance matrix of state estimation uncertainty are now calculated using eqs. (5.9) and (5.10).

$$\hat{\mathbf{x}}_{k+1}^{-} = \mathrm{E}[\boldsymbol{\phi}_k(\hat{\mathbf{x}}_k) + \boldsymbol{w}_k] = \boldsymbol{\Phi}_k \hat{\mathbf{x}}_k \tag{5.9}$$

$$\mathbf{P}_{k+1}^{-} = \mathrm{E}[(\mathbf{x}_{k+1} - \hat{\mathbf{x}}_{k+1}^{-})(\mathbf{x}_{k+1} - \hat{\mathbf{x}}_{k+1}^{-})^{\mathrm{T}}] = \boldsymbol{\Phi}_k \mathbf{P}_k \boldsymbol{\Phi}_k^{\mathrm{T}} + \mathbf{G}_k \boldsymbol{\mathcal{Q}}_k \mathbf{G}_k^{\mathrm{T}} \tag{5.10}$$

where $\boldsymbol{\Phi}_k$ is the linearization of $\boldsymbol{\phi}_k$ (here $\boldsymbol{\Phi}_k = \boldsymbol{\phi}_k$ as $\boldsymbol{\phi}_k$ is linear), $(^-)$ indicates the *a priori* values of the variables (i.e. before the measurement information is used) and $(^+)$ indicates the *a posteriori* values (i.e. after the measurement information is used). To calculate the *a posteriori* estimates of the state, the estimation is split in two distinct parts: the time–update and the measurement–update parts. When no information is available from the sensors, the estimation relies only on the model of the system, this is the time–update. In this case the posterior state estimates and the posterior values of $\mathbf{P}_k$ are obtained using eqs. (5.11) and (5.12).

$$\hat{\mathbf{x}}_{k+1} = \hat{\mathbf{x}}_{k+1}^{-} \tag{5.11}$$

$$\mathbf{P}_{k+1} = \mathbf{P}_{k+1}^{-} \tag{5.12}$$

If some information is available from the sensors, the estimation relies now on both the model of the system and the information of the sensors; this is the measurement update, which provides a closed loop correction of the estimates. The *a posteriori* state estimates and the *a posteriori* covariance matrix are now obtained using eqs. (5.13) and (5.14).

$$\hat{\mathbf{x}}_{k+1} = \hat{\mathbf{x}}_{k+1}^{+} = \hat{\mathbf{x}}_{k+1}^{-} + \bar{\mathbf{K}}_{k+1}(\mathbf{y}_{k+1} - \hat{\mathbf{y}}_{k+1}^{-}) \tag{5.13}$$

$$\mathbf{P}_{k+1} = \mathbf{P}_{k+1}^{+} = \mathbf{P}_{k+1}^{-} - \bar{\mathbf{K}}_{k+1}\mathbf{H}_{k+1}\mathbf{P}_{k+1}^{-} \tag{5.14}$$

The Kalman gain and the predicted measurements are calculated with eqs. (5.15) and (5.16) respectively.

$$\begin{aligned}\bar{\mathbf{K}}_{k+1} &= \mathrm{E}[(\mathbf{x}_{k+1} - \hat{\mathbf{x}}_{k+1}^{-})(\mathbf{y}_{k+1} - \hat{\mathbf{y}}_{k+1}^{-})^{\mathrm{T}}] \times \mathrm{E}[(\mathbf{y}_{k+1} - \hat{\mathbf{y}}_{k+1}^{-})(\mathbf{y}_{k+1} - \hat{\mathbf{y}}_{k+1}^{-})^{\mathrm{T}}]^{-1} \\ &= \mathbf{P}_{k+1}^{-}\mathbf{H}_{k+1}^{\mathrm{T}}(\mathbf{H}_{k+1}\mathbf{P}_{k+1}^{-}\mathbf{H}_{k+1}^{\mathrm{T}} + \boldsymbol{\mathcal{R}})^{-1}\end{aligned} \tag{5.15}$$

$$\hat{\mathbf{y}}_{k+1}^{-} = \mathrm{E}[\mathbf{h}_{k+1}(\hat{\mathbf{x}}_{k+1}^{-}) + \boldsymbol{v}_k] = \mathbf{H}_{k+1}\hat{\mathbf{x}}_{k+1}^{-} \tag{5.16}$$

5.3 Multibody formulations and integrators

In this work, the systems of interest are mechanical systems. They are MB systems made of rigid and/or flexible bodies that are interconnected by joints and usually undergo large translational and rotational displacements. Their dynamics can be represented by the Lagrange's eq. (5.17) which lead to a set of *second order DAEs of index 3*.

$$\begin{aligned}\mathbf{M}\ddot{\mathbf{q}} + \boldsymbol{\Phi}_{\mathbf{q}}^{\mathrm{T}}\boldsymbol{\lambda} &= \mathbf{Q} \\ \boldsymbol{\Phi} &= \mathbf{0}\end{aligned} \tag{5.17}$$

where $\mathbf{M}$ is the positive semidefinite mass matrix, $\ddot{\mathbf{q}}$ is the vector of dependent accelerations, $\boldsymbol{\Phi}$ is the vector of constraints, $\boldsymbol{\Phi}_{\mathbf{q}}$ is the Jacobian matrix of the constraints, $\boldsymbol{\lambda}$ is the vector of Lagrange multipliers and $\mathbf{Q}$ contains the external forces, the velocity–dependent inertia forces and those obtained from a potential. These equations are not independent from each

other as they are linked by the constraint equations. However, with a view to employ MB models in state estimation, the KF approach requires the equations to be independent from each other; in other words the equations of motion have to be ODEs. In this research, two different MB formulations have been employed to convert the DAEs into ODEs: the state-space reduction method known as the projection matrix–R method and the penalty formulation (García de Jalón and Bayo, 1994). Both formulations eliminate the Lagrange multipliers related to the restrictions in such a way that the variables behave as if they were independent.

5.3.1 State–space reduction method – matrix–R method

This method transforms the DAEs expressed in dependent variables into ODEs expressed in independent variables. Therefore, the dimension of the ODE (n_i) is equal to the number of DOF of the system. Equation (5.18), the first base equation of this method, relates the vector of dependent velocities $\dot{\mathbf{q}}$ (of dimension n_d) to the independent vector $\dot{\mathbf{z}}$ (of dimension n_i, n_i<n_d).

$$\dot{\mathbf{q}} = \mathbf{R}\dot{\mathbf{z}} \tag{5.18}$$

Matrix $\mathbf{R}$ can be calculated first using the derivative of the constraint equations, as shown in eq. (5.19) and then expressing the dependent velocities $\dot{\mathbf{q}}$ as linear combinations of the independent ones $\dot{\mathbf{z}}$.

$$\mathbf{\Phi_q}\dot{\mathbf{q}} = \mathbf{0} \tag{5.19}$$

The second base equation, eq. (5.20), is the time–derivative of eq. (5.18).

$$\ddot{\mathbf{q}} = \mathbf{R}\ddot{\mathbf{z}} + \dot{\mathbf{R}}\dot{\mathbf{z}} \tag{5.20}$$

Finally, the equations of motion, shown in eq. (5.21), are derived by premultiplying eq. (5.17) by $\mathbf{R}^{\mathrm{T}}$ and using eq. (5.19) to remove the Lagrange multipliers.

$$\ddot{\mathbf{z}} = (\mathbf{R}^{\mathrm{T}}\mathbf{M}\mathbf{R})^{-1}\left[\mathbf{R}^{\mathrm{T}}(\mathbf{Q} - \mathbf{M}\dot{\mathbf{R}}\dot{\mathbf{z}})\right] \equiv \bar{\mathbf{M}}^{-1}\bar{\mathbf{Q}} \equiv \boldsymbol{\mathcal{F}}(\mathrm{t}, \mathbf{z}, \dot{\mathbf{z}}) \tag{5.21}$$

where $\boldsymbol{\mathcal{F}}$ is a nonlinear continuous–time function, $\bar{\mathbf{M}} = \mathbf{R}^T\mathbf{M}\mathbf{R}$ and $\bar{\mathbf{Q}} = \mathbf{R}^T(\mathbf{Q} - \mathbf{M}\dot{\mathbf{R}}\dot{\mathbf{z}})$. The formulations in independent coordinates, like the one obtained through the matrix–R method, have the advantage of reducing considerably the number of equations to be integrated (n_i). However this imposes an increase in the computational cost since the position and velocity problems have to be solved after each function evaluation.

5.3.2 Penalty formulation

This second method converts the DAEs into ODEs by introducing into the equations of motion the constraint equations as a dynamical system penalized by large factors. The rigid constraints in the DAEs are converted into constraints that can be violated in the ODEs, but only in a small amount in order to still represent the DAEs with negligible approximation errors. The Lagrange multipliers are approximated using the dynamical system demonstrated in eq. (5.22), meaning that the constraint forces depend on the constraint violations.

$$\boldsymbol{\lambda} \simeq \boldsymbol{\alpha}(\ddot{\mathbf{\Phi}} + 2\boldsymbol{\zeta}\boldsymbol{\omega}\dot{\mathbf{\Phi}} + \boldsymbol{\omega}^2\mathbf{\Phi}) \tag{5.22}$$

where, for each constraint, the vectors $\boldsymbol{\alpha}$ contains the penalty factors (usually $> 10^7$, its dimension depends on the type of constraints), $\boldsymbol{\zeta}$ the dimensionless damping ratios (usually $\simeq 1$) and $\boldsymbol{\omega}$ the natural frequencies (usually $\simeq 10$ rad/s). Finally, the equations of motion (eq. (5.23)) are obtained by replacing the Lagrange multipliers of eq. (5.22) in eq. (5.17).

$$\ddot{\mathbf{q}} = (\mathbf{M} + \boldsymbol{\Phi}_{\mathbf{q}}^{\mathrm{T}} \boldsymbol{\alpha} \boldsymbol{\Phi}_{\mathbf{q}})^{-1} \left[\mathbf{Q} - \boldsymbol{\Phi}_{\mathbf{q}}^{\mathrm{T}} \boldsymbol{\alpha} (\dot{\boldsymbol{\Phi}}_{\mathbf{q}} \dot{\mathbf{q}} + 2\boldsymbol{\zeta}\boldsymbol{\omega}\dot{\boldsymbol{\Phi}} + \boldsymbol{\omega}^2 \boldsymbol{\Phi}) \right] \equiv \boldsymbol{\mathcal{F}}(\mathrm{t}, \mathbf{q}, \dot{\mathbf{q}}) \tag{5.23}$$

This formulation has a greater number of equations (n_d) to be integrated than matrix R method (n_i). Nevertheless it is not necessary to solve the position and velocity problems to pass from independent to dependent coordinates after each function evaluation.

5.3.3 Integrators

In order to integrate the equations of motion, two integration schemes have been considered: the trapezoidal rule (TR), an implicit scheme shown in eq. (5.24), and the second order explicit Runge–Kutta 2 (RK2) method presented in eq. (5.25).

$$\mathbf{v}_{\mathrm{k+1}} = \mathbf{v}_{\mathrm{k}} + \frac{\Delta \mathrm{t}}{2} (\dot{\mathbf{v}}_{\mathrm{k}} + \dot{\mathbf{v}}_{\mathrm{k+1}}) \tag{5.24}$$

$$\mathbf{v}_{\mathrm{k+1}} = \mathbf{v}_{\mathrm{k}} + \frac{\Delta \mathrm{t}}{2} (\mathbf{k}_1 + \mathbf{k}_2) \qquad \text{with } \mathbf{k}_1 = \mathbf{f}(\mathrm{t}, \mathbf{v}_{\mathrm{k}}) \text{ and } \mathbf{k}_2 = \mathbf{f}(\mathrm{t} + \Delta \mathrm{t}, \mathbf{v}_{\mathrm{k}} + \Delta \mathrm{t}\, \mathbf{k}_1) \tag{5.25}$$

where $\mathbf{v}(\mathrm{t}) = \begin{bmatrix} \mathbf{q}(\mathrm{t}) \\ \dot{\mathbf{q}}(\mathrm{t}) \end{bmatrix}$ and $\mathbf{f}(\mathrm{t})$ is a system of *first–order ODE* equations coming from reshaping the *second–order ODE* equations obtained with either the matrix–R method or the penalty formulation and using variable duplication. Equation (5.26) demonstrates how $\mathbf{f}(\mathrm{t})$ is obtained.

$$\ddot{\mathbf{q}} = \boldsymbol{\mathcal{F}}(\mathrm{t}, \mathbf{q}, \dot{\mathbf{q}}) \Rightarrow \dot{\mathbf{v}}(\mathrm{t}) \equiv \begin{bmatrix} \dot{\mathbf{q}} \\ \dot{\mathbf{w}}(\mathrm{t}) \end{bmatrix} = \begin{bmatrix} \mathbf{w}(\mathrm{t}) \\ \boldsymbol{\mathcal{F}}(\mathrm{t}, \mathbf{q}, \mathbf{w}) \end{bmatrix} \equiv \mathbf{f}(\mathbf{v}(\mathrm{t}), \mathrm{t}) \tag{5.26}$$

If an MB formulation in independent coordinates is used, $\mathbf{q}$ has to be replaced by $\mathbf{z}$ in the previous equations. Implicit integrators are often employed in MB simulations to overcome stability problems and energy loss while explicit integrators are commonly used in applications requiring hard real–time.

5.4 Nonlinear Kalman filters using multibody models

The original formulation of the KF is intended only to linear systems. To apply the KF to nonlinear systems, the process and measurement models have to be approximated in some way. The differences between the KF variants for nonlinear systems arise mainly from distinct approximation approaches. In this section, two types of nonlinear Kalman filters are discussed: the EKF, which is the *de facto* KF for nonlinear systems, and the SPKFs. For the EKF, only the continuous–time form is taken into account while only the discrete–form is considered for the SPKFs. The advantages of discrete–form filters over continuous–form ones is exemplified in section 5.5.2.

5.4.1 The Extended Kalman Filter

Theory

The EKF, the *de facto* KF for nonlinear systems, propagates Gaussian random variables (GRVs) through the system dynamics represented by the nonlinear continuous–time eq. (5.1). Unlike in the KF, here $\mathbf{f}(t)$, $\mathbf{h}(t)$ can be nonlinear functions. While the optimal quantities can be calculated in eqs. (5.3) and (5.5) for linear systems, this is not the case for nonlinear systems. As a consequence, the optimal terms have to be approximated in some way. The EKF approximates first the continuous–time eq. (5.3) by eq. (5.27), where the derivative of the state vector is function of the state vector, and then eq. (5.5) by eq. (5.28), where the predicted measurements are function of the estimates. As for the KF, the Kalman gain is obtained using eq. (5.4) and the covariance matrix of the state estimation uncertainty using eq. (5.6) but the linearizations $\mathbf{F}$ and $\mathbf{H}$ have to be calculated as shown in eq. (5.29).

$$\dot{\hat{\mathbf{x}}} = \mathrm{E}[\mathbf{f}(\hat{\mathbf{x}}(t), t) + \boldsymbol{w}(t)] + \bar{\mathbf{K}}(t)[\mathbf{y}(t) - \hat{\mathbf{y}}(t)] \simeq \mathbf{f}(\hat{\mathbf{x}}(t)) + \bar{\mathbf{K}}(t)[\mathbf{y}(t) - \hat{\mathbf{y}}(t)] \tag{5.27}$$

$$\hat{\mathbf{y}}(t) = \mathrm{E}[\mathbf{h}(\hat{\mathbf{x}}(t), t) + \boldsymbol{v}(t)] \simeq \mathbf{h}(\hat{\mathbf{x}}(t)) \tag{5.28}$$

$$\dot{\mathbf{P}}(t) \simeq \mathbf{F}(t)\mathbf{P}(t) + \mathbf{P}\mathbf{F}^{\mathrm{T}}(t) - \bar{\mathbf{K}}\boldsymbol{\mathcal{R}}\bar{\mathbf{K}}^{\mathrm{T}} + \mathbf{G}(t)\boldsymbol{\mathcal{Q}}\mathbf{G}^{\mathrm{T}}(t) \tag{5.29}$$

The EKF with MB models

In previous researches, the EKF in its continuous–time form has been employed with MB models (Barreiro et al., 2008; Cuadrado et al., 2008, 2009a, 2010, 2011). Hereafter, the methods employed to use the aforementioned MB formulations with the continuous–time form of the EKF are presented and discussed.

Matrix–R method – First, the case of the projection matrix–R method is covered. As in section 5.3.3, variable duplication is employed to define the state vector, as shown in eq. (5.30). Consequently, the state vector has dimension $(2n_i)$. Equation (5.21) can be reshaped using eq. (5.30) in order to convert the *second order ODE* (eq. (5.21)) into a *first order ODE* (eq. (5.31)). As a consequence, the latter equation and eq. (5.1) have now the same form meaning that the dynamical system of the filter can be an MB model that uses the projection matrix–R method.

$$\mathbf{x}(t) = \begin{bmatrix} \mathbf{z}(t) \\ \mathbf{w}(t) \end{bmatrix} \tag{5.30}$$

$$\begin{aligned} \dot{\mathbf{x}}(t) \equiv \begin{bmatrix} \dot{\mathbf{z}}(t) \\ \dot{\mathbf{w}}(t) \end{bmatrix} &= \begin{bmatrix} \mathbf{w}(t) \\ \bar{\mathbf{M}}^{-1}\bar{\mathbf{Q}} \end{bmatrix} \equiv \begin{bmatrix} \mathbf{w} \\ (\mathbf{R}^{\mathrm{T}}\mathbf{M}\mathbf{R})^{-1}\left[\mathbf{R}^{\mathrm{T}}(\mathbf{Q} - \mathbf{M}\dot{\mathbf{R}}\mathbf{w})\right] \end{bmatrix} \\ &= \mathbf{f}(\mathbf{x}(t), t) \end{aligned} \tag{5.31}$$

where $\mathbf{w}(t) = \dot{\mathbf{z}}(t)$. Taking into account the chosen state vector, eq. (5.27) can be written as shown in eq. (5.32).

$$\begin{bmatrix} \dot{\hat{\mathbf{z}}} \\ \dot{\hat{\mathbf{w}}} \end{bmatrix} = \begin{bmatrix} \hat{\mathbf{w}} \\ (\mathbf{R}^{\mathrm{T}}\mathbf{M}\mathbf{R})^{-1}\left[\mathbf{R}^{\mathrm{T}}(\mathbf{Q} - \mathbf{M}\dot{\mathbf{R}}\hat{\mathbf{w}})\right] \end{bmatrix} + \begin{bmatrix} \bar{\mathbf{K}}^{\mathbf{z}} \\ \bar{\mathbf{K}}^{\mathbf{w}} \end{bmatrix} (\mathbf{y} - \hat{\mathbf{y}}) \tag{5.32}$$

where $\bar{\mathbf{K}}^{\mathbf{z}}$ and $\bar{\mathbf{K}}^{\mathbf{w}}$ are the two blocks of $\bar{\mathbf{K}}$. It is worth pointing out that all the elements of the state vector are independent by definition. Therefore, when the state vector contains positions and velocities, the Kalman corrections are applied to velocities and accelerations

independently. This implies that the time–derivative relation between position and velocity as well as between velocity and acceleration is not thoroughly respected. This is not a problem since the filter tries to provide the best estimate of the velocity , which should overcome the effect of the derivation of the position estimation error. The same last comment applies also to the estimate of the acceleration. The resulting equations have then to be integrated. If the TR is chosen, eq. (5.24) can be expressed as shown in eq. (5.33). This last equation can now be substituted in eq. (5.32), taken at time step (k+1), leading to eq. (5.34). This equation can be scaled by a factor of $\Delta t/2$ for numerical purposes, leading to eq. (5.35).

$$\begin{bmatrix} \hat{\mathbf{z}}_{k+1} \\ \hat{\mathbf{w}}_{k+1} \end{bmatrix} = \begin{bmatrix} \hat{\mathbf{z}}_{k} \\ \hat{\mathbf{w}}_{k} \end{bmatrix} + \frac{\Delta t}{2} \begin{bmatrix} \dot{\hat{\mathbf{z}}}_{k} + \dot{\hat{\mathbf{z}}}_{k+1} \\ \dot{\hat{\mathbf{w}}}_{k} + \dot{\hat{\mathbf{w}}}_{k+1} \end{bmatrix} \tag{5.33}$$

$$\begin{bmatrix} \frac{2}{\Delta t}(\hat{\mathbf{z}}_{k+1} - \hat{\mathbf{z}}_{k}) - \dot{\hat{\mathbf{z}}}_{k} - \mathbf{w}_{k+1} - \bar{\mathbf{K}}^{\mathbf{z}}_{k+1}(\mathbf{y}_{k+1} - \hat{\mathbf{y}}_{k+1}) \\ \frac{2}{\Delta t}(\hat{\mathbf{w}}_{k+1} - \hat{\mathbf{w}}_{k}) - \dot{\hat{\mathbf{w}}}_{k} - \bar{\mathbf{M}}^{-1}\left[\mathbf{R}^{\mathrm{T}}(\mathbf{Q} - \mathbf{M}\dot{\mathbf{R}}\dot{\hat{\mathbf{w}}}_{k+1})\right] - \bar{\mathbf{K}}^{\mathbf{w}}_{k+1}(\mathbf{y}_{k+1} - \hat{\mathbf{y}}_{k+1}) \end{bmatrix} = \mathbf{0} \tag{5.34}$$

$$\mathbf{g}(\hat{\mathbf{x}}_{k+1}) = \begin{bmatrix} (\hat{\mathbf{z}}_{k+1} - \hat{\mathbf{z}}_{k}) - \frac{\Delta t}{2}\left[\dot{\hat{\mathbf{z}}}_{k} - \mathbf{w}_{k+1} - \bar{\mathbf{K}}^{\mathbf{z}}_{k+1}(\mathbf{y}_{k+1} - \mathbf{h}(\hat{\mathbf{x}}_{k+1}))\right] \\ \bar{\mathbf{M}}\hat{\mathbf{w}}_{k+1} - \bar{\mathbf{M}}\hat{\mathbf{w}}_{k} - \frac{\Delta t}{2}\left[\bar{\mathbf{M}}\dot{\hat{\mathbf{w}}}_{k} - \bar{\mathbf{Q}}_{k+1} - \bar{\mathbf{M}}\bar{\mathbf{K}}^{\mathbf{w}}_{k+1}(\mathbf{y}_{k+1} - \mathbf{h}(\hat{\mathbf{x}}_{k+1}))\right] \end{bmatrix} = \mathbf{0} \tag{5.35}$$

where $\mathbf{g}$ is a nonlinear function that can be solved using the Newton–Raphson method. This method is based on a linearization of $\mathbf{g}$ that consists in replacing the function by the first two terms of its expansion in Taylor series around a certain approximation $\mathbf{x}_i$ to the desired solution, as described in eq. (5.36). To accurately approximate vector $\hat{\mathbf{x}}_{k+1}$, an initial approximation of it (i.e. $\mathbf{x}_0$) is calculated using an explicit integrator and then the iterative formula shown eq. (5.36) is used until the approximation error makes insignificant, as demonstrated eq. (5.37). The tangent matrix has been approximated as shown in eq. (5.38).

$$\mathbf{g}(\hat{\mathbf{x}}_{i+1}) \simeq \mathbf{g}(\hat{\mathbf{x}}_{i}) + \frac{\partial \mathbf{g}(\hat{\mathbf{x}}_{i})}{\partial \hat{\mathbf{x}}_{i}}(\hat{\mathbf{x}}_{i+1} - \hat{\mathbf{x}}_{i}) = \mathbf{0} \tag{5.36}$$

$$\hat{\mathbf{x}}_{k+1} = \hat{\mathbf{x}}_{i+1} \quad \text{when } (\hat{\mathbf{x}}_{i+1} - \hat{\mathbf{x}}_{i}) \simeq 0 \tag{5.37}$$

$$\begin{aligned} \frac{\partial \mathbf{g}(t, \hat{\mathbf{x}})}{\partial \hat{\mathbf{x}}} &= \begin{bmatrix} \frac{\partial \mathbf{g}(\hat{\mathbf{x}})}{\partial \hat{\mathbf{z}}} & \frac{\partial \mathbf{g}(\hat{\mathbf{x}})}{\partial \hat{\mathbf{w}}} \end{bmatrix} \\ &\simeq \begin{bmatrix} \mathbf{I} + \frac{\Delta t}{2}\bar{\mathbf{K}}^{\mathbf{z}}\mathbf{H}^{\mathbf{z}} & \frac{\Delta t}{2}\left(-\mathbf{I} + \bar{\mathbf{K}}^{\mathbf{z}}\mathbf{H}^{\mathbf{w}}\right) \\ \mathbf{R}^{\mathrm{T}}\mathbf{K}\mathbf{R} + \bar{\mathbf{M}}\bar{\mathbf{K}}^{\mathbf{w}}\mathbf{H}^{\mathbf{z}} & \bar{\mathbf{M}} + \frac{\Delta t}{2}\left(\mathbf{R}^{\mathrm{T}}(\mathbf{C}\mathbf{R} + \mathbf{M}\dot{\mathbf{R}}) + \mathbf{M}\bar{\mathbf{K}}^{\mathbf{w}}\mathbf{H}^{\mathbf{w}}\right) \end{bmatrix} \end{aligned} \tag{5.38}$$

where $\mathbf{K} = -\frac{\partial \mathbf{Q}}{\partial \mathbf{z}}$ [1] and $\mathbf{C} = -\frac{\partial \mathbf{Q}}{\partial \mathbf{w}}$ are the stiffness and the damping matrices respectively and $\mathbf{H}^{\mathbf{z}}$ and $\mathbf{H}^{\mathbf{w}}$ are the blocks of $\mathbf{H}$ shown in eq. (5.39).

$$\mathbf{H}(t, \mathbf{x}) \equiv \frac{\partial \mathbf{h}(t, \mathbf{x})}{\partial \hat{\mathbf{x}}} = \begin{bmatrix} \frac{\partial \mathbf{h}(t)}{\partial \hat{\mathbf{z}}} & \frac{\partial \mathbf{h}(t)}{\partial \hat{\mathbf{w}}} \end{bmatrix} = \begin{bmatrix} \mathbf{H}^{\mathbf{z}} & \mathbf{H}^{\mathbf{w}} \end{bmatrix} \tag{5.39}$$

To calculate the Kalman gain $\bar{\mathbf{K}}$, the covariance matrix of state estimation uncertainty $\mathbf{P}$ has to be calculated. To this end, the Riccati equation (eq. (5.29)) can be solved for example

[1] The reader should take care not to confuse the stiffness matrix $\mathbf{K}$ and the Kalman gain $\bar{\mathbf{K}}$.

iteratively using fixed point iteration, for which the linearization of the dynamical system of the filter, $\mathbf{F}$, takes the form shown in eq. (5.40) and can be approximated by eq. (5.41). However, it has been checked in simulation that explicit methods like forward Euler provide the same results.

$$\mathbf{F}(\mathrm{t}) \equiv \frac{\partial \mathbf{f}(\mathrm{t})}{\partial \mathbf{x}} = \begin{bmatrix} \mathbf{0} & \mathbf{I} \\ \dfrac{\partial(\bar{\mathbf{M}}^{-1}\bar{\mathbf{Q}})}{\partial \mathbf{z}} & \dfrac{\partial(\bar{\mathbf{M}}^{-1}\bar{\mathbf{Q}})}{\partial \mathbf{w}} \end{bmatrix} \tag{5.40}$$

$$\mathbf{F}(\mathrm{t}) \simeq \begin{bmatrix} \mathbf{0} & \mathbf{I} \\ -\bar{\mathbf{M}}^{-1}\mathbf{R}^{\mathrm{T}}(\mathbf{K}\mathbf{R} + 2\mathbf{M}\mathbf{R}_{\mathbf{q}}\mathbf{R}\dot{\mathbf{w}}) & -\bar{\mathbf{M}}^{-1}\mathbf{R}^{\mathrm{T}}(\mathbf{C}\mathbf{R} + \mathbf{M}\dot{\mathbf{R}}) \end{bmatrix} \tag{5.41}$$

The variable duplication carried out in eq. (5.30) yield a size of $(2n_i)$ for the equations of the observer. These equations have been integrated separately using eq. (5.24), as shown in eq. (5.35). This last equation has a size of $(2n_i)$ and its tangent matrix $(2n_i) \times (2n_i)$. It is possible to reduce the size of the problem for the integration to (n_i) by substituting the upper block of equations in eq. (5.35) into the corresponding lower block of equations. This reduction is carefully explained and justified hereafter.

First the upper block has to be written as shown in eq. (5.42) that provides the best estimates of the velocities of the real mechanism as function of the estimates of the positions. It is worth pointing out that apart from the classical terms appearing in the right–hand side (RHS) of this equation, the rest of them correspond to corrections coming from the filter and based on the information of the sensors. After that, $\mathbf{w}_{\mathrm{k+1}}$ can be substituted in the lower block of equations in eq. (5.33), leading to eq. (5.43) that gives the accelerations of the model based on the best estimates of the velocities and the positions.

$$\mathbf{w}_{\mathrm{k+1}} = \left[\frac{2}{\Delta \mathrm{t}}(\hat{\mathbf{z}}_{\mathrm{k+1}} - \hat{\mathbf{z}}_{\mathrm{k}}) - \dot{\hat{\mathbf{z}}}_{\mathrm{k}}\right] - \bar{\mathbf{K}}^{\mathbf{z}}_{\mathrm{k+1}}\Delta \mathbf{y}_{\mathrm{k+1}} \tag{5.42}$$

$$\begin{aligned} \dot{\hat{\mathbf{w}}}_{\mathrm{k+1}} &= \frac{2}{\Delta \mathrm{t}}\left[\frac{2}{\Delta \mathrm{t}}(\hat{\mathbf{z}}_{\mathrm{k+1}} - \hat{\mathbf{z}}_{\mathrm{k}}) - \dot{\hat{\mathbf{z}}}_{\mathrm{k}} - \bar{\mathbf{K}}^{\mathbf{z}}_{\mathrm{k+1}}\Delta \mathbf{y}_{\mathrm{k+1}} - \hat{\mathbf{w}}_{\mathrm{k}}\right] - \dot{\hat{\mathbf{w}}}_{\mathrm{k}} \\ &= \frac{4}{\Delta \mathrm{t}^2}(\hat{\mathbf{z}}_{\mathrm{k+1}} - \hat{\mathbf{z}}_{\mathrm{k}}) - \frac{2}{\Delta \mathrm{t}}\left[\dot{\hat{\mathbf{z}}}_{\mathrm{k}} - \bar{\mathbf{K}}^{\mathbf{z}}_{\mathrm{k+1}}\Delta \mathbf{y}_{\mathrm{k+1}}\right] - \dot{\hat{\mathbf{w}}}_{\mathrm{k}} \end{aligned} \tag{5.43}$$

where $\Delta \mathbf{y}_{\mathrm{k+1}} = (\mathbf{y}_{\mathrm{k+1}} - \mathbf{h}(\hat{\mathbf{x}}_{\mathrm{k+1}}))$ is the innovation. Finally, $\dot{\hat{\mathbf{w}}}_{\mathrm{k+1}}$ can be substituted in the lower block of equations in eq. (5.32) so that the only term referring to the next time step is $\mathbf{z}_{\mathrm{k+1}}$, as shown in eq. (5.44). For numerical purposes, this equation can be scaled by a factor of $^{\Delta \mathrm{t}^2}/_4$ to yield eq. (5.45). Then, the nonlinear function $\mathbf{g}$ can be solved for example using

the Newton–Raphson method and the corresponding tangent matrix shown in eq. (5.46).

$$\left(\frac{4}{\Delta t^2}\bar{\mathbf{M}}+\frac{2}{\Delta t}\tilde{\mathbf{R}}\right)(\hat{\mathbf{z}}_{k+1}-\hat{\mathbf{z}}_k)-\left(\frac{2}{\Delta t}\bar{\mathbf{M}}+\tilde{\mathbf{R}}\right)\dot{\hat{\mathbf{z}}}_k-\frac{2}{\Delta t}\bar{\mathbf{M}}\hat{\mathbf{w}}_k-\bar{\mathbf{M}}\dot{\hat{\mathbf{w}}}_k-\mathbf{R}^{\mathrm{T}}\mathbf{Q} - \left[\left(\frac{2}{\Delta t}\bar{\mathbf{M}}+\tilde{\mathbf{R}}\right)\bar{\mathbf{K}}^{\mathbf{z}}_{k+1}-\bar{\mathbf{K}}^{\mathbf{w}}_{k+1}\right]\Delta\mathbf{y}_{k+1}=\mathbf{0} \tag{5.44}$$

$$\mathbf{g}(\hat{\mathbf{z}}_{k+1})=\left(\bar{\mathbf{M}}+\frac{\Delta t}{2}\tilde{\mathbf{R}}\right)(\hat{\mathbf{z}}_{k+1}-\hat{\mathbf{z}}_k)-\left(\frac{\Delta t}{2}\bar{\mathbf{M}}+\frac{\Delta t^2}{4}\tilde{\mathbf{R}}\right)\dot{\hat{\mathbf{z}}}_k-\frac{\Delta t}{2}\bar{\mathbf{M}}\hat{\mathbf{w}}_k - \frac{\Delta t^2}{4}\left[\bar{\mathbf{M}}\dot{\hat{\mathbf{w}}}_k-\mathbf{R}^{\mathrm{T}}\mathbf{Q}-\left[\left(\frac{2}{\Delta t}\bar{\mathbf{M}}+\tilde{\mathbf{R}}\right)\bar{\mathbf{K}}^{\mathbf{z}}_{k+1}-\bar{\mathbf{K}}^{\mathbf{w}}_{k+1}\right]\Delta\mathbf{y}_{k+1}\right]=\mathbf{0} \tag{5.45}$$

$$\frac{\partial\mathbf{g}(\hat{\mathbf{z}}_{k+1})}{\partial\mathbf{z}_{k+1}}=\bar{\mathbf{M}}+\frac{\Delta t^2}{4}\mathbf{R}^{\mathrm{T}}\left[\mathbf{K}\mathbf{R}+(\mathbf{C}\mathbf{R}+\mathbf{M}\dot{\mathbf{R}})\left(\frac{2}{\Delta t}+\bar{\mathbf{K}}^{\mathbf{z}}\mathbf{H}^{\mathbf{z}}\right)\right]+ \frac{\Delta t}{2}\bar{\mathbf{M}}\left[\bar{\mathbf{K}}^{\mathbf{z}}\mathbf{H}^{\mathbf{z}}+\bar{\mathbf{K}}^{\mathbf{z}}\mathbf{H}^{\mathbf{w}}\left(\frac{2}{\Delta t}+\bar{\mathbf{K}}^{\mathbf{z}}\mathbf{H}^{\mathbf{z}}\right)+\frac{\Delta t}{2}\left(\bar{\mathbf{K}}^{\mathbf{w}}\mathbf{H}^{\mathbf{z}}+\bar{\mathbf{K}}^{\mathbf{w}}\mathbf{H}^{\mathbf{w}}(\frac{2}{\Delta t}+\bar{\mathbf{K}}^{\mathbf{z}}\mathbf{H}^{\mathbf{z}})\right)\right] \tag{5.46}$$

where $\tilde{\mathbf{R}}=\mathbf{R}^T\mathbf{M}\dot{\mathbf{R}}$. These equations have shown how to reduce the problem size from $(2n_i)$ to (n_i).

Penalty formulation – The use of the penalty formulation with the EKF in its continuous form is treated hereafter. As for the matrix–R method, variable duplication (eq. (5.47)) is used to reshape the equations of motion (eq. (5.23)) as first order ODEs (eq. (5.48)). Then, the estimates (eq. (5.27)) can be written as shown in eq. (5.49). The sames comments as for the matrix–R method regarding the interpretation of the Kalman corrections can be made.

$$\mathbf{x}(t)=\begin{bmatrix}\mathbf{q}(t)\\ \mathbf{w}(t)\end{bmatrix} \tag{5.47}$$

$$\dot{\mathbf{x}}(t)\equiv\begin{bmatrix}\dot{\mathbf{q}}(t)\\ \dot{\mathbf{w}}(t)\end{bmatrix}=\begin{bmatrix}\mathbf{w}(t)\\ \bar{\mathbf{M}}^{-1}\bar{\mathbf{Q}}\end{bmatrix} =\begin{bmatrix}\mathbf{w}\\ (\mathbf{M}+\boldsymbol{\Phi}_{\mathbf{q}}^{\mathrm{T}}\boldsymbol{\alpha}\boldsymbol{\Phi}_{\mathbf{q}})^{-1}\left[\mathbf{Q}-\boldsymbol{\Phi}_{\mathbf{q}}^{\mathrm{T}}\boldsymbol{\alpha}(\dot{\boldsymbol{\Phi}}_{\mathbf{q}}\dot{\mathbf{q}}+2\zeta\boldsymbol{\omega}\dot{\boldsymbol{\Phi}}+\boldsymbol{\omega}^2\boldsymbol{\Phi})\right]\end{bmatrix}\equiv\mathbf{f}(\mathbf{x}(t),t) \tag{5.48}$$

$$\begin{bmatrix}\dot{\hat{\mathbf{q}}}\\ \dot{\hat{\mathbf{w}}}\end{bmatrix}=\begin{bmatrix}\hat{\mathbf{w}}\\ (\mathbf{M}+\boldsymbol{\Phi}_{\mathbf{q}}^{\mathrm{T}}\boldsymbol{\alpha}\boldsymbol{\Phi}_{\mathbf{q}})^{-1}\left[\mathbf{Q}-\boldsymbol{\Phi}_{\mathbf{q}}^{\mathrm{T}}\boldsymbol{\alpha}(\dot{\boldsymbol{\Phi}}_{\mathbf{q}}\dot{\mathbf{q}}+2\zeta\boldsymbol{\omega}\dot{\boldsymbol{\Phi}}+\boldsymbol{\omega}^2\boldsymbol{\Phi})\right]\end{bmatrix}+\begin{bmatrix}\bar{\mathbf{K}}^{\mathbf{q}}\\ \bar{\mathbf{K}}^{\mathbf{w}}\end{bmatrix}(\mathbf{y}-\hat{\mathbf{y}}) \tag{5.49}$$

where now $\mathbf{w}(t)=\dot{\mathbf{q}}(t)$. As before, the last equation is integrated using the TR (eq. (5.24)), leading to eq. (5.50), that can be expanded as was done for the matrix–R method. Again the Newton–Raphson method is used to solve this equation. The tangent matrix for the penalty

formulation (eq. (5.51)) has been approximated as shown in eqs. (5.52) and (5.53).

$$\mathbf{g}(\hat{\mathbf{x}}_{k+1}) = \mathbf{0} \tag{5.50}$$

$$\frac{\partial \mathbf{g}(t, \hat{\mathbf{x}})}{\partial \hat{\mathbf{x}}} = \left[\begin{array}{cc} \dfrac{\partial \mathbf{g}(\hat{\mathbf{x}})}{\partial \hat{\mathbf{q}}} & \dfrac{\partial \mathbf{g}(\hat{\mathbf{x}})}{\partial \hat{\mathbf{w}}} \end{array} \right] \tag{5.51}$$

$$\frac{\partial \mathbf{g}(\hat{\mathbf{x}})}{\partial \hat{\mathbf{q}}} \simeq \left[\begin{array}{c} \mathbf{I} + \dfrac{\Delta t}{2} \bar{\mathbf{K}}^{\mathbf{q}} \mathbf{H}^{\mathbf{q}} \\ \dfrac{\Delta t}{2} (\mathbf{K} + \boldsymbol{\omega}^2 \boldsymbol{\Phi}_{\mathbf{q}}^{\mathrm{T}} \boldsymbol{\alpha} \boldsymbol{\Phi}_{\mathbf{q}} + \bar{\mathbf{M}} \bar{\mathbf{K}}^{\mathbf{w}} \mathbf{H}^{\mathbf{q}}) \end{array} \right] \tag{5.52}$$

$$\frac{\partial \mathbf{g}(\hat{\mathbf{x}})}{\partial \hat{\mathbf{w}}} \simeq \left[\begin{array}{c} \dfrac{\Delta t}{2} \left(-\mathbf{I} + \bar{\mathbf{K}}^{\mathbf{q}} \mathbf{H}^{\mathbf{w}} \right) \\ \bar{\mathbf{M}} + \dfrac{\Delta t}{2} \left(\mathbf{C} + \boldsymbol{\Phi}_{\mathbf{q}}^{\mathrm{T}} \boldsymbol{\alpha} (\dot{\boldsymbol{\Phi}}_{\mathbf{q}} + 2\zeta\boldsymbol{\omega} \boldsymbol{\Phi}_{\mathbf{q}}) + \mathbf{M} \bar{\mathbf{K}}^{\mathbf{w}} \mathbf{H}^{\mathbf{w}} \right) \end{array} \right] \tag{5.53}$$

Finally the linearization $\mathbf{F}$ of the dynamical system of the filter (eq. (5.54)) can be approximated as can be seen in eqs. (5.55) and (5.56).

$$\mathbf{F}(t) \equiv \frac{\partial \mathbf{f}(t)}{\partial \mathbf{x}} = \left[\begin{array}{cc} \mathbf{0} & \mathbf{I} \\ \dfrac{\partial (\bar{\mathbf{M}}^{-1} \bar{\mathbf{Q}})}{\partial \mathbf{q}} & \dfrac{\partial (\bar{\mathbf{M}}^{-1} \bar{\mathbf{Q}})}{\partial \mathbf{w}} \end{array} \right] \tag{5.54}$$

$$\frac{\partial (\bar{\mathbf{M}}^{-1} \bar{\mathbf{Q}})}{\partial \mathbf{q}} \simeq -\bar{\mathbf{M}}^{-1} (\mathbf{K} + \boldsymbol{\omega}^2 \boldsymbol{\Phi}_{\mathbf{q}}^{\mathrm{T}} \boldsymbol{\alpha} \boldsymbol{\Phi}_{\mathbf{q}} + 2 \boldsymbol{\Phi}_{\mathbf{q}}^{\mathrm{T}} \boldsymbol{\alpha} \boldsymbol{\Phi}_{\mathbf{q}\mathbf{q}} \dot{\mathbf{w}}) \tag{5.55}$$

$$\frac{\partial (\bar{\mathbf{M}}^{-1} \bar{\mathbf{Q}})}{\partial \mathbf{w}} \simeq -\bar{\mathbf{M}}^{-1} \left[\mathbf{C} + \boldsymbol{\Phi}_{\mathbf{q}}^{\mathrm{T}} \boldsymbol{\alpha} (\dot{\boldsymbol{\Phi}}_{\mathbf{q}} + 2\zeta\boldsymbol{\omega} \boldsymbol{\Phi}_{\mathbf{q}}) \right] \tag{5.56}$$

Hereafter, it is demonstrated that extra steps are necessary to properly estimate the states using the penalty formulation.

First implementation using a 4–bar linkage

The theoretical developments on the use of MB models with the EKF in its continuous form have first been tested on a simple mechanism: a 4–bar linkage with a spring–damper element (Cuadrado et al., 2008, 2009a). A scheme of the mechanism is shown in fig. 5.1 where the points A and B are fixed points and s is the distance between points A and C. The mechanism has been modeled using mixed coordinates (García de Jalón and Bayo, 1994) with the vector of dependent Cartesian coordinates presented in eq. (5.57).

$$\mathbf{q}^T = [x_D \; y_D \; x_C \; y_C \; \mathrm{s}] \tag{5.57}$$

The motion of the real mechanism has been simulated but the magnitudes that correspond to sensor data have been passed to the observers with their respective noises. In order to allow the simulated real mechanism and the model of the filter to have similar but different behaviors, the gravity for the model of the filter has been set to 8.81 m/s^2. Employing a simulated real mechanism allows a comparison of all the states, including those that cannot be measured experimentally. As a consequence, all the variables of the model of the filter (i.e. the virtual sensors and the variables estimated through the state observer) can be compared to their exact magnitudes. In this way, comparisons of the performances of the filters are more genuine and comprehensive. Regarding the test motion, each mathematical model has a different initial position ($s_0 = 1.80$ m for the real mechanism and $s_0 = 1.85$ m for the model of the filter) that enable them to move freely until reaching their stable positions.

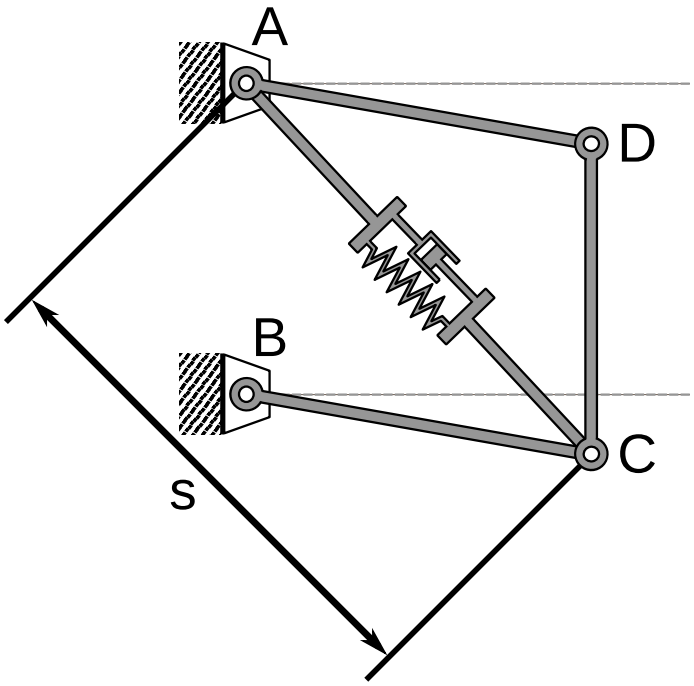

Figure 5.1: Scheme of the 4–bar linkage with a spring–damper element

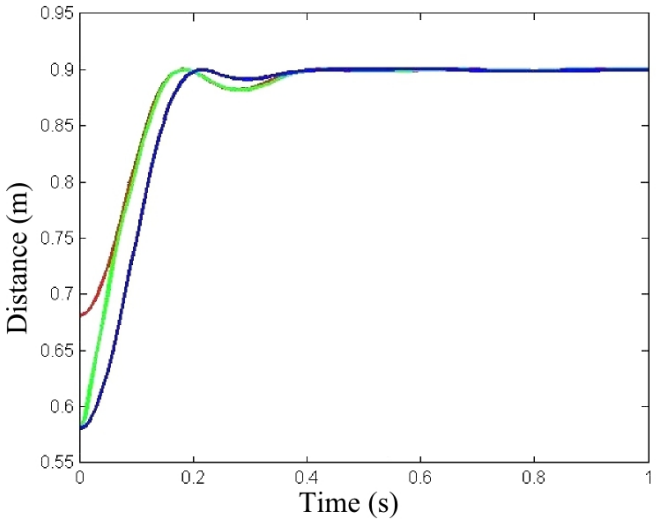

Figure 5.2: Coordinate x_D of the 4–bar linkage

It has been demonstrated in (Cuadrado et al., 2009a) that the state estimation method previously mentioned for the penalty formulation is not convenient. Indeed, while the distance s is estimated properly, this is not the case for the rest of elements of the state vector as demonstrated in fig. 5.2 for the coordinate $\mathbf{x}_D$, following the color code of table 5.1. This can be explained by the fact that the filter estimates independently each element of the state vector (that contains the dependent coordinates and their time derivatives) while the penalty factors enforce to fulfill the constraints. Both objectives are not compatible. Practically, this can be demonstrated using the lower part of eq. (5.49) premultiplied by $(\mathbf{M} + \mathbf{\Phi}_\mathbf{q}^T \boldsymbol{\alpha} \mathbf{\Phi}_\mathbf{q})$, as shown in eq. (5.58). In this equation, an increment in the penalty factor yield a better

Color	MB formu.
red	real mechanism
green	matrix–R
blue	penalty formulation

Table 5.1: Color code for the figures of the 4–bar linkage

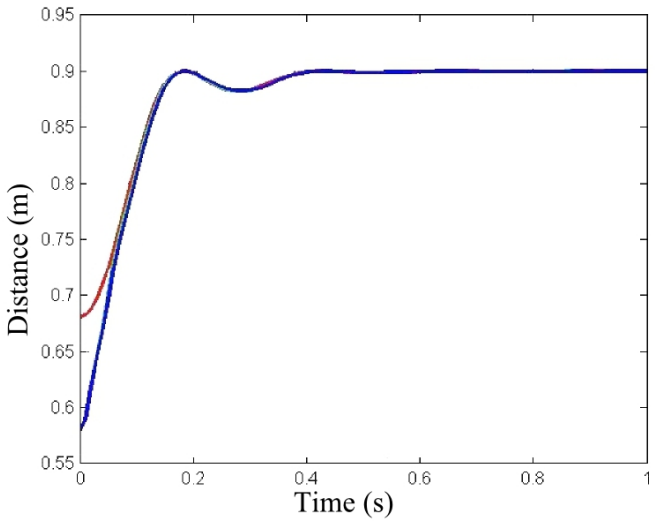

Figure 5.3: Coordinate x_D of the 4–bar linkage with the modified penalty formulation

MB form.	Matrix–R	Penalty form.	Mod. penalty form.
CPU time (%)	100	81.8	164

Table 5.2: CPU times for the 4–bar linkage simulations

fulfillment of the constraints but also an increment in the Kalman corrections.

$$(\mathbf{M}+\boldsymbol{\Phi}_{\mathbf{q}}^{\mathrm{T}}\boldsymbol{\alpha}\boldsymbol{\Phi}_{\mathbf{q}})\dot{\hat{\mathbf{w}}} = \left[\mathbf{Q}-\boldsymbol{\Phi}_{\mathbf{q}}^{\mathrm{T}}\boldsymbol{\alpha}(\dot{\boldsymbol{\Phi}}_{\mathbf{q}}\dot{\mathbf{q}}+2\boldsymbol{\zeta}\boldsymbol{\omega}\dot{\boldsymbol{\Phi}}+\boldsymbol{\omega}^2\boldsymbol{\Phi})\right]+(\mathbf{M}+\boldsymbol{\Phi}_{\mathbf{q}}^{\mathrm{T}}\boldsymbol{\alpha}\boldsymbol{\Phi}_{\mathbf{q}})\bar{\mathbf{K}}^{\mathbf{W}}(\mathbf{y}-\hat{\mathbf{y}}) \quad (5.58)$$

This problem can be avoided by solving the kinematic position and velocity problems at each function evaluation. In this way, the dependent coordinates are updated using the estimate of distance s leading to a better convergence of the filter, as shown in fig. 5.3. This workaround, which is similar to the one employed later in section 5.4.2 to use the penalty formulation with SPKFs, has an important drawback: a higher computational cost compared to the penalty formulation without the extra updating steps. The central processing unit (CPU) times for the matrix–R method, the penalty formulation and the modified penalty formulation are shown in table 5.2. It appears clearly that contrarily to what could have been expected, the matrix–R method is better suited to the EKF in its continuous form than the penalty formulation.

In a posterior work (Cuadrado et al., 2009b), the influence of the choice of the sensors of the filter has been investigated using the matrix–R method. New insights on the accuracy and computational efficiency of the filter and on the calculation of the linearization of the measurement sensitivity matrix have been demonstrated. The subject of this last work,

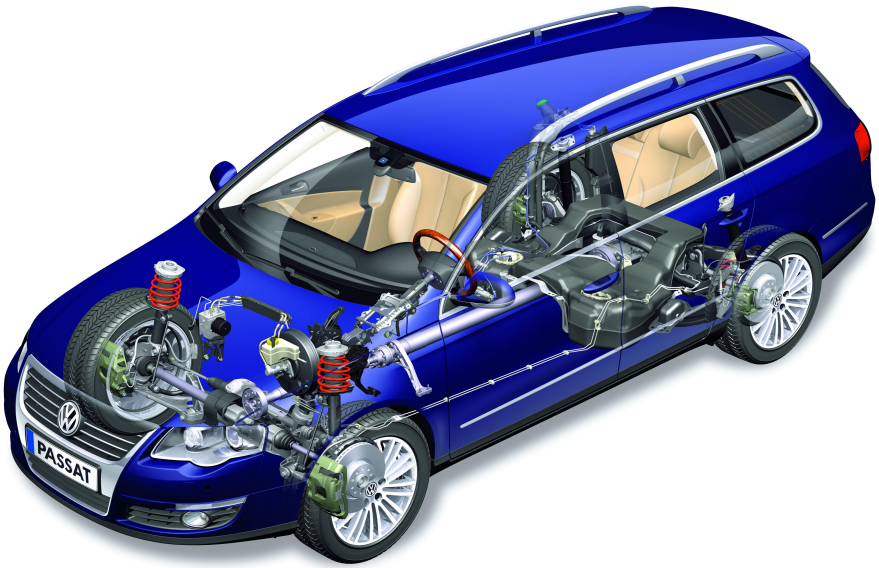

Figure 5.4: 3D model of the Volkswagen Passat

directly related to the concept of observability in the field of control theory, is a subject for future research.

Application to automotive observers

The filter based on the EKF and the matrix–R method with size (n_i) has been applied to a complex mechanical system: the *Volkswagen Passat* (Cuadrado et al., 2010, 2011). As for the 4–bar linkage, the vehicle, shown in fig. 5.4, has been modeled using natural coordinates (44 points and 24 unit vectors) (García de Jalón and Bayo, 1994) along with some relative coordinates (4 angles and 7 distances) thus leading to a total number of 215 variables. A scheme representing all the points and vectors used for the vehicle modeling is presented in fig. 5.5. The number of constraints that relate the variables is 208 and as some of them are redundant the number of DOFs is 15: chassis translations and rotations (6 DOFs), steering (1 DOF), motion of the four suspensions (4 DOFs), and rotation of the wheels (4 DOFs). The front suspension is of McPherson type while the rear multi–link suspension possesses a kinematic structure with no DOF if ideal kinematic pairs are considered: it can only move due to the flexibility provided by the bushings placed at the hinges. To avoid the difficult numerical integration of highly stiff bushings, the MB vehicle model does not include them. Therefore, the kinematic structure of the rear suspension has been slightly modified to enable a motion without using bushings and conserving almost perfectly the suspension kinematics. Regarding the dynamics, the behavior of the tire has been modeled by means of a basic linearized formulation with saturation ellipse, the suspensions using linear springs and dampers, and the anti-roll bars by linear torsional springs too. Finally, the known vehicle inputs are the torques of the wheels that include driving and braking torques, and the steering displacement. The maneuver duration is 22.90 s although only 20 s have been represented in the following figures for clarity. As the steering is kinematically guided, the number of dynamic DOFs of the system is reduced to 14.

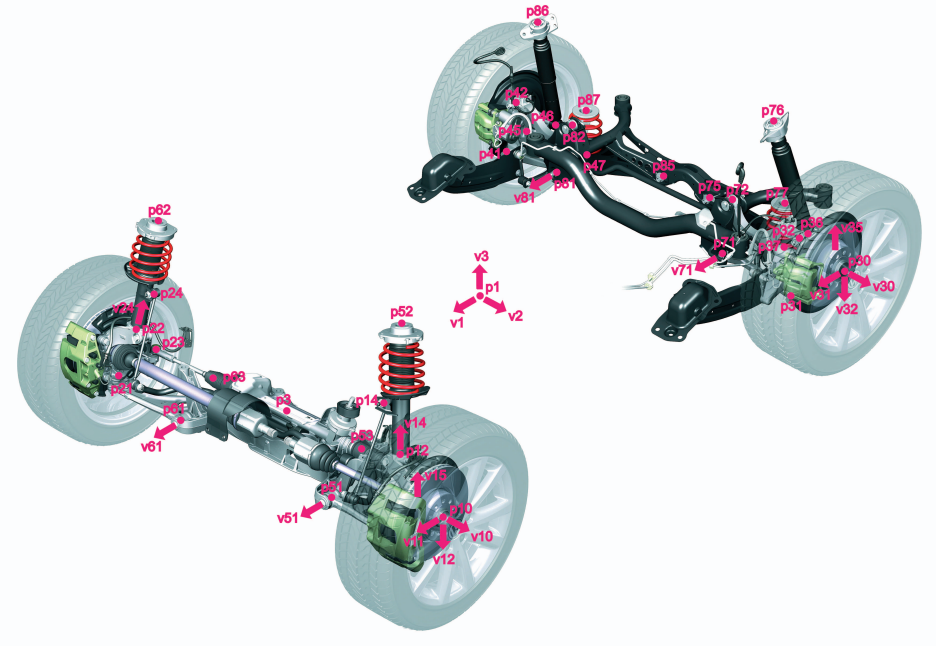

Figure 5.5: Points and vectors for the modeling of the Volkswagen Passat

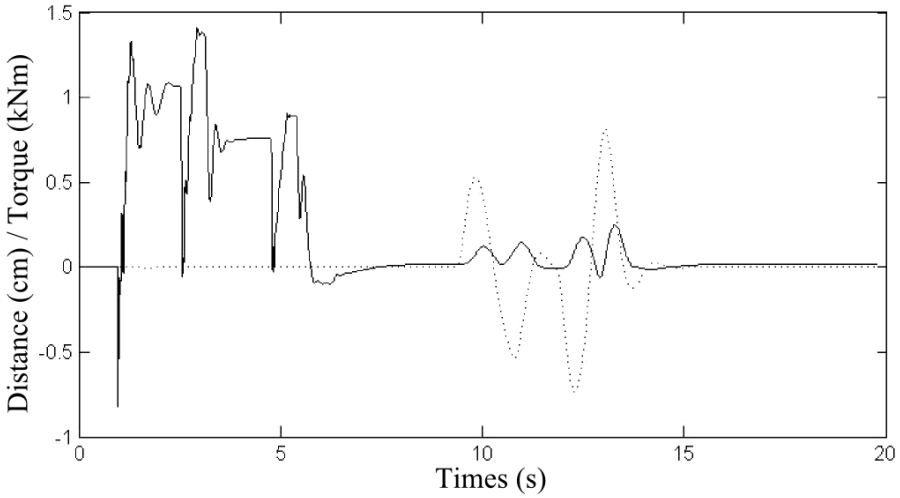

Figure 5.6: Model inputs of the Volkswagen Passat

Similarly to what has been done previously for the 4–bar linkage, the real vehicle has been simulated and the information of the sensors passed to the observer with the corresponding noises, although the final objective is to use the data of the sensors gathered in real–time from the DAS of the vehicle. A double lane change has been carried out in simulation at around 90 km/h using 3 vehicle models: the simulated real vehicle, the observer and the vehicle model used by the filter. The corresponding model inputs are shown in fig. 5.6 where the dotted line represents the rack and pinion system displacement and the solid line represents the wheel torques. The model used by the observer is the same than that used to simulate the real vehicle but not its parameters. Indeed, the model of the filter is 100 kg heavier. It has then been considered that the available data from the sensors correspond to 10 of the 14 DOFs: chassis translations and rotations, motion of the four suspensions. Figures 5.7

	Vehicle	Model	Observer	Observer ($\Delta t = 5\,ms$)
CPU time (s)	48	48	297	64
num. of iterations	22938	22935	141183	29384

Table 5.3: CPU time and number of iterations for $\Delta t = 1\,ms$

and 5.8 present the longitudinal, lateral and vertical displacements as well as the chassis rotation angles of the vehicle for a simulation using an integration time step of 1 ms. For all the figures of this section, the solid line represents the real vehicle, the dashed lines is for the model used by the observer and the dotted line is for the observer. The CPU times and the number of iterations for the simulated real vehicle, the observer and the model used by the observer can be seen in table 5.3. This table reveals that the observer case is notably less efficient than the others. However, this effect is fully due to the rise in the number of iterations required to attain convergence in the Newton–Raphson procedure carried out at each time-step, as proven by the almost constant ratio between the number of iterations and the CPU times. Therefore, the observer formulation does not suppose an extra cost with respect to the model formulation, thus justifying the effort addressed to reduce the size of formulation to the number of DOFs, n_i. The effect of taking a larger integration time step on the efficiency and accuracy of the observer have been evaluated by increasing the time step from 1 ms to 5 ms. The corresponding translations and rotations for the chassis are shown in figs. 5.9 and 5.10 while the CPU time and the number of iterations in this case are summarized in table 5.3. The results are similar to those of the previous case. However it can be seen that states are not properly estimated, like the vertical coordinate of the chassis center of mass and the chassis pitch angle.

This example was intended to evaluate the efficiency of the EKF in its continuous form when used with complex MB models employing the matrix–R method. It has been seen that the matrix–R method without observer is not sufficiently efficient to simulate the model of the Volkswagen Passat in real–time. Consequently, the EKF using this method is less efficient even when the problem is kept equal to the number of DOF n_i. New theoretical researches are therefore necessary in order to further reduce the computational cost and reach real–time for complex MB models. The involved calculation of the linearization for the EKF should also be underlined as its derivation is error-prone and laborious. To this end, in the next section, recent KFs, the SPKFs, have been considered.

5.4.2 The Sigma-Point Kalman Filters

The SPKFs are KFs for nonlinear systems with a linearization approach substantially different from the one of the EKF (Julier and Uhlmann, 2004). Instead of first approximating the estimates as function of the prior estimates propagated through the nonlinear system function and then linearizing the dynamic equations to determine the covariances, a set of deterministically chosen weighted sample points is propagated through the nonlinear system function. The sample points, called *sigma–points*, capture at least the first two moments (mean and covariance) of the prior and posterior (i.e. after propagation through the nonlinear function) random variables. Two SPKF versions are briefly reminded hereafter: the UKF and the SSUKF. All the equations and the most important characteristics of these filters when

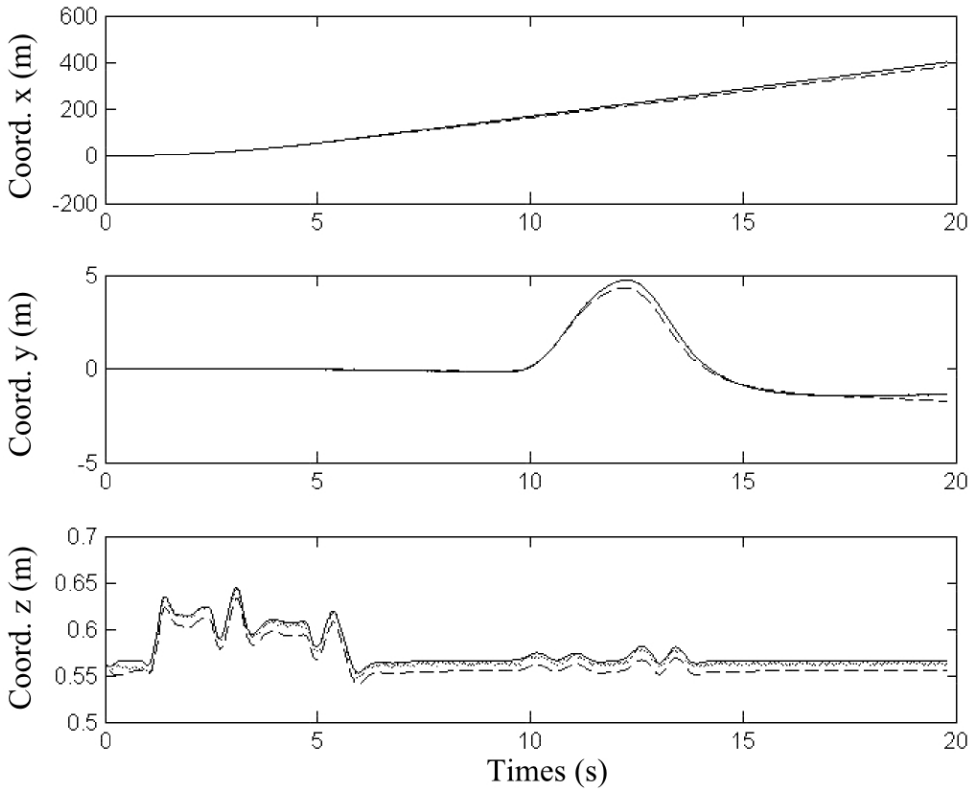

Figure 5.7: Displacements of the vehicle for an integration time step of 1 ms

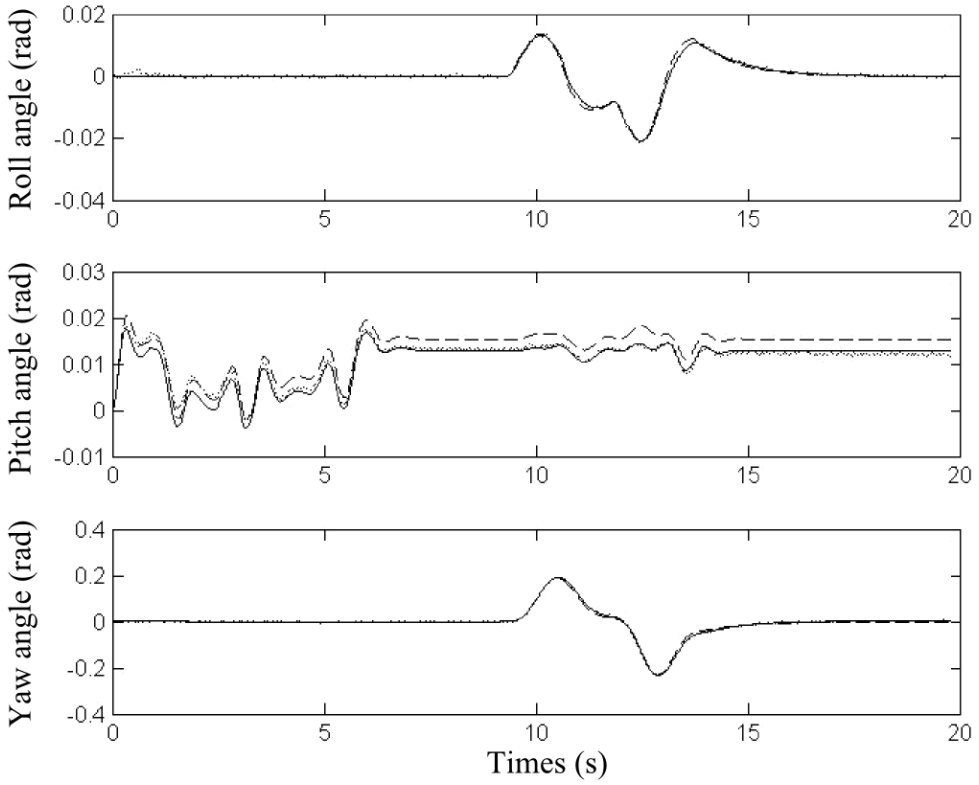

Figure 5.8: Rotation angles of the vehicle for an integration time step of 1 ms

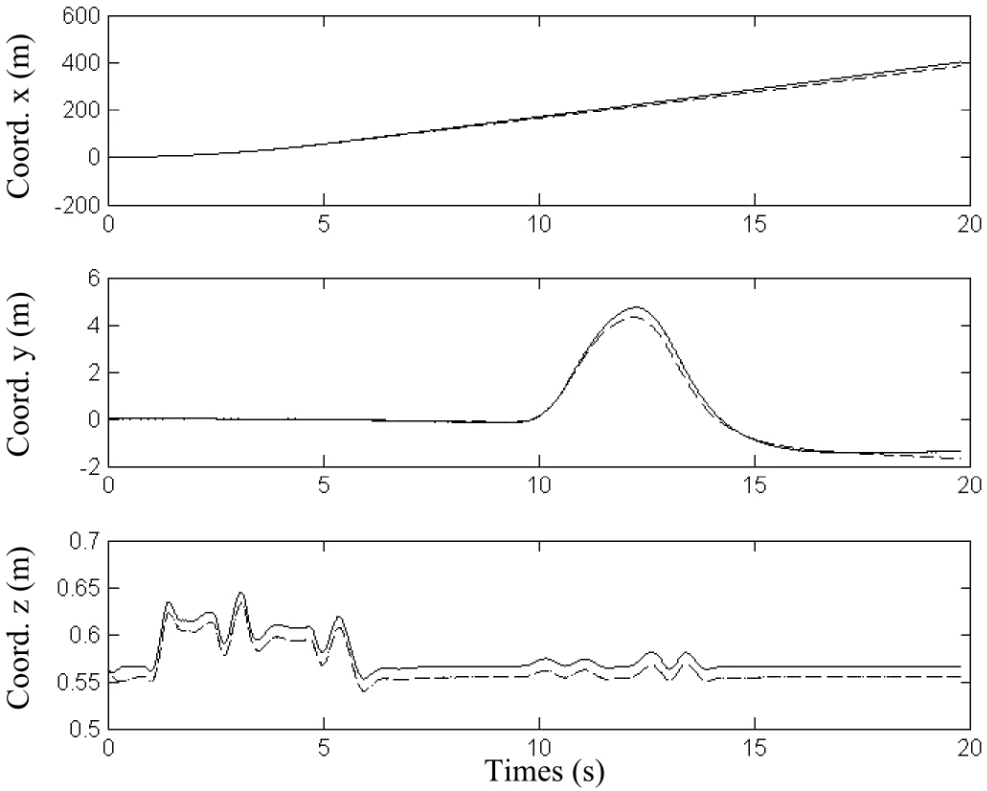

Figure 5.9: Displacements of the vehicle for an integration time step of 5 ms

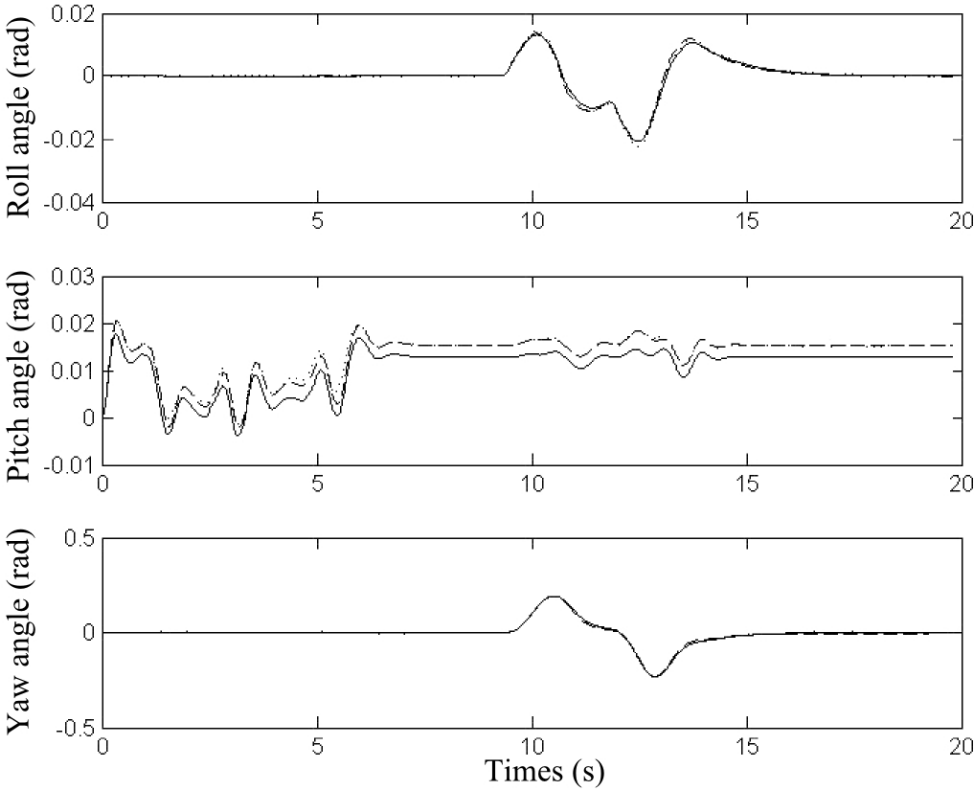

Figure 5.10: Rotation angles of the vehicle for an integration time step of 5 ms

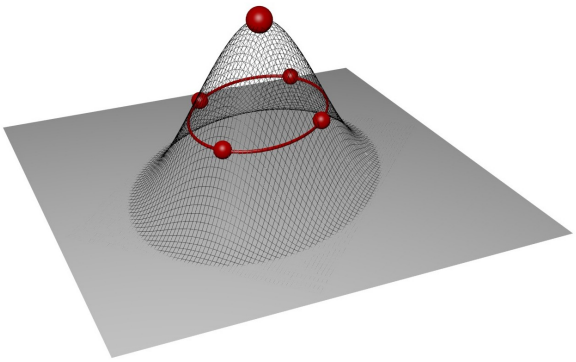

Figure 5.11: UKF: sigma–points for a 2 dimensional GR variable

used with MB models are presented.

Theory – The unscented Kalman filter

As previously mentioned, the time–update equations of the UKF differ substantially from the ones of the EKF . Firstly, the set of n_{sp} sigma–points for the UKF has to be calculated, where $n_{sp} = (2\mathsf{L} + 1)$ points (L is the dimension of the state vector). The zeroth point is the unchanged state estimate while the rest of points is calculated using the zeroth point and the square–root decomposition of the covariance matrix of state estimation uncertainty as shown in eq. (5.59).

$$\boldsymbol{\chi}_{\mathrm{i,k}} = \begin{cases} \hat{\mathbf{x}}_{\mathrm{k}} & \mathrm{i} = 0 \\ \hat{\mathbf{x}}_{\mathrm{k}} + \gamma \left(\sqrt{\mathbf{P}_{\mathrm{k}}}\right)_{\mathrm{i}} & \mathrm{i} = 1, \ldots, \mathsf{L} \\ \hat{\mathbf{x}}_{\mathrm{k}} - \gamma \left(\sqrt{\mathbf{P}_{\mathrm{k}}}\right)_{\mathrm{i}} & \mathrm{i} = \mathsf{L}+1, \ldots, 2\mathsf{L} \end{cases} \tag{5.59}$$

where $\boldsymbol{\chi}_{\mathrm{k}}(\mathrm{i})$ is the i^{th} sigma–point, $\gamma = \sqrt{\mathsf{L} + \lambda}$, $\lambda = \alpha^2(\mathsf{L}+\kappa)$, α and κ are user–defined tuning parameters, $\sqrt{\cdot}$ is the matrix square–root using lower triangular Cholesky decomposition, k is the index for the time step and $(\cdot)_i$ represents the i^{th} column. $0 < \alpha \leq 1$ is a scaling factor defining the extension of the spread of the sigma–points around the mean of the estimates. κ is another scaling factor, usually set to 0. Figure 5.11 exemplifies the weighted sigma–point set for a 2–dimensional Gaussian random variable ($n_{sp} = 5$). The size of the points represents their weights.

After that, each sigma–point is propagated through the system dynamics eq. (5.7) as illustrated in eq. (5.60). There are as many function evaluations as sigma–points. It is worth pointing out that these function evaluations are independent from each other allowing to parallelize the computations using several cores for example.

$$\boldsymbol{\chi}^{-}_{\mathrm{k+1}} = \boldsymbol{\phi}_{\mathrm{k}}(\boldsymbol{\chi}_{\mathrm{k}}) \tag{5.60}$$

The *a priori* state estimates and covariance matrix of state estimation uncertainty are approximated by taking the weighted mean and covariances of the propagated sigma–points

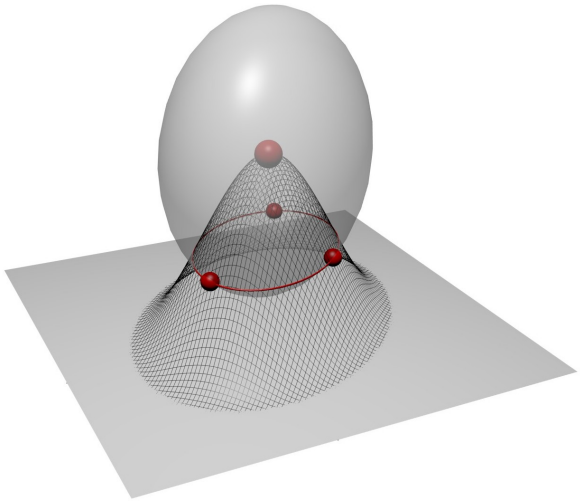

Figure 5.12: SSUKF: sigma–points for a 2 dimensional GR variable

as shown in eqs. (5.61) and (5.62).

$$\hat{\mathbf{x}}^{-}_{k+1} = \mathrm{E}[\boldsymbol{\phi}_k(\hat{\mathbf{x}}_k) + \boldsymbol{w}_k] \simeq \sum_{i=0}^{n_{sp}-1} w_i^m \boldsymbol{\chi}^{-}_{i,k+1} \tag{5.61}$$

$$\begin{aligned}\hat{\mathbf{P}}^{-}_{k+1} &= \mathrm{E}[(\mathbf{x}_{k+1} - \hat{\mathbf{x}}^{-}_{k+1})(\mathbf{x}_{k+1} - \hat{\mathbf{x}}^{-}_{k+1})^{\mathrm{T}}] \\ &\simeq \sum_{i=0}^{n_{sp}-1} w_i^c (\boldsymbol{\chi}^{-}_{i,k+1} - \hat{\mathbf{x}}^{-}_{k+1})(\boldsymbol{\chi}^{-}_{i,k+1} - \hat{\mathbf{x}}^{-}_{k+1})^{\mathrm{T}}\end{aligned} \tag{5.62}$$

where $w_0^m = \lambda/(\mathsf{L}+\lambda)$, $w_0^c = w_0^m + (1-\alpha^2+\beta)$, $w_i^c = w_i^m = 1/[2(\mathsf{L}+\lambda)]$ for $i = 1 \ldots n_{sp}-1$ and β is a scaling factor used to control the weighting of the zeroth sigma–point. Then, if no information is available from the sensors, eqs. (5.11) and (5.12)) are used.

If some information is available, the measurement–update equations, which also differ substantially from the ones of the EKF, are employed. The Kalman gain is obtained using the weighted covariances as shown in eq. (5.63).

$$\begin{aligned}\bar{\mathbf{K}}_{k+1} &= \mathrm{E}[(\mathbf{x}_{k+1} - \hat{\mathbf{x}}^{-}_{k+1})(\mathbf{y}_{k+1} - \hat{\mathbf{y}}^{-}_{k+1})^{\mathrm{T}}] \cdot \mathrm{E}[(\mathbf{y}_{k+1} - \hat{\mathbf{y}}^{-}_{k+1})(\mathbf{y}_{k+1} - \hat{\mathbf{y}}^{-}_{k+1})^{\mathrm{T}}]^{-1} \\ &= \mathbf{P}_{\mathbf{x}_{k+1}\mathbf{y}_{k+1}} \mathbf{P}_{\mathbf{y}_{k+1}\mathbf{y}_{k+1}} \\ &\simeq \sum_{i=0}^{n_{sp}-1} w_i^c (\boldsymbol{\chi}^{-}_{i,k+1} - \hat{\mathbf{x}}^{-}_{k+1})(\boldsymbol{\mathcal{Y}}^{-}_{i,k+1} - \hat{\mathbf{y}}^{-}_{k+1})^{\mathrm{T}} \cdot \sum_{i=0}^{n_{sp}-1} w_i^c (\boldsymbol{\mathcal{Y}}^{-}_{i,k+1} - \hat{\mathbf{y}}^{-}_{k+1})(\boldsymbol{\mathcal{Y}}^{-}_{i,k+1} - \hat{\mathbf{y}}^{-}_{k+1})^{\mathrm{T}}\end{aligned} \tag{5.63}$$

Finally the predicted measurements are approximated by the weighted means of the estimates propagated through the measurement sensitiviy matrix $\mathbf{h}_k$, as can be seen in eqs. (5.64) and (5.65)). The *a posteriori* covariance matrix is now obtained using eq. (5.66) and the *a posteriori* state estimates using eq. (5.13).

$$\hat{\mathbf{y}}^{-}_{k+1} = \mathrm{E}[\mathbf{h}_{k+1}(\hat{\mathbf{x}}^{-}_{k+1}) + \boldsymbol{v}_k] \simeq \sum_{i=0}^{n_{sp}-1} w_i^c \boldsymbol{\mathcal{Y}}^{-}_{i,k+1} \tag{5.64}$$

$$\boldsymbol{\mathcal{Y}}^{-}_{k+1} = \mathbf{h}_{k+1}(\boldsymbol{\chi}_{k+1}) \tag{5.65}$$

$$\mathbf{P}_{k+1} = \mathbf{P}^{-}_{k+1} - \bar{\mathbf{K}}_{k+1} \mathbf{P}_{\mathbf{y}_k\mathbf{y}_k} \bar{\mathbf{K}}^{\mathrm{T}}_{k+1} \tag{5.66}$$

Theory – The spherical simplex UKF

The structure and the equations of the SSUKF are similar to those of the UKF (Julier, 2003). The first difference between the two filters is the rule adopted for the selection of the sigma–point set, and consequently their number: $n_{sp} = (\mathsf{L} + 2)$ for the SSUKF and $n_{sp} = (2\mathsf{L} + 1)$ for the UKF. As a consequence, the number of function evaluations is smaller for this filter, meaning that the computational cost is reduced. The weighted sigma–point set for the SSUKF is calculated using eq. (5.67).

$$\boldsymbol{\chi}_{\mathrm{i}}^{\mathrm{j}} = \begin{cases} \begin{bmatrix} \boldsymbol{\chi}_{0}^{\mathrm{j}-1} \\ \mathbf{0} \end{bmatrix} & \text{for } \mathrm{i} = 0 \\ \begin{bmatrix} \boldsymbol{\chi}_{\mathrm{i}}^{\mathrm{j}-1} \\ -\dfrac{1}{\sqrt{\mathrm{j}(\mathrm{j}+1)w_1}} \end{bmatrix} & \text{for } \mathrm{i} = 1, \ldots, \mathrm{j} \\ \begin{bmatrix} \mathbf{0}_{\mathrm{j}-1} \\ \dfrac{1}{\sqrt{\mathrm{j}(\mathrm{j}+1)w_1}} \end{bmatrix} & \text{for } \mathrm{i} = \mathrm{j}+1 \end{cases} \tag{5.67}$$

where $\mathrm{j} = 2, \ldots, \mathrm{n}$, w_0 is the weight of the zeroth sigma–point and also a user–defined parameter that affects the fourth and higher moments of the sigma–points set ($0 \leq w_0 \leq 1$), w_{i} are the weights of the rest of sigma–points ($w_{\mathrm{i}} = (1 - w_0)/(\mathrm{n} + 1)$) and finally the initial values to calculate the set of sigma–points are: $\boldsymbol{\chi}_0^1 = \mathbf{0}$, $\boldsymbol{\chi}_1^1 = -\dfrac{1}{\sqrt{2w_1}}$ and $\boldsymbol{\chi}_2^1 = \dfrac{1}{\sqrt{2w_1}}$. All the points (apart from the zeroth point) lie on a hypersphere, the radius of which is $\sqrt{\mathsf{L}}/(1 - w_0)$, as it is exemplified in Figure 5.12. The second difference with respect to the UKF is related to the weights used in eqs. (5.61) to (5.63)) where only one set of weights is employed: w_{i} for $\mathrm{i} = 0, \ldots, n_{sp} - 1$.

UKFs using MB models

First, the approach to employ the projection matrix–R method with the UKF and the SSUKF will be described. In order to match the *nonlinear difference equations* of the filter (eq. (5.7)), the equations of motion (eq. (5.21)) have to be integrated using either the TR (eq. (5.24)) or the RK2 method (eq. (5.25)). Subsequently, the choice of the variables to include in the state vector is a crucial point that will condition the implementation of the remaining equations of the filter. The first important comment is that, unlike in the EKF, the variable duplication is not imposed in this filter. As a consequence, there are no constraints for the selection of the states apart from the independence of the equations. As the projection matrix–R method is a formulation in independent coordinates, the state vector could be made for instance of some of the following vectors: $\mathbf{z}_{\mathrm{k}}$, $\dot{\mathbf{z}}_{\mathrm{k}}$ or $\ddot{\mathbf{z}}_{\mathrm{k}}$. Nevertheless, another important issue when choosing the state vector is to attempt to maintain the dimension of the state vector as small as possible in order to calculate the minimum number of sigma–points, thus reducing the overall computational cost. For this filter, the state vector has been chosen equal to the independent acceleration vector $\ddot{\mathbf{z}}$. In this way, the time–derivative relation between positions, velocities and accelerations is preserved. The equations of motion (eq. (5.7)) and the *a posteriori* state estimates (eq. (5.13)) corresponding to the new state vector are presented in eqs. (5.68) and (5.69). A direct physical significance can be given to the Kalman corrections, namely $\bar{\mathbf{K}}_{\mathrm{k}+1}(\mathbf{y}_{\mathrm{k}+1} - \hat{\mathbf{y}}_{\mathrm{k}+1}^{-})$ in eq. (5.69). Indeed as $\mathbf{x}_{\mathrm{k}} = \ddot{\mathbf{z}}_{\mathrm{k}}$, the Kalman corrections are also accelerations, meaning that these corrections can be understood as forces introduced to guide

the system towards its real motion (partially given by the information of the sensors) after the information from a sensor is available.

$$\ddot{\mathbf{z}}_{k+1} = \boldsymbol{\phi}_k(\ddot{\mathbf{z}}_k) + \boldsymbol{w}_k \tag{5.68}$$

$$\hat{\ddot{\mathbf{z}}}_{k+1} = \hat{\ddot{\mathbf{z}}}^{+}_{k+1} = \hat{\ddot{\mathbf{z}}}^{-}_{k+1} + \bar{\mathbf{K}}_{k+1}(\mathbf{y}_{k+1} - \hat{\mathbf{y}}^{-}_{k+1}) \tag{5.69}$$

Once the state vector has been defined, the equations of the filter can be applied. First, the set of sigma–point is calculated using eq. (5.59) for the UKF or eq. (5.67) for the SSUKF. Then, each sigma–point is propagated through the nonlinear discrete–time system function (eq. (5.60)), in other words, a function evaluation of the MB model is performed for each sigma–point. The posterior independent acceleration vector $\hat{\ddot{\mathbf{z}}}_{k+1}$ is obtained using eq. (5.61). Then, it is used to assess the posterior independent position ($\mathbf{z}_{k+1}$) and velocity ($\dot{\mathbf{z}}_{k+1}$) vectors by means of the TR. If no information from the sensors is available, the covariance matrix is obtained through eq. (5.10) and the time–update eqs. (5.11) and (5.12)) are applied. If any sensor data are available, the measurement–update eqs. (5.63) to (5.66) and (5.69) are applied.

After having placed a proposal to employ the projection matrix–R with UKFs, it is also of great interest to describe how to use the penalty approach, because of its lower computational cost. Only a few details differ from the previous explanation. First, in this case the dependent vector of coordinates has been augmented with the independent coordinate vector, as follows: $\mathbf{q} = \begin{bmatrix} \mathbf{q}_d \\ \mathbf{q}_i \end{bmatrix}$. However, as before, the state vector is taken as equal to the independent acceleration vector. Therefore, an extra step is necessary to update the remaining elements of $\ddot{\mathbf{q}}$ (i.e. $\ddot{\mathbf{q}}_d$) when $\ddot{\mathbf{z}} \equiv \ddot{\mathbf{q}}_i$ is updated by the filter, as shown in eq. (5.70). The updates of $\ddot{\mathbf{z}}$ take place in eq. (5.61) and eq. (5.69).

$$\ddot{\mathbf{q}}_k = \mathbf{R}_k\, \dot{\mathbf{z}}_k + \dot{\mathbf{R}}_k\, \dot{\mathbf{z}}_k \tag{5.70}$$

5.5 Observer performance comparisons using a 5-bar linkage

5.5.1 Experimental set-up

A 5–bar linkage has been employed to exemplify the implementation and the performances of all the aforementioned nonlinear observers. The mechanism parameters have been obtained from the experimental 5-bar linkage shown in Figure (5.13) and the sensor characteristics from off-the-shelf sensors to reproduce a realistic simulation. A scheme of the mechanism is shown in fig. 5.14 where the points A and E are fixed points. The mechanism has been modeled using mixed coordinates (García de Jalón and Bayo, 1994) with the vector of dependent Cartesian coordinates presented in eq. (5.71).

$$\mathbf{q}^T = [x_B\ y_B\ x_C\ y_C\ x_D\ y_D\ \phi_1\ \phi_2] \tag{5.71}$$

As a first step, the motion of the real mechanism has been simulated but the magnitudes that correspond to sensor data are passed to the observers with their respective noises and sample rates. After that, some known errors (lengths, mass, inertia measuring errors for example) have to be considered for the system dynamics model of the filters, in order to allow the simulated real mechanism and the model of the filter to have similar but different behaviors. Employing a simulated real mechanism allows a comparison of all the states, including those

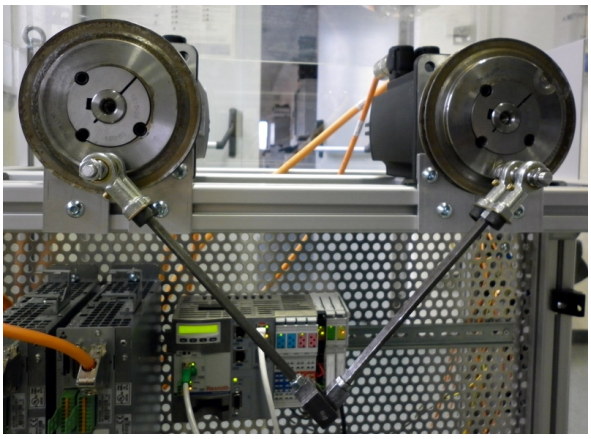

Figure 5.13: Photo of the 5-bar linkage

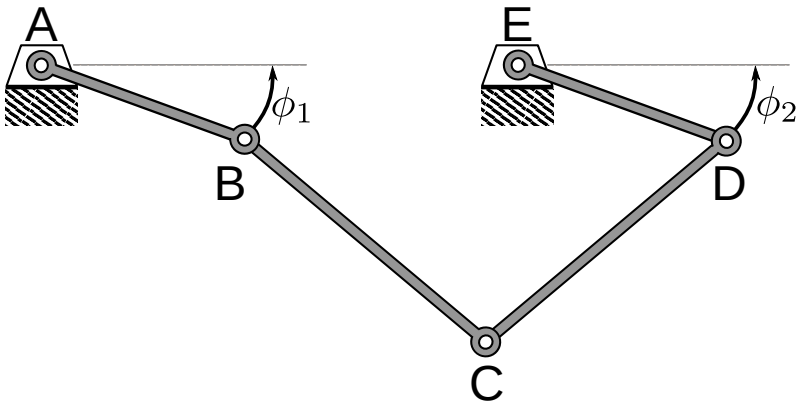

Figure 5.14: Scheme of the 5–bar linkage

that cannot be measured experimentally. As a consequence, all the variables of the model of the filter (i.e. the virtual sensors and the variables estimated through the state observer) can be compared to their exact magnitudes. In this way, comparisons of the performances of the filters are more genuine and comprehensive.

The motion selected to exemplify clearly the behavior of the filters should be as simple as possible. As a consequence, both cranks start from an initial angle and then turn freely (i.e. without any inputs nor external forces) during the rest of the simulation. Figures 5.18 to 5.20 show this motion for the real mechanism, the system dynamics model used in the filters and the observers. The color code for the figures is shown in table 5.4. The behavior discrepancies between the real mechanism and the system dynamics model without observer are clearly demonstrated. It is worth pointing out that all the observers follow the motion of the real mechanism with accuracy.

5.5.2 Comparisons of observer performances

As previously mentioned, the motion of the real mechanism is completely known as it is simulated. Therefore, in order to compare the observer performances, it is more pertinent to represent the errors of the filters with respect to the real mechanism instead of looking at the motion of the observers. The sensors for all the filters are the two crank encoders. Figures 5.18 to 5.20 show the errors in positions, velocities and accelerations of the left crank

Color	Filter	MB formu.	Integrator	Note
gray	-	-	-	encoder noise
green	no	matrix–R	TR	system dynamics model
black	EKF	matrix–R	TR	-
red	UKF	matrix–R	TR	-
brown	SSUKF	matrix–R	TR	-
blue	SSUKF	matrix–R	RK2	-
violet	SSUKF	penalty	RK2	-

Table 5.4: Color code for the figures of the 5–bar linkage

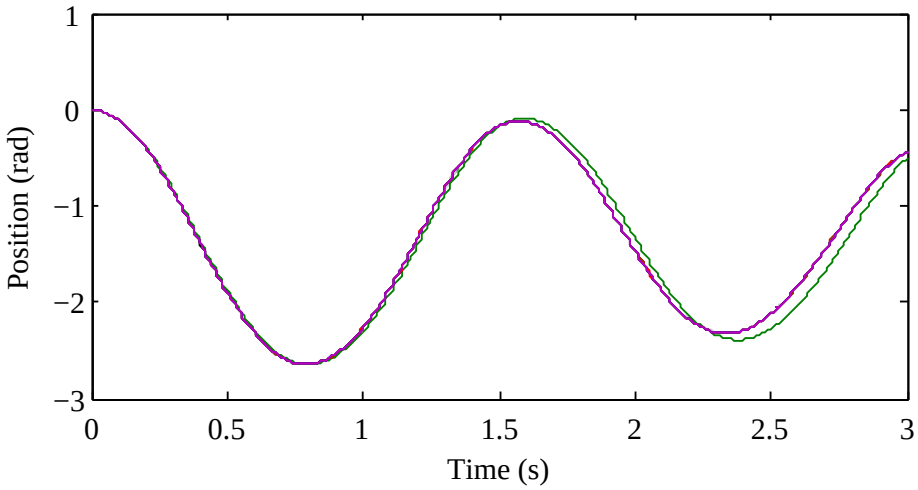

Figure 5.15: Angle of the left crank

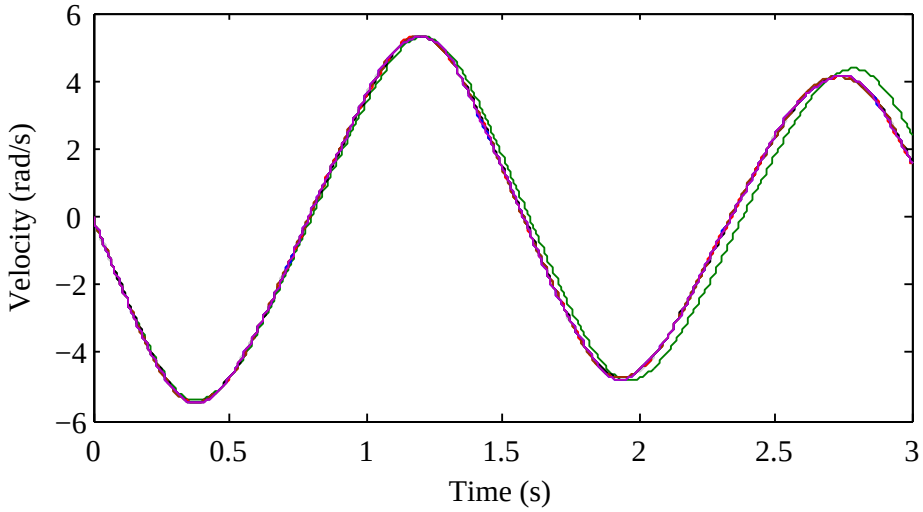

Figure 5.16: Angular velocity of the left crank

for an integration time step Δt_i of 2 ms and an update time step of the sensors Δt_s of 2 ms.

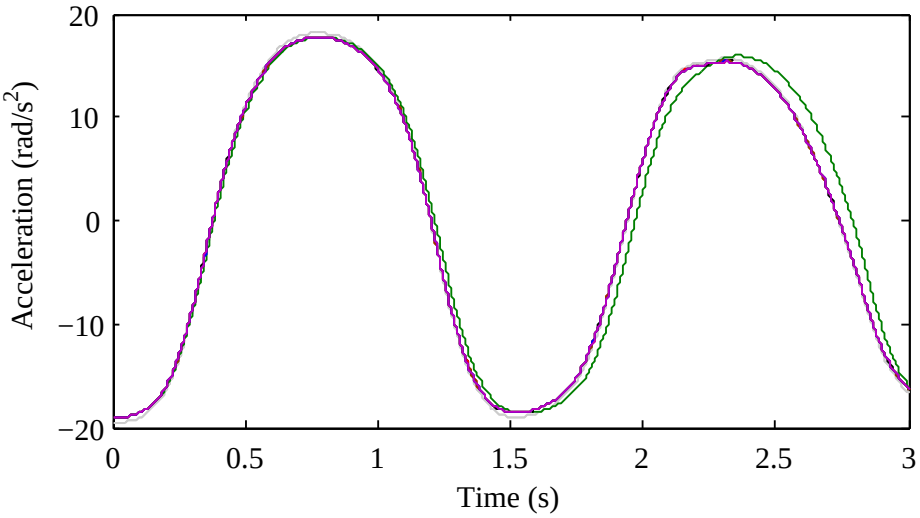

Figure 5.17: Angular acceleration of the left crank

This means that data from each sensor is available at each integration time step. In a similar way, figs. 5.21 to 5.23 show the same errors but for an update time step of the sensors Δt_s of 6 ms. The CPU time for all the mentioned filters with respect to the filter with the lower computational cost are presented in table 5.5. The root mean squared errors (RMSEs), where the error is the difference between the predicted measurements and the actual measurements, are also presented in table 5.5. It is worth pointing out that, when the update time step of the sensors is equal to the integration time step, the most accurate filter is the EKF, with an RMSE slightly superior to the noise standard deviation (10^{-3}). The rest of filters present also very similar results, while correcting only the independent acceleration vector. However, when the update time step of the sensors is greater than the integration time step, the RMSE of the EKF increases dramatically compared to the RMSE of the other filters. When the update time step of the sensors increases, the corrections of the filter are less frequent and less information on the behavior of the real mechanism is available. Therefore, the model of the filter has more difficulties to follow accurately the motion of the real mechanism and the RMSE increases. The bad behavior of the EKF in multi–rate situations is in part due to the assumptions made in section 5.4.1. Indeed, in the theory of the EKF in continuous form, it is assumed that information of the sensors is available at any instant. As it is not the case in multi–rate situations, a zero–order hold (ZOH) is applied to $\mathbf{y}(t)$ and the calculation of the Kalman corrections in eq. (5.27) is not correct at each integration time step. Subsequently, high frequency noise appears due to the incorrect corrections, as shown in fig. 5.23. Then, it can be seen in table 5.5 that, in multi–rate situations, all the SPKFs have a slightly lower computational cost as less calculations of the measurement–update equations have to be performed, and the EKF has a slightly greater computational cost due to convergence difficulties.

In light of the results, the continuous form of the EKF is not suitable for multi–rate situations. Filters in discrete–form like the one used for the SPKFs yield much better accuracy in these situations. Consequently, the EKF in discrete–form should be considered to handle multi–rate situations with this type of filter. Then, the SPKFs have proved to have a slightly lower accuracy than the EKF (except in multi–rate situations). However, the EKF has

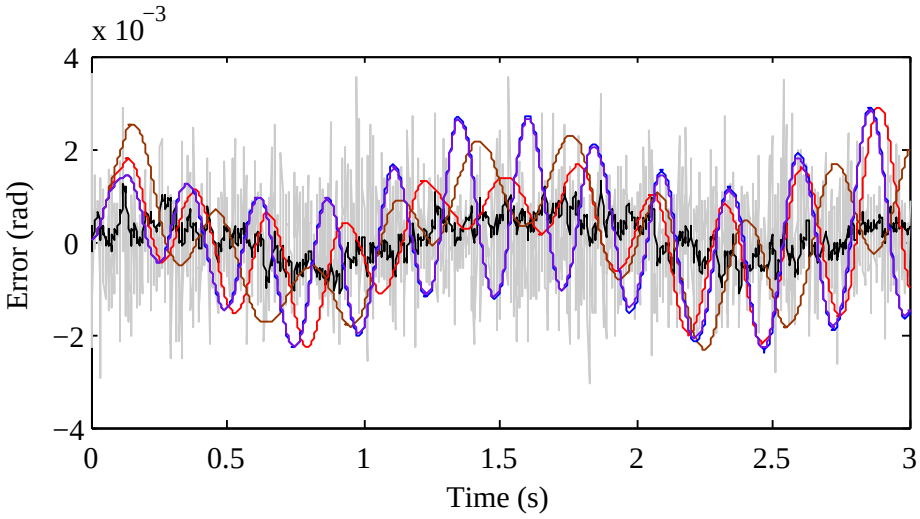

Figure 5.18: Errors of the filters for the angle of the left crank

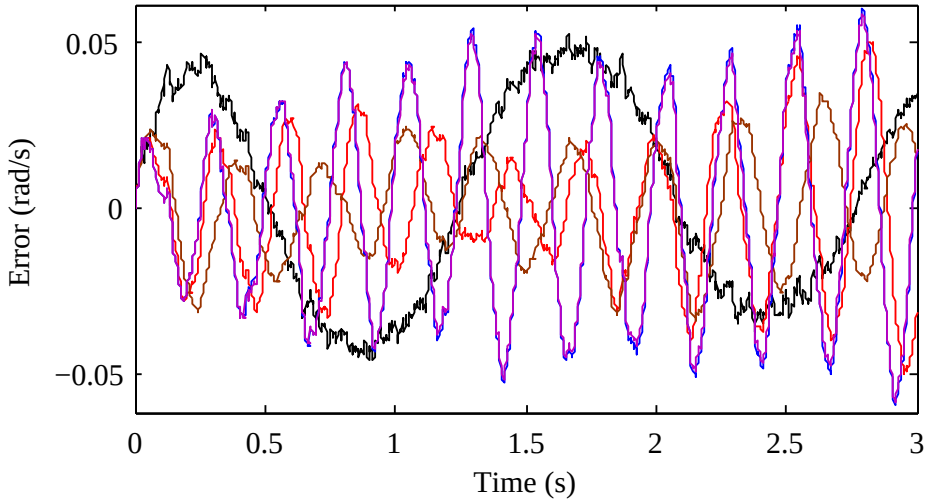

Figure 5.19: Errors of the filters for the angular velocity of the left crank

Kalman corrections in accelerations and velocities, while the SPKFs only have corrections in accelerations. Therefore, it can be said that the SPKFs would be much more precise than the EKF if velocities and accelerations were estimated, at the expense of an additional computational cost.

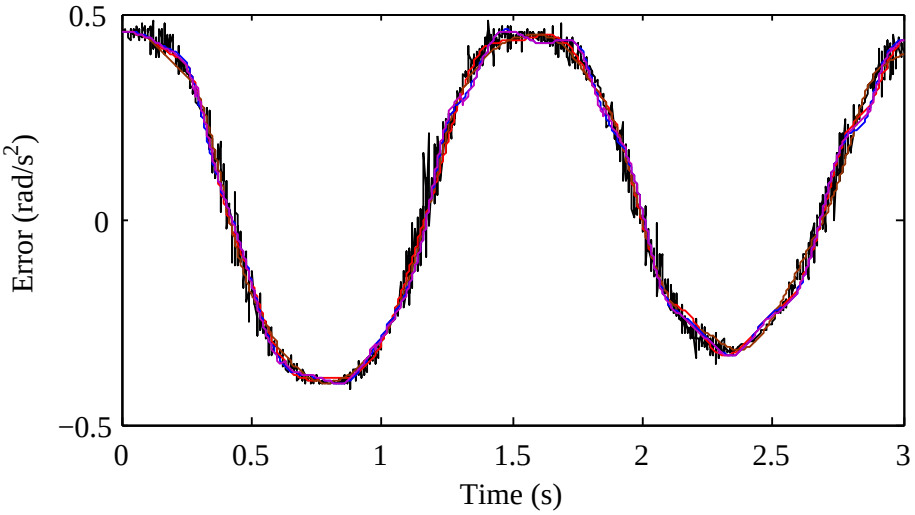

Figure 5.20: Errors of the filters for the angular acceleration of the left crank

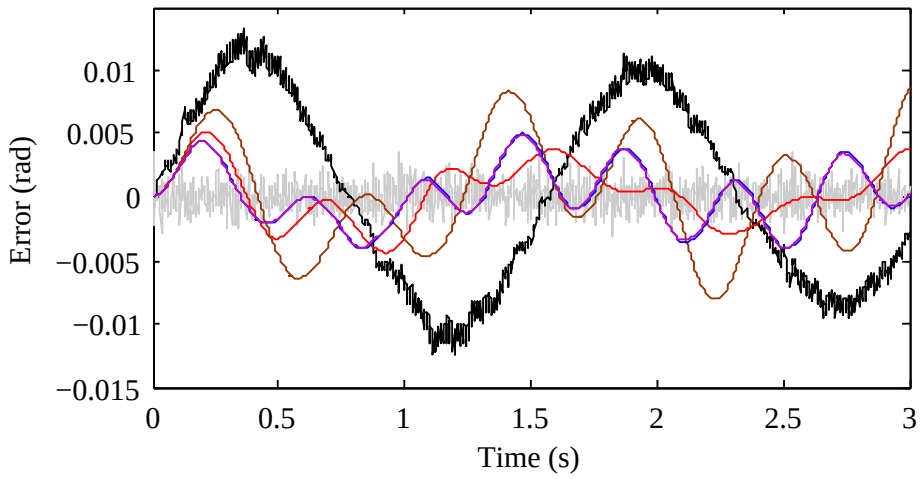

Figure 5.21: Errors of the filters for the angle of the left crank

			$\Delta t_i = 2ms$ and $\Delta t_s = 2ms$		$\Delta t_i = 2ms$ and $\Delta t_s = 6ms$	
Filter	MB formu.	Integ.	CPU time	RMSE (10^{-3})	CPU time	RMSE (10^{-3})
SSUKF	penalty	RK2	107%	2.13	100%	3.14
EKF	matrix–R	TR	111%	1.36	114%	9.22
SSUKF	matrix–R	RK2	128%	2.16	121%	3.17
SSUKF	matrix–R	TR	196%	2.18	188%	5.35
UKF	matrix–R	TR	232%	1.98	225%	3.1

Table 5.5: CPU times and RMSE

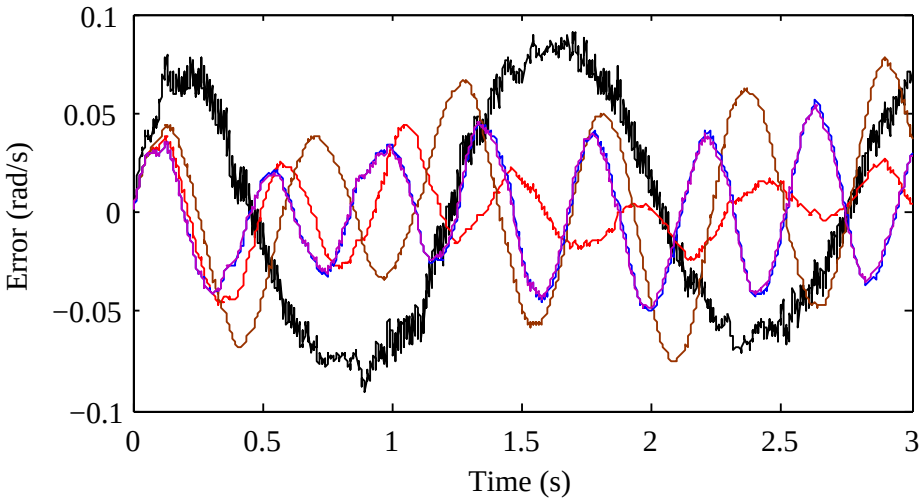

Figure 5.22: Errors of the filters for the angular velocity of the left crank

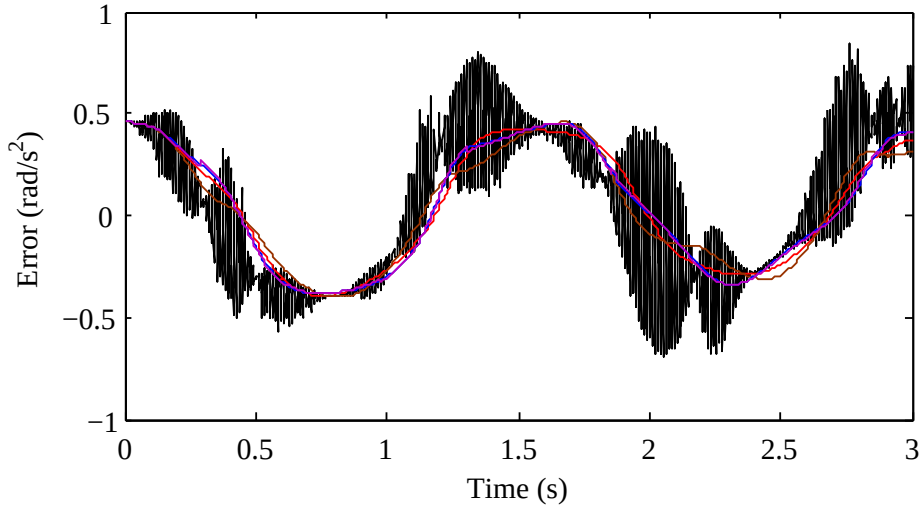

Figure 5.23: Errors of the filters for the angular acceleration of the left crank

Chapter 6

Conclusion

6.1 Conclusions

This thesis has focused on the research on real-time vehicle MB models and their application to state observers. Its main aim has been to extract useful guidelines to develop such models and to investigate theoretically and practically their use in state observers.

First, the validity of the predictions of the simulations is a crucial point to be examined. For this purpose, part of the complete methodology developed to validate the vehicle MB model of the NADS has been applied. To this end, an XBW vehicle prototype has been built and automated in order to repeat reference maneuvers and generate experimental benchmark data. During the development of this prototype, strong emphasis has been made on the driver's force feedback system of the SBW system. A general approach for the accurate modeling of amplifier-motor-gearbox assemblies has been developed and validated, using the low cost driver's torque feedback system. This system consists of a two stage planetary gearbox, a coreless PMDC motor and a four quadrant linear amplifier. This general approach that takes into account backlash, flexibility, friction for stiction and sliding, identification procedures, is applicable to a wide range of amplifier-motor-gearbox assemblies.

After having the XBW vehicle prepared, two low speed maneuvers involving the longitudinal and lateral vehicle dynamics have been repeated several times in a test area at the campus of the engineering school. Experimental benchmark data has been extracted from both maneuvers for vehicle model validation purposes.

After that, the second part of this thesis has been devoted to the development of a mathematical model of the aforementioned XBW vehicle prototype. A real–time MB model with 14 DOFs has been setup using a self-developed MB `FORTRAN` library as well as a simulation environment programmed in `C++` that includes a close graphical environment, a true road profile and collision detection. The true road profile has been obtained from a topographical survey of the test track. Subsystems like brakes or tires have also been modeled.

In order to check the validity of the model, the experimental benchmark data gathered from the sensors of the vehicle have been input in the model to repeat both test maneuvers in the simulation environment. Selected simulation variables have then been compared to their experimental counterparts provided with the appropriate confidence interval that characterizes the field testing process errors. The results of the comparisons have then been interpreted to extract useful guidelines to build real–time vehicle MB models.

Finally, the use of real–time MB models with state observers has been investigated. The first observer considered in this thesis has been the EKF in its continuous form. The use of two MB formulations (the matrix-R formulation and the penalty formulation) has been investigated using a 4–bar linkage. The matrix–R method, which showed better behavior and efficiency than the penalty formulation, has then been applied to a complex MB model: the model of a Volkswagen Passat. Although the filter has proved to be accurate for this model, real–time has not been achieved. Consequently, new theoretical developments and practical implementations using another type of nonlinear state observers, the SPKFs, have been carried out using a 5–bar linkage. From the application of these observers, it has been shown that the use of implicit integrators is not worth compared to their explicit counterparts thus leading to a lower computational cost for all the mentioned observers. The SPKFs have demonstrated better accuracy but higher computational costs than the EKF in its continuous form. However, they present several advantages over the latter: easy implementation, parallel computing structure that helps to reach real–time and use of any MB formulation that also

helps to reduce the computational cost. In light of the results, the choice of the most suitable set of *filter, MB formulation and integrator* depends on the application requirements and is a trade–off between estimation accuracy and computational efficiency.

6.2 Future research

Regarding future work, several lines corresponding to the different parts of this thesis are still open and would require new researches. First, a controller employing a torque observer for the driver's torque feedback of the SBW system could be designed by means of its current model, to compensate the gearbox drawbacks and to provide the best possible feeling to the driver through the steering wheel. Then, the vehicle MB model and its subsystems could be improved by carrying out new test maneuvers, especially at high speeds. It is expected that, in this case, bushings, chassis flexibility, accurate tire curves, etc, should be taken into account. The use of different MB formulations allowing for lower computational costs and compatible with the considered state observers should be the way to reach real–time in the state estimation of complex systems. The theoretical research on the use of MB models with nonlinear state observers has just been opened and it could be extended to a wider range of filters as for example the EKF in discrete form. Finally, once state observers using complex MB models reach real–time on conventional PCs (while simulating the real mechanism), these techniques could be implemented on the XBW vehicle prototype using the MB model running on the on–board PC and the DAS to pass the information of the sensors to the observer.

Appendix A

Data acquisition system

MICROSTAR LABORATORIES™

2265 116th Avenue N.E., Bellevue, WA 98004
Sales & Customer Support: (425) 453-2345
Finance & Administration: (425) 453-9489
Fax: (425) 453-3199
World Wide Web: http://www.mstarlabs.com/

Technical Note TN-212 **Version 1.1**

Technical Product Information for the DAP 4200a ™

The DAP 4200a/526 model

- has an Intel i486 DX4 processor onboard
- provides 14-bit A/D converter resolution
- works with the 5V PCI bus for Pentium/Pentium II platforms
- comes with 16M of DRAM onboard memory
- transfers data to PC at high rates — up to 3.2M samples per second
- offers low latency—0.2 ms task time quantum—for fast response
- offers sampling period resolution to 100 ns
- samples or updates the digital section at up to 1.66 million values per second
- samples analog inputs at up to 769K samples per second at 12-bit accuracy
- updates analog outputs at up to 833K samples per second each
- provides onboard emulation of DSP routines
- provides the same input and output voltage ranges as the DAP 3200a
- allows fast real-time processing
- is compatible with other a-Series boards
- has expandable analog and digital inputs/outputs
- complies with the European EMC Directive and is CE marked.

There is only one DAP 4200a model: the DAP 4200a/526. This technical note describes features and architecture of the DAP 4200a.

The DAP 4200a provides 14-bit A/D resolution for its 16 onboard analog inputs, and 12-bit D/A resolution for its 2 onboard analog outputs. The onboard analog input channels sample at an overall 769k samples per second at 12-bit accuracy, and sample at 588k samples per second at 14-bit accuracy. The 16 onboard digital input channels sample at an overall rate of 1.66M words per second.

The DAP 4200a has a PCI host interface, and is capable of high speed data transfers to the host PC. The DAP 4200a requires a 5V 32-bit PCI slot. Using bus mastering DMA transfers, the DAP 4200a can transfer data to the host PC at 3.2M samples per second. This transfer rate is more than three times faster than that of the DAP 3200a.

The onboard multitasking operating system, DAPL™, runs on the DAP 4200a, and ensures that hardware-level differences are transparent. DAPL 2000 is a complete software environment for real-time data acquisition. Tasks that perform averaging, triggering, PID control, fast Fourier transforms, filtering, arithmetic operations and many other functions are pre-coded in DAPL. These tasks are chained together to form a complete data acquisition application. To aid application development, DAPL has many system diagnostics in addition to automatic memory and system checks that are done at initialization.

Much of the DAP 4200a design is similar to that of the DAP 3200a/415. The DAP 4200a uses the same type of analog and digital connectors as the DAP 3200a, so the DAP 4200a is compatible with all the same cabling and external boards for termination and expansion. Accessories used with any a-Series Data Acquisition Processor™ can be used with the DAP 4200a.

The DAP 4200a provides the same level of processing performance as the DAP 3200a/415, but offers more memory. The DAP 4200a has an onboard Intel 486 DX4 processor running at 96MHz, and has 16Mbyte of memory. The PCI bus allows the DAP 4200a to transfer data to the PC at high rates – up to 3.2M samples per second.

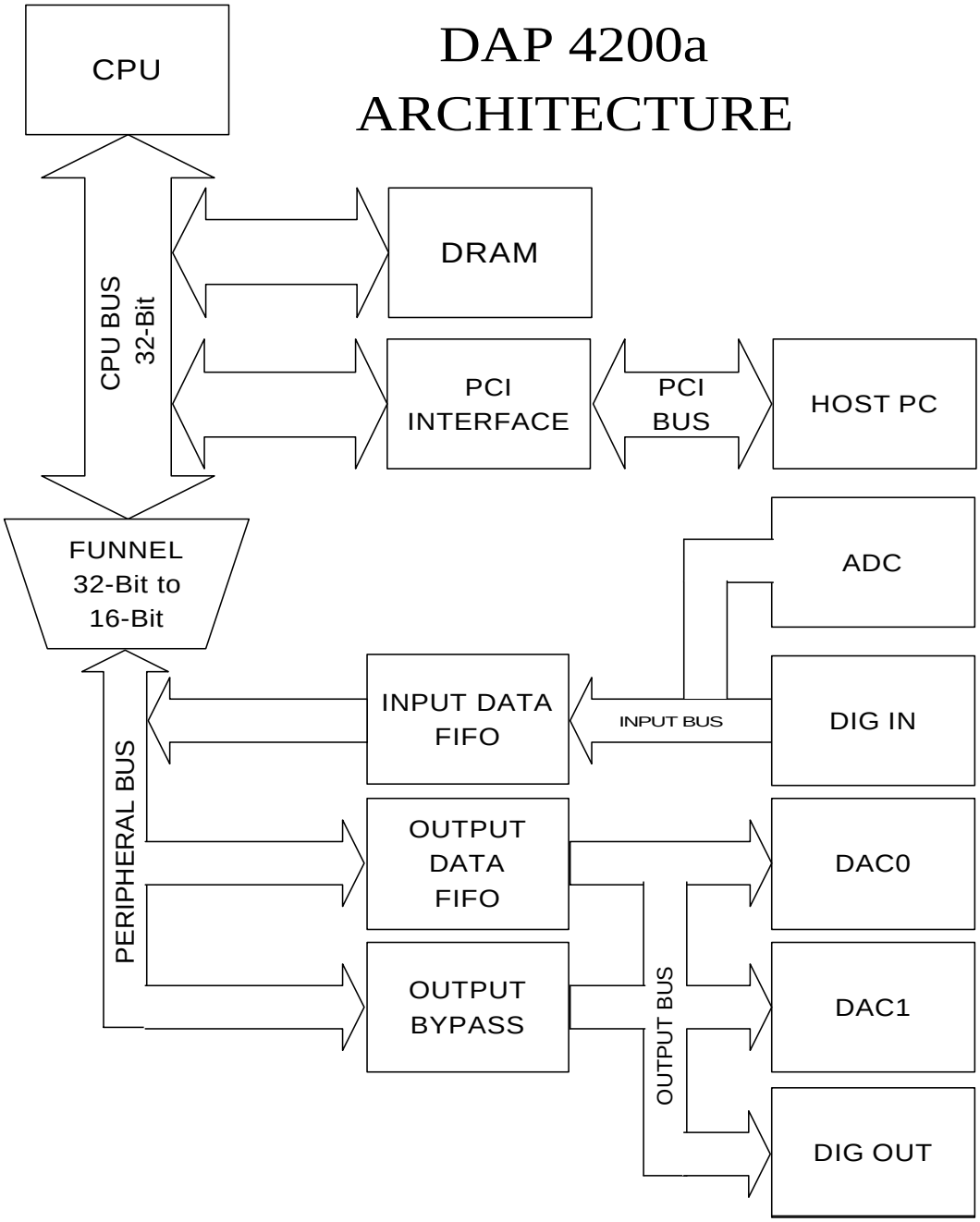

Figure 1: DAP 4200a Data Acquisition Hardware

Figure 1 displays the hardware architecture of the DAP 4200a. The figure shows that the PCI host interface is connected directly to the processor bus. This intimate connection allows fast and efficient data transfers

to the host PC. The figure also shows the two FIFOs on the DAP 4200 that handle data acquisition. The data FIFOs are unidirectional, buffering data for input and output.

Data are acquired or updated via dedicated hardware clocking circuitry at a rate of up to 1.66 million samples per second. Acquisition is clocked at a sampling rate or output rate controlled in software, and the rate is accurately maintained by onboard crystal-controlled timers. The sample period is specified with a resolution of 100 nanoseconds and the sample rate is accurate to 50 parts per million.

In addition to onboard timing, the DAP 4200 also has provisions for external triggering and clocking for the input and output sections. The DAP 4200a has an improved input sampling pipeline. Data are sampled and read by the processor in the same input clock cycle.

The 16-bit digital input port and the analog-to-digital converter are attached to the Input Data FIFO, one of the unidirectional data FIFOs. The maximum aggregate sample rate is 1.66M samples per second. Digital input alone can run at up to 1.66M samples per second. The maximum analog input sample rate is 769K samples per second.

The digital output port and the two analog outputs are attached to the Output Data FIFO. The maximum aggregate update rate is 1.66M updates per second. Digital output alone, like digital input, can run at up to 1.66M updates per second. Each of the analog outputs can be updated at 833K updates per second.

The Bypass section shown in Figure 1 allows the processor to asynchronously update either the digital or analog outputs. This means that periodic timing is not guaranteed, rather the processor will attempt to update the outputs whenever a time slice for this task becomes available. This is useful in control application where a digital output, for example, needs to open or close a valve at irregular intervals.

In addition to the processor and data transfer hardware, some important hardware specifications of the DAP 4200a are provided in Table 1 below.

Table 1: DAP 4200a Typical Hardware Specifications
Preliminary

Specification	**DAP 4200a/526**
Dimensions	12.28" x 4.2"
Weight	11.5 oz
CPU type	Intel 80486DX4
CPU clock speed	96 MHz
CPU DRAM	16 Mbytes
Bus support	PCI
PC interface hardware	PCI interface
PC transfer mode	Bus Mastering
Maximum transfer rate	3.2 M samples/sec
Power requirements	+5V, 3.0 Amps
Operating temperature	0-50° C
Accuracy of crystal clocks	50 parts per million
Type of A⇒D converter	Successive Approximation
Model of A⇒D converter	Linear Tech LTC1419
Max. analog sampling rate[1] Gain = 1 Gain = 10 Gain = 100 Gain = 500	 769 K samples/sec 125 K samples/sec 25 K samples/sec 2 K samples/sec
Number of analog channels	16
Expandable to	512
Input voltage ranges	0 to 5 V; -2.5 to 2.5 V; -5 to 5 V; -10 to 10 V
Resolution -5 to 5 V range	14 bits 0.61 mV
Accuracy -5 to 5 V range	±1 LSB ±0.61 mV
Non-linearity	0.012%
Input bias current	12 nA
Analog input impedance	>> 10 MΩ
Common mode rejection	90 dB
Type of D⇒A converter	Voltage Output
Model of D⇒A converter	Analog Devices AD767
Maximum analog update rate[2]	833K updates/sec
Max. input voltage (fault-protected multiplexers)	±25V

Table 1: DAP 4200a Typical Hardware Specifications, continued

[1] The sampling rates are for 12-bit accuracy. The gain 1 sampling rate for 14-bit accuracy is 588k samples/sec.

[2] The DAP 4200a can update each of its two standard analog outputs independently at 833K updates per second. When analog output expansion is used, the update rate for expanded channels is determined by the maximum update rate of the digital port.

Expanded Analog Output Rate = 1.6M / (4 * Number of Channels)

Number of output channels	2
Expandable to	66
Output ranges	0 to 5 V -2.5 to 2.5 V -5 to 5 V -10 to 10 V
Resolution -5 to 5 V range	12 bits 2.4 mV
Accuracy -5 to 5 V range	±1 LSB, ±2.4 mV
Analog output signal to noise ratio	0.0002% of full scale
Output impedance	0.05 Ω
Current source maximum	±1 mA
Digital output logic	FCT TTL
Digital input logic	FCT TTL
Maximum digital update rate[3]	2M words/sec
Number of input bits Number of output bits	16 16
Expandable to	128 input bits and 1024 output bits
Digital input Min. logical high Max. logical low Max. current sink Max. current source	 2 V 0.8 V 5 µA 5 µA
Digital output Min. logical high Max. logical low Max. current sink Max. current source	 2.6 V 0.5 V 12 mA 15 mA
External clock input min. pulse width	25 ns
External trig. input min. pulse width	60 ns
Trigger modes	GATED ONE-SHOT

[3] This figure is the maximum throughput of simultaneous digital input and output. Either digital input or digital output operating alone can maintain a throughput of 1.6 M words/sec.

Custom command for the TBW system

```
// MODULE  THLECTRL3M
// Copyright (c) 02/2010, Roland Pastorino.
//
// Control program based on the motor RPM's for the stepper motor of the throttle pedal
//
// THLECTRL3 (p1, p2, min_interval, sample_time, velocity_threshold, dac_num1, dac_num2)
//    - Read data from pipe 'p1' (= velocity pipe)
//    - Read data from pipe 'p2' (= velocity reference pipe)
//    - min_interval is the minimum time interval between two motor steps in ms (= velocity of the
    stepper motor)
//    - tiempo de muestreo de la senal de referencia en ms
//       - velocity_threshold define la tolerancia en la velocidad para la generacion de pulsos
    del motor paso a paso
//       - output data to DAC 'dac_num1' (= step signal)
//       - output data to DAC 'dac_num2' (= direction signal)
//
// Module name THLECTRL3M must be distinct from the DAPL command name
// assigned below.

#define  COMMAND  "THLECTRL3"
#define  ENTRY    THLECTRL3_entry

#include "DTDMOD.H"
#include "DTD.H"

int __stdcall     ENTRY (PIB **plib);

extern "C" __declspec(dllexport) int __stdcall
   ModuleInstall(void *hModule)
{   return (CommandInstall(hModule, COMMAND, ENTRY, NULL)) ; }

// - - - - -  command implementation section  - - - - - - - - - - -

int __stdcall  ENTRY (PIB **plib)
{
  // Storage for parameters
    void **argv;
    int argc;
    PIPE  * in_pipe1;
    PIPE  * in_pipe2;
        short int min_interval;
        short int sample_time;
        short int velocity_threshold;
        short int dac_num1;
        short int dac_num2;
  // Storage for processing
    GENERIC_SCALAR velocity;
        GENERIC_SCALAR velocity_ref;
        unsigned long int time;
        short int diff;
        short int flag_pulse;
        unsigned long int elaps_time_pulse2;
        unsigned long int elaps_time_pulse1;
  // Access parameters
    argv = param_process (plib, &argc, 7, 7, T_PIPE_W, T_PIPE_W, T_CONST_W, T_CONST_W, T_CONST_W,
        T_CONST_W, T_CONST_W);
    in_pipe1 = (PIPE *) argv[1];
    in_pipe2 = (PIPE *) argv[2];
        min_interval = *(short int const*) argv[3];
        sample_time = *(short int const*) argv[4];
        velocity_threshold = *(short int const*) argv[5];
        dac_num1 = *(short int const*) argv[6];
        dac_num2 = *(short int const*) argv[7];
  // Perform initializations
    pipe_open (in_pipe1, P_READ);
    pipe_open (in_pipe2, P_READ);
        time = sys_get_time();  //Get time in ms
        pipe_value_get(in_pipe2,&velocity_ref);
        pipe_value_get(in_pipe1,&velocity);
        flag_pulse = 0;
  // Begin continuous processing
    while (1)
    {
                //Removes all data except one of the input pipe if the input contains more than 1
                    value
                if (pipe_num_complete(in_pipe1,1) != 0)
                {
                        pipe_rem(in_pipe1,(pipe_num_complete(in_pipe1,1)-1));
                }
                //Regenerate the logged signal based on its sample time
                //Update the input pipe each sample time
                if (short int((sys_get_time() - time)) >= sample_time)
                {
                        pipe_value_get(in_pipe2,&velocity_ref);
                        time = sys_get_time();
```

```
                }
                //Calculates the error
                pipe_value_get(in_pipe1,&velocity);
                diff = (velocity_ref._i16 - velocity._i16);

                //Generate the step signal and the direction signal
                //Each time "velocity != velocity_ref" a step is send to the stepper motor
                if ( ((diff >= velocity_threshold) || (diff <= -velocity_threshold)) && (flag_pulse
                     == 0))
                {
                        //Generate the direction signal
                        if (diff <= 0)
                        {
                                dac_out(dac_num2,-32767);
                        }
                        else
                        {
                                dac_out(dac_num2,32767);
                        }
                        dac_out(dac_num1,32767);//Step signal
                        flag_pulse = 2;
                        elaps_time_pulse2 = sys_get_time();//Get time in ms
                }
                if (flag_pulse == 2)
                {
                        //Wait until "min_interval" ms has passed to set the step signal to zero
                        if ((sys_get_time()-elaps_time_pulse2) < (min_interval))
                        {task_switch();}
                        else
                        {
                                dac_out(dac_num1,0);//Step signal
                                flag_pulse = 1;
                                elaps_time_pulse1 = sys_get_time();//Get time in ms
                        }
                }
                //Wait until "min_interval" ms has passed to set the step signal to one
                if (flag_pulse == 1)
                {
                        if((sys_get_time()-elaps_time_pulse1) < (min_interval))
                        {task_switch();}
                        else
                        {
                                flag_pulse = 0;
                        }
                }
    }
    return 0;
}
```

Custom command for the BBW system

```
//  MODULE BRKPCTRL3M
//  Copyright (c) 06/2010, Roland Pastorino
//
//  Control program (ASYNCHRONOUS) for the stepper motor of the brake outfitted with the CN0173
    step pulse generator
//
//  BRKPCTRL3 (p1, p2, sample_time, Pressure_Threshold, Pressure_Min, offset, dac_num1, dac_num2)
//              - read data from pipe 'p1' (= brake pressure)
//      - read data from pipe 'p2' (= brake pressure reference)
//      - tiempo de muestreo de la senal de referencia en ms
//              - below "Pressure_Threshold" (digital pressure), the reference pressure is achieved
//              - below "Pressure_Min" (digital pressure), the step generation stops
//              - the motor actuates "offset" samples in advance = delay correction
//              - output data to DAC 'dac_num1' (= step signal)
//              - output data to DAC 'dac_num2' (= direction signal)
//
// Module name BRKPCTRL3M must be distinct from the DAPL command name
// assigned below.
//
// Remarks:     Stepper motor : Lead = 0.157 in/rev = 0.39878 cm/rev = 0.0011077 cm/deg
//              Step angle = 0.72deg/0.36deg/0.288deg/0.18deg/0.144deg/0.09deg/0.072deg/0.036deg
    /0.0288deg/0.018deg/0.0144deg/0.009deg/0.0072deg/0.00576deg/0.0036deg/0.00288deg
//              Step lead = 0.00079756 cm/0.00039878 cm ...

#define  COMMAND  "BRKPCTRL3"
#define  ENTRY    BRKPCTRL3_entry

#include "DTDMOD.H"
#include "DTD.H"

int __stdcall   ENTRY (PIB **plib);

extern "C" __declspec(dllexport) int __stdcall
   ModuleInstall(void *hModule)
{   return (CommandInstall(hModule, COMMAND, ENTRY, NULL)) ; }

// - - - - -  command implementation section  - - - - - - - - - - -
int __stdcall  ENTRY (PIB **plib)
{
  // Storage for parameters
    void **argv;
    int argc;
        PIPE * in_pipe1;
        PIPE * in_pipe2;
        short int sample_time;
        short int Pressure_Threshold;
        short int Pressure_Min;
        short int offset;
        short int dac_num1;
        short int dac_num2;
  //Storage for processing
        GENERIC_SCALAR value_pressure;
        GENERIC_SCALAR reference_pressure;
        short int diff_sample_number = 0;
        long int sample_number_prg = 0;
        long int sample_number_real = 0;
        unsigned long int time_elapsed;
        unsigned long int time_init;
        short int diff;
  // Access parameter
    argv = param_process (plib, &argc, 8, 8, T_PIPE_W, T_PIPE_W, T_CONST_W, T_CONST_W, T_CONST_W,
        T_CONST_W, T_CONST_W, T_CONST_W);
        in_pipe1 = (PIPE *) argv[1];
        in_pipe2 = (PIPE *) argv[2];
        sample_time =  *(short int const*) argv[3];
        Pressure_Threshold =  *(short int const*) argv[4];
        Pressure_Min =  *(short int const*) argv[5];
        offset =  *(short int const*) argv[6];
        dac_num1 = *(short int const*) argv[7];
        dac_num2 = *(short int const*) argv[8];
  // Perform initializations
        pipe_open (in_pipe1, P_READ);
        pipe_open (in_pipe2, P_READ);
        pipe_value_get(in_pipe2,&reference_pressure);
        pipe_value_get(in_pipe1,&value_pressure);
        time_init = sys_get_time();      //Get time in ms
        dac_out(dac_num1,32000); //Set the DAC(dac_num1) to 5V to disable the step pulse generator
            (0V enables the step generation)
  // Begin continous processing
    while(1)
        {
                //Regenerate the logged signal based on its sample time
                //If the time elapsed is higher than the sample time, the correct number of samples
                      are deleted and the corresponding sample is downloaded
                        time_elapsed = (sys_get_time() - time_init);
```

```
                sample_number_real = time_elapsed / sample_time;
                diff_sample_number = short int(sample_number_real + offset -
                    sample_number_prg);
                if (diff_sample_number == 1)
                {
                        pipe_value_get(in_pipe2,&reference_pressure);
                        sample_number_prg++;
                }
                else if (diff_sample_number >= 2)
                {
                        pipe_rem(in_pipe2,(diff_sample_number-1));
                        sample_number_prg = sample_number_prg + (diff_sample_number-1);
                        pipe_value_get(in_pipe2,&reference_pressure);
                        sample_number_prg++;
                }
        //Removes old data of the input pipe if the input contains more than 1 value
        //Gets a value from in_pipe1 if there is available data
        //Avoids that 'pipe_value_get' goes to sleep until the pipe contains data
                if (pipe_num_complete(in_pipe1,1) != 0)//Does the pipe contain any data ?
                {
                        pipe_rem(in_pipe1,(pipe_num_complete(in_pipe1,5)-1));
                        pipe_value_get(in_pipe1,&value_pressure);
                }
        //Error between the reference and the pressure
                diff = (reference_pressure._i16 - value_pressure._i16);
        //Enables-disables the step pulse generator
                if ((reference_pressure._i16<Pressure_Min)&(value_pressure._i16<
                    Pressure_Min))
                {dac_out(dac_num1,32000);//Stops pulse generation
                        task_switch();
                }
                else
                {
                        if (((diff >= Pressure_Threshold) || (diff <= -Pressure_Threshold))
                            )
                        {
                                dac_out(dac_num1,0);//Starts pulse generation
                        }
                        else
                        {
                                dac_out(dac_num1,32000);//Stops pulse generation
                                task_switch();
                        }
                }
        //Generate the direction signal
                if (diff <= 0)
                {
                        dac_out(dac_num2,32000);//Move backward
                }
                else
                {
                        dac_out(dac_num2,0);//Move forward
                }
        }
        return 0;
}
```

Custom command for the RWM of the SBW system

```
//  MODULE CREMBOUNDEDM
//  Copyright (c) 2008, Roland Pastorino
//  Version 1.0
//
//  CREMBOUNDEDM (p1,p2,ThetaMax,Kp,Ki,Kd,DACnum,clamp_low,clamp_high)
//              - read data from pipe 'p1' (= ThetaENC1 = setpoint = encoder volante)
//              - read data from pipe 'p2' (= ThetaENC2 = feedback = encoder cremallera)
//      - returns TorqueValue using saturated PID (based on "SPID2" example) if ThetaENC2<ThetaMax
//              - Use ThetaMax as reference if ThetaENC2>ThetaMax to maintain ThetaENC2 in his
    actuation zone
//              - output data (=Steering Torque) to DAC specified by DACnum
//
//      Nota: -25600<Kp<25600, -16000<Ki<16000, -25600<Kd<25600
//                  Divide by 100 to have the real coeficients (=scaling)
//  Warning : be careful to use the sampling rate to calculate the right PID coeficients (see paper
     "Tuning PID Control by Simulation")
//
// Module name CREMBOUNDEDM must be distinct from the DAPL command name
// assigned below.

#define  COMMAND  "CREMBOUNDED"
#define  ENTRY    CREMBOUNDED_entry

#include "DTDMOD.H"
#include "DTD.H"


int __stdcall   ENTRY (PIB **plib);

extern "C" __declspec(dllexport) int __stdcall
   ModuleInstall(void *hModule)
{   return (CommandInstall(hModule, COMMAND, ENTRY, NULL)) ; }

// - - - - -  command implementation section  - - - - - - - - - - -

#define INITIAL_STATE 0 //Value used to initialize PID computations
#define SETPOINT 0 //Error=0
static PID *PID_block;

int __stdcall  ENTRY (PIB **plib)
{
  // Storage for parameters
    void **argv;
    int argc;
        PIPE * in_pipe1;
        PIPE * in_pipe2;
    long int ThetaMax;
        short int Kp;
        short int Ki;
        short int Kd;
        short int DAC;
        short int clamp_low;
        short int clamp_high;
  //Storage for processing
        GENERIC_SCALAR pipe_value1;
        GENERIC_SCALAR pipe_value2;
        long int angular_error;
        short int angular_error_sat;
        long int reference;
  // Access parameter
    argv = param_process (plib, &argc, 9, 9, T_PIPE_L, T_PIPE_L, T_CONST_W | T_CONST_L, T_CONST_W,
        T_CONST_W, T_CONST_W, T_CONST_W, T_CONST_W, T_CONST_W, T_CONST_W);
        in_pipe1 = (PIPE *) argv[1];
        in_pipe2 = (PIPE *) argv[2];
        ThetaMax = *(long int const*) argv[3];
        Kp = *( short int const*) argv[4];
        Ki = *( short int const*) argv[5];
        Kd = *( short int const*) argv[6];
        DAC = *( short int const*) argv[7];
        clamp_low = *( short int const*) argv[8];
        clamp_high = *( short int const*) argv[9];
  // Perform initializations
        pipe_open (in_pipe1, P_READ);
        pipe_open (in_pipe2, P_READ);
        PID_block = pid_open (INITIAL_STATE);
        static PIDCOEF coeffs =
                {
                SETPOINT, /*setpoint : error=0*/
                Kp,       /*Proportinal1*/
                100,      /*Proportinal2*/
                Ki,       /*Integral1*/
                100,      /*Integral2*/
                Kd,       /*Derivative1*/
                100,      /*Derivative2*/
                clamp_low,
```

```
                clamp_high
        };
        pid_tune(PID_block, &coeffs);
  // Begin continous processing
    while(1)
        {
                pipe_value_get(in_pipe2,&pipe_value2);
                pipe_value_get(in_pipe1,&pipe_value1);
                if (fabs(pipe_value1._i32) <= ThetaMax) /*Is ThetaENC2 inside its range ?*/
                        reference = pipe_value1._i32;
                else
                        {if (pipe_value1._i32 > 0)
                                reference = ThetaMax;
                        else
                                reference = -ThetaMax;
                        }

                //Saturate angular error to avoid overflow in high transient response
                angular_error = reference + pipe_value2._i32;
                if (fabs(angular_error) < 32700)
                        angular_error_sat = angular_error;
                else
                        {if (angular_error > 0)
                                angular_error_sat = 32700;
                        else
                                angular_error_sat = -32700;
                        }

                dac_out(DAC, pid_compute(PID_block,angular_error_sat));
                task_switch();
        }
    return 0;
}
```

Custom command for the SWM of the SBW system

```
//  MODULE VOLRETORROOKIEM
//  Copyright (c) 2008, Roland Pastorino
//  Version 1.1
//
//  VOLRETORROOKIE (p1,p2,LimitTorque,ThetaMax,TorqueScale,p3)
//              - read data from pipe 'p1' (= Rack/PinionTorque)
//      - read data from pipe 'p2' (= Steering wheel angle)
//      - returns LimitTorque if ThetaENC1>ThetaMax or -LimitTorque if ThetaENC1<-ThetaMax
//              - defines the maximum angle ThetaMax
//              - returns scaled sensor torque if |ThetaENC1| <= Theta Max, 0<=TorqueScale<=100% of
     sensor torque
//              - output data to pipe 'p3' (=Steering Wheel Torque)
//
// Module name VOLRETORROOKIEM must be distinct from the DAPL command name
// assigned below.

#define  COMMAND  "VOLRETORROOKIE"
#define  ENTRY    VOLRETORROOKIE_entry

#include "DTDMOD.H"
#include "DTD.H"

int __stdcall   ENTRY (PIB **plib);

extern "C" __declspec(dllexport) int __stdcall
   ModuleInstall(void *hModule)
{   return (CommandInstall(hModule, COMMAND, ENTRY, NULL)) ; }

// - - - - -  command implementation section  - - - - - - - - - -

int __stdcall  ENTRY (PIB **plib)
{
  // Storage for parameters
    void **argv;
    int argc;
        PIPE * in_pipe1;
        PIPE * in_pipe2;
        PIPE * out_pipe;
    short int LimitTorque;
        long int ThetaMax;
        short int TorqueScale;

  //Storage for processing
        long int value_encoder;

  // Access parameter
    argv = param_process (plib, &argc, 6, 6, T_CONST_W, T_PIPE_L, T_CONST_W, T_CONST_L, T_CONST_W,
         T_PIPE_W );
        in_pipe1 = (PIPE *) argv[1];
        in_pipe2 = (PIPE *) argv[2];
        LimitTorque = *(short int const*) argv[3];
        ThetaMax = *(long int const*) argv[4];
        TorqueScale = *(short int const*) argv[5];
        out_pipe = (PIPE *) argv[6];

  // Perform initializations
        pipe_open (in_pipe1, P_READ);
        pipe_open (in_pipe2, P_READ);
        pipe_open (out_pipe, P_WRITE);

  // Begin continous processing
    while(1)
        {
                SWTorque = pipe_get(in_pipe1); /*Sensor Torque*/
                value_encoder1 = pipe_get(in_pipe2); /*Steering Wheel Angle*/
                SWTorque_scaled = (TorqueScale/100)*SWTorque; /*Sensor Torque scaled*/
                if (value_encoder > ThetaMax)
                        pipe_put(out_pipe, LimitTorque);
                else if (value_encoder < - ThetaMax)
                        pipe_put(out_pipe, - LimitTorque);
                else
                        pipe_put(out_pipe, SWTorque_scaled);
        }
    return 0;
}
```

Appendix B

Sensors specifications

Agilent Technologies

Quick Assembly Two and Three Channel Optical Encoders

Technical Data

HEDM-550x/560x
HEDS-550x/554x
HEDS-560x/564x

Features

- **Two Channel Quadrature Output with Optional Index Pulse**
- **Quick and Easy Assembly**
- **No Signal Adjustment Required**
- **External Mounting Ears Available**
- **Low Cost**
- **Resolutions Up to 1024 Counts Per Revolution**
- **Small Size**
- **-40°C to 100°C Operating Temperature**
- **TTL Compatible**
- **Single 5 V Supply**

Description

The HEDS-5500/5540, HEDS-5600/5640, and HEDM-5500/5600 are high performance, low cost, two and three channel optical incremental encoders. These encoders emphasize high reliability, high resolution, and easy assembly.

Each encoder contains a lensed LED source, an integrated circuit with detectors and output circuitry, and a codewheel which rotates between the emitter and detector IC. The outputs of the HEDS-5500/5600 and HEDM-5500/ 5600 are two square waves in quadrature. The HEDS-5540 and 5640 also have a third channel index output in addition to the two channel quadrature. This index output is a 90 electrical degree, high true index pulse which is generated once for each full rotation of the codewheel.

The HEDS series utilizes metal codewheels, while the HEDM series utilizes a film codewheel allowing for resolutions to 1024 CPR. The HEDM series is nont available with a third channel index.

These encoders may be quickly and easily mounted to a motor. For larger diameter motors, the HEDM-5600, and HEDS-5600/5640 feature external mounting ears.

The quadrature signals and the index pulse are accessed through five 0.025 inch square pins located on 0.1 inch centers.

Standard resolutions between 96 and 1024 counts per revolution are presently available. Consult local Agilent sales representatives for other resolutions.

Applications

The HEDS-5500, 5540, 5600, 5640, and the HEDM-5500, 5600 provide motion detection at a low cost, making them ideal for high volume applications. Typical applications include printers, plotters, tape drives, positioning tables, and automatic handlers.

Note: Agilent Technologies encoders are not recommended for use in safety critical applications. Eg. ABS braking systems, power steering, life support systems and critical care medical equipment. Please contact sales representative if more clarification is needed.

ESD WARNING: NORMAL HANDLING PRECAUTIONS SHOULD BE TAKEN TO AVOID STATIC DISCHARGE.

3100 Series Compact High Pressure OEM Pressure Transmitter

- 6 bar to 2200bar pressure ranges
- Less than 25mm long
- Choice of outputs

For OEMs that need consistent high levels of performance, reliability and stability the 3100 Series sputtered thin film units offer unbeatable price performance ratio in a small package size with all stainless steel wetted parts in the volumes required. A wide choice of electrical outputs as well as both electrical and pressure connections means the unit is suitable for most applications without modification. The compact construction of the 3100 series makes it ideal for installation where space is at a premium.

Specifications

Input														
Pressure Range (bar)	**6**	**10**	**16**	**25**	**40**	**60**	**100**	**160**	**250**	**400**	**600**	**1000**	**1600**	**2200**
Max. Over Pressure	3x			2x									1.4x	
Min. Burst Pressure	40x			20x				10x			>4000 bar (test limit)			
Fatigue Life	Designed for more than 100,000,000 cycles													
Performance														
Long Term Drift	0.1% FS/year non cumulative													
Accuracy	±0.25% FS (Temp O/P ± 3%FS)													
Thermal Error	±1% typical/100°C													
Compensated Temperature	-40° to 125°C													
Operable	-40° to 125°C													
Zero Tolerance	±0.5% of span													
Span Tolerance	±0.5% of span													
Mechanical Construction														
Pressure Port	See ordering chart													
Wetted Parts	17-4 PH Stainless Steel/304 Stainless Steel													
Electrical Connection	See ordering chart													
Enclosure	IP65 for electrical code B, G (with connector fitted) IP67 for electrical codes E, F, 6, 7, 8 and 9													
Vibration	20G, 10-2000Hg sinusuidal													
Shock	Withstands free fall to IEC 68-2-32 procedure 1													
Approvals	CE													
Weight	35 gms													

Individual Specifications

Voltage Output Units	
Output	See ordering chart (current 4.5mA)
Supply Voltage	1 Volt above Full Scale, to max 30 Volts
External load (sink/source current)	2mA Max
Current Output Units	
Output	4-20mA
Supply Voltage	8 to 30Vdc (24Vdc max for 110° and above)
Max. Loop Resistance	(Vs-8) x 50 ohms
Min. Loop Resistance	(Vs-24) x 50 ohms
Ratiometric Output Units	
Output	0.5 to 4.5Vdc (3.5mA max)
Supply Voltage	5Vdc, ± 10%

Electrical Connectors

AMP Superseal 1.5

DIN 43650C Industrial

DIN 72585 Bayonet

M12 Ranges

Deutsch DTD4-4P

Packard Metri-pack

Integral Cable

MECHANICAL FITTINGS

Code 01
G 1/4 EXT

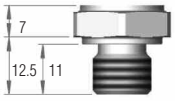

Code 04
7/16"-20 UNF
with 37° Flare

Code 1J
7/16"-20 UNF
O-Ring

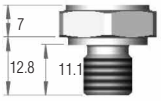

Code 02
1/4"-18 NPT

Code 08
1/8"-27 NPT

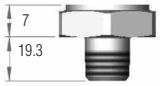

Code 05
G 1/4"A
Integral Face Seal

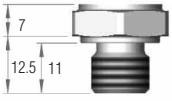

Code 0L
M12 x 15

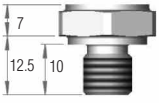

Code 2T
M12x1.5 HP
[metal washer seal]

Code IG
7/16"Schraeder

Hex is 22mm [.866] Across Flats (A/F) for deep socket mounting.

Other thread forms available. Consult factory.

NOTE: Dimensions in mm

Indicators and Accessories Pages 64-69

How to Order

Use the **Bold** characters from the chart below to construct a product code

Series **310X** **X** **XXXXX** **XX** **X** **X** **03**

Variants to Standard Types
- **00** - Pressure output
- **01** - Pressure and temperature output (see **Note 1**)

Output
- **B** - 4-20mA
- **C** - 1-6V
- **H** - 1-5V
- **N** - 0.5 to 4.5V Non Ratiometric
- **S** - 0-10V
- **T** - 0.5 to 4.5 Ratiometric
- **R** - 0-5 V
- **P** - 1-10 V

Pressure Range
- **0006G** – 6barG
- **0010G** – 10barG
- **0016G** – 16barG
- **0025G** – 25barG
- **0040G** – 40barG
- **0060G** – 60barG
- **0100S** – 100barS
- **0160S** – 160barS
- **0250S** – 250barS
- **0400S** – 400barS
- **0600S** – 600barS
- **1000S** – 1000barS)
- **1600S** – 1600barS) (see **Note 2**)
- **2200S** – 2200 barS)

Integral Pressure Connection
- **01** - G1/4 External
- **02** - 1/4- 18 NPT External
- **04** - 7/16-20 UNF External
- **05** - G1/4 External Soft Seal
- **08** - 1/8 NPT External
- **1G** - Schraeder Deflator (Short)
- **1J** - 7/16 - 20 UNF External '0' Ring Seal
- **0L** - M12 x 1.5 - 6g (600b and below)
- **2T** - M12 x 1.5-6g (1000b and above)

Cable Length (metres)
Maximum 10 metres **F** connector only

Restrictor
- **0** - No Resistor
- **R** - Restrictor Fitted

Electrical Connection
- **6** - AMP Superseal 1.5 Series
- **7** - DIN 72585 Bayonet
- **8** - Deutsch Series DT-04
- **9** - Packard Metripak
- **B** - Industrial DIN
- **E** - M12x 1 4 pin
- **F** - Integral cable
- **G** - EN 175301-803 (ex DIN 43650A)

For mating electrical connectors and cables see page 67.

Note 1 Pressure and temperature output available with voltage output and electrical connectors B, E, 7 and 6 only

Note 2 Ranges 1000 bar and above available with 2T pressure port only.

ELECTRICAL CONNECTOR

Code B
DIN43650C Industrial

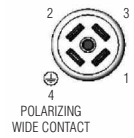

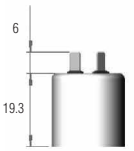

Pin #	Function	
	Current	Voltage
1	N/A	Press O/P +VE
2	+VE	Supply +VE
3	N/A	Temp O/P +VE
4	-VE	Common

Code E
M12 x 1P

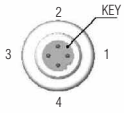

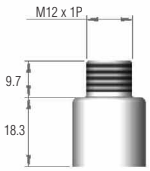

Pin #	Function	
	Current	Voltage
1	+VE	Supply +VE
2	N/A	Press O/P +VE
3	-VE	Common
4	N/A	Temp O/P +VE

Code 8
Deutsch DT04-4P

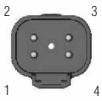

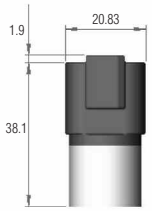

Pin #	Function	
	Current	Voltage
1	-VE	Common
2	+VE	Supply +VE
3	N/A	Temp O/P +VE
4	N/A	Press O/P +VE

Code 7
DIN72585A1-4, 1

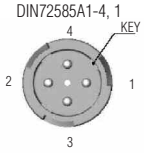

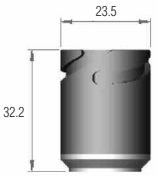

Pin #	Function	
	Current	Voltage
1	+VE	Supply +VE
2	-VE	Common
3	N/A	Press O/P +VE
4	N/A	Temp O/P +VE

Note: The diameter of all cans is 19mm [.748]

Code 9
Packard MetriPack

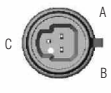

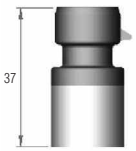

Pin #	Function	
	Current	Voltage
A	-VE	Common
B	+VE	Supply +VE
C	N/A	Press O/P +VE

Code 6
Amp Superseal 1.5

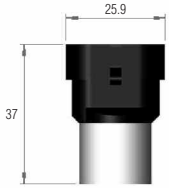

Pin #	Function	
	Current	Voltage
1	N/A	Press O/P +VE
2	-VE	Common
3	+VE	Supply +VE

Code G
DIN 43650A

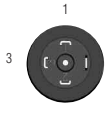

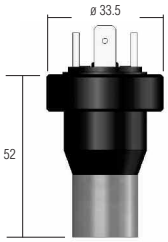

Pin #	Function	
	Current	Voltage
1	Positive	Supply +VE
2	Negative	Common
3	N/A	Press O/P +VE
4	N/A	N/A

Code F
DIN

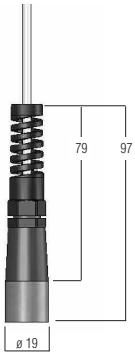

Pin #	Function	
	Current	Voltage
1	Positive	Supply +VE
2	N/A	Press O/P +VE
3	Negative	Common
4	N/A	N/A

FUTEK MODEL TFF350

REACTION TORQUE SENSOR

(Previously T5162)

Drawing Number: FI1139			
INCH [mm]	R.O.= Rated Output		
WIRING CODE (WC1)			
+Excitation	-Excitation	+Signal	-Signal
RED	BLACK	GREEN	WHITE

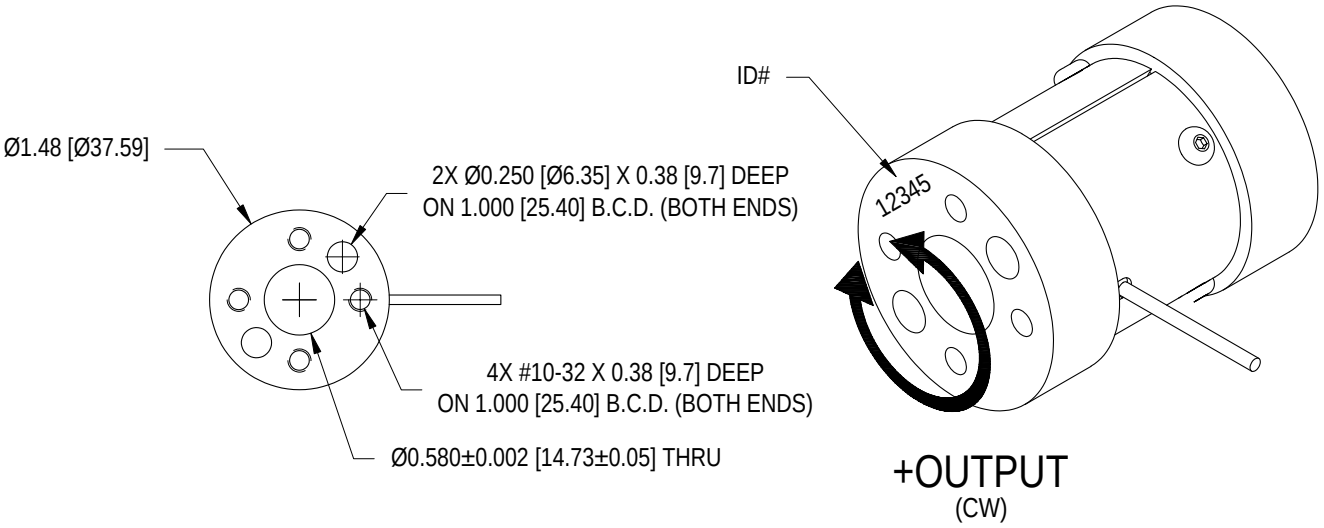

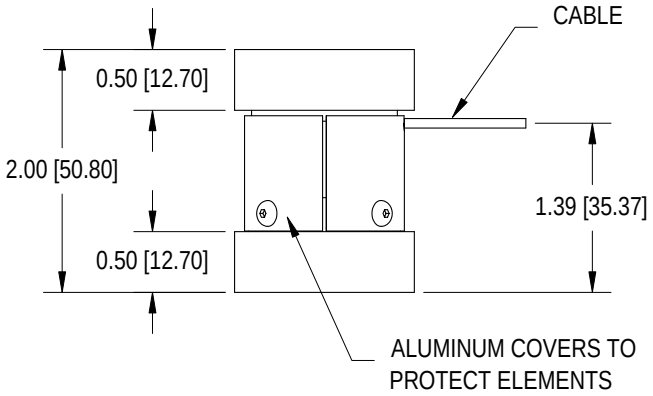

STK#	CAPACITY in-lb	CAPACITY Nm	TORSIONAL STIFFNESS in-lb/rad	WEIGHT
FSH00645	100	11	67000	2.9 oz [82.2 g]
FSH00646	150	15	86000	3.0 oz [85.0 g]
FSH00647	500	60	3.22×10^5	3.4 oz [94.4 g]
FSH00648	1300	150	8.09×10^5	3.5 oz [99.2 g]
FSH00649	3000	339	1.31×10^6	8.7 oz [246.6 g]

SPECIFICATIONS:

RATED OUTPUT	*2 mV/V nom.*
SAFE OVERLOAD	*150% of R.O.*
ZERO BALANCE	*±1% of R.O.*
EXCITATION (VDC OR VAC)	*18 MAX*
BRIDGE RESISTANCE	*700 Ω nom.*
NONLINEARITY	*±0.2% of R.O.*
HYSTERESIS	*±0.2% of R.O.*
NONREPEATABILITY	*±0.1% of R.O.*
TEMP. SHIFT ZERO	*±0.005% of R.O./°F [0.01% of R.O./°C]*
TEMP. SHIFT SPAN	*±0.01% of LOAD/°F [0.018% of LOAD/°C]*
COMPENSATED TEMP.	*60 to 160°F [15 to 72°C]*
OPERATING TEMP.	*-60 to 200°F [-50 to 93°C]*
MATERIAL (100 - 1300 in-lb)	*ALUMINUM*
MATERIAL (3000 in-lb)	*17-4PH S.S.*

CABLE: #29 AWG, 4 Conductor, Spiral Teflon Cable 6 in [152] Long

ACCESSORIES AND RELATED INSTRUMENTS AVAILABLE

CALIBRATION (STD)	*2 pt. CW; 100KΩ SHUNT CAL. VALUE*
CALIBRATION TEST EXCITATION	*10 VDC*

FUTEK
ADVANCED SENSOR TECHNOLOGY, INC.

10 THOMAS
IRVINE, CA 92618 USA
1-800-23-FUTEK (38835)

INTERNET:
http://www.futek.com

FUTEK MODEL CSG110 (JM-2AD)
STOCK # FSH01449

DIN RAIL MOUNT AMPLIFIER MODULE
±10 VDC, 0-20 mA OUTPUTS
DC POWERED, UNIVERSAL STRAIN GAGE SIGNAL CONDITIONER

Drawing Number: FI1045-B	
INCH [mm]	R.O.= Rated Output

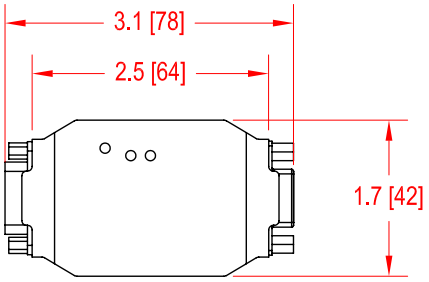

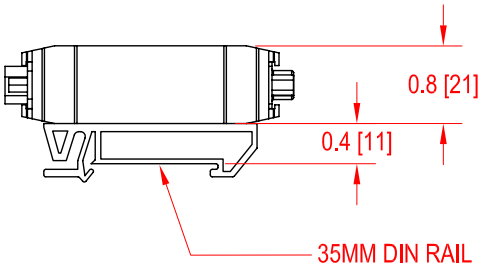

FEMALE DB 9

PIN #	WIRING CODE
1	+EXC / +SENSE *
2	+SIGNAL
3	-SIGNAL
4	-EXCITATION
5	SHIELD
7	-SENSE *

USED WITH 6 WIRE SYSTEM
*SENSE CONNECTION OPTIONAL

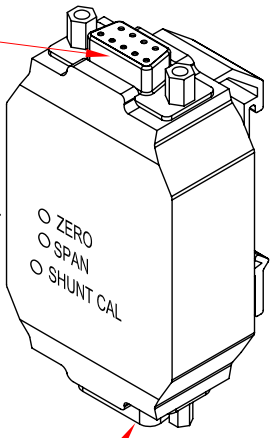

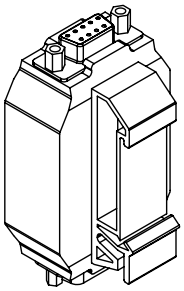

MALE DB 9

PIN #	WIRING CODE	CABLE COLOR CODE
9	+12 TO 24 VDC	RED
8	SIGNAL OUT (VOLTAGE)	GREEN
7	RETURN (VOLTAGE)	ORANGE
6	GROUND (POWER)	BLACK
2	RETURN (CURRENT)	BLUE
1	SIGNAL OUT (CURRENT)	WHITE

Features

- Bipolar Output, Differential Input
- ± 5 or ± 10 VDC Solder Jumper Selectable Outputs
- 4-20, 0-20, 5-25 mA Solder Jumper Selectable Outputs
- Bridge Excitation 5 or 10 VDC
- Ranges: 0.5, 1.0, 1.5, 2.0, 3.0, 4.0 mV/V (Solder Jumper)
- Interchangeable Socket Mounted 60.4K Ω Shunt Cal
- Externally Accessible Shunt Cal Activation Button
- Internal Span and Offset Adjust Resistor Locations
- Sensor Polarity Reversal Jumpers
- Weight: 1.4 oz [40 g]

Environment

Parameter	Min	Typ	Max	Unit
Operating Temperature †	32		158	°F
	0		70	°C
Storage Temperature	-40		185	°F
	-40		85	°C
Relative Humidity: 95% at 100 °F [39 °C]				
IP Rating IP31				

† Wider Range Available

* Specified at 10 VDC Output, 2mV/V range with 350 ohm bridge.
Default settings @ 2mV/V, 10 VDC excitation and ± 10 VDC Output unless otherwise specified.
RO Stands For Rated Output.

Notes

1. Adjusting Zero Will Not Affect Calibration.
2. Adjusting Span Will Affect Calibration.
3. Power Supply Must Source 150mA minimum.
4. Carefully Remove Cover To Access Selection Solder Jumpers.

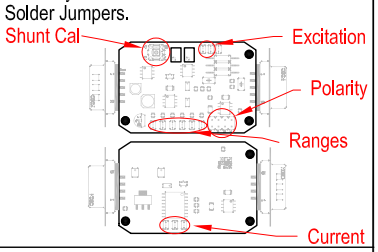

Electrical Specifications

Parameter	Min	Typ	Max	Unit
Power Supply	12		24	VDC
Input Current	110			mA
Output Impedance			1200	Ohms
Sensor Impedance	120			Ohms
Frequency Response -3db BW		1000		Hz
Common Mode Rejection Ratio	107			dB
Noise			60	mV p-p
Output Span Range	-15		5	% of RO*
Output Zero Range	-7.2		7.2	% of RO*

Accessories And Options

Description	Stock Number
28 AWG 6 Conductor 5 ft Long Cable w/ DB9 Female (Included)	FSH01077
DB9 Male With Housing (Included)	FSH01075
28 AWG, 4 Conductor 5 ft Long Cable with DB9 Male	FSH01129
DB9 Male with Screw Terminal Blocks (Sensor Side - Figure 1.)	FSH02236
DB9 Female with Screw Terminal Blocks (Output Side)	FSH02237
3KHz -3db Frequency Response	QSH00425
5KHz -3db Frequency Response	QSH00501
11KHz -3db Frequency Response	QSH00602

Figure 1.

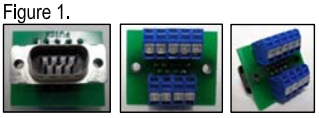

FUTEK
ADVANCED SENSOR TECHNOLOGY, INC.

10 THOMAS
IRVINE, CA 92618 USA
1-800-23-FUTEK (38835)

INTERNET:
http://www.futek.com

Vehicle Sensors

90360 Series

WHEEL TORQUE SENSOR

This telemetry based wheel torque sensor is used to measure the torque, speed, and temperature of tire/brake systems without the need for wheel rim modifications or anti-rotation brackets. The 90360 series consists of three primary components: The torque sensor, vehicle adapter plates to integrate the sensor, and the digital FM telemetry to transmit and process signals. All output signals are conditioned to a high level analog output.

Wheel Sensor w/ Tire

VIDEO

FEATURES

- Non-contact signal transmission.
- High level analog outputs for torque, speed, and temperature (2 temp channels).
- High extraneous load carrying capabilities.
- RS-232 serial output (torque only).
- On-board shunt calibration and power switch.
- 9V Battery powered transmitter.
- Vehicle adapter plates with minimal centerline offset (no rim modifications).
- Custom wheel rims available to maintain tire centerline.
- Custom capacities and configurations available.

System Components

SPECIFICATIONS

Typical full scale loads ..... 7,000in-lbs to 60,000inlbs
Maximum rpm 1200
Temperature reading range (RTD based) ..... -100 to +500° C
Analog output (receiver) ..... 0 to +/- 5V (FS)
Sensor low pass filter ..... 300Hz, 4-pole Butterworth type
Sensor Hysteresis ..... 0.25% of full scale
Sensor Non-linearity ..... 0.25% of full scale
Sensor signal sample rate ..... 950 Hz
Cross-talk ..... <2% full scale

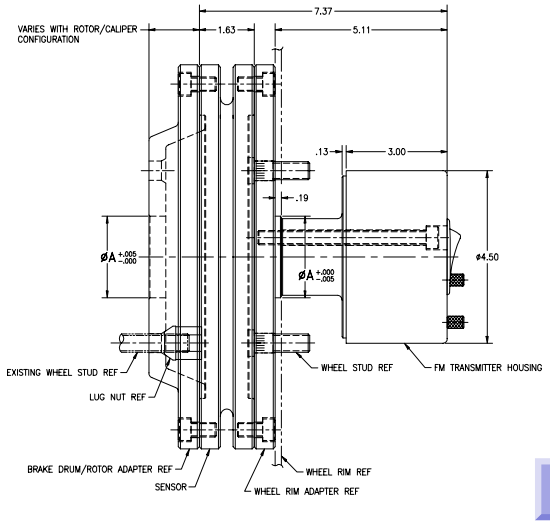

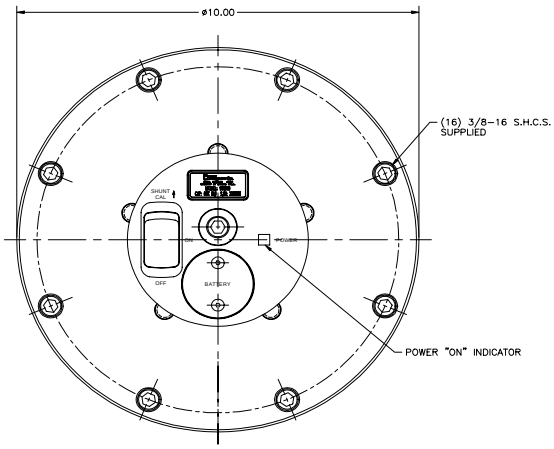

DWG

ORDER TOLL FREE 1-888-SENSOR-1

Solid State Sensors

GT1 Series

Hall Effect Gear Tooth Sensors

TYPICAL APPLICATIONS

Automotive and Heavy Duty Vehicles:

- Camshaft and crankshaft speed/ position
- Transmission speed
- Tachometers
- Anti-skid/traction control

Industrial:

- Sprocket speed
- Chain link conveyor speed and distance
- Stop motion detector
- High speed low cost proximity
- Tachometers, Counters

FEATURES

- Senses ferrous metal targets
- Digital current sinking output (open collector)
- Better signal-to-noise ratio than variable reluctance sensors, excellent low speed performance, output amplitude not dependent on RPM
- Sensor electronically *self-adjusts* to slight variations in runout and variations in temperature, simplifying installation and maintenance
- Fast operating speed – over 100 kHz
- EMI resistant
- Reverse polarity protection and transient protection (integrated into Hall I.C.)
- Wide continuous operating temperature range (–40° to 150°C), short term to 160°C

GENERAL INFORMATION

1GT1 Series Gear Tooth Sensors use a magnetically biased Hall effect integrated circuit to accurately sense movement of ferrous metal targets. This specially designed I.C., with discrete capacitor and bias magnet, is sealed in a probe type package for physical protection and cost effective installation.

Units will function from a 4.5 to 24 VDC power supply. Output is digital, current sinking (open collector). Reverse polarity protection is standard. If power is inadvertently wired backwards, the sensor will not be damaged. Built-in protection against pulsed transients to +60V, –40V is also included.

Optimum sensor performance is dependent on the following variables which must be considered in combination:

- Target material, geometry, and speed
- Sensor/target gap
- Ambient temperature
- Magnetic material in close proximity

GT1 ORDER GUIDE

Catalog Listing	Description
1GT101DC	Gear Tooth Sensor

MOUNTING DIMENSIONS (For reference only)

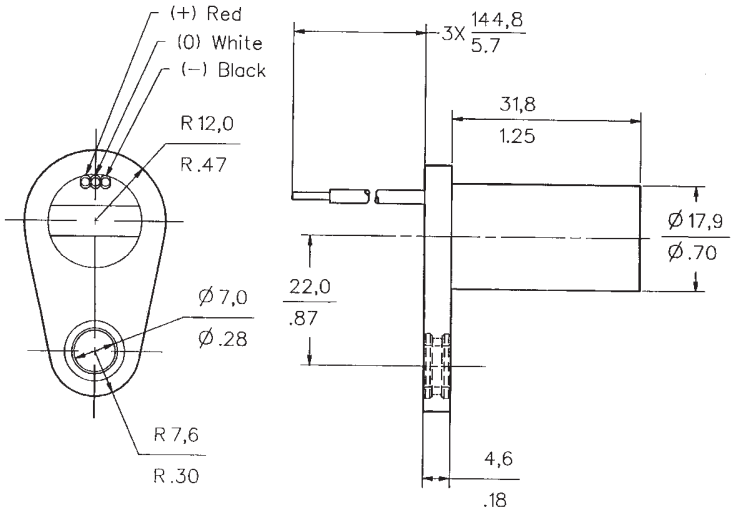

Solid State Sensors

GT1 Series

Hall Effect Gear Tooth Sensors

SENSOR SPECIFICATIONS

All values were measured using 1 K pull-up resistor.

Electrical Characteristics	Supply Voltage	4.5 to 24 VDC
	Supply Current	10 mA typ., 20 mA max.
	Output Voltage (output low)	0.4 V max.
	Output Current (output high)	10 μA max. leakage into sensor
	Switching Time	
	Rise (10 to 90%)	15 μsec. max.
	Fall (90 to 10%)	1.0 μsec. max.
Absolute Maximum Ratings*	Supply Voltage (Vs)	±30 VDC continuous
	Voltage Externally Applied To Output (output high)	−0.5 to +30 V
	Output Current	40 mA sinking
	Temperature Range	
	Storage	−40 to 150° (−40 to 302°F)
	Operating	−40 to 150° C (−40 to 302°F)
Switching Characteristics**	Operate Point	3.7±1.25° (3,28±1,13 mm)
	Release Point	4.7±2.50° (4,16±2,21 mm)
	Differential Travel	8.4±3.70° (7,45±3,34 mm)

* As with all solid state components, sensor performance can be expected to deteriorate as rating limits are approached; however, sensors will not be damaged unless the limits are exceeded.
** See Reference Target table.

TARGET GUIDELINES

The Target Guidelines table provides basic parameters when an application is not restricted to a specific target.

Any target wheel that exceeds the following minimum specifications can be sensed over the entire temperature range of −40° to 150°C with any sensing gap up to .080 in. (2,0 mm). This data is based on a 4 in. (102 mm) diameter wheel, **rotating 10 to 3600 RPM.**

Reference Target Dimensions

Tooth Height:	.200 in. (5,06 mm) min.
Tooth Width:	.100 in. (2,54 mm) min.
Tooth Spacing:	.400 in. (10,16 mm) min.
Target Thickness:	.250 in. (6,35 mm)

Sensor Output (with pull-up resistor added to output circuit)

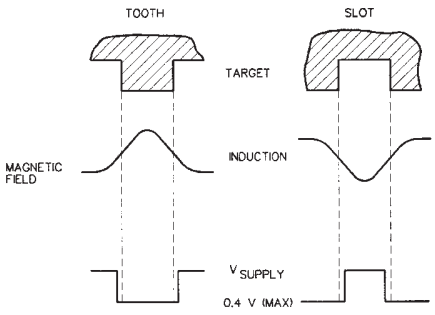

REFERENCE TARGET/CONDITIONS

Characteristics will vary due to target size, geometry, location, and material. Sensor specifications were derived using a cold-rolled steel reference target. See table, right, for reference target configuration and evaluation conditions.

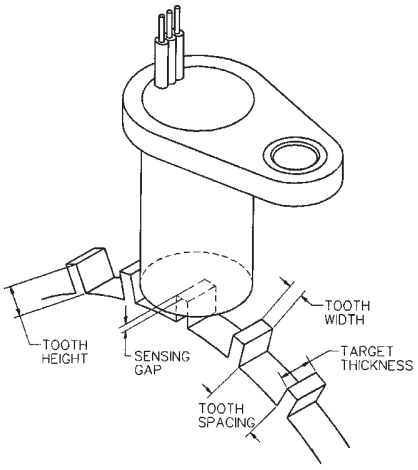

Target	
Diameter:	4 in. (101,6 mm)
Tooth Width:	.350 in. (8,89 mm)
Thickness:	.250 in. (6,35 mm)

Test Conditions	
Air Gap:	.040 to .080 in. (1,02 to 2,03 mm)
V Supply:	4.5 to 24 V
RPM:	10 min., 3600 max.

Integral Magnet

CXL-LF Series

HIGH SENSITIVITY ACCELEROMETERS

- Low g, 1-axis and 3-axis Accelerometers
- Excellent Offset Stability Over Temperature
- Low Noise Density 70 µg/Hz½

Applications

- Instrumentation
- Orientation Measurements

LF Series

The LF Series single and three axis accelerometers are precision, ± 1 g and ± 2 g acceleration sensors. Common applications include instrumentation, modal analysis, and orientation measurements.

The LF Series sensing element is a bulk micro-machined three layer silicon structure. The three layers form a differential capacitor with low noise. The sensor is bonded to a high-quality ceramic substrate where it is coupled to signal conditioning electronics. The entire package design is optimized for minimal thermal hysteresis, yielding superior DC response.

The LF Series operates on a single 5 VDC or a 6 - 30 VDC unregulated supply with the -R option. The LF Series sensor provides a direct high-level analog voltage signal output. The output requires no external signal conditioning and is easy to interface to standard data acquisition systems.

Each module's offset and scale factor are factory calibrated and tested. Standard modules have a bandwidth of 50 Hz.

The module should be securely attached using screws or adhesive. The LF Series accelerometers are available in two package options - nylon (both single and tri-axial), and high temperature aluminum (both single and tri-axial).

For data logging requirements, Crossbow offers the AD128 and AD2000 data logging systems. These devices allow users a turn-key data recording system for seismic data acquisition, structural testing, and other measurement applications. Check the Accelerometer accessories section for more details on the AD128 and AD2000 data logger.

Standard Package

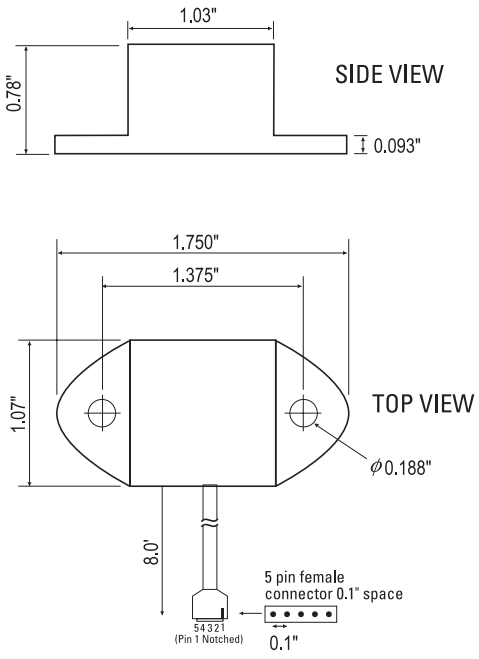

Document Part Number: 6020-0002-01 Rev E

Specifications	CXL01LF1 CXL01LF3	CXL02LF1 CXL02LF1Z CXL02LF3	Remarks
Performance			
Input Range (g)	± 1	± 2	± 5%
Zero g Drift (mV)	± 30	± 30	0°C to +70°C
Sensitivity (V/g)	2	1	± 5%
Transverse Sensitivity (%FS)	± 5	± 5	Max
Non-Linearity (%FS)	± 3	± 2	Typical
Alignment Error (deg)	± 2	± 2	Typical
Noise Density (µg/Hz½)	70	140	Typical
Noise (mg rms)	0.5	1.0	Typical
Bandwidth (Hz)	DC-50	DC-50	± 5%
Environment			
Temperature Range (°C)	-40 to +85	-40 to +85	
Shock (g)	2000	2000	
Electrical			
Supply Voltage (Volts)	+5 ± 0.25	+5 ± 0.25	
Zero g Output (Volts)	+2.5 ± 0.15	+2.5 ± 0.15	@ +25°C
Supply Voltage -R option (Volts)	+6 to +30	+6 to +30	Unregulated
Supply Current (mA)	4/axis	4/axis	Typical
Span Output (Volts)	± 2.0 ± 0.1	± 2.0 ± 0.1	@ +25°C
Output Loading	>20kΩ, <30 nF	>20kΩ, <30 nF	
Physical			
Standard package			
Size (in)	0.78 x 1.75 x 1.07	0.78 x 1.75 x 1.07	
(cm)	1.98 x 4.45 x 2.72	1.98 x 4.45 x 2.72	
Weight	1.62 oz (46 gm)	1.62 oz (46 gm)	
Aluminum package			
Size (in)	0.95 x 2.00 x 1.20	0.95 x 2.00 x 1.20	
(cm)	2.41 x 5.08 x 3.05	2.41 x 5.08 x 3.05	
Weight	2.40 oz (68 gm)	2.40 oz (68 gm)	

Notes
All frequency break points are -3 dB, single pole, -6 dB per octave roll-off. Non-linearity is the deviation from a best fit straight line at full scale. Transverse sensitivity is error measured in the primary axis output created by forces induced in the orthogonal axis. Transverse sensitivity error is primarily due to the effects of misalignment. Zero g drift is specified as the typical change in 0 g level from its initial value at +25 °C to its worst case value at Tmin or Tmax.

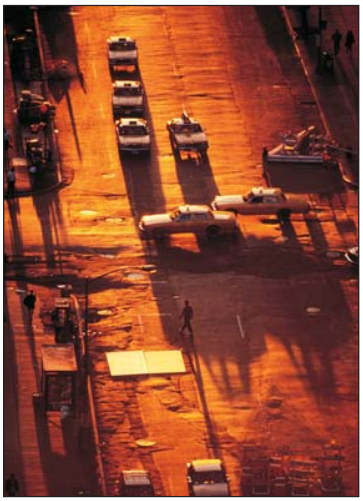

Pin	Color	Function
1	Red	Power In
2	Black	Ground
3	White	X-axis Out
4	Yellow	Y-axis Out
5	Green	Z-axis Out

Pin Diagram

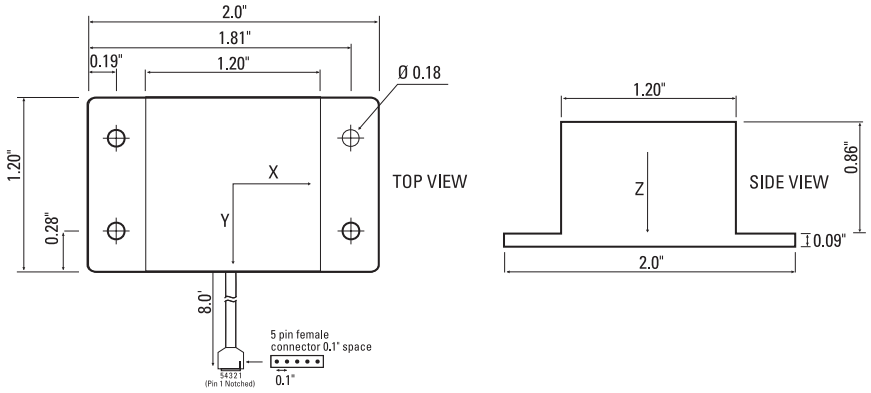

High Temperature Package

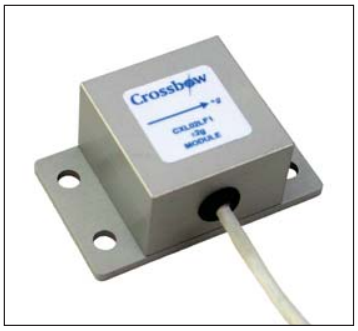

Ordering Information

Model	Axes	Span (g)	Sensitivity (V/g)	Noise (mg rms)	Bandwidth (Hz)
CXL01LF1	X	±1	2	0.5	DC-50
CXL01LF3	TRI	±1	2	0.5	DC-50
CXL02LF1	X	±2	1	1	DC-50
CXL02LF1Z	Z	±2	1	1	DC-50
CXL02LF3	TRI	±2	1	1	DC-50
OPTIONS					
-R	Voltage Regulator, 6 – 30 VDC input				
-AL	High Temperature Package (see package drawing above)				

CRS03
Angular Rate Sensor

A robust and affordable mass-produced gyroscope for automotive and commercial customers.

Angular rate sensors are used wherever rate of turn sensing is required without a fixed point of reference. The sensor will output a DC voltage proportional to the rate of turn and input voltage.

High performance motion sensing even under severe shock and vibration.

Whatever your application, the unique silicon ring technology, coupled with closed loop electronics, gives advanced and stable performance over time and temperature, overcoming the mount sensitivity problems experienced with simple beam or tuning fork based sensors.

Key Features

- Four model types available
- Excellent performance over temperature
- Repeatable drift characteristic
- High shock and vibration operation
- High reliability
- Metalised housing

CRS03
Angular Rate Sensor

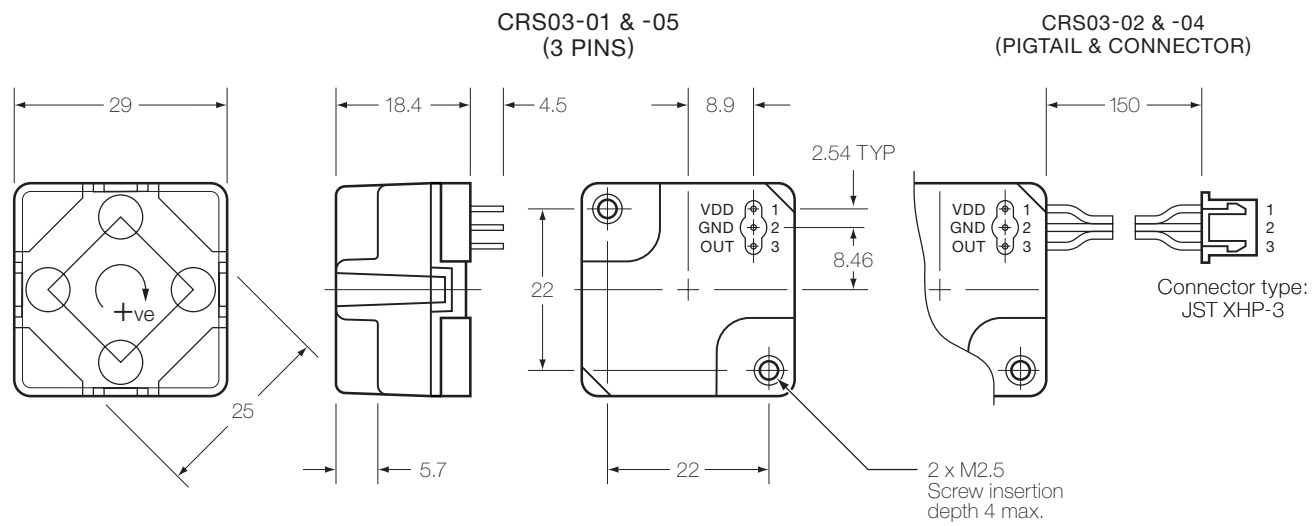

All measurements in millimetres.

Typical Data

	-01S & -02S	-04S	-05S
Angular Rate Range	±100°/s	±200°/s	±80°/s
Output	Analogue voltage (ratiometric)		
Scale Factor			
Nominal	20mV/°/s	10mV/°/s	25mV/°/s
Variation over temperature range	< ±3%		
Nonlinearity	< ±0.5% of full scale		
Bias			
Setting tolerance	< ±3°/s	< ±6°/s	< ±4°/s
Variation over temperature range	< ±3°/s	< ±6°/s	< ±4°/s
Ratiometric error	< ±1°/s	< ±2°/s	< ±0.8°/s
Drift vs. time	< ±0.55°/s in any 30s period (after start-up time)		
g sensitivity	< ±0.1°/s/g on any axis		
Bandwidth	10Hz (−3dB)		
Quiescent Noise	< 1mV rms (3Hz to 10Hz)		
Environment			
Temperature	−40°C to +85°C		
Linear acceleration	< 100g		
Shock	200g (1ms, ½ sine)		
Vibration	2g rms (20Hz to 2kHz, random)		
Cross-axis sensitivity	< 5%		
Mass	< 18 gram		
Electrical			
Supply voltage	+4.75V to +5.25V		
Supply current	< 35mA (steady state)		
Noise and ripple	< 15mV rms (DC to 100Hz)		
Start-up time	< 0.2s		
RoHS Compliant	Yes (R & S suffix)		

Pin Connections

1	+5V
2	0V
3	Rate Output

Silicon Sensing Systems Limited
Clittaford Road Southway
Plymouth Devon
PL6 6DE United Kingdom

T: +44 (0)1752 723330
F: +44 (0)1752 723331
E: sales@siliconsensing.com
W: siliconsensing.com

Silicon Sensing Systems Japan Limited
1-10 Fuso-Cho
Amagasaki
Hyogo 6600891 Japan

T: +81 (0)6 6489 5868
F: +81 (0)6 6489 5919
E: sssj@spp.co.jp
W: siliconsensing.com

Specification subject to change without notice.

Silicon Sensing Systems Limited Registered in England & Wales No. 3635234 Clittaford Road, Southway, Plymouth, Devon PL6 6DE
The device mark Silicon Sensing is a registered trade mark of Silicon Sensing Systems Community Trade Mark 003587664

CRS03-00-0100-131 Rev 2
DCR No. 616971

Data Sheet

SCA121T DUAL AXIS INCLINOMETER MODULES

The SCA121T Series contain 3D-MEMS-based dual axis inclinometer modules that provide instrumentation grade performance for leveling applications in harsh environment. The measuring axes of the sensing elements are parallel to the mounting plane and orthogonal to each other. Low temperature dependency, high resolution and low noise, together a with robust sensing element design, make the SCA121T the ideal choice for leveling instruments. The VTI inclinometers are insensitive to vibration, due to their over damped sensing elements, and can withstand mechanical shocks of up to 20000 g.

Features

- Dual axis inclination measurement (X and Y)
- Measuring ranges ±30° and ± 90°
- 0.0035° resolution (10 Hz BW, analog output)
- Sensing element controlled over damped frequency response (-3dB 18Hz)
- Robust design, high shock durability (20000g)
- High stability over temperature and time
- Single +5 V supply and unregulated 7…35V supply
- RoHS compliant

Applications

- Platform leveling and stabilization
- 360° vertical orientation measurement
- Leveling instruments
- Cabin leveling
- Solar panel control systems

1 Electrical Specifications

The SCA121T product family comprises three versions, the SCA121T-D03, the SCA121T-D05 and the SCA121T-D07 that differs in measurement range and supply voltage. The product version specific performance specifications are listed in the table SCA121T performance characteristics below.

1.1 Absolute Maximum Ratings

Supply voltage SCA121T-D05(V_{DD})	Regulated -0.3 V to +5.5V
Supply voltage SCA121T-D03 and D07	Unregulated -0.3 V to +35V
Voltage at input / output pins	-0.3V to 5.3
Storage temperature	-55°C to +85°C
Operating temperature	-40°C to +85°C
Mechanical shock	Drop from 1 meter onto a concrete surface (20000g). Powered or non-powered

1.2 Performance Characteristics

Parameter	Condition	SCA121T-D03	SCA121T-D05	SCA121T-D07	Units
Measuring range	Nominal	±90	±90	±30	°
		±1	±1	±0.5	g
Supply Voltage		7…35	5±0.25	7…35	V
Offset (Output at 0g)		2.5	Vdd/2	2.5	V
Offset calibration error	Max deviation	±1.5	±1.5	±1.5	°
Sensitivity		2	2	4	V/g
	between 0…1° (1	35	35	70	mV/°
Sensitivity calibration error		±1.5	±1.5	±1.5	%
Offset temperature dependency	-25…85°C	±1	±1	±1	°
	0…70°C	±0.5	±0.5	±0.5	°
Sensitivity temperature dependency	-25...85°C	-1.5...+0.5	-1.5...+0.5	-1.5...+0.5	%
	0…70°C	-0.8...+0.3	-0.8...+0.3	-0.8...+0.3	%
Typical non-linearity	Measuring range			±0.57	°
Frequency response	–3dB LP (2	8-28	8-28	8-28	Hz
Ratiometric error	Vdd = 4.75...5.25V		±2		%
Cross-axis sensitivity	Max.	4	4	4	%

Note 1. The angle output has SIN curve relationship to voltage output.

Note 2. The frequency response is determined by the sensing element's internal gas damping.

Honeywell

CSN Series
CSNS300
Closed loop current sensor

Features

- Small footprint
- Increased measuring range in small package
- Measures dc, ac and impulse currents
- Flexible mounting
- Large primary conductor hole
- Three connection styles
- Operating temperature -40 °C to 85 °C
- High accuracy

Typical applications

- Variable speed drives
- Overcurrent protection
- Power supply systems
- Frequency converters
- Uninterruptible power supplies UPS
- Robotics
- Battery management systems
- Welding equipment

This new series of closed loop current sensor offers a flexible solution to measuring currents up to ± 600 A. The sensors are small and have a large primary through hole to accept either a cable or a variety of different busbar sizes. The sensors can be mounted vertically or horizontally and come with connection options of integral Molex connector, pcb mounting pins, or a flying lead.

The sensors are closed loop devices and based on the principle of Hall effect and null balance method. The output from the current sensor is the balancing current that is the perfect image of the primary current reduced by the number of secondary turns at any time. The current can be expressed as a voltage by passing it through a load resistor.

WARNING

PERSONAL INJURY

DO NOT USE these products as safety or emergency stop devices, or in any other application where failure of the product could result in personal injury.

Failure to comply with these instructions could result in death or serious injury.

WARNING

MISUSE OF DOCUMENTATION

- The information presented in this product sheet (or catalogue) is for reference only. DO NOT USE this document as product installation information.
- Complete installation, operation and maintenance information is provided in the instructions supplied with each product.

Failure to comply with these instructions could result in death or serious injury.

CSNS300 Series Current Sensor

Technical information

Electrical			
Nominal current (In):		300 A.t rms	
Measuring range (dc or ac peak):		0 to ± 600 A.t	
Measuring resistance (@ +70 °C) [1]:		Rm min.	Rm max.
with ± 15 V	@ ± 200 A.t rms max.	5 Ohm	95 Ohm
	@ ± 300 A.t rms max.	5 Ohm	50 Ohm
Nominal analogue output current:			
	@ 300 A	150 mA	
Turns ratio:		1/2000	
Accuracy @ 25 °C:		max. ± 0.5 % @ In	
Supply voltage:		± 15 Vdc (± 5 %)	
Galvanic isolation:		6 kV rms/50 Hz/1 minute	
Accuracy - dynamic performance			
Zero offset current at 25 °C		< ± 0.2 mA	
Thermal drift of offset current 0 °C to 70 °C		< ± 0.4 mA	
Linearity		< ± 0.1 %	
Response time		< 500 ns	
Bandwidth		dc to 150 kHz	
di/dt		> 100 A/us	
General data			
Operating temperature		-40 °C to 85 °C	
Storage temperature		-40 °C to 90 °C	
Current consumption		10 mA plus output current	
Secondary internal resistance (@ 70 °C)		34 Ohm	
Sensor housing		Insulated plastic case	
Connection	CSNS300M	Molex connector	
	CSNS300P	PCB connection	
	CSNS300F	Flying lead and Molex connector	

Note

[1] Values to be confirmed at temperature

Appendix C

Motors and drivers specifications

High performance size 23 hybrid stepper motors HSX series

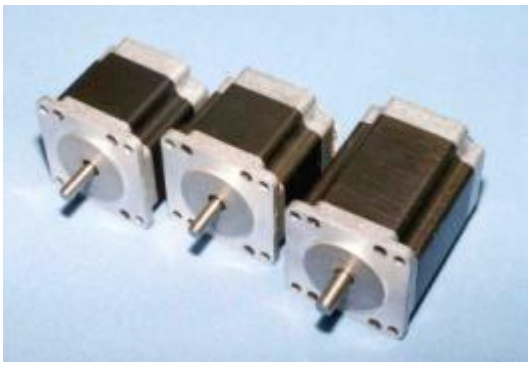

The high performance 23HSX series hybrid stepper motors conform to the international NEMA standard, and provide 200 steps/rev when used with full step drives or 400 steps per revolution in the preferred half step drive mode.

Features:

- High energy Neodymium magnets for increased performance
- 50% more torque than conventional hybrid types
- Choice of single or double shaft options
- Optional encoder or parking brake.
- High quality & Economical prices
- Available with a choice of precision planetary gearheads for increased torque and resolution at reduced speed.
- 8 leads provide the choice of Uni-polar or Bi-polar operation
- Non-standard customised executions available to special order
- Wide range of matched drives and control modules enable complete systems to be economically constructed based on 'in-service proven' technology.

Dimensions mm

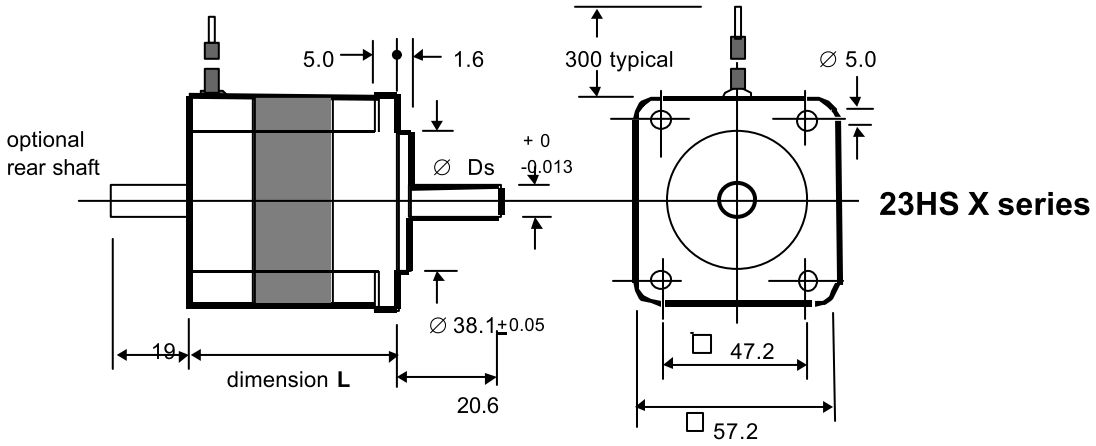

Mechanical Specification: 1.8 degree high performance stepper motors

motor type	length 'L' mm	Shaft diameter ' Ds ' Mm	number of leads	mass Kg	Uni-polar Holding Torque Ncm	Bi-polar Holding Torque Ncm	Rotor Inertia $Kgcm^2$
23HSX-102	41	6.35	8	0.5	37	47	0.077
23HSX-202 **23HSX-206**	55	6.35	8	0.7	75	98	0.22
23HSX-306	78.5	8.0	8	1.0	125	163	0.34

Electrical Specification:

Uni-polar operation

motor type	Resistance per phase ohms	Current per phase Amps	Inductance per phase mH
23HSX-102	4.6	1.0	4.6
23HSX-202	6.2	1.0	8.8
23HSX-206	0.7	3.0	0.9
23HSX-306	1.1	3.0	1.7

Bi-polar operation

Current / phase Series connection Amps	Current / phase Parallel connection Amps
0.7	1.4 max.
0.7	1.4 max
2.1	4.2 max.
2.1	4.2 max.

Note Rear shaft may be specified by adding '**E**' to part number EXAMPLE: 23HSX-206**E**

23HSX stepper motor lead colours:

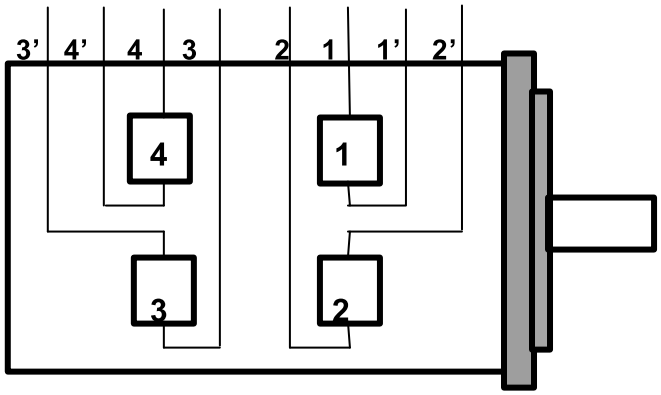

Motor Types	lead or terminal identification					
Lead identity	1	1' 2'	2	3	3' 4'	4
23HSX 102 23HSX 202 23HSX 206 23HSX 306	Red	Red/ White Yellow/ White	Yellow	Orange	Orange/ White Brown/ White	Brown

Typical performance

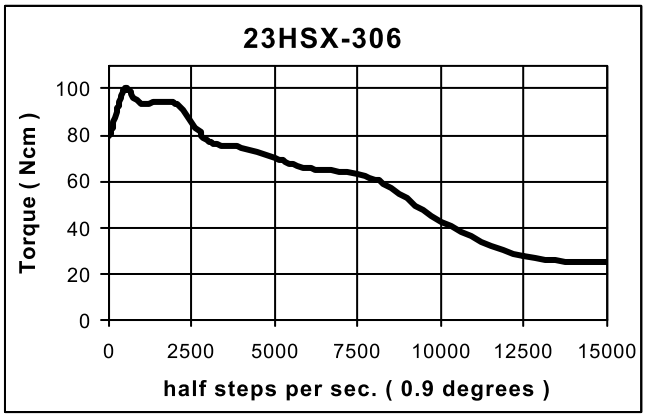

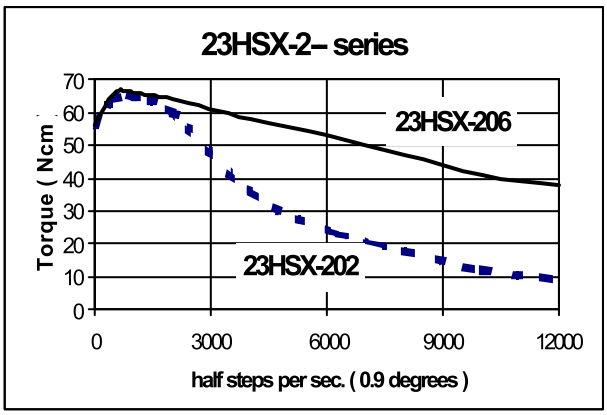

Performance Curves

Bi-polar operation, coils in parallel

Motor	Current Per phase (Amps)	Rail Voltage (Vdc)
23HSX-102	1.4	36
23HSX-202	1.4	36
23HSX-206	4.0	70
23HSX-306	4.0	70

Multi-role instrument gearhead MRIG series

The MRIG series gearheads have been designed for use in heavy duty instrumentation or light duty industrial drive application. The combination of a hardened metal spur gear train coupled with a precision die-cast housing results in a robust design with a high torque transmission capability.

MRIG has been designed to fit a wide range of motors including:

- high torque reversible ac synchronous types
- permanent magnet & hybrid stepper motors
- dc servo motors with optional brake, encoder or tachogenerator.
- brushless dc motors

Robust construction with built motor mounting flexibility

A key feature of the MRIG design is it's ability to accept standard motor shafts without the need for modification. This enables a wide range of motors including NEMA size 23 stepper motors to be fitted directly to the unit while dc and brushless servo motors are fitted using a simple mounting adapter. Gear strength is a key feature of the MRIG design. The use of steel gears and pinions with carefully selected hardness grades ensures a high torque transmission capacity and long life while a robust precision diecast metal housing offers excellent protection in industrial installations.

In it's standard form MRIG gearheads are provided with heavy duty sleeve bearing on the output shaft, ball bearings being available to special order

Standard Gear ratios

Fast-track delivery of the following ratios is ensured by the maintenance of comprehensive stock levels. Geared motor combinations based on the MRIG gearhead series are assembled in our fast response assembly cell to provide our customers with fast delivery to meet their changing demands.

Order Code	Gear ratio	Number of stages	Direction of rotation**	Efficiency	Maximum continuous output torque
MRIG02 *	5:1	3	opposite	72%	1.5 Nm
MRIG06 *	25:2	3	opposite	72%	2.5 Nm
MRIG11 *	25:1	4	same	65%	4.0 Nm
MRIG17 *	50:1	4	same	65%	4.0 Nm
MRIG22 *	100:1	5	opposite	58%	4.0 Nm
MRIG23 *	125:1	5	opposite	58%	5.0 Nm
MRIG27 *	250:1	6	same	52%	6.0 Nm
MRIG34 *	500:1	6	same	52%	7.0 Nm

Note: * Add '**S**' for standard Sleeve Bearings on Output shaft
' **B**' for ball bearings
* * Direction of rotation of output compared to input

Mclennan Servo Supplies Ltd.

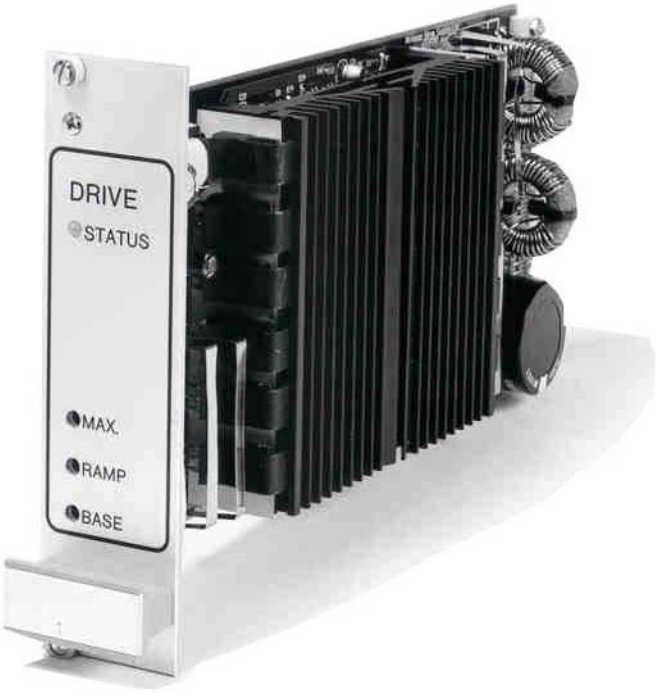

Bipolar Stepper Motor Translator

User Handbook

PM546

Mclennan Servo Supplies Ltd.
Unit 1, The Royston Centre
Lynchford Road
Ash Vale
GU12 5PQ UK

Telephone: +44 (0)8707 700 700
FAX: +44 (0)8707 700 699

E-mail: sales@mclennan.co.uk
tech@mclennan.co.uk

1.0 Overview

This unit is designed to be an economic and compact bi-polar drive for stepper motors. It conforms to the international 3U extended eurocard standard. They are ideally suited for use with 2/4 phase hybrid stepper motors with current ratings from 2.5 to 6.0 amps per phase such as the NEMA size 23 & 34 HS series. The ability to operate with rail voltages up to 80V DC provide enhanced high speed performance with a choice of full step or half step phase control when improved low speed and mid range stability is achieved.

1.1 Features

- Chopped constant current power stages provide increased performance and reduced current consumption.
- Full or half step phase control logic.
- Suitable for 4, 6 & 8 lead size 23 to 34 hybrid and permanent magnet stepper motors.
- Current settings from 2.5A to 6A per phase, set by on board DIP switches.
- Automatic or externally controlled reduced current setting for operating motor in stationary condition.
- Opto-isolated control inputs.
- On board selection of full step/half step control.
- On board motor direction reversal.
- Heatsink overtemperature sensor with selectable automatic drive shutdown.
- On board ramping oscillator for manual control.
- Front panel status LED indicator
- Opto-isolated drive healthy status output.
- Standard 100 x 220mm extended EUROCARD format.
- PM546 is fitted with a front panel for fitting in a 3U rack.

2.0 Specifications

Supply:	20V – 80V DC.
Motor output:	2 phase bi-polar, chopped constant current.
Current/phase:	2.5 to 6.0 amps/phase; set by on board switches.
Reduced current:	Approximately 20 - 25% of set current.
Reduced current control:	Automatic at standstill (switch selectable) or by external control input.
Step logic:	Full or half step; selected by on board switch.
Step control:	Opto-isolated input. 20KHz maximum, 6µS minimum pulse width.
Direction control:	Opto-isolated input. Sense of direction reversed by on board switch.
Enable control:	Opto-isolated input. Enable or disable selected by on board switch.
Oscillator control:	Opto-isolated inputs. OSC-RUN - Starts oscillator running. OSC-HIGH - Selects BASE speed or HIGH speed.
Oscillator speed control:	BASE set by on board pot (2-600Hz). HIGH set by external pot (600-15KHz). RAMP rate set by on board pot.
Thermal protection:	80ºC thermal sensor. Automatic latched drive disable selected by on board switch. Reset on power on.
Status LED:	GREEN - Drive OK and enabled. YELLOW - Drive not enabled. RED - Fault (overtemperature).
Status output:	Opto-isolated output. 10mA maximum. On when OK.
Opto-isolated inputs:	3-5V or 10-30V inputs. Fully isolated.
Step./ direction outputs	Open collector (30V 5mA maximum).
Packaging:	3U high extended eurocard for 19” rack mounting. 7E wide. 228 x 100 x 34 mm without front panel 245 x 128 x 35 mm with front panel

Warning!
Do not connect or disconnect the motor whilst the unit is powered.

Compact Design and High Positioning Accuracy

The actuator size was reduced by using Oriental Motor's original technology. The compact and lightweight body houses the rotating components as well as the linear motion mechanism of the stepping motor. The **DRL** Series helps to achieve a significant reduction in the size of your equipment and system.
To meet the user's requirements for higher positioning accuracy, all models can be ordered with a ground ball screw model [repetitive positioning accuracy: ±0.005 mm (±0.0002 in.)].

Reliable Design and Structure

The hollow rotor shaft incorporates large bore bearings for the direct handling of thrust loads. Minimizing the number of parts involved in linear conversion results in higher reliability.

Large Bore Thrust Bearing
+
Hollow Rotor

Significantly Fewer Parts and Required Man-Hours

The compact body houses the entire linear-motion mechanism, with some of the conventional parts eliminated for a more streamlined structure. This substantially reduces the man-hours required for design and assembly of your equipment, so you will enjoy higher production efficiency.

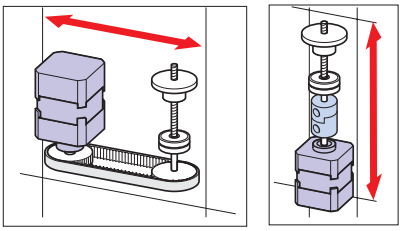

DRL Series

Significantly Fewer Parts and Required Man-Hours

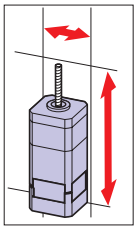

Actual Size

DRL20PB1-02

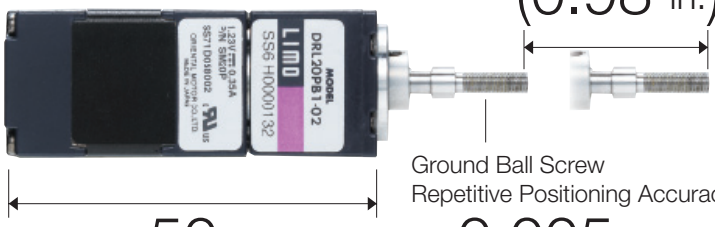

Max. Stroke
25 mm
(0.98 in.)

Ground Ball Screw
Repetitive Positioning Accuracy
±0.005 mm
(±0.0002 in.)

Length 50 mm
(1.97 in.)

Frame Size
20 mm
(0.79 in.)

●An external anti-spin mechanism must be provided with the standard type.

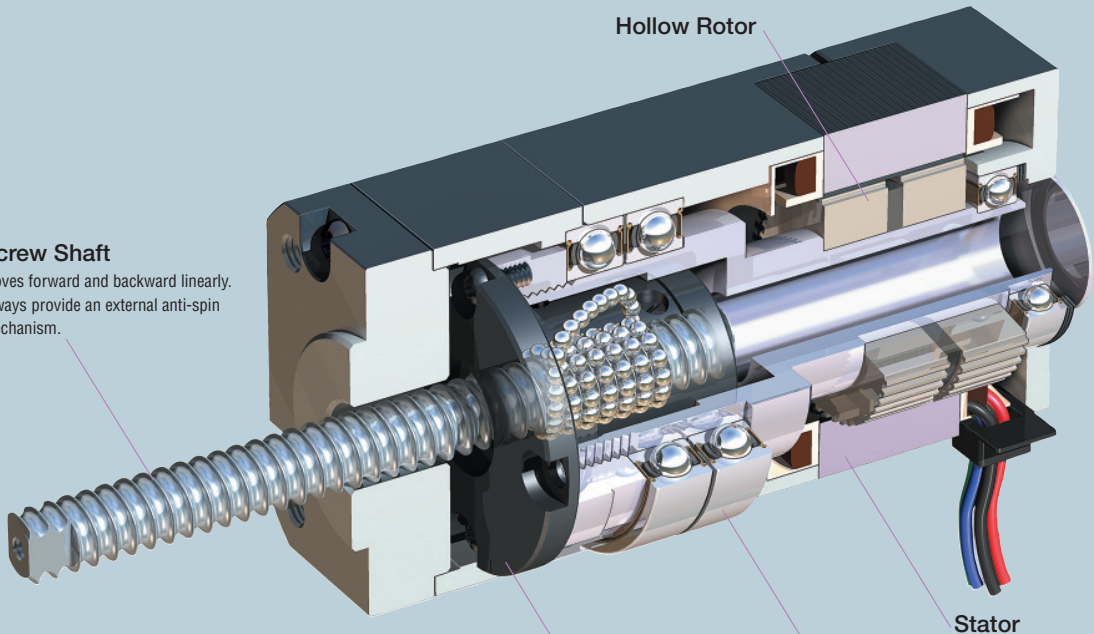

●The figure above shows a structure of the standard type (rolled screw shaft). A set collar (on the screw shaft), which prevents the screw shaft from retracting completely into the case, is being omitted in this figure.

Ground Ball Screw, Standard Motor RoHS

Model			DRL20PB1-02G DRL20PB1-02NG	DRL28PB1-03G DRL28PB1-06G DRL28PB1-03NG	DRL42PB2-04G DRL42PB2-10G DRL42PB2-04NG	DRL42PB2-04MG	DRL60PB4-05G DRL60PB4-10G DRL60PB4-05NG	DRL60PB4-05MG
Electromagnetic Brake			Not equipped	Not equipped	Not equipped	Equipped	Not equipped	Equipped
Max. Vertical Transportable Mass[*1]		kg (lb.)	1.5 (3.3)	3 (6.6)	10 (22)		30 (66)	
Maximum Speed[*2]		mm/s (in./s)	20 (0.79)	24 (0.94)	30 (1.18)		32 (1.26)	
Maximum Acceleration		m/s² (ft./s²)	0.2 (0.66)	0.2 (0.66)	0.4 (1.3)		0.26 (0.85)	
Maximum Thrust Force[*3]		N (lb.)	15 (3.3)	30 (6.7)	100 (22)		300 (67)	
Maximum Holding Force	At Excitation[*4]	N (lb.)	15 (3.3)	30 (6.7)	100 (22)		300 (67)	
	At Non-Excitation	N (lb.)	0	0	0	0	0	0
	Electromagnetic Brake	N (lb.)	–	–	–	100 (22)	–	300 (67)
Repetitive Positioning Accuracy		mm (in.)	±0.005 (0.0002)					
Lost Motion		mm (in.)	0.05 (0.002)					
Resolution[*5]		mm (in.)	0.002 (0.000079)	0.002 (0.000079)	0.004 (0.00016)		0.008 (0.00031)	
Lead		mm (in.)	1 (0.039)		2 (0.079)		4 (0.157)	
Stroke		mm (in.)	25 (0.98)	**03**: 30 (1.18) **06**: 60 (2.36)	**04**: 40 (1.57) **10**: 100 (3.94)	40 (1.57)	**05**: 50 (1.97) **10**: 100 (3.94)	50 (1.97)
Mass [Mass with adjusting knob]		kg (lb.)	0.08 (0.17) [0.08 (0.17)]	**03**: 0.18 (0.39) [0.19 (0.41)] **06**: 0.18 (0.39)	**04**: 0.6 (1.32) [0.6 (1.32)] **10**: 0.63 (1.38)	0.8 (1.76)	**05**: 1.3 (2.8) [1.35 (2.9)] **10**: 1.38 (3.0)	1.7 (3.7)
Actuator Dimensions No.			11	**03**: 12 **06**: 13	**04**: 16 **10**: 17	18	**05**: 19 **10**: 20	21

Ground Ball Screw, Standard Motor, Guide Type RoHS

Model			DRL20PB1G-02G DRL20PB1G-02NG	DRL28PB1G-03G DRL28PB1G-03NG	DRL42PB2G-04G DRL42PB2G-04NG	DRL42PB2G-04MG	DRL60PB4G-05G DRL60PB4G-05NG	DRL60PB4G-05MG
Electromagnetic Brake			Not equipped	Not equipped	Not equipped	Equipped	Not equipped	Equipped
Max. Horizontal Transportable Mass (Fig. A)		kg (lb.)	0.5 (1.1)	1 (2.2)	2 (4.4)		3 (6.6)	
Max. Vertical Transportable Mass (Fig. B)[*1]		kg (lb.)	1 (2.2)	1.5 (3.3)	5 (11)		15 (33)	
Maximum Speed[*2]		mm/s (in./s)	20 (0.79)	24 (0.94)	30 (1.18)		32 (1.26)	
Maximum Acceleration		m/s² (ft./s²)	0.2 (0.66)	0.2 (0.66)	0.4 (1.3)		0.26 (0.85)	
Maximum Thrust Force[*3]		N (lb.)	15 (3.3)	30 (6.7)	100 (22)		300 (67)	
Maximum Holding Force	At Excitation[*4]	N (lb.)	15 (3.3)	30 (6.7)	100 (22)		300 (67)	
	At Non-Excitation	N (lb.)	0	0	0	0	0	0
	Electromagnetic Brake	N (lb.)	–	–	–	100 (22)	–	300 (67)
Maximum Load Moment		N·m (oz-in)	M_P: 0 M_Y: 0 M_R: 0	M_P: 0 M_Y: 0 M_R: 0	M_P: 0.5 (71) M_Y: 0.25 (35) M_R: 0.8 (113)		M_P: 0.6 (85) M_Y: 0.35 (49) M_R: 2.2 (310)	
Repetitive Positioning Accuracy		mm (in.)	①±0.005 (0.0002) ②±0.01 (0.00039)	①±0.005 (0.0002) ②±0.02 (0.00079)	①±0.005 (0.0002) ②±0.01 (0.00039)			
Lost Motion		mm (in.)	0.05 (0.002)					
Resolution[*5]		mm (in.)	0.002 (0.000079)	0.002 (0.000079)	0.004 (0.00016)		0.008 (0.00031)	
Lead		mm (in.)	1 (0.039)		2 (0.079)		4 (0.157)	
Stroke		mm (in.)	25 (0.98)	30 (1.18)	40 (1.57)		50 (1.97)	
Mass [Mass with adjusting knob]		kg (lb.)	0.14 (0.3) [0.15 (0.33)]	0.25 (0.55) [0.26 (0.57)]	0.8 (1.76) [0.8 (1.76)]	1.0 (2.2)	1.8 (3.9) [1.85 (4.0)]	2.2 (4.8)
Actuator Dimensions No.			22	23	24	25	26	27

*1 When the power is turned off, or output current is turned off (non-excitation state), the actuator loses its thrust force or holding force. As such, it can no longer keep the load in position or withstand an external force.

*2 Use each actuator at or below the following maximum speed in a low-temperature environment [0 to +10°C (+32 to +50°F)].
DRL20: 13 mm/s (0.51 in./s), **DRL28**: 15 mm/s (0.59 in./s), **DRL42**: 20 mm/s (0.79 in./s), **DRL60**: 24 mm/s (0.94 in./s)

*3 The maximum thrust force is measured during constant-speed operation in horizontal operation with no load applied to the moving parts (screw shaft and joint). Thrust force varies with load mass and acceleration.

*4 The maximum holding force at excitation is the value when the automatic current cutback function is ON (50% of the rated current).

*5 25 resolutions can be set.

Note:

● Use the actuator in conditions where its surface temperature will not exceed 90°C (194°F). The repetitive positioning accuracy is measured at a specified temperature under a specified load.

● Maximum Transportable Mass

Figure A

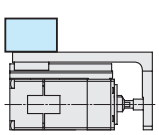

Figure B

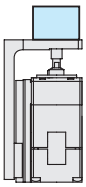

● Load Moment

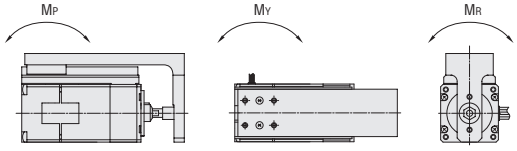

● Repetitive Positioning Accuracy

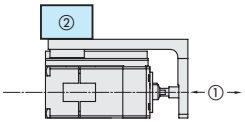

① Repetitive positioning accuracy is measured at the end of the guide.

② Repetitive positioning accuracy is measured on the linear-guide.

If footnote ① or ② is not indicated, then the accuracy values are identical.

CENTENT

CN0173 STEP PULSE GENERATOR

100 kHz Max
Settable Accel / Decel
Settable Base Speed

The CN0173 is a panel mounted speed control for step motor drives. The speed is set manually by the "Speed" potentiometer. The rate of acceleration and base speed are set by the respective trimpots.

Switching the "Start" input to ground causes the motor to begin accelerating from the "Base Speed" at a rate set by the "Acceleration" trimpot until the set speed is reached. The motor continues to run at this rate until the "Start" switch is opened. The motor then decelerates down to the base speed and then stops.

The CN0173 panel mounts through a ¼ inch hole and the "Speed" potentiometer takes a .125 inch shaft adjustment knob.

Operator's Manual (PDF format 159K)

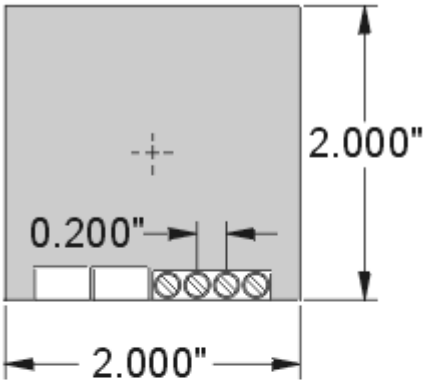

Specifications:

Power Supply Voltage	5 VDC
Current	30 ma
Step Frequency	0 to 100 kHz
Acceleration Time	50 ms to 10 sec
Interface	TTL compatible
Operating Temperature	0 to 70 Deg C
Weight	8 Oz
Size	2" X 2" X .2"

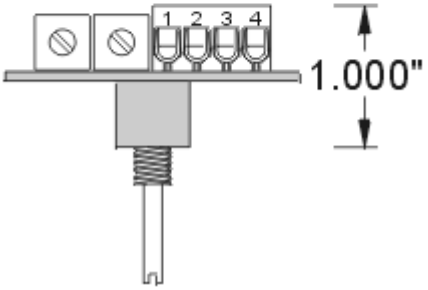

Compact, Lightweight Microstep Driver

Compact DC Input Board Driver Meeting the Space-Saving Needs

The compact, lightweight driver implements microstep drive. The new IC provides a wide range of functions, including the following:

- Smooth Drive Function
- 1-pulse/2-pulse input mode switching
- 25 microstep drive resolutions
- Power LED
- Photocoupler input
- Connector with safety lock (by MOLEX)
- Conforming to major safety standards

Smooth Drive Function Embodies Quieter Operation

The Smooth Drive Function automatically controls the motor's microstep drive operation at the same travel and speed in the full-step mode, without the operator having to change the pulse input settings. This function is especially useful when used in the full-step or half-step mode.

■ Comparison of Speed Fluctuation

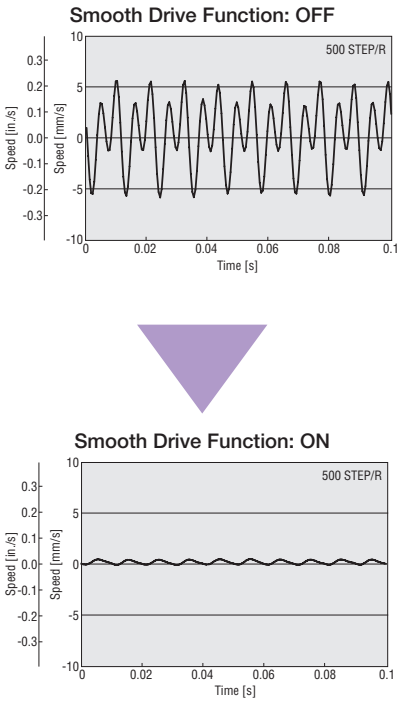

● Compact Microstep Driver

The microstep drive system allows you to set high resolutions up to one-250th of the basic resolution of the actuator. This function is effective in meeting your low-vibration/low-noise operation needs at low speeds. The high-performance driver is also compact and lightweight, achieving a reduction of approximately 47% in size compared with a conventional microstep driver.

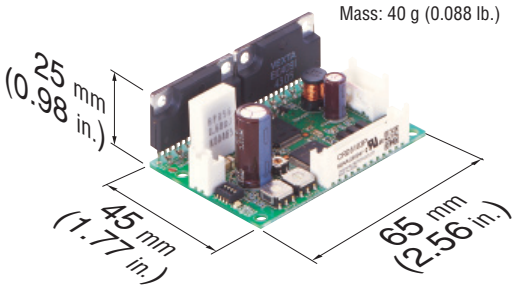

■ Comparison of Driver Size and Mass

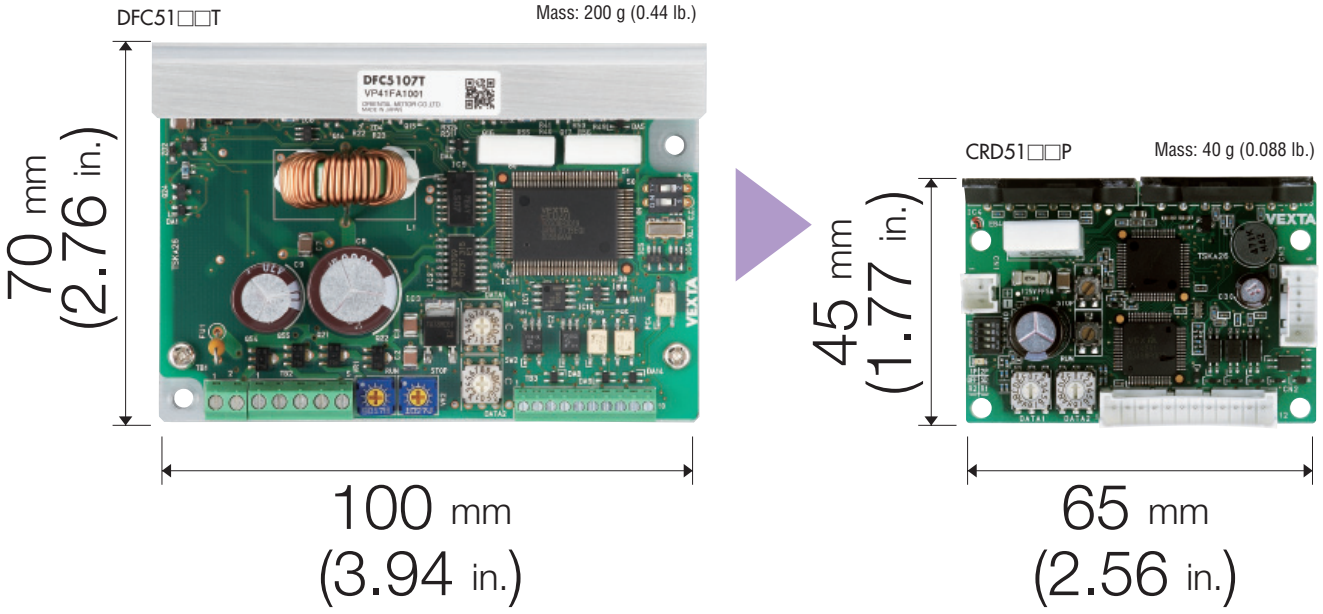

Connection and Operation

Names and Functions of Driver Parts

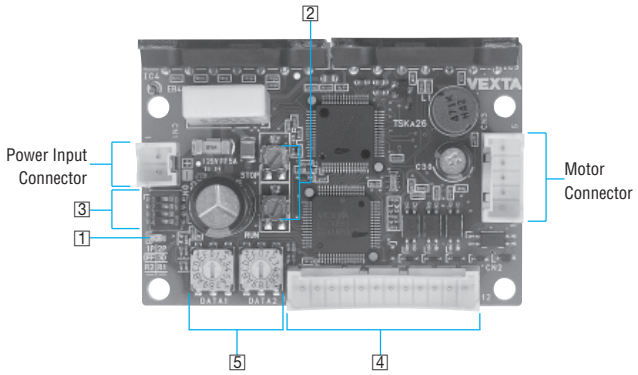

1 Power Input Display

Color	Function	When Activated
Green	Power Supply Indication	Lights when power is on

2 Current Adjustment Potentiometer

Indication	Potentiometer Name	Function
RUN	Motor Operating Current Adjustment Potentiometer	For adjusting the operating current of the motor
STOP	Motor Standstill Current Adjustment Potentiometer	For adjusting the standstill current of the motor

3 Function Switch

Indication	Switch Name	Function
1P/2P	Pulse Input Mode Switch	Switches between 1-pulse input mode and 2-pulse input mode
OFF/SD	Smooth Drive Function Switch	Enables or disables the smooth drive function
R2/R1	Resolution Select Switch	Switches the base resolution between R1 and R2

4 Input/Output Signal

Indication	I/O	Pin No.	Signal Name	Function
CN2	Input Signal	1	Pulse Signal (CW Pulse Signal)	Operation command pulse signal (The motor will rotate in the CW direction when in 2-pulse input mode)
		2		
		3	Rotation Direction Signal (CCW Pulse Signal)	Rotation direction signal Photocoupler OFF: CCW, photocoupler ON: CW (The motor will rotate in the CCW direction when in 2-pulse input mode)
		4		
		5	All Windings Off Signal	Turns off the output current to the motor so that the motor shaft can be rotated by external force
		6		
		7	Resolution Select Signal	Switches to the resolution set in DATA1 and DATA2
		8		
		9	Current Cutback Release Signal	Disables the automatic current cutback function
		10		
	Output Signal	11	Excitation Timing Signal	This signal is output when the excitation sequence is in step "0."
		12		

5 Resolution Setting Switch

Indication	Switch Name	Function
DATA1	Resolution Setting Switch	Each switch can be set to the desired resolution from the 16 resolution levels.
DATA2		

Low inertia dc servo motor M66 series

The M66CE is a high performance low inertia dc servo motor, providing up to 30W output power and offers smooth operation over a wide speed range. The M66CE motor incorporates a skewed ironless rotor thereby ensuring linear speed and torque characteristic combined with rapid acceleration and reversal capabilities.
The type M66CT includes an integral dc tachogenerator for optimum velocity control using analogue control techniques while M66CI series is provided with an integral dual track incremental encoder for use with digital control circuits.

Dimensions: mm

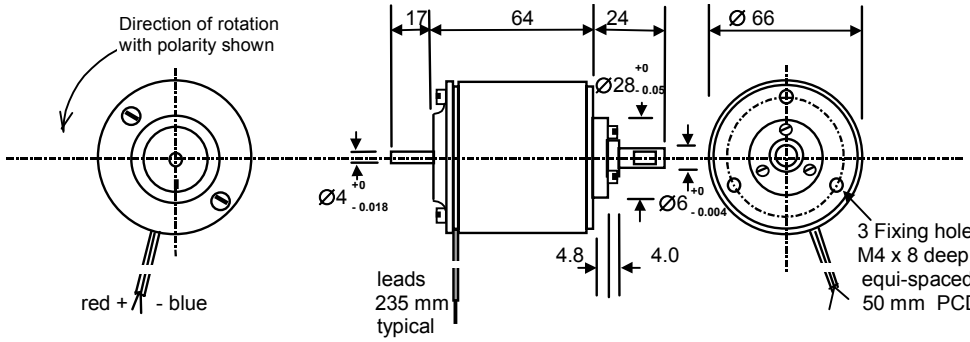

Servo motor M66CE

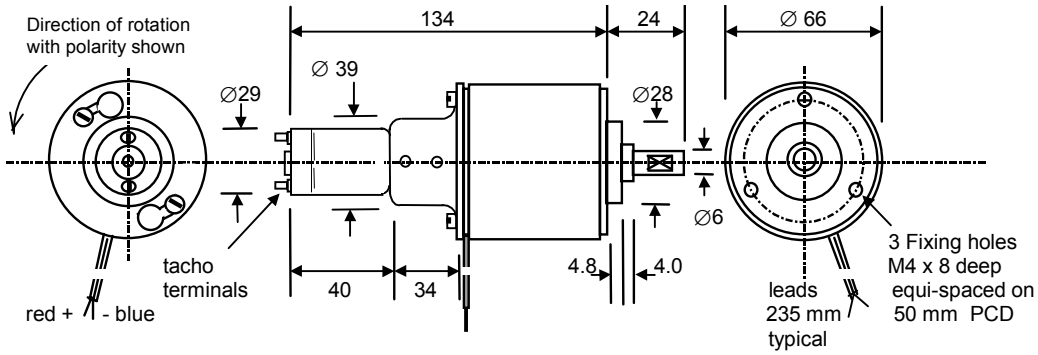

motor-tacho M66CT

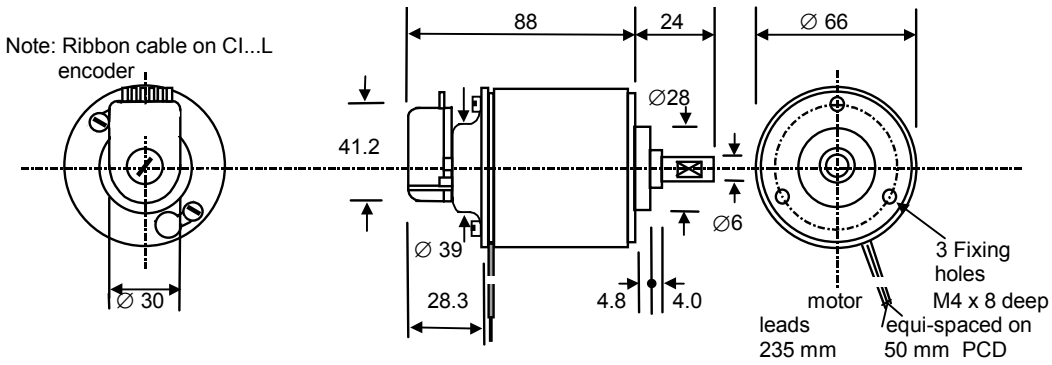

motor-encoder M66CI

Typical performance

Motor	No-load Speed (rpm)	Rated Speed (rpm)	Rated Torque (Ncm)	Rated Current (Amps)	Peak Torque (Ncm)	using Servo Amplifier	DC Supply (Vdc)	Power Supply for AC operation (110-240 Vac)
M66-12 series	2,700	1,700	8	2.0	16	**MSE421**	12	suitable for use with 12 Vdc battery
M66 -24 series	2,300	1,600	9	1.0	27	**PM121-10***	N/A	integral in amplifier
	2,300	1,600	9	1.0	27	**MSE421-30**	24	MSE 171E
	2,300	1,600	12	1.3	27	**MSE421-60**	24	MSE 171E

Note* Specify PM121-10T when using matched M66 C24T3/T6-tacho unit

30 Watt Ironless rotor dc servo motor M66 series

Specification dc servo motor type M66CE

M66 Motor- options:	M66CE-	-12	-24	Performance @ 24 Vdc
Nominal Voltage	(Vdc)	12	30	24
Maximum Output Power	(Watts)	15	30	20
No-load speed	(rpm)	2,700	2,900	2,300
Speed @ rated torque	(rpm)	1,800	2,300	1,600
Rated Torque	(Ncm)	8	12	12
Peak Torque	(Ncm)	25	36	27
Max. No load current	(milli Amps)	120	65	60
Rotor Inertia	($Kgcm^2$)	0.214	0.214	
Mechanical time constant	(milli secs)	24.5	17	
Torque Constant	(Ncm / A)	4.1	9.8	
Voltage Constant	(V / 1000 rpm)	4.27	10.3	
Rotor Resistance	(Ohms)	1.9	7.8	
Rotor inductance	(mH)	1.0	5.0	
Commutation		copper -graphite		
Bearings		pre-loaded ball		
Maximum radial load		100 N, 12 mm from bearing face		
Maximum axial load		15 N		
Ambient operating temperature range		-10 to +60 ^{O}C		

motor-tacho versions M66CT series

types:		M66C12 T3	M66C24 T3	M66C24 T6
Nominal Voltage		12Vdc	24-30 Vdc	24-30 Vdc
Motor specification:		As above		
Tacho Specification		**T.3 series**		**T.6 series**
Voltage constant	V/1000 rpm	3.25		6.50
Average ripple	peak / peak	3% (ripple frequency 18 cycles per rev.)		
Rotor resistance	Ohms	12		47
Max. continuous speed	rpm	3,000		

motor-encoder version M66-CI...series

types:		M66CI ...T-12		M66CI ...T-24
		M66CI ...L-12		M66CI ...L-24
Nominal Voltage		12Vdc		24Vdc
Motor specification:		As above		
Encoder type		**CI...T**	**CI...L**	
Supply	Vdc	5 ± 0.5	5 ± 0.5	
Max. Output signal	Vdc	5	5	
Signal wave form		Square	Square	
Output Circuit		TTL	RS 422	
Output Configuration		Dual Track Quadrature	Dual Track + Index (complementary)	
Number of Lines		100 or 500	100 or 500	

Typical Motor-encoder part number: M66 CI 500 L-24

500 line dual track encoder with Index

24-30 Vdc motor winding

Note:

M66 servo motors are also available with an integral parking brake (M66DB)
If a parking brake is required please contact us for full specification of M66DB options

Industrial Planetary gearheads IP series

Ratio Options:

IP series gearheads are available in a wide range of ratios, many of which being from stock as shown below:

Single stage units	2 stage units	3 stage units
• **5:1**	• **25:1**	250:1
• **10:1**	• **50:1**	500:1
	• **100:1**	1000:1

- **Standard ratios:**

Gear ratio options shown in **bold** are usually available from stock.

Dimensions:

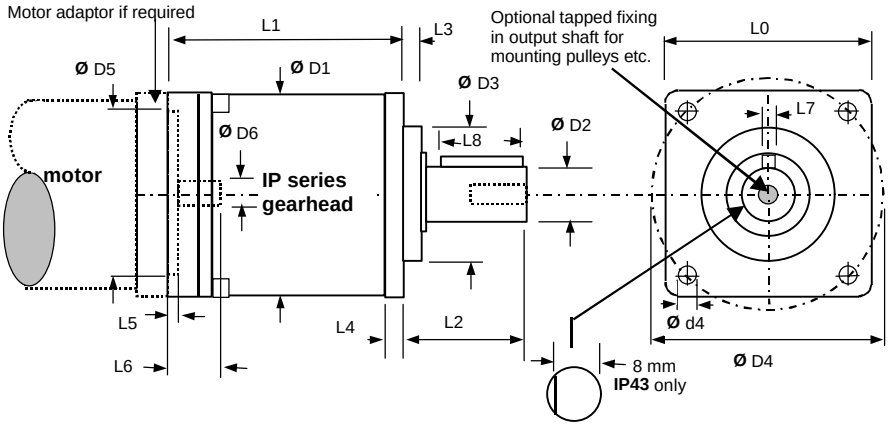

Table of dimensions: mm

Gearhead model		IP43 MO1	IP43 MO2	IP43 MO3	IP 57 MO1	IP 57 MO2	IP 57 MO3
Gearhead flange square	L0	42.8			57.2		
Gearhead Length Ratios 3:1 4:1 **5:1** **10:1** **25:1** **50:1** **100:1** 250:1 500:1 1000:1	L1	47	56	66	54 67.75	66 79.75	92.75
Shaft length from flange	L2	16			25.4		
Output Register length	L3	1.5			1.6		
Flange thickness	L4	4.3			5.2		
Input register length	L5	2.0			2.5		
Max. input shaft length	L6	To be advised			Dependent on adapter length		
Output shaft Key width	L7	See shaft flat details on IP43			3.2		
Output shaft key length	L8	Shaft flat length 15 mm			19.0		
Diametric dimensions							
Gearhead diameter	D1	42.8			57.2		
Output shaft diameter	D2	9.504 / 9.516 *			12.67 / 12.69 *		
Output register diameter	D3	22.2 / 22.225			38.05 / 38.10		
Mounting hole PCD	D4	50.8			66.68		
Mounting hole diameter	D4	3.78			5.1		
Input register diameter	D5	22.22 / 22.24			38.10 / 38.12		
Max. motor shaft dia.	D6	To be advised			8 .		

Specification

Gearhead	Number of stages	Maximum Continuous Torque * (Nm)	Max. Peak Torque* (Nm)	Typical Backlash (arc min.)	Efficiency	Max. Input Speed (rpm)	Max. Radial Load (N)	Max. Axial Load (N)
IP043-M01	1	3.3	6.0	20	92%			
IP043-M02	2	6.7	12	30	84%	6000	500	350
IP043-M03	3	10.0	20	40	78%			
IP057-M01	1	6.0	12	20	92%			
IP057-M02	2	12	24	30	84%	5000	500	350
IP057-M03	3	20	40	40	78%			

Note * De-rate by10% for gear ratios 10:1 & 100:1

maxon motor

maxon motor control — ADS_E 50/5

Order number 166143

Operating Instructions — April 2006 Edition

The ADS_E 50/5 is a powerful servo-amplifier for driving permanent magnet DC motors up to 250 watts.

Four modes can be selected by
DIP switches on the board:

- Speed control using tacho signals
- Speed control using encoder signals
- IxR compensated speed control
- Torque or current control

The ADS_E 50/5 is protected against excess current, excess temperature and short circuit on the motor winding.

With the FET power transistors incorporated in the servoamplifier, an efficiency of up to 95% is achieved.
A built in motor choke combined with the high PWM frequency of 50 kHz allows the connection of motors with a very low inductivity. In most cases an external choke can be omitted.
Thanks to the wide input power supply range of 12 - 50 VDC, the ADS_E 50/5 is very versatile and can be used with various power supplies.
The Europa card size allows the unit to be installed in a 19“-subrack or in a plug-in card system. Thanks to the controller circuit design, the ADS_E 50/5 is easily and quickly installed.

Table of Contents

The latest edition of these operating instructions may be downloaded from the internet as a PDF-file under www.maxonmotor.com, category «Service & Downloads», Order number 166143.

2 Performance Data

2.1 Electrical data

Supply voltage V_{CC} (Ripple < 5%)	12 - 50 VDC
Max. output voltage	$0.9 \cdot V_{CC}$
Max. output current I_{max}	10 A
Continuous output current I_{cont}	5 A
Switching frequency	50 kHz
Max. Efficiency	95 %
Band width current controller	2.5 kHz
Built-in motor choke	150 µH / 5 A

2.2 Inputs

"Set value"	-10 ... +10 V (R_i = 20 kΩ)
"Enable"	+4 ... +50 VDC (R_i = 15 kΩ)
Input voltage DC tacho "Tacho Input"	min. 2 VDC, max. 50 VDC (R_i = 14 kΩ)
Encoder signals "Channel A, A\, B, B\"	max. 100 kHz, TTL level

2.3 Outputs

Current monitor "Monitor I", short-circuit protected	-10 ... +10 VDC (R_0 = 100 Ω)
Speed monitor "Monitor n", short-circuit protected	-10 ... +10 VDC (R_0 = 100 Ω)
Status reading "READY"	
Open collector	max. 30 VDC ($I_L \leq\leq$ 20 mA)

2.4 Voltage outputs

Aux. voltage, short-circuit protected	+12 VDC, -12 VDC, max. 12 mA (R_0 = 1 kΩ)
Encoder supply voltage	+5 VDC, max. 80 mA

2.5 Trim potentiometers

IxR compensation
Offset
n_{max}
I_{max}
gain

2.6 LED indicator

Bi-colour LED	READY / ERROR
	green = READY, red = ERROR

2.7 Ambient temperature- / Humidity range

Operating	-10 ... +45°C
Storage	-40 ... +85°C
noncondensating	20 ... 80 %

2.8 Mechanical data

Weight	approx. 175 g
Dimensions	see dimension drawing, chapter 12

2.9 Terminal

Connector DIN 41612	Version H7/F24

Mclennan Servo Supplies Ltd.

MSE421 / PM421

Linear Servo Motor Amplifier
User Handbook

Mclennan Servo Supplies Ltd.
Unit 1, The Royston Centre
Lynchford Road
Ash Vale
GU12 5PQ UK

Telephone: +44 (0)8707 700 700
Fax: +44 (0)8707 700 699
E-mail: sales@mclennan.co.uk
tech@mclennan.co.uk
Web: www.mclennan.co.uk

MSE421/PM421

The MSE421 EuroAmp is a linear amplifier. It features

* Linear MOSFET output stage
* Operates from a single supply rail
* Adjustable current limiting
* Torque or Velocity control
* Tachometer or Armature voltage feedback
* Adjustable velocity control parameters
* Enable and directional limit inputs
* Rack mounting extended eurocard format
* MSE421 when fitted with front panel is referred to as PM421

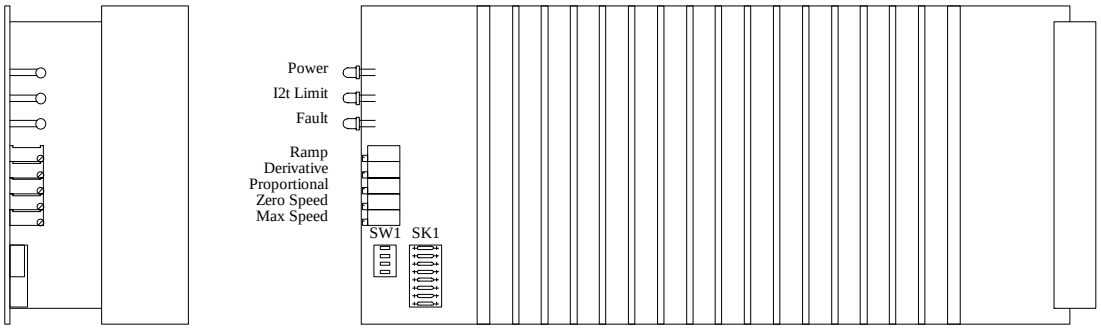

Block Diagram

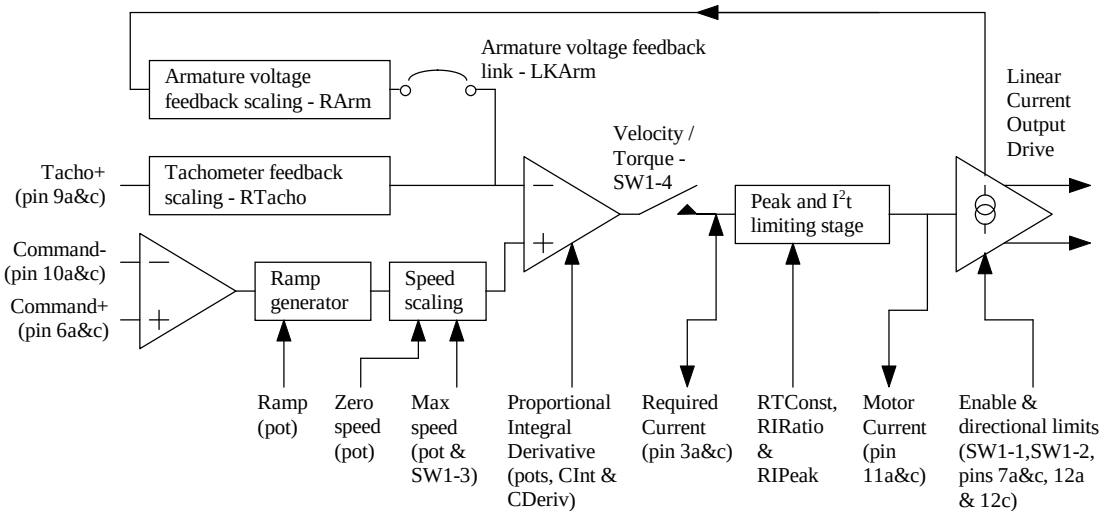

The amplifier has a linear output stage whose output current is proportional to the input voltage. It is also controlled by an enable input and directional limit inputs. The enable input may be used to enable or disable the output. The directional limit inputs may be used to prevent the output driving in a particular direction and therefore may be used as end of travel limits. The action of these inputs may be inverted by the switches SW1-1 and SW1-2 (see set up section).

Appendix D

Other devices

SOKKIA

Series30R

Reflectorless Total Stations

30cm to 350m / 1ft. to 1,140ft. Reflectorless Range*
Cutting-Edge Technologies Packed in a Compact Body

* Class 3R models

Laser beam image is simulated.

Series30R REFLECTORLESS TOTAL STATIONS

SET230R3 · SET330R3 · SET530R3 · SET230R · SET330R · SET530R · SET630R

SPECIFICATIONS

Model	SET230R3	SET330R3	SET530R3	SET230R	SET330R	SET530R	SET630R
Laser class*1	Class 3R Laser Product			Class 2 Laser Product			
Telescope	Fully transiting, coaxial sighting and distance measuring optics						
Magnification / Resolving power	30x / 2.5"						26x / 3.5"
Others	Length: 171mm (6.7in.), Objective aperture: 45mm (1.8in.) (EDM 48mm (1.9in.)), Image: Erect, Field of view: 1°30' (26m/1,000m), Minimum focus: 1.3m (4.3ft.), Reticle illumination: 5 brightness levels						
Angle measurement	Photoelectrical absolute encoder scanning, both circles adopt diametrical detection						
Unit / Display resolutions	Degree / Gon / Mil, selectable / 1" / 5", 0.2 / 1mgon, 0.005 / 0.02mil, selectable						
Accuracy (ISO17123-3:2001)	2" / 0.6mg / 0.01mil	3" / 1mg / 0.015mil	5" / 1.5mg / 0.025mil	2" / 0.6mg / 0.01mil	3" / 1mg / 0.015mil	5" / 1.5mg / 0.025mil	6" / 1.9mg / 0.03mil
Measuring time	0.5s or less, continuous						
Measurement mode	H: Clockwise / Counterclockwise, selectable; 0 set, Hold, Angle input, Repetition, available V: Zenith 0 / Horizontal 0 / Horizontal 0± / Slope in %, selectable						
Automatic dual-axis compensator	Dual-axis liquid tilt sensor, Working range: ±3' (±55mg)						
Collimation compensation	Yes / No, selectable						
Fine motion screws	2-speed motion	1-speed motion		2-speed motion	1-speed motion		
Distance measurement	Modulated laser, phase comparison method with red laser diode, coaxial optics						
Laser output	Reflectorless mode: Class 3R (max. 5mW) Prism/Sheet mode: Class 1 equivalent (max. 0.22mW)			Reflectorless mode: Class 2 (max. 0.99mW) Prism/Sheet mode: Class 1 equivalent (max. 0.22mW)			
Unit / Display resolutions	meters / feet / feet-inches, selectable / Fine, Rapid single: 0.001m / 0.01ft. / 1/8in. Tracking: 0.01m / 0.1ft. / 1/2in.						
Measuring range (slope distance) — Reflectorless*2 (with Kodak Gray Card)	0.3 to 350m (1 to 1,140ft.) (White side, 90% reflective) 0.3 to 170m (1 to 550ft.) (Gray side, 18% reflective)			0.3 to 200m (1 to 650ft.) (White side, 90% reflective) 0.3 to 80m (1 to 260ft.) (Gray side, 18% reflective)			0.3 to 150m (490ft.) (white side, 90% reflective)
With reflective sheet target*3/*8	RS90N-K: 1.3 to 500m (1,640ft.), RS50N-K: 1.3 to 300m (980ft.), RS10N-K: 1.3 to 100m (320ft.)						
With mini prisms	CP01: 1.3 to 800m (2,620ft.), OR1PA: 1.3 to 500m (1,640ft.)						
With 1 AP prism A*4	1.3 to 4,000m (13,120ft.)						1.3 to 3,000m (9,840ft.)
With 1 AP prism G*5	1.3 to 5,000m (16,400ft.)						1.3 to 4,000m (13,120ft.)
With 3 AP prisms A*4	to 5,000m (16,400ft.)						to 4,000m (13,120ft.)
With 3 AP prisms G*5	to 6,000m (19,680ft.)						to 5,000m (16,400ft.)
Accuracy (D=measuring distance, unit: mm) — Reflectorless*2/*6 (Fine mode)	0.3 to 200m (1 to 650ft.): ±(3 + 2ppm x D)mm Over 200 to 350m (over 650 to 1,140ft.): ±(5 + 10ppm x D)mm			0.3 to 100m (1 to 320ft.): ±(3 + 2ppm x D)mm Over 100 to 200m (over 320 to 650ft.): ±(5 + 10ppm x D)mm			0.3 to 100m (1 to 320ft.): ±(3 + 2ppm x D)mm Over 100 to 150m (over 320 to 490ft.): ±(5 + 10ppm x D)mm
Reflectorless*2/*6 (Rapid single mode)	0.3 to 200m (1 to 650ft.): ±(6 + 2ppm x D)mm Over 200 to 350m (over 650 to 1,140ft.): ±(8 + 10ppm x D)mm			0.3 to 100m (1 to 320ft.): ±(6 + 2ppm x D)mm Over 100 to 200m (over 320 to 650ft.): ±(8 + 10ppm x D)mm			0.3 to 100m (1 to 320ft.): ±(6 + 2ppm x D)mm Over 100 to 150m (over 320 to 490ft.): ±(8 + 10ppm x D)mm
With reflective sheet target	Fine: ±(3 + 2ppm x D)mm, Rapid single: ±(6 + 2ppm x D)mm						
With AP prism	Fine: ±(2 + 2ppm x D)mm, Rapid single: ±(5 + 2ppm x D)mm						
Measuring time — Fine mode / Rapid single / Tracking	Fine repeat: Every 0.9s (initial 1.7s) / Rapid single: 1.4s / Tracking: Every 0.3s (initial 1.4s)						
Measuring mode	Fine (single / repeat / average), Rapid (single), Tracking						
Atmospheric correction / Prism constant correction	Temperature / Pressure / ppm input, available / -99 to +99mm (1mm steps), 0 fixed in reflectorless mode						
Refraction & earth-curvature correction	YES (K=0.142 / 0.20) / NO, selectable						
Scale factor setting / Sea level correction	0.5 to 2.0 / Yes / No						
Data storage and transfer							
Data storage — Internal memory	Approx. 10,000 points						
CF memory card unit	Factory option, the 64MB CF card stores approx. 576,000-point data						n/a
Interface	Asynchronous serial RS-232C compatible, Baud rate 1,200 to 38,400bps / *Bluetooth* wireless communication is available as a factory option						
SFX wireless data transfer	Provided						
Printer output	Centronics compatible (with optional DOC46 printer cable)						
General							
Display / Keyboard	Alphanumeric/graphic dot matrix LCD, 192 x 80 dots, with backlight, with contrast adjustment / 4 soft keys and 11 keys						
Control panel location	On both faces						On one face
Wireless keyboard SF14	Optional						n/a
Laser-pointer function	ON (auto off in 5 minutes) / OFF, selectable (Does not work simultaneously with the Guide Light)						
Guide light GDL1	Factory option						
Sensitivity of levels — Plate level	30" / 2mm*7	30" / 2mm		30" / 2mm*7	30" / 2mm		40" / 2mm
Circular / Graphic	Circular level: 10' / 2mm / Graphic LCD level: 3' / outer circle						
Optical plummet / Tribrach	Image: Erect, Magnification: 3x, Minimum focus: 0.3m (0.98ft.) / Detachable						
Dust and water protection / Operating temperature	Conforms to IP66 (IEC 60529) / -20 to +50°C (-4 to +122°F)(-30 to +50°C (-22 to +122°F) with Low Temperature Models of SET530R3/530R)						
Instrument height / Size with handle and battery	236mm (9.3in.) from tribrach bottom / W 165 x D 171 x H 341 mm (W 6.5 x D 6.7 x H 13.5 in.)						
Weight with handle and battery	Approx. 5.4kg (12 lb.)						Approx. 5.3kg (11.6 lb.)
Power supply	7.2V DC						
BDC46A detachable Li-Ion rechargeable battery	2 BDC46A are included						1 BDC46A is included
Continuous use per battery at 25°C (77°F)	Approx. 7 hours (800 points) for single measurement every 30s, Approx. 8.5 hours for angle measurement only						
Recharging time at 25°C (77°F)	Within 2 hours with CDC68 standard quick charger						
BDC57 external Ni-MH battery (optional)							
Continuous use at 25°C (77°F)	Approx. 26 hours for single measurement every 30s Approx. 34.5 hours for angle measurement only			Approx. 27 hours for single measurement every 30s Approx. 36 hours for angle measurement only			n/a
Continuous use at -30°C (-22°F)	With Low Temperature Model of SET530R3: Approx. 22 hours for single measurement every 30s, Approx. 29 hours for angle measurement only With Low Temperature Model of SET530R: Approx. 22.5 hours for single measurement every 30s, Approx. 30 hours for angle measurement only						
Automatic power cut-off / Resume function	Auto-off time is selectable from 30, 15, 10, 5 minutes or none / On / Off selectable (backed up for approx. 1 week)						

*1 IEC 60825-1Amd.2: 2001 / FDA CDRH 21 CFR Part1040.10 and 1040.11 (Complies with FDA performance standards for laser products except for deviations pursuant to Laser Notice No.50, dated July 26, 2001.)
*2 Reflectorless range/accuracy may vary according to measuring objects, observation situations and environmental conditions.
*3 At temperatures -30 to -20°C (-22 to -4°F) using the Low Temperature Models: 1.3 to 300m (980ft.) with RS90N-K, 1.3 to 180m (590ft.) with RS50N-K, 1.3 to 60m (190ft.) with RS10N-K.
*4 Average conditions: Slight haze, visibility about 20km (12 miles), sunny periods, weak scintillation. *5 Good conditions: No haze, visibility about 40km (25 miles), overcast, no scintillation. *6 With Kodak Gray Card White Side (90% reflective).
*7 20" / 2mm plate level is available as a factory option for SET230R3 and SET230R. *8 When the beam's angle of incidence is within ±30° up and down / right and left in relation to the surface of the target.

Sokkia is a sponsor of the International Federation of Surveyors

SOKKIA CO., LTD. Head Office, Japan Phone +81-46-248-7984 www.sokkia.co.jp ISO9001 Certified (JQA-0557)
SOKKIA CORPORATION Head Office U.S.A. Phone +1-913-492-4900 www.sokkia.com
SOKKIA CORPORATION Head Office Canada Phone +1-905-238-5810 www.sokkia.com
SOKKIA LATIN AMERICA Head Office Latin America Phone +1-305-599-4701 www.sokkia.com
SOKKIA PTY. LTD. Head Office Australia, New Zealand and South Pacific Phone +61-2-9638-2400 www.sokkia.com.au
SOKKIA B.V. Head Office Europe & other CIS countries Phone +31-(0)36-5496000 www.sokkia.net
SOKKIA KOREA CO., LTD. Head Office Republic of Korea Phone +82-2-514-0491 www.sokkia.co.kr
SOKKIA SINGAPORE PTE. LTD. Head Office South & Southeast Asia, Middle East, and Africa Phone +65-6479-3966 www.sokkia.com.sg
SOKKIA SURVEYING INSTRUMENTS TRADING (SHANGHAI) CO., LTD. Shanghai Office, People's Republic of China Phone +86-21-63541844 www.sokkia.com.cn
SOKKIA SURVEYING INSTRUMENTS TRADING (SHANGHAI) CO., LTD. Beijing Office People's Republic of China Phone +86-10-65056066 www.sokkia.com.cn

A-182-E-10-0605-CH-AB Printed in Japan on 100% recycled paper with ecologically safe soy ink.

List of publications

A total number of 11 papers have been published in several international journals and also in national and international congresses. A last paper will be presented in November in the *Congreso Nacional de Ingeniería Mecánica*.

Journal papers

Cuadrado J. , Dopico D. , Pérez J. A. , and Pastorino R. . Automotive observers based on multibody models and the Extended Kalman Filter. *Multibody System Dynamics*, 27(1):3–19, 2011. doi: 10.1007/s11044-011-9251-1. iv, 4, 105, 112

Pastorino R. , Naya M. A. , Pérez J. A . , and Cuadrado J. . Geared PM coreless motor modelling for driver's force feedback in steer–by–wire systems. *Mechatronics*, 21(6):1043–1054, 2011. doi: 10.1016/j.mechatronics.2011.05.006. 20

Congress papers

Cuadrado J. , Dopico D. , Pérez J. A. , and Pastorino R. . Influence of the sensored magnitude in the performance of observers based on multibody models and the extended Kalman filter. In *Proceedings of the Multibody Dynamics ECCOMAS Thematic Conference*, Warsaw, Poland, June 2009. 4, 100, 111

Cuadrado J. , Dopico D. , Naya M. A. , and Pastorino R. . Automotive observers based on multibody models and the extended Kalman filter. In *The 1st Joint International Conference on Multibody System Dynamics*, Lappeenranta, Finland, May 2010. iv, 4, 105, 112

Pastorino R. . La simulation des systèmes multicorps dans l'automobile. *Interface, revue des ingénieurs des INSA de Lyon, Rennes, Rouen, Toulouse*, (111):22, 3ème et 4ème trimestre 2011.

Pastorino R. , Naya M. A. , Pérez J. A. , and Cuadrado J. . X–by–wire vehicle prototype: a steer–by–wire system with geared PM coreless motors. In *Proceedings of the 7th EUROMECH Solid Mechanics Conference*, Lisbon, Portugal, September 2009. 10

Pastorino R. , Naya M. A. , Luaces A. , and Cuadrado J. . X–by–wire vehicle prototype: automatic driving maneuver implementation for real–time MBS model validation. In *Proceedings of the 515th EUROMECH Colloquium*, Blagoevgrad, Bulgaria, 2010. 10, 14

Pastorino R. , Dopico D. , Sanjurjo E. , and Naya M. A. . Validation of a multibody model for an x–by–wire vehicle prototype through field testing. In *Proceedings of the ECCOMAS Thematic Conference Multibody Dynamics 2011*, Brussels, Belgium, 2011a.

Pastorino R. , Naya M. A. , Luaces A. , and Cuadrado J. . X–by–wire vehicle prototype : a tool for research on real–time vehicle multibody models. In *Proceedings of the 13th EAEC European Automotive Congress*, Valencia, Spain, June 2011b.

Pastorino R. , Richiedei D. , Cuadrado J. , and Trevisani A. . State estimation using multibody models and unscented Kalman filters. In *Proceedings of the 524th EUROMECH Colloquium*, Enschede, Netherlands, 2012a.

Pastorino R. , Richiedei D. , Cuadrado J. , and Trevisani A. . State estimation using multibody models and nonlinear Kalman filters. In *The 2nd Joint International Conference on Multibody Systems Dynamics*, Stuttgart, Germany, May 2012b.

Sanjurjo E. , Pastorino R. , Dopico D. , and Naya M. A. . Validación experimental de un modelo multicuerpo de un prototipo de vehículo automatizado. In *XIX Congreso Nacional de Ingeniería Mecánica (to be presented)*, Castellón, Spain, Nov. 2012.

References

Ambrósio J. A. C. . Crash analysis and dynamical behaviour of light road and rail vehicles. *Vehicle System Dynamics*, 43(6–7):385–411, 2005. 4

Ambrósio J. A. C. and Goncalves J. P. C. . Complex flexible multibody systems with application to vehicle dynamics. *Multibody System Dynamics*, 6(2):163–182, 2001. 3

Armstrong-Hélouvry B. , Dupont P. , and Wit Canudas de C. . A survey of models, analysis tools and compensation methods for the control of machines with friction. *Automatica*, 30:1083–1138, 1994. 20

Bae D. S. , Lee J. K. , Cho H. J. , and Yae H. . An explicit integration method for realtime simulation of multibody vehicle models. *Computer Methods in Applied Mechanics and Engineering*, 187(1–2): 337–350, June 2000. 4

Bajçinca N. , Cortesão R. , and Hauschild M. . Robust control for steer–by–wire vehicles. *Autonomous robots*, 19:193–214, 2005. 20, 21, 24

Bakker E. , Nyborg L. , , and Pacejka H. B. . Tyre modelling for use in vehicle dynamics studies. *SAE*, (Technical Paper 870421), 1987. doi: 10.4271/870421. 73

Bakker E. , Pacejka H. , and Lidner L. . A new tire model with an application in vehicle dynamics studies. *SAE*, (Technical Paper 890087), 1989. doi: 10.4271/890087. 73

Barreiro A. , Delgado E. , Cuadrado J. , and Dopico D. . Extended–kalman–filter observers for multibody dynamical systems. In *Sixth EUROMECH Nonlinear Dynamics Conference ENOC*, Saint Petersburg, Russia, June 2008. 4, 100, 105

Bayo E. and Ledesma R. . Augmented lagrangian and mass-orthogonal projection methods for constrained multibody dynamics. *Nonlinear Dynamics*, 9:113–130, 1996. ISSN 0924-090X. doi: 10.1007/BF01833296. 10.1007/BF01833296. 48

Bayo E. , Jalón García de J. , and Serna M. A. . A modified Lagrangian formulation for the dynamic analysis of constrained mechanical systems. *Computer Methods in Applied Mechanics and Engineering*, 71(2):183–195, 1988. 48

Bianchi N. , Bolognani S. , Dai Pré M. , Tomasini M. , Peretti L. , and Zigliotto M. . The steering effect. *IEEE industry applications magazine*, 14:40–48, 2008. 19

Blundell M. and Harty D. . *The multibody systems approach to vehicle dynamics*. Elsevier, September 2004. 3

Canudas de Wit C. , Olsson H. , Aström K. J. , and Lischinsky P. . A new model for control of systems with friction. *IEEE transactions on automatic control*, 40:419–425, 1995. 20, 25

Caracciolo R. , Richiedei D. , and Trevisani A. . Experimental validation of a model-based robust controller for multi-body mechanisms with flexible links. *Multibody System Dynamics*, 20(2):129–145, 2008. ISSN 1384-5640. doi: 10.1007/s11044-008-9113-7. 10.1007/s11044-008-9113-7. 100

Carvalho J. A. C. , M.and Ambrósio. Identification of multibody vehicle models for crash analysis using an optimization methodology. *Multibody System Dynamics*, 24(3):325–345, october 2010. 4

Chang Y.P. , El-Gindy M. , and Streit D. A. . Literature survey of transient dynamic response tyre models. *International Journal of Vehicle Design*, 34(4):354–386, May 2004. 73

Cheli F. and Sabbioni E. . A dynamic light–duty vehicle model: validation with indoor and outdoor experimental tests. In *ASME International Design Engineering Technical Conferences/Computers and Information in Engineering Conference*, volume 3, pages 1067–1074, Las Vegas, USA, Sept. 2007. 8

Chrstos J. P. and Grygier P. A. . Experimental testing of a 1994 ford taurus for NADSdyna validation. *SAE*, 106(6):895–908, Feb. 1997. 9

Chrstos J. P. and Heydinger G. J. . Evaluation of VDANL and VDM RoAD for predicting the vehicle dynamics of a 1994 Ford Taurus. *SAE*, (970566), 1997. 8

Cuadrado J. , Cardenal J. , Morer P. , and Bayo E. . Intelligent simulation of multibody dynamics: Space-state and descriptor methods in sequential and parallel computing environments. *Multibody System Dynamics*, 4:55–73, 2000. ISSN 1384-5640. doi: 10.1023/A:1009824327480. 10.1023/A:1009824327480. iii, 49

Cuadrado J. , Dopico D. , Naya M. A. , and González M. . Penalty, semi–recursive and hybrid methods for MBS real–time dynamics in the context of structural integrators. *Multibody System Dynamics*, 12(2):117–132, 2004a. iii

Cuadrado J. , Gutiérrez R. , Naya M. A. , and González M. . Experimental validation of a flexible MBS dynamic formulation through comparison between measured and calculated stresses on a prototype car. *Multibody System Dynamics*, 11(2):147–166, 2004b. iii, 3

Cuadrado J. , Dopico D. , Barreiro A. , and Delgado E. . Real–time state observers based on multibody models and the extended kalman filter. In *Proceedings of the 4th Asian Conference on Multibody Dynamics*, number 127, Jeju, Korea, August 2008. 4, 100, 105, 109

Cuadrado J. , Dopico D. , Barreiro A. , and Delgado E. . Real–time state observers based on multibody models and the extended kalman filter. *Journal of Mechanical Science and Technology*, 23(4): 894–900, 2009a. doi: 10.1007/s12206-009-0308-5. 4, 100, 105, 109, 110

Cuadrado J. , Dopico D. , Pérez J. A. , and Pastorino R. . Influence of the sensored magnitude in the performance of observers based on multibody models and the extended Kalman filter. In *Proceedings of the Multibody Dynamics ECCOMAS Thematic Conference*, Warsaw, Poland, June 2009b. 4, 100, 111

Cuadrado J. , Dopico D. , Naya M. A. , and Pastorino R. . Automotive observers based on multibody models and the extended Kalman filter. In *The 1st Joint International Conference on Multibody System Dynamics*, Lappeenranta, Finland, May 2010. iv, 4, 105, 112

Cuadrado J. , Dopico D. , Pérez J. A. , and Pastorino R. . Automotive observers based on multibody models and the Extended Kalman Filter. *Multibody System Dynamics*, 27(1):3–19, 2011. doi: 10.1007/s11044-011-9251-1. iv, 4, 105, 112

Dohring M. E. , Lee E. , and Newman W. S. . A load–dependent transmission fricton model: theory and experiments. In *ieee international conference on robotics and automation*, volume 3, pages 430–436, 1993. 26

Dopico D. , Luaces A. , Gonzalez M. , and Cuadrado J. . Dealing with multiple contacts in a human–in–the–loop application. *Multibody System Dynamics*, 25(2):167–183, 2011. 80, 81, 83

Evers W. J. , Besselink I. , Nijmeijer H. , and Knaap Van der A. . Development and validation of a modular simulation model for commercial vehicles. *International Journal of Heavy Vehicle Systems*, 16(1/2):132–153, 2009. 8

Fischer E. . Standard multi–body system software in the vehicle development process. *Proceedings of the institution of mechanical engineers, part K: journal of multi–body dynamics*, 221:13–20, 2007. 2

García de Jalón J. and Bayo E. . *Kinematic and Dynamic Simulation of Multibody Systems: The Real–Time challenge*. Springer–Verlag, 1994. 4, 48, 103, 109, 112, 120

Jalón García de Javier . Twenty–five years of natural coordinates. *Multibody System Dynamics*, 18: 15–33, 2007. ISSN 1384-5640. doi: 10.1007/s11044-007-9068-0. 10.1007/s11044-007-9068-0. 48

Garrott W. Riley , Grygier Paul A. , Chrstos Jeffrey P. , Heydinger Gary J. , Salaani Kamel M. , Howe J. Gavin , and Guenther Dennis A. . Methodology for validating the National Advanced Driving Simulator Vehicle Dynamics (NADSdyna). *SAE*, 106(6):882–894, Feb. 1997. doi: 10.4271/970562. iii, 8, 9

Gillespie T. D. . *Fundamentals of Vehicle Dynamics*. Society of Automotive Engineers, 1992. 2, 73

Grewal M. S. and Andrews A. P. . *Kalman Filtering – Theory and Practice Using MATLAB*. John Wiley & Sons, Inc., 3rd edition, 2008. iv, 100

Gualino D. and Adounkpé I. J. . Force–feedback system design for the steer–by–wire: optimisation and performance evaluation. In *Proceedings of the IEEE ITSC*, pages 181–187, Toronto, Canada, September 2006. 20

Hegazy S. , Rahnejat H. , and Hussain K. . Multi–body dynamics in full–vehicle handling analysis under transient manoeuvre. *Vehicle System Dynamics*, 34:1–24, July 2000. 3

Heitzer D. and Seewald A. . Development of a fault tolerant steer–by–wire steering system. *SAE*, (2004–21–0046), 2004. 20

Heydinger G. J. , Salaani M. K. , Garrott W. R. , and Grygier P. A. . Vehicle dynamics modelling for the National Advanced Driving Simulator. In *Proceedings of the institution of mechanical engineers, part D: journal of automobile engineering*, volume 216, pages 307–318, 2002. 4

Heydinger G. J. , Schwarz C. , and Salaani Grygier P. A. , M. K. Model validation of the 2006 BMW 330i for the National Advanced Driving Simulator. *SAE*, SP–2138(2007–01–0817), Apr. 2007. 9, 10

Hirschberg W. , Rill G. , and Weinfurter H. . Tire model TMeasy. *Vehicle System Dynamics*, 45: 101–119, 2007. 74, 76

Hoskins A.H. and El-Gindy M. . Technical report: Literature survey on driving simulator validation studies. *International Journal of Heavy Vehicle Systems*, 13(3):241–252, 2006. iii, 2, 8

Hussain K. , Rahnejat H. , and Hegazy S. . Transient vehicle handling analysis with aerodynamic interactions. *Proceedings of the Institution of Mechanical Engineers, Part K: Journal of Multi–body Dynamics*, 221(21):21–32, 2007. doi: 10.1243/1464419JMBD41. 3

Iyasere E. , Black J. , Kinstle M. , Post B. , Wagner J. , and Dawson D. . A real time re–configurable steering simulator for system design studies. In *Proceedings of the 2007 american control conference*, volume 1–13, pages 3760–3766, New York, USA, July 2007. 20

Jazar R. N. . *Vehicle Dynamics: Theory and Application*. Number 978–0–387–74243–4. Springer, March 2008. 2, 73

Julier S. J. . The spherical simplex unscented transformation. In *Proceedings of the American Control Conference*, volume 3, pages 2430–2434, June 2003. 100, 119

Julier S. J. and Uhlmann J. K. . A new extension of the kalman filter to nonlinear systems. In *The 11th International Symposium on Aerospace/Defense Sensing, Simulation and Controls*, pages 182–193, Orlando, FL, USA, 1997. 100

Julier S. J. and Uhlmann J. K. . Unscented filtering and nonlinear estimation. In *Proceedings of the IEEE*, volume 92, pages 401–422, March 2004. iv, 100, 114

Julier S. J. , Uhlmann J. K. , and Durrant-Whyte H. F. . A new approach for filtering nonlinear systems. In *Proc. American Control Conf*, volume 3, pages 1628–1632, 1995. doi: 10.1109/ACC.1995.529783. 100

Julier S.J. and Uhlmann J.K. . Reduced sigma point filters for the propagation of means and covariances through nonlinear transformations. In *Proceedings of the American Control Conference*, volume 2, pages 887–892, November 2002. 100

Kalman R. E. and Bucy R. S. . New results in linear filtering and prediction theory. *Transactions of the ASME. Series D, Journal of Basic Engineering*, 83:95–107, 1961. 100

Kalman Rudolph Emil . A new approach to linear filtering and prediction problems. *Transactions of the ASME–Journal of Basic Engineering*, 82(Series D):35–45, 1960. 100

Katsura S. , Matsumoto Y. , and Ohnishi K. . Modeling of force sensing and validation observer for force control. *IEEE transactions on industrial electronics*, 54:530–538, 2007. 21

Kim C. . An accurate full car ride model using model reducing techniques. *Journal of Mechanical Design*, 124(4):697–705, 2002a. 4

Kim K. , Kim J. , Huh K. S. , Yi K. , and Cho D. . A real–time multi–vehicle simulator for longitudinal controller design. *Vehicle System Dynamics*, 44(5):369–386, May 2006. 4

Kim S. S. . A subsystem synthesis method for efficient vehicle multibody dynamics. *Multibody System Dynamics*, 7(2):189–207, 2002b. 4

Kim S. S. and Jeong W. H. . Real–time multibody vehicle model with bush compliance effect using quasi–static analysis for hils. *Multibody System Dynamics*, 22(4):367–382, May 2009. 4

Kim S. S. , Jung H. K. , Shim J. S. , and Kim C. W. . Development of vehicle dynamics model for real–time electronic control unit evaluation system using kinematic and compliance test data. *International Journal of Automotive Technology*, 6(6):599–605, 2005. 8

Kinjawadekar T. , Dixit N. , Heydinger G. J. , Guenther D. A. , and Salaani M. K. . Vehicle dynamics modeling and validation of the 2003 ford expedition with esc using carsim. *SAE*, SP–2221 (2009–01–0452), Apr. 2009. 8

Körtum W. , W & Schiehlen. General purpose vehicle system dynamics software based on multibody formalisms. *Vehicle System Dynamics*, 14(4–6):229–263, 1985. iii, 2

Kuiper E. and Van Oosten J. J. M. . The pac2002 advanced handling tire model. *Vehicle System Dynamics*, 45(1):153–167, 2007. 73, 74

Lehtonen T. J. . Validation of an agricultural tractor MBS model. *International Journal of Heavy Vehicle Systems*, 12(1):16–27, 2005. 8

Lugner P. and Plöch M. . Modelling in vehicle dynamics of automobiles. *Journal of Applied Mathematics and Mechanics*, 84(4), April 2004. 2

Márton L. and Lantos B. . Control of mechanical systems with stribeck friction and backlash. *Systems & Control Letters*, 58:141–147, 2009. 20

Menon K. and K. Krishnamurthy . Control of low velocity friction and gear backlash in a machine tool feed drive system. *Mechatronics*, 9:33–52, 1999. 20

Naya M. A. , Dopico D. , Pérez J. A . , and Cuadrado J. . Real–time multi–body formulation for virtual–reality–based design and evaluation of automobile controllers. In *Proceedings of the institution of mechanical engineers, part K: journal of multi–body dynamics*, volume 221, pages 261–276, 2007. iii, 2, 4

Nordin M. and Gutman P. O. . Controlling mechanical systems with backlash – a survey. *Automatica*, 38:1633–1649, 2002. 20, 24

Nørgaard M. , Poulsen N. K. , and Ravn O. . New developments in state estimation for nonlinear systems. *Automatica*, 36(11):1627 – 1638, 2000. ISSN 0005-1098. doi: 10.1016/S0005-1098(00)00089-3. 100

Pacejka H. B. . *Tire and Vehicle Dynamics*. Butterworth-Heinemann, Oxford, 2002. 73

Pacejka H. B. . *Tire and Vehicle Dynamics*. SAE International and Elsevier, Dec. 2005. 73

Pacejka H. B. and Bakker E. . The magic formula tyre model. In Pacejka H.B. , editor, *Proceedings of 1st Colloquium on Tyre Models for Vehicle Analysis*, number 21, Delft, 1993. Suppl. Vehicle System Dynamics. 73

Pacejka H. B. and Besselink I. J. M. . Magic formula tyre model with transient properties. *Vehicle System Dynamics*, 27:234–249, 1997. 73

Pacejka H. B. and Sharp R. S. . Shear force development by pneumatic tyres in steady state conditions: A review of modelling aspects. *Vehicle System Dynamics*, 20(3-4):121–175, 1991. doi: 10.1080/00423119108968983. 73

Pankiewicz E. and Rulka W. . From off–line to real time simulations by model reduction and modular vehicle modelling. In *ASME 2003 Design Engineering Technical Conferences and Computers and Information in Engineering Conference*, Chicago, Illinois, USA, September 2003. 4

Parker M. W. , Shoopa S. A. , Coutermarsha B. A. , Wessona K. D. , and Stanley J. M. . Verification and validation of a winter driving simulator. *Journal of Terramechanics*, 46(4):127–139, Aug. 2009. 8

Pastorino R. . La simulation des systèmes multicorps dans l'automobile. *Interface, revue des ingénieurs des INSA de Lyon, Rennes, Rouen, Toulouse*, (111):22, 3ème et 4ème trimestre 2011.

Pastorino R. , Naya M. A. , Pérez J. A. , and Cuadrado J. . X–by–wire vehicle prototype: a steer–by–wire system with geared PM coreless motors. In *Proceedings of the 7th EUROMECH Solid Mechanics Conference*, Lisbon, Portugal, September 2009. 10

Pastorino R. , Naya M. A. , Luaces A. , and Cuadrado J. . X–by–wire vehicle prototype: automatic driving maneuver implementation for real–time MBS model validation. In *Proceedings of the 515th EUROMECH Colloquium*, Blagoevgrad, Bulgaria, 2010. 10, 14

Pastorino R. , Dopico D. , Sanjurjo E. , and Naya M. A. . Validation of a multibody model for an x–by–wire vehicle prototype through field testing. In *Proceedings of the ECCOMAS Thematic Conference Multibody Dynamics 2011*, Brussels, Belgium, 2011a.

Pastorino R. , Naya M. A. , Luaces A. , and Cuadrado J. . X–by–wire vehicle prototype : a tool for research on real–time vehicle multibody models. In *Proceedings of the 13th EAEC European Automotive Congress*, Valencia, Spain, June 2011b.

Pastorino R. , Naya M. A. , Pérez J. A . , and Cuadrado J. . Geared PM coreless motor modelling for driver's force feedback in steer–by–wire systems. *Mechatronics*, 21(6):1043–1054, 2011c. doi: 10.1016/j.mechatronics.2011.05.006. 20

Pastorino R. , Richiedei D. , Cuadrado J. , and Trevisani A. . State estimation using multibody models and unscented Kalman filters. In *Proceedings of the 524th EUROMECH Colloquium*, Enschede, Netherlands, 2012a.

Pastorino R. , Richiedei D. , Cuadrado J. , and Trevisani A. . State estimation using multibody models and nonlinear Kalman filters. In *The 2nd Joint International Conference on Multibody Systems Dynamics*, Stuttgart, Germany, May 2012b.

Popp K. and Schielhen W. . *Ground Vehicle Dynamics*. Springer, 2010. 3, 73

Radke A. and Gao Z. . A survey of state and disturbance observers for practitioners. In *Proceedings of the American Control Conference*, pages 5183–5188, Minneapolis, Minnesota, USA, June 2006. 100

Rao S. J. , Heydinger G. J. , Salaani M. K. , and Guenther D. . Vehicle dynamics modeling and validation for the 2003 ford expedition with ESC using adams view. *SAE*, SP–2221(2009–01–0453), 2009. 8

Rauh J. . Virtual development of ride and handling characteristics for advanced passenger cars. *Vehicle System Dynamics*, 40(1):135–155, 2003. 2

Rebelle J. , Mistrot P. , and Poirot R. . Development and validation of a numerical model for predicting forklift truck tip–over. *Vehicle System Dynamics*, 47(7):771–804, 2009. 8

Rill G. . First order tire dynamics. In *III European Conference on Computational Mechanics: Solids, Structures and Coupled Problems in Engineering*, Lisbon, Portugal, June, 5–8 2006a. 74

Rill G. . Vehicle modeling by subsystems. *Journal of the Brazilian Society of Mechanical Sciences and Engineering*, 28(4):430–442, 2006b. 3

Rill G. . Wheel dynamics. In *Proceedings of the XII International Symposium on Dynamic Problems of Mechanics (DINAME 2007)*, Ilhabela, SP, Brazil, Feb. 2007. 74

Rill G. . Dynamic tire forces with smooth transition to stand–still. In *7th EUROMECH Solid Mechanics Conference*, Lisbon, Portugal, September 2009. 74

Rill G. and Cornelius Chucholowski . Real time simulations of large vehicle systems. In *Proceedings of the ECCOMAS thematic conference Multibody Dynamics 2007*, Milano, Italy, June 2007. 4

Romano R. . Real–time multi–body vehicle dynamics using a modular modelling methodology. In *SAE 2003 World Congress & Exhibition*, Detroit, MI, USA, March 2003. doi: 10.4271/2003--01--1286. 8

Romano R. and Schultz S. . Validation of real–time multi–body vehicle dynamics models for use in product design and acquisition. In *SAE 2004 World Congress & Exhibition*, Detroit, MI, USA, March 2004. doi: 10.4271/2004--01--1582. 8

Rulka W. and Pankiewicz E. . MBS approach to generate equations of motions for HiL-simulations in vehicle system dynamics. *Multibody System Dynamics*, 14(3–4):367–386, Dic. 2005. 4

Salaani M. , Scwarz C. , Heydinger G. J. , and Grygier P. A. . Parameter determination and vehicle dynamics modeling for the National Advanced Driving Simulator of the 2006 BMW 330i. *SAE*, SP–2138(2007–01–0818), 2007. 4, 10

Salaani M. K. and Heydinger G. J. . Model validation of the 1997 Jeep Cherokee for the National Advanced Driving Simulator. In *Proceedings of the SAE 2000 World Congress*, number 2000–01–0700, Detroit, USA, Mar. 2000. 9, 10

Salaani M. K. , Chrstos J. P. , and Guenther D. A. . Parameter measurement and development of a NADSdyna validation data set for a 1994 ford taurus. *SAE*, (970564), 1997a. 10

Salaani M. K. , Heydinger G. J. , and Guenther D. A. . Validation results from using NADSdyna vehicle dynamics simulation. *SAE*, (970565), 1997b. 10

Salaani M. K. , Grygier P. A. , and Heydinger G. J. . Model validation of the 1998 chevrolet malibu for the National Advanced Driving Simulator. *SAE*, (2001–01–0141), Mar. 2001. 9, 10

Samin J. C. and Fisette P. . *Symbolic Modeling of Multibody Systems*. Springer, 2004. 4

Sanjurjo E. , Pastorino R. , Dopico D. , and Naya M. A. . Validación experimental de un modelo multicuerpo de un prototipo de vehículo automatizado. In *XIX Congreso Nacional de Ingeniería Mecánica (to be presented)*, Castellón, Spain, Nov. 2012.

Sayers M. W. . A generic multibody vehicle model for simulating handling and braking. *Vehicle System Dynamics*, 25(S):599–613, 1996. 4

Sayers M. W. . Vehicle models for RTS applications. *Vehicle System Dynamics*, 32(4–5):421–438, November 1999. 4, 8

Shiiba T. . Development of driving simulator with full vehicle model of multibody dynamics. *JSAE Review*, 23(2):223–230, 2002. 4

Shiiba T. and Suda Y. . Evaluation of driver's behavior with multibody–based driving simulator. *Multibody System Dynamics*, 17(2–3):195–208, april 2007. 4

Sousa L. , Verissimo P. , and Ambrósio J. . Development of generic multibody road vehicle models for crashworthiness. *Multibody System Dynamics*, 19(1–2):133–158, february 2008. 4

Swevers J. , Al-Bender F. , Ganseman C. G. , and Prajogo T. . An integrated friction model structure with improved presliding behavior for accurate friction compensation. *IEEE transactions on automatic control*, 45:675–686, 2000. 20, 25

Tseng H.E. , Ashrafi B. , Madau D. , Allen Brown T. , and Recker D. . The development of vehicle stability control, vehicle at ford. *IEEE/ASME Transactions on Mechatronics*, 4(3):223–234, September 1999. iv, 2

Merwe Van der R. and Wan E.A. . The square–root unscented Kalman filter for state and parameter–estimation. In *IEEE International Conference on Acoustics, Speech, and Signal Processing*, volume 6, pages 3461–3464, Salt Lake City, USA, 2001. 100

Merwe Van der R. , Wan E. A. , and Julier S. . Sigma–point Kalman filters for nonlinear estimation and sensor–fusion – applications to integrated navigation. In *AIAA Guidance, Navigation, and Control Conference and Exhibit*, Rhode Island, USA, August 2004. 100

Verschuren R.M.A.F. and Duringhof H.M. . Design of a steer–by–wire prototype. *SAE International*, (2006–01–1497), 2006. 20

Wei-qun Ren , Yun-qing Zhang , and Guo-dong Jin . A new application of multi–body system dynamics in vehicle–road interaction simulation. *Wuhan University Journal of Natural Sciences*, 8:379–382, 2003. ISSN 1007–1202. 10.1007/BF02907215. 8

Wernholt E. and Gunnarsson S. . Nonlinear identification of a physically parameterized robot model. In *14th IFAC Symposium on system identification*, pages 143–148, Newcastle, Australia, 2006. 20, 24

Wong J. Y. . *Theory of ground vehicles*. John Wiley & Sons, Inc., 2001. 2, 73

Yih P. and Gerdes J. C. . Modification of vehicle handling characteristics via steer–by–wire. *IEEE transactions on control systems technology*, 13(6):965–976, 2005. 19